HVDC Transmission and AC hubs for Offshore Wind Generation

Jonathan Mark Stevens

School of Engineering

Cardiff University

A thesis submitted for the degree of

Doctor of Philosophy

September, 2015

To my partner Anett, and to my entire family for their unwavering support and encouragement throughout this endeavour.

Acknowledgements

Abstract

Name of University: Cardiff University

Candidate's Name: Jonathan Mark Stevens

Degree Title: Doctor of Philosophy

Thesis Title: HVDC Transmission and AC Hubs for Offshore Generation

Date: September 2015

The offshore AC hub was identified as a feasible network topology for an offshore node applied in a future pan-European Supergrid. A model of an offshore AC hub was developed in SimPowerSystems^{TM} using the round three offshore wind development zone Dogger Bank, as a case study.

Two control philosophies, master-slave and droop control, are shown to successfully manage the voltage, current and complex power flow in the offshore AC hub following planned changes in operating conditions.

The impacts of three different fault scenarios on the offshore AC hub are investigated. It is shown that each fault severely impedes normal operation of equipment in the offshore AC hub, as equipment ratings are exceeded. In addition, the loss of infeed to the onshore UK power network is extensive. Based on these outcomes, it is identified that additional fault management systems are required.

A novel centralised fault management system is then developed based on an online OPF algorithm. The performance is compared to de-centralised fault management system, and advantages and disadvantages of the two methods are discussed. The centralised fault management system is implemented on a real-time platform as hardware-in-the-loop, with the offshore AC hub implemented on a Real Time Digital Simulator. The simulation and experimental results are then compared to confirm the validity of the simulation results.

Contents

List of Figures

List of Tables

Abbreviations

AC	Alternating current
CB	Circuit breaker
CSC	Current source converter
DC	Direct current
EU	European Union
FRC	Fully rated converter
FRT	Fault ride through
GEP	Grid entry point
HV	High voltage
IGBT	Insulated gate bi-polar transistor
IP	Interface point
LCC	Line commutated converter
MITS	Main interconnected transmission system
MMC	Multi-modular converter
MV	Medium voltage
OPF	Optimal power flow
PWM	Pulse width modulation
SCADA	Supervisory control and data acquisition
TSO	Transmission system operator
VSC	Voltage source converter
WT	Wind turbine
XLPE	Cross linked polyethylene

1   Chapter 1 – Introduction

1.1   Background

Significant change is on the horizon for the way in which electricity is generated, transmitted and consumed in the UK, Europe and indeed the rest of the world. An ever increasing world population demands increasing amounts of electricity generation. Currently, the majority of electricity generation is met through the burning of fossil fuels, which are of course a finite resource. Furthermore, the burning of these fossil fuels contributes a significant portion of the greenhouse gases which are being released into the atmosphere. Therefore it is widely recognised that if significant climate change is to be avoided, a change in the mix of electricity generation is required.

As energy production currently accounts for the largest share of UK greenhouse gas emissions, the UK government has recognised the importance of low-carbon and renewable forms of energy production in avoiding significant climate change. In 2008, The Climate Change Act came into force, which legally requires the UK to reduce greenhouse gas emissions to at least 80% below 1990 levels by 2050 [1]. On a European level, the EU Climate and Energy Package has committed the EU to achieving a 20% reduction in greenhouse gas emissions, a 20% improvement in energy efficiency and for 20% of energy to come from renewable resources by 2020. Under this agreement, the UK has a target to deliver 15% of its energy from renewable energy resources by 2020 [2].

1.2   Offshore Wind Farms

The UK is fortunate to have a vast amount of renewable energy resources both on and offshore. In fact, the UK has the largest potential wind energy resource in Europe with the North Sea alone able to provide hundreds of Gigawatts of wind power [3]. Offshore wind is more technologically challenging and expensive than onshore wind, however it has a larger potential energy yield due to a more consistent wind resource out at sea [2].

To allow access to this vast offshore wind energy resource within UK territorial limits, the Crown Estate has held a number of leasing rounds, allocating defined areas of the seabed to potential wind farm developers. In 2000, the first Round (Round 1), permitted developers to install small wind farms, consisting of a maximum of 30 wind turbines, in water depths of less than 20m and no further than 12km offshore. Round 2 followed in 2003, with 15 projects having a combined capacity of 7.2GW and located no further than 40km offshore. In 2010, Round 3 development zones were defined which allocated enough seabed area for generation capacity of around 35GW and located at distances of up to 290km offshore. Figure 1.1 shows the offshore wind development zones as defined by the Crown Estate [4].

Figure 1.1 – Offshore Wind development zones as described by the Crown Estate [4]
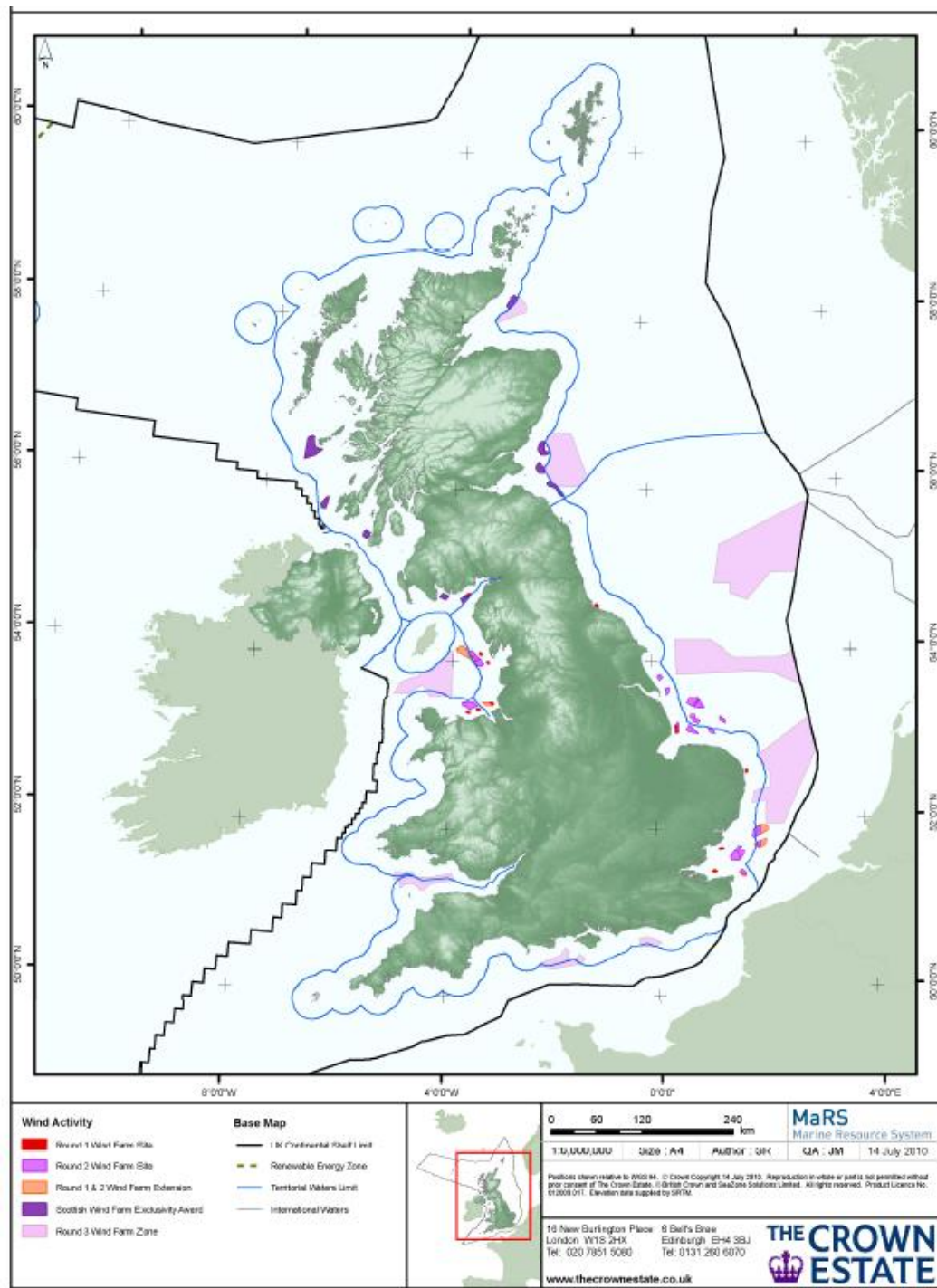
1.3 HVDC Transmission and the Supergrid

The challenge lies in how this wind power can be harvested efficiently, in terms of both cost and performance. The extent of the challenge is largely dependent on the scale of the project considered and the distance it is to be located offshore. In fact, many of the largest wind farms are located a considerable distance from

shore. This causes problems for the transmission of energy using conventional High Voltage Alternating Current (HVAC) transmission cables, because the capacitance of the cable causes excessive charging currents leaving less capacity for useful current flow. High Voltage Direct Current (HVDC) transmission, by its very nature does not have oscillatory charging currents and therefore has been thoroughly explored as a solution to this problem [5]–[8].

Additionally, reinforcement of the onshore grid infrastructure is required to facilitate the connection of the offshore wind generation and transport the energy to load centres accordingly. This is another important factor influencing the final connection distance from an offshore wind farm to the onshore connection point, because the closest point to shore may not be acceptable for receiving a connection for technical and or environmental reasons [4].

Parallel to the requirements for increased power generation from renewable energy sources, there exists the necessity to maintain and/or improve security of supply. A major driving force behind the movement to increase offshore wind generation in the UK is to reduce its dependency on gas and oil from unstable regions. Of course, renewable energy is an intermittent resource. Including various sources of renewable energy (i.e. wind, solar and hydro), located in different locations, can overcome the intermittency of any single resource. One method of achieving this is to increase interconnection between other countries. This would allow any abundance of renewable energy to be exported and any shortfall made up from imported, renewable energy resources. Realistically, there will need to be some form of back-up capacity provided from flexible fossil-fuel power stations, however it is environmentally advantageous to keep this to a minimum [2].

In light of the aforementioned challenges associated with the integration of renewable energy resources, there has been widespread support from various parties for the formation of a pan-European transmission network or as it is widely known, a European Supergrid. The term "Supergrid" is not new to electricity infrastructure; it was first used to describe the 275/400kV British national electricity system developed in the 1950's. In the 21st century, the term "Supergrid" describes a system performing two main functions. One being to

4

provide interconnection between the different electricity transmission networks located within Europe and the second being to aggregate renewable energy resources using the same infrastructure [9].

The implementation of a Supergrid is by no means straightforward. Many technical and economic challenges exist if such a scheme is to be realised. While there is considerable experience in the use of HVDC transmission technology for point-to-point connections, there is very little experience of using HVDC within a grid topology. The topology, components, control and protection arrangements of such a Supergrid are still the subject of on-going research, attracting a large amount of interest from both Industry and Academia.

1.4   Research Objectives

The objective of this thesis is to investigate the viability of using Voltage Source Converter (VSC) HVDC links to both interconnect onshore HVAC transmission systems and provide for the connection of offshore wind farms in remote locations. Particular contributions of this thesis include:

- To **design a suitable control system for operating an offshore AC hub under planned changes in operating conditions**. This is achieved through the implementation of both master-slave and droop control schemes.

- To **identify the implications of various faults in an offshore AC hub**, in particular, the loss of infeed to the main interconnected transmission system.

- To **design a suitable control system to manage the impacts of faults in an offshore AC hub**. The performance of the novel centralised fault management system presented in this thesis is compared with a de-centralised method adapted from literature.

- To **design and build an experiment using hardware in the loop to demonstrate and validate the novel control system for managing the impact of faults in an offshore AC hub**. A Real Time Digital Simulator (RTDS) was used along with a dSPACE real time control platform.

2 Chapter 2 – Literature Review

2.1 The Supergrid

From a European perspective, it is widely considered that offshore infrastructure development will result in the development of a pan-European transmission network, dubbed the "Supergrid", as shown in Figure 2.1.
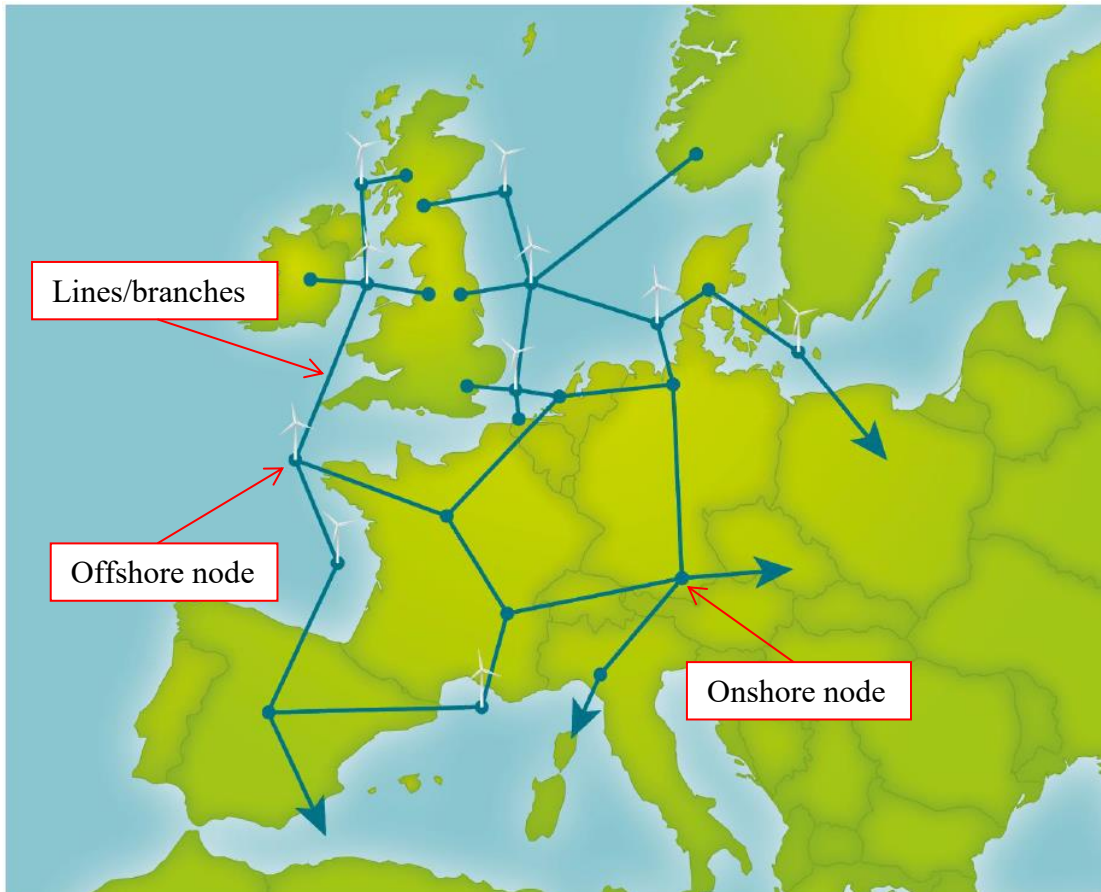
Figure 2.1 – Overview of a pan-European Supergrid in 2050 (adapted from [10])

Upon investigation of the driving factors behind the requirement for such a Supergrid, the following points are most prominent [11]–[13],

- All European member states have agreed to legally binding targets to cut greenhouse gas emissions.

- Offshore Wind has the potential to generate 500TWh per year by 2030, with hundreds of Gigawatts available in the North Sea alone.

- A reliable, modernised and efficient grid is required, both onshore and offshore in order to integrate renewable energy sources.

6

- The challenge offshore is to connect harvested energy from the sea, while building a system, which can actively contribute to stability and security of supply and increase trade links.

Of course, individual member states could act to meet their own obligations towards the integration of renewable energy resources, through the development of isolated offshore infrastructure systems, however, it is identified that the Supergrid concept would provide a number of benefits as listed in the following points [10], [12], [13],

- A Supergrid will facilitate the integration of large offshore renewable energy projects, often located in remote locations.

- It will enable spatial smoothing through aggregation of resources, thus the variability of the renewable energy sources is reduced (e.g. Interconnection with Scandinavia will provide access to hydro energy storage facilities).

- Overcomes many of the issues associated with installing new overhead lines or underground cables within onshore networks, effectively a bypass is provided thus reducing congestion of power flows from energy source to load centre.

- It will increase the security of supply through reduced dependency on gas and oil from unstable regions.

- It will improve trade and competition in energy markets through provision of more interconnections between countries, resulting in increased possibilities for arbitrage and limitation of price spikes.

For any development to take place there must be the relevant impetus from key parties with an inherent association or stake in such a scheme. Many of those key parties are described below,

- The European Commission has published "Guidelines for trans-European energy infrastructure", which has identified 12 priority corridors concerning various mediums for the transportation of energy (electricity, gas, oil and carbon dioxide) throughout Europe. One energy corridor highlighted which is of particular interest to this work is the Northern Seas Offshore Grid (NSOG) [14].

- ENTSO-E which represents the European TSOs has established a working group called the "2050 Electricity highways working group". The task of the working group is to develop a method to support the planning of a future pan-European

transmission network between 2020 and 2050 [15]. To achieve the renewable targets up to 2020, another working group called the North Seas Countries' Offshore Grid Initiative (NSCOGI) was formed. The task of NSCOGI is to evaluate and facilitate the co-ordinated development of an offshore grid in the North sea [16].

- The OffshoreGrid project consortium has provided an in-depth analysis of how to build a cost-efficient offshore grid in the north and Baltic seas. The project is supported by the EC's Intelligent Energy Europe program. The project partners consist of a number of renewable energy consultancies and agencies. (3E, ForWind, EWEA, Senergy Econnect etc) [11].

- The Friends of the Supergrid (FOSG) is a group of companies that have a mutual interest in promoting and influencing the policy and regulatory framework required to enable large-scale interconnection in Europe [10].

Finally, the basic elements of such a Supergrid were investigated and are as follows,

- Lines/branches: These include HVAC or HVDC links that provide the route by which the power can flow between onshore and offshore nodes.

- Offshore Nodes or Hubs: These provide a common connection point for a number of offshore wind farms and serve as intersections between network branches to provide interconnection between European member states.

- Onshore Nodes or Connection points: These provide the connection point between the offshore transmission system and onshore transmission system.

2.2 Offshore Transmission

Considering the development of offshore wind generation in the UK, two main factors are apparent which influence the choice of transmission medium. One factor is the rated generation output of the offshore wind farm and therefore the number of cables required to transmit the rated output. The other factor is the distance between the offshore wind farm and the onshore connection point and therefore the required cable route length. The three main transmission mediums used to date include Medium Voltage AC (MVAC, typically 33kV), High Voltage AC (HVAC, typically 132kV) and High Voltage DC (HVDC).

8

MVAC is typically only used for small wind farms with a capacity no greater than 100MW and which are located less than 30km offshore [17]. When considering a Supergrid, it is unlikely that such a small wind farm would be connected within the Supergrid as it will be cheaper to make a connection directly back to the onshore system, rather than trying to connect to a point offshore. In addition, the low transmission capacity would limit any further function to transmit power within a Supergrid. MVAC will mostly be utilised for the inter-array cabling of an offshore wind farm.

While it is expected that both HVAC and HVDC will be necessary transmission mediums for branches within a Supergrid, the majority of branches will be HVDC. This is due to a number of factors as is discussed in section 2.2.1 & 2.2.2.

2.2.1   HVAC Transmission

Current XLPE cable technology permits voltages of up to 420kV AC for single core cables and 275kV AC for three core cables. Although single-core cables typically provide higher rating, three separate conductors must be laid which increases installation costs. A typical three-core XLPE HVAC cable with 800mm2 copper conductors at a voltage of 220kV has a rated transmission capacity of approximately 330MVA [18].

An inherent limiting factor of HVAC cables is their high shunt capacitance [19]. The effect of this increased capacitance is to generate a large amount of reactive power along the cable's length. The generation of reactive power replaces what would be useful active power flow through the cable for a given MVA rating. In addition, reactive power compensation must be installed, usually at both ends of the cable to absorb the reactive power [4], [20] and prevent undesirable voltage rises at low load.

The reactive power, Q_C, generated in a cable due to the capacitance is given by the following equation:

$$Q_C = 2\pi f l C V^2 \qquad (2.1)$$

Where f is the frequency (Hz), V is the rated voltage (kV), l is the length of the cable (km) and C is the capacitance of the cable per unit length (F/km) [17].

It can be seen that the generated reactive power increases proportionally with the length of the cable. In addition, it increases with the square of the voltage. Hence longer,

higher voltage cables require significantly more compensation. HVAC cables offer feasible transmission of power for distances of up to approximately 90km [17].

2.2.2 HVDC Transmission

HVDC transmission has been in operation commercially for more than 50 years [5]. Over this time, the technology used to perform the transition between AC and DC (rectification) and vice versa (inversion), known generally as static power conversion, has changed dramatically.

2.2.2.1 Line commutated current source converters (LCC-CSC),

The majority of HVDC transmission infrastructure installed today is based on the LCC-CSC configuration, as presented in Figure 2.2.
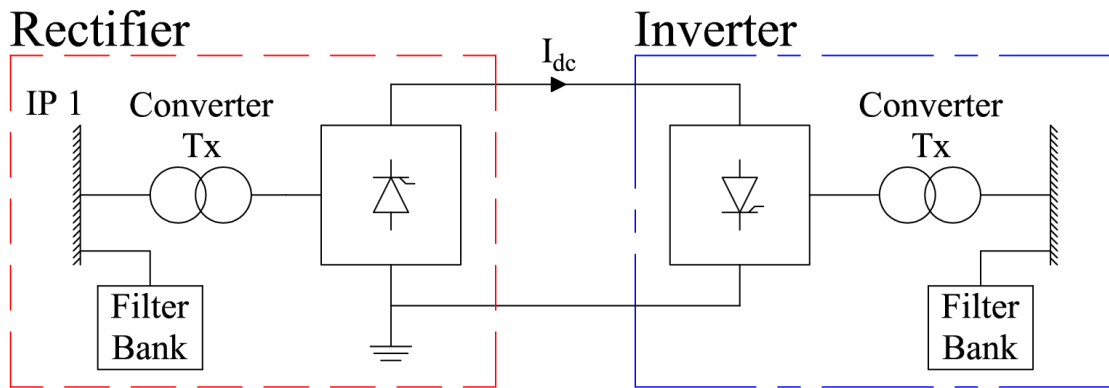
Figure 2.2 – Single line diagram of an LCC-CSC

The term 'line commutated converter' refers to the commutation source of the switching devices within the static power converter, where each switching device is commutated by the natural current zeros of the AC line to which it is connected. The term 'current source converter' refers to the constant quantity on the DC side in which a constant direct current is maintained and the DC voltage is controlled according to the switching of the devices, thus controlling the amount of power transferred [21].

Thyristors are used as the switching devices within LCC-CSC and benefit from being able to handle a large amount of current, being reliable in operation and having relatively low on-state losses [22]. The standard thyristors or Silicon Controlled Rectifier (SCR) as it is otherwise known can be turned on by an external gate input but cannot be turned off by the gate input. Thyristors have been developed which can be turned off using the gate input such as the Gate Turn Off (GTO) thyristors and Insulated Gate Commutated Thyristor (IGCT). However, GTOs and IGCTs require complex gate

circuits to turn the device on and off, which adds additional cost and complexity. For that reason, SCRs are most commonly used in HVDC applications [21].

For the SCR, a firing angle is specified which determines the delay between the voltage crossing between two phases and the firing instant. The instant at which the device is turned on determines the DC voltage level and hence active power transfer through the link. In order to turn off the device, the current must fall below a certain value for a certain amount of time, hence the requirement for line commutation [21].

The total duration required to turn-off one device and turn on the next is known as the commutation time. The commutation time is strongly influenced by the AC system reactance, AC voltage and firing angle. A larger AC system reactance will reduce the rate of change of current and hence lengthen the commutation time. The consequence of an increased commutation time is an increased current lag behind the voltage, hence an increase in consumption of reactive power (Q). Some commutation delay is always present even without power transfer and hence the LCC-CSC always draws reactive power. Figure 2.3 shows the change in reactive power drawn by an LCC-CSC with a change in active power (P) transfer [21].
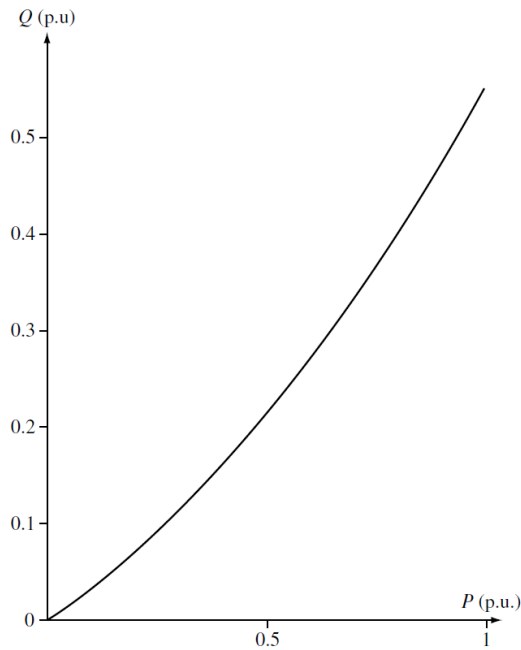
Figure 2.3 – Change in reactive power consumption against active power transfer [23]

Active power transfer through a branch of a Supergrid is likely to vary significantly. Consequently, the compensation requirements also vary, thus adding additional cost and

complexity to the system. When the LCC-CSC is transferring maximum active power, the reactive power drawn could be as much as 60% of this value [21].

Additionally, the relatively slow switching frequency of the LCC-CSC (each arm switches just once per cycle) causes significant harmonics on the voltage waveform. To compensate for these harmonics, a significant amount of filter capacity is required again contributing to the cost and complexity of the system. Finally, the LCC-CSC is susceptible to commutation failures in the presence of voltage instability or faults on the AC system. As a consequence, the AC connection point must be electrically strong, hence a minimum short circuit ratio (SCR) of 2 is required, where SCR is defined as short circuit power to converter power [21], [5].

The characteristics of LCC-CSC have dictated the applications in which HVDC transmission has been used over the past 50 years or so. Due to the large power handling capability of LCC-CSC, the technology lends itself to the transmission of large amounts of power over long distances. This has been particularly useful in applications for connecting large renewable generation sources which are located in remote locations. For example, the Xiangjiaba-Shanghai LCC-CSC link in China, in operation since 2010, has a DC voltage of ±800kV and the capacity to transmit up to 7200MW of power over 2000km from the Xiangjiaba hydropower plant, located in the southwest of China, to Shanghai [24].

2.2.2.2 Voltage Source Converters (VSC),

Over the past few decades, advances in power semiconductor devices have led to the commercial availability of self-commutated static power converters. These power converters, often referred to as VSCs most commonly use Insulated-Gate-Bipolar Transistors (IGBTs) as the switching devices [21]. IGCTs could also be used however they commutate more slowly which means the switching frequency is limited [21]. An IGBT based static power converter or VSC is presented in Figure 2.4.
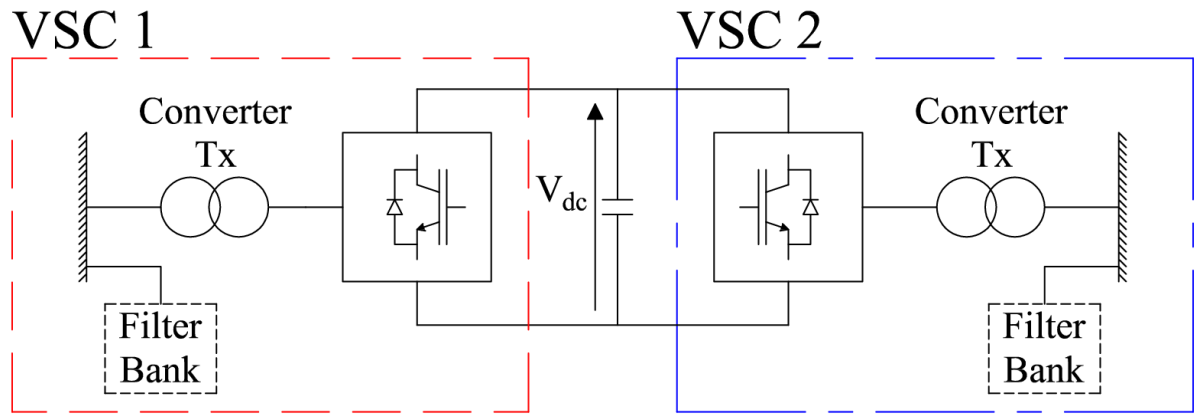
Figure 2.4 – Single line diagram of a VSC

The term 'self-commutated converter' refers to the commutation source of the switching devices within the static power converter, where each switching device is commutated by a gate input which is provided by a Pulse Width Modulation (PWM) switching algorithm. The term 'voltage source converter' refers to the constant quantity of the DC side in which a constant direct voltage is maintained and the current is controlled according to the switching of the devices, thus controlling power transfer [21].

Early generations of VSCs were two level topologies, which refers to the two possible output voltages produced by the VSC across the a.c terminals, as shown in Figure 2.5.
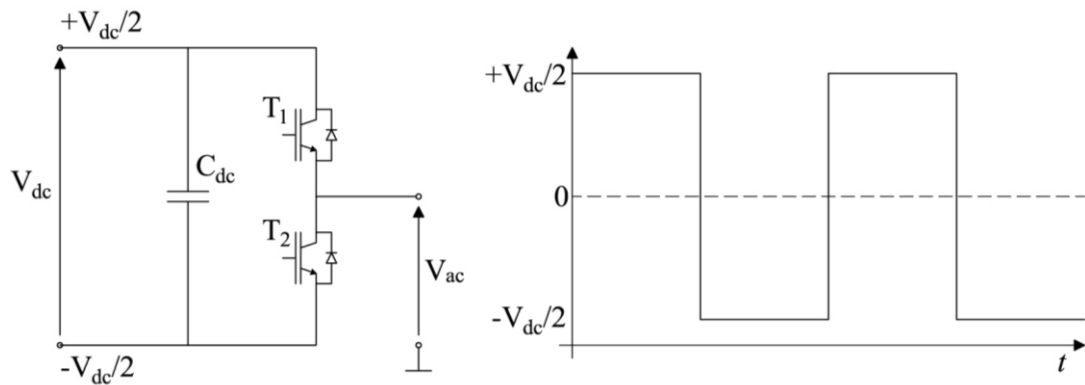
Figure 2.5 - Two level VSC and square wave output

By commutating between the two switch positions, T1 and T2, the output voltage changes from one level to another, thus creating a square waveform output. By performing this switching action many times in the line period, it is possible to replicate an a.c waveform at a given fundamental frequency (with the addition of some harmonics).

The quality of a.c waveform produced by the VSC is improved by increasing the switching frequency. This results in lower harmonic content which reduces the filtering

requirements however, as the devices are switched on and off more in a given period, the losses increase. Typical switching frequencies of two-level VSCs is in the region of $1 - 2$ kHz [21].

The latest VSCs are based on what is known as a multi-modular converter (MMC) topology as shown in Figure 2.6.
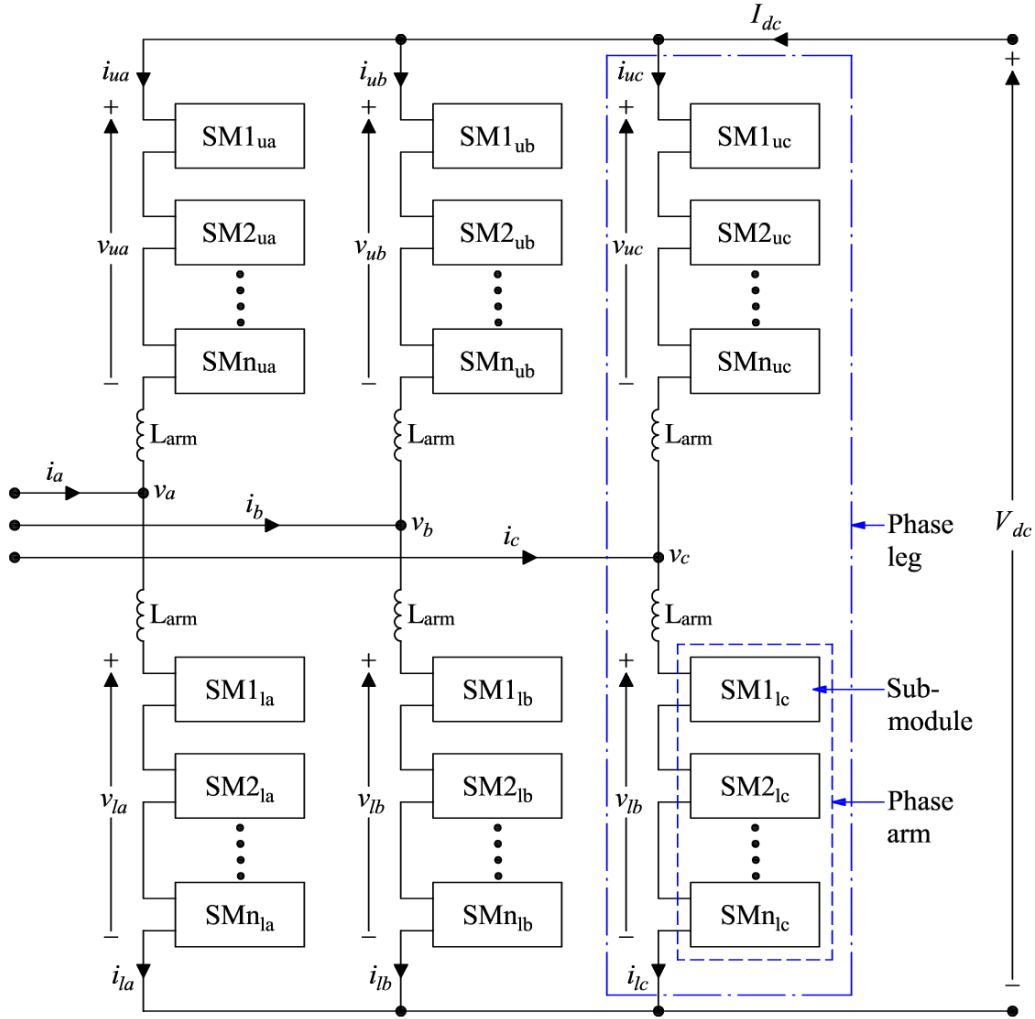
Figure 2.6 – Single line diagram of an MMC

The MMC topology contains many individual cells or sub-modules, each of which can be either a half-bridge or full bridge configuration as shown in Figure 2.7.
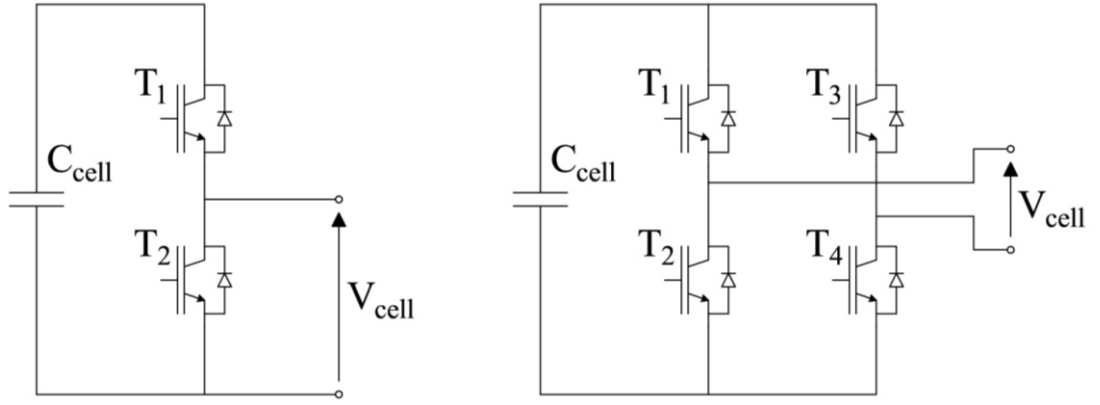
Figure 2.7 – Left: Half-bridge cell arrangement, Right: Full-bridge cell arrangement

The half-bridge cell consists of a cell capacitor, and two IGBTs plus anti-parallel diodes. The cell output can be either V_{cell} or 0. By adding two more switch positions, the full bridge arrangement or 'H' bridge as it is sometimes known, is realised. The full-bridge cell output can be V_{cell}, $-V_{cell}$ or 0. This is significant as an MMC arrangement containing full-bridge cells can block fault current contribution from the AC network in the event of a DC fault [25].

The main advantage of the MMC VSC over a two-level VSC is the improvement in quality of the a.c waveform produced. A typical MMC topology contains hundreds of cells, and therefore can be produce multiple voltage levels at its output. This results in lower filtering requirements, or in some cases, the output filters can be removed altogether [26]. The main disadvantage to MMC technology over two-level is an increase in the number of IGBTs required, where a half-bridge MMC requires twice as many IGBTs as an equivalent two-level VSC and a full-bridge MMC requires four times as many.

2.2.2.3 Comparison of the LCC-CSC and VSC

A number of key differences between LCC-CSC and VSC have meant that the latter is favoured for various applications including the connection of offshore wind generation. These include [21]:

- As VSCs are self-commutating, a separate (external) voltage source is not required for commutation as is the case for LCC-CSCs.

- VSCs can independently generate or absorb reactive power as required. LCC-CSC always absorbs reactive power, the amount of which varies according to the amount of active power transfer.

- LCC-CSCs require a minimum short circuit ratio (SCR) of 2 in order to avoid causing voltage instability within the network. VSCs however have no minimum SCR requirement.

- LCC-CSCs require a large filter capacity in order to remove the low order harmonics generated by the typically 12-pulse switching cycle. The filter capacity is typically between 20 and 30% of the converter rating. The latest VSC configurations practically remove the filter requirements altogether [26]. This implies a significant space saving, which is particularly useful in offshore applications.

- LCC-CSCs are also more susceptible to onshore AC system faults as this can lead to commutation failures and thus disrupt power transfer. VSCs are less susceptible as they are self-commutated [27].

- During a DC link fault, the LCC-CSCs are able manage any fault current contribution from the AC network, using control action [27]. Half-bridge based VSCs cannot manage fault current due to the presence of free-wheeling diodes, thus greater reliance is exerted upon the AC breakers which cause a larger delay when returning to normal operation [25]. Full-bridge based VSCs can block DC fault currents however they are more costly due to the increased number of IGBTs required and increased losses.

- The main advantage of LCC-CSCs is that they have a lower power loss than that of VSCs [21]. This is due to the high switching losses associated with PWM techniques. Recent advances in VSC topologies such as that presented in [26] are quickly reducing this advantage as the PWM conversion process becomes more efficient.

An example of a VSC-HVDC link used for connecting offshore wind is the Borwin1 HVDC Light installation. The Borwin1 HVDC Light installation connects the BARD Offshore 1 wind farm, which is located 130km from the coast, to the German main interconnected transmission system, with the receiving station located at Diele which is 75km from the coast. The wind turbine generators feed power into a 36kV AC cable system which is transformed to 154kV for the HVDC Light offshore station. The HVDC Light system operates with a DC bus voltage of ±150kV. The power is injected into the onshore grid at 380kV. The power rating of the HVDC Light system is 400MW [28].

The final choice of transmission medium is dependent upon a number of factors which vary according to the branch in question. As the Supergrid is likely to interconnect large wind farms which are located a considerable distance from shore, HVDC technology will likely be the technology of choice. While VSCs do have many advantages over LCC-CSCs, LCC-CSCs do have the ability to transfer larger amounts of power from one point to another. Additionally, the majority of HVDC installations to date are LCC-CSC based. It is of the author's opinion that both VSC and LCC-CSC technologies will feature in a future European Supergrid because of these complimentary characteristics.

2.3 Offshore Nodes or Hubs

2.3.1 The Offshore hub

The offshore hub is an offshore transmission network which facilitates aggregation of wind energy resources and provides interconnection between countries. Two prominent offshore hub solutions are presented in the literature [10], [29]–[31]:

- The Offshore AC hub concept (Figure 2.8) – consists of multiple point-to-point HVDC links, centred on an AC hub, serving to interconnect different member states while integrating a large wind farm. Crucially, all power transfer must flow through the AC-hub.

- The MT-HVDC concept (Figure 2.9) – still requires some form of AC hub arrangement, however interconnection is performed on a DC bus and therefore not all power transfer must flow through the AC hub arrangement.
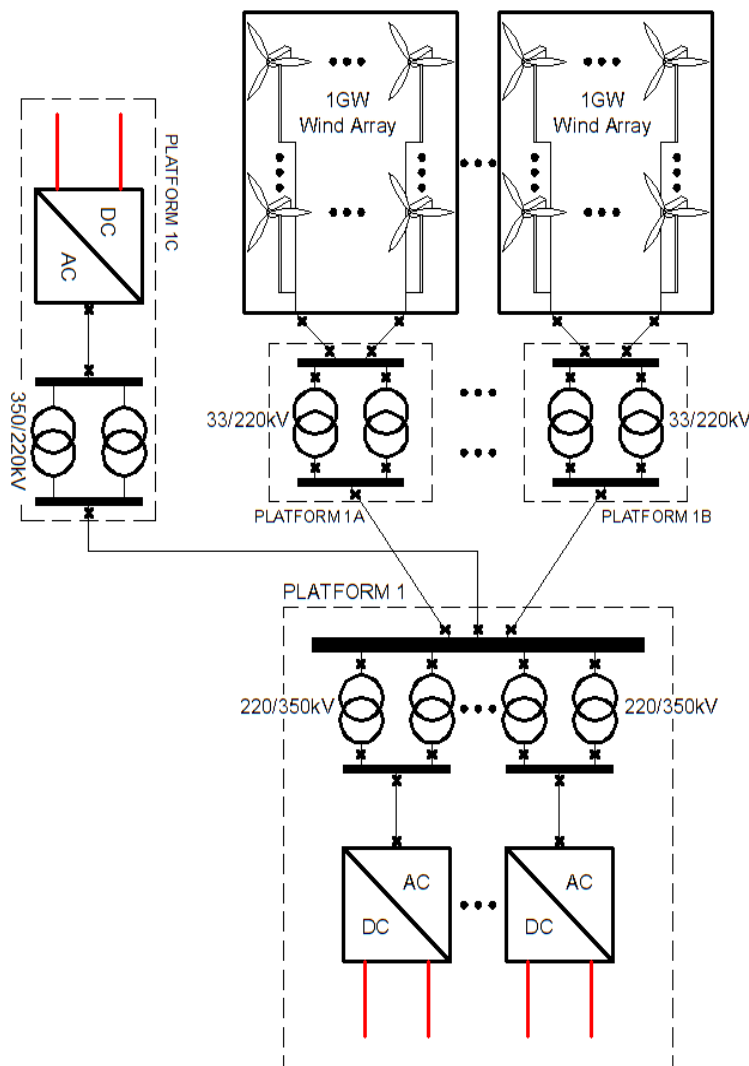
Figure 2.8 – The offshore AC hub concept
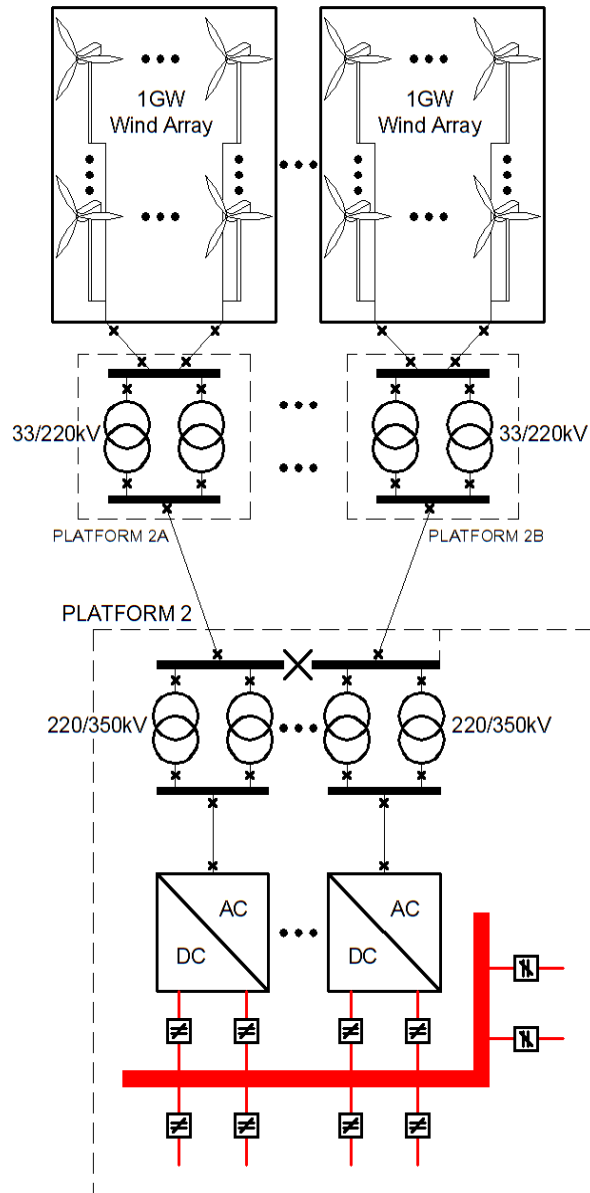
Figure 2.9 – The multi-terminal DC hub concept

Considering a straightforward hub arrangement consisting of 4 x 1 GW Wind Arrays, connected to the UK via 2 x 2GW HVDC links. There are two main differences between each concept, one is the point of aggregation, where the offshore AC hub aggregates the output of each wind array at the 220kV bus bar and the MT-HVDC solution aggregates the output on the DC bus bar. Assuming there is a fault with one of the HVDC converters, the MT-HVDC system is less robust as no power can now be transferred from the wind array connected to the faulted HVDC converter. To overcome this, the MT-HVDC concept would likely include a second point of aggregation at the 220kV bus bar similar to the offshore AC hub concept. The other main difference is the requirement for HVDC circuit breakers for the MT-HVDC system.

19

For many years HVDC circuit breakers (CBs) were a potential technological obstacle to the implementation of a MT-DC grid. Now commercial scale designs have been presented by the manufacturers but there are none in operation around the world [32]. As they are a new, yet unproven technology, the risks and associated costs are higher. In addition, the space requirements for a HVDC CB are considerable, which is a problem offshore where space is at a premium.

If an interconnection is made to Norway, another HVDC converter, transformers and associated equipment is required for the offshore AC hub concept, obviously putting it at a disadvantage over the MT-HVDC system in terms of extra infrastructure requirement. However, when the same connection is made to the MT-HVDC system, the new interconnection must be entirely compatible with the rest of the system. As previously mentioned, the MT-HVDC concept relies upon HVDC CBs, therefore additional CBs are required for the extra link and will require the same rating as all those throughout the rest of the system; a significant disadvantage if the new link is at a significantly lower or higher rating. In addition, the voltage level will need to be the same for all links, unless some form of DC-DC transformer is employed. This would be difficult and costly, as no DC-DC transformer exists now or in the near future capable of handling enough power and operating with high enough efficiency. Finally, manufacturers use proprietary control methodologies; these must be fully compatible to avoid causing negative effects on the network.

In addition, the offshore AC hub can be integrated with improvements in HVDC technology as they come about (i.e. increased voltage/current levels, better control schemes, and introduction of HVDC CBs) and are also potentially compatible with classical HVDC schemes such as LCC – HVDC.

The salient feature of the offshore AC hub concept is its flexibility in design, which enables it to adopt a modular approach to building a Supergrid. If one considers the 400kV AC Supergrid built in the UK in the 50s and 60s, it is evident that it was built in a gradual, systematic process over a number of years. With that in mind, the offshore AC hub is a topology which allows for the Supergrid to evolve in a similar manner, with optimised solutions in terms of cost and performance as and when new infrastructure is installed.

2.4 Control systems in VSCs and FRC-WTs located in offshore transmission networks

2.4.1 Point-point HVDC transmission systems for offshore wind generation

The majority of HVDC transmission systems in operation around the world are point-point HVDC transmission systems. However, only a handful are used for offshore wind generation and currently, all of them are owned by TenneT TSO GmbH and are located in the North Sea off the North German coast [33]. The infrastructure arrangement in the German offshore HVDC transmission systems BorWin2 and HelWin1 follows that presented in Figure 2.10 [34].
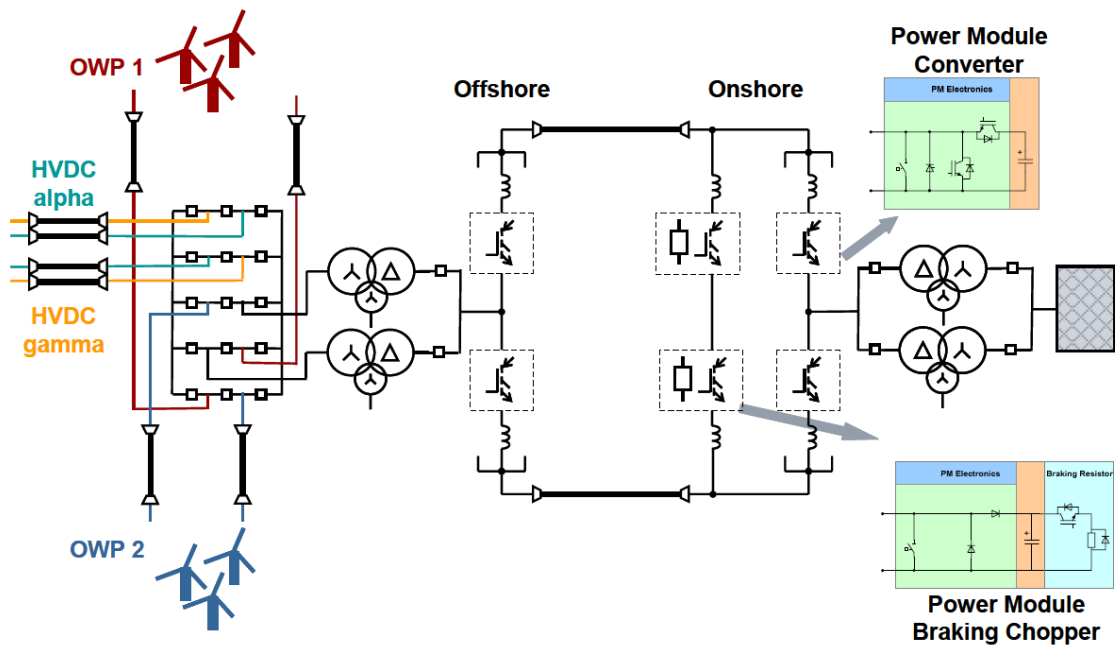
Figure 2.10 – Offshore infrastructure arrangement in BorWin2 and Helwin1 [34]

A MV collection array is used to aggregate the power generated by the individual wind turbines. The collection array consists of a number strings, each of which connects up to 10 WTs to an offshore AC platform. The offshore AC platform includes a MV bus bar which provides a point of connection for the WA strings. A transformer(s) is present on the AC platform to step up the voltage to HV levels typically to 155 kV [34]. A HV cable circuit then connects the offshore AC platform to the offshore HVDC platform.

The HVDC link de-couples the offshore AC network from the onshore system. Therefore, to ensure all WTs and offshore network infrastructure operates satisfactorily; the voltage and frequency must be managed. As the VSC has full active/reactive power

control, it is most suited to managing the voltage and frequency in response to varying wind power generation [35].

In its simplest form the VSC is a controllable voltage source and has full control over the voltage magnitude, phase and frequency it produces. The VSC is connected to a network bus by a reactance, as shown in Figure 2.11.
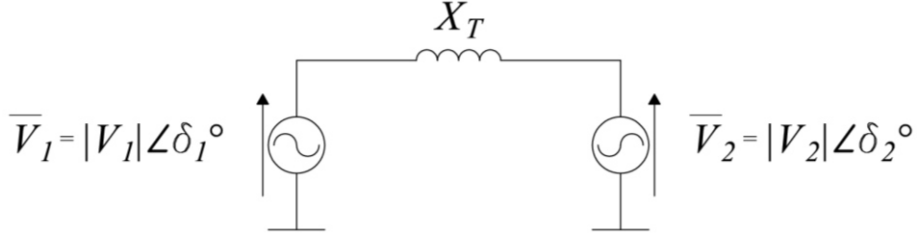
Figure 2.11 – VSC connection through a reactance

V_1 represents the rms voltage magnitude and δ_1 the voltage angle produced at the valves of the VSC. V_2 represents the rms voltage magnitude and δ_2 the voltage angle at the point of connection to the offshore AC network. The reactance X_T which couples the two voltage sources represents the equivalent reactance of the VSC arm inductors and converter transformer(s).

The frequency of V_1 is fixed at a nominal value of 50 Hz. As frequency is a common quantity across any AC system, the WTs must lock on to the nominal frequency using a Phase Locked Loop (PLL). Given a common frequency, the active and reactive power transferred through the VSC is manipulated according to the following equations:

$$P = \frac{V_1 V_2}{X_T} \sin(\delta_2 - \delta_1) \qquad (2.2)$$

$$Q = \frac{V_1 V_2}{X_T} \cos(\delta_2 - \delta_1) - \frac{V_2^2}{X_T} \qquad (2.3)$$

It can be seen from (2.2) that an increase in the phase difference across the interface reactance results in an increase in the active power transfer to the VSC. Therefore, any increase in wind generation will result in an increase of δ_2 with respect to δ_1. Assuming the voltage angle at the point of connection should be fixed at zero ($\delta_2 = 0$), the VSC can maintain this by modulating δ_1 as necessary.

It can be seen from (2.3) that an increase in the voltage difference across the interface reactance results in an increase in the reactive power transfer to the VSC. As the wind generation varies, so too does the amount of reactive power transferred. Assuming the

voltage magnitude at the point of connection should be fixed at the nominal voltage ($V_2 = 1$ pu); the VSC can maintain this by modulating V_1 as necessary.

Vector control schemes are usually employed to perform these control functions [36]–[38]. A vector control scheme is one that manipulates direct and quadrature (dq) components instead of three-phase components. In addition, the dq components are DC quantities as they are transferred to a synchronous reference frame. Figure 2.12 presents the vector control scheme for the purposes of maintaining voltage/frequency in the offshore AC network.
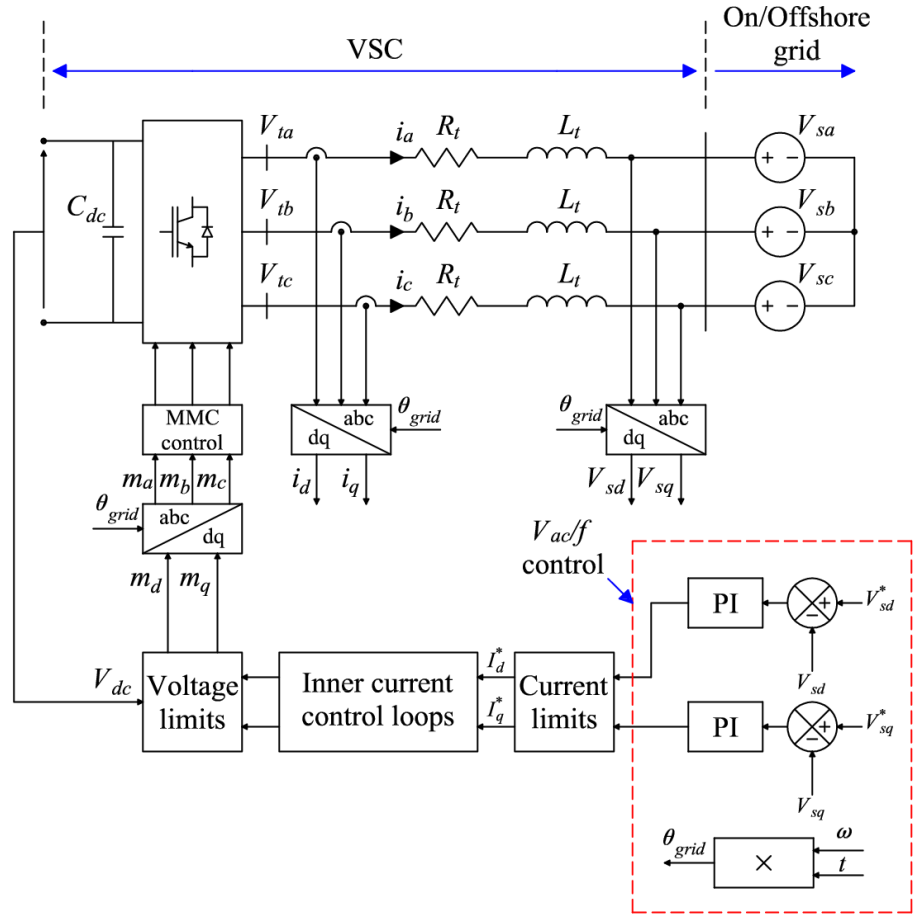
Figure 2.12 – Vector control scheme used in VSCs

2.4.2 Parallel point-point HVDC transmission systems for offshore wind generation

To date, no parallel point-point HVDC transmission systems for offshore wind generation are in operation. However, parallel point-point schemes do exist between countries such as the Skagerrak projects which link the onshore transmission systems of Denmark and Norway. In fact, the latest project Skagerrak 4 is notable as it combined

the use of a new VSC monopole link with an existing CSC link in to a bi-pole system [39].

Presently VSC HVDC links have a rating up to 2 GW [35]. With wind array development zones in the UK having feasible capacities of up to 9 GW it is obvious that more than one VSC HVDC link is required [4]. Two or more HVDC links could be installed to serve a single large WA with offshore platforms located relatively close to one another. However, these systems are not said to be operating in parallel until there is an AC electrical connection between them.

Various studies have examined the possibility of paralleling point-point HVDC transmission systems for offshore wind generation on the AC side [19], [40]. The offshore VSC HVDC platform BorWin 2 has the provision for an AC connection to another HVDC platform, as was shown in Figure 2.10 [34]. The main benefit of paralleling HVDC transmission links is the increased redundancy it brings. That is, if one HVDC transmission link should fail, the other(s) may have spare capacity to avoid or minimise the loss of infeed to the onshore transmission system.

2.4.2.1 Control implications

The paralleling of two HVDC links has significant implications on the control of voltage, frequency and complex power. The AC link between two offshore transmission systems effectively joins them in to a single large islanded offshore transmission network. This forces them to share the same operating frequency. The active power generated by the wind turbines must now be shared between the parallel offshore VSCs, as must the reactive power if compensation is provided by the VSCs. Similar topologies have been observed in small onshore electrical systems called Microgrids, when operating in islanded mode [41]–[44].

Various options exist for the control of voltage, frequency and complex power including [40]:

- Droop control: All offshore VSCs operate according to an active power/frequency and reactive power/droop characteristic. Given the same droop gains then the load should be shared equally among the offshore VSCs.
- Master-slave control: One offshore VSC is designated as a Master and controls the voltage and frequency in the network. The other offshore VSCs act as slaves and control the active/reactive power according to dispatch orders.

- A combination of the above.

2.5 Faults in offshore transmission systems

2.5.1 AC faults

Faults affecting onshore AC networks are a regular occurrence and are usually handled seamlessly without major effect on the integrity of the power system. In an offshore transmission network, the AC faults are more likely to be permanent. This is because the most common cause of faults in onshore AC systems is lightning strikes affecting overhead transmission lines and AIS switchgear. In an offshore system, sub-marine cables and GIS switchgear are used; therefore they are not exposed to lightning strikes. Faults in offshore transmission systems could be due to mechanical damage or the breakdown of insulation in equipment [45]. Both of these faults will result in permanent outages, possibly affecting the whole offshore transmission system.

2.5.2 DC faults

DC faults are those that affect the DC side of a HVDC link. A large amount of research has gone in to analysing DC faults, particularly when applied in a MT-DC grid [45]–[47]. This is understandable because the effects of a DC fault occurring in a DC grid can be far reaching and severe [48]. The extent to which a DC fault impedes the normal operation of a HVDC system is dependent upon the type of fault and the topology of the system [45].

In a HVDC transmission system, a DC fault will either be a line-ground or line-line fault. DC faults could occur within the station or somewhere along the transmission line. In offshore HVDC systems, underground and sub-marine cables are used. Therefore, a fault will most likely be permanent as they are inherently protected from lightning strikes and not easily repaired. In addition, the cause of the fault is most likely to be from external mechanical damage or insulation breakdown, both of which require extensive repairs [45].

A DC fault in a HVDC link is generally characterised by the following three stages [45], [48]–[52]:

1. A high initial fault current corresponding to the first wave front. This is due to the discharge of the cable capacitance and depending on the topology, the VSC capacitance.

2. A transient phase which is due to the dynamics of the system (i.e. DC inductors interacting with the capacitance)
3. A steady-state condition which is due to the in-feed from the AC system as the anti-parallel diodes form an uncontrolled diode bridge (half-bridge VSCs only).

The duration of the excessive fault current is largely dependent upon the time taken to arrest the fault current. VSCs using full-bridge cells are able to block DC fault currents almost instantaneously. VSCs using half-bridge cells are not able to block DC fault currents and are therefore reliant upon external CBs. Unfortunately, the use of full-bridge VSCs requires twice as many IGBTs as a half-bridge arrangement which significantly increases the capital cost of a VSC. Significant research is being carried out in to the hybrid topologies, such as the Alternate Arm Converter [53], which offer fault blocking without doubling the number of IGBTs [25]. However, these are still some way off commercialisation.

In point-point HVDC links, the fault current in-feed from the AC side is limited by AC circuit breakers (CBs). Modern AC CBs can usually operate in the order of two cycles of the fundamental frequency [54]. This means that any equipment in the fault current path must still be able to deal with excessive fault currents for approximately 60 ms, including a 20 ms tripping delay.

From the AC side, the faulted VSC will appear as a large inductive load. Depending on the SCR of the AC system, this may or may not drag down the AC voltage at the interface point. Should the AC voltage reduce, any generation connected to the interface point will be required to ride through the fault [55].

2.6   Managing faults in offshore transmission systems

The likelihood and severity of a fault will dictate the extent of the efforts to manage a fault. Clearly, any offshore transmission network contains valuable assets that must be safeguarded against the effects of a fault. To that extent, standard protection equipment such as circuit breakers and surge arresters are used. As offshore transmission systems have grown in power rating, so too has the importance of managing faults, particularly those that affect the onshore transmission network.

As highlighted in Section 2.5, a fault in an offshore transmission network is likely to be permanent. On occurrence of a DC fault in a point-point HVDC link serving a WA, the AC breaker would open and remain open for a significant period of time. This will

isolate the offshore wind generation and no power will be transferred. This situation is acceptable providing the loss of infeed to the MITS remains below stipulated levels and local protection ensures no assets are damaged [55].

2.6.1 Fault ride through

A fault occurring at or near the onshore interface point can greatly affect the offshore transmission system if not properly managed. This type of fault is usually temporary and results in a severe voltage depression at the IP [56]. National Grid define fault ride through (FRT) connection limits for onshore VSCs connected to the MITS [55]. Assuming the FRT conditions are met at the onshore IP, for faults lasting up to 140 ms the onshore VSC must ride through having zero volts at the IP. For faults lasting longer than 140 ms, the voltage/fault duration requirements are described in Figure 2.13 [55].
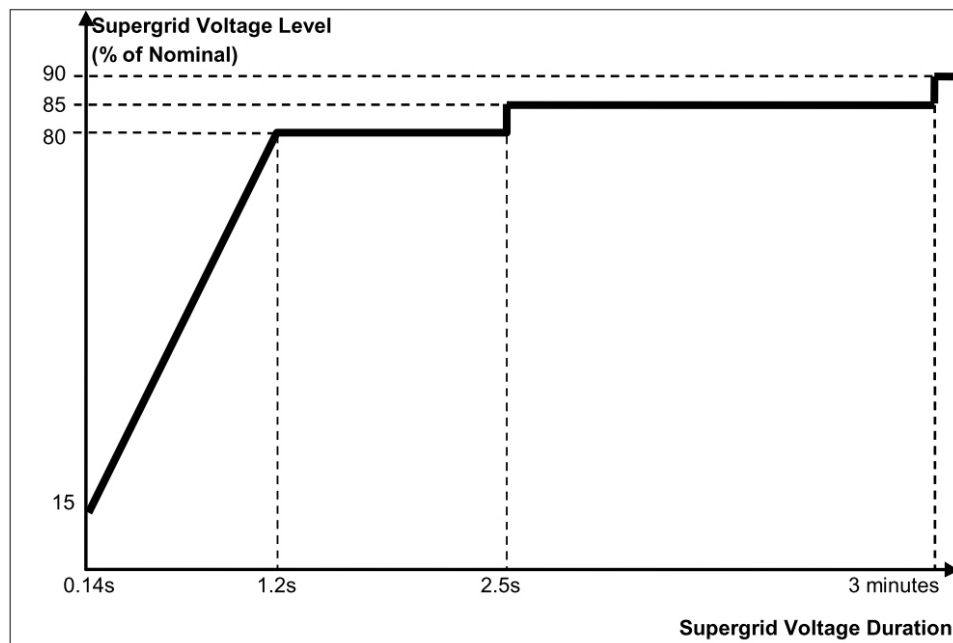
Figure 2.13 – Voltage reduction duration diagram for onshore IP [55]

A reduction of voltage at the IP will inhibit the ability of the onshore VSC to transfer active power to the MITS. This in turn causes a power imbalance in the HVDC link. The result of the power imbalance is damaging over-voltages on the DC link [56].

The majority of research on managing faults affecting offshore HVDC transmission systems has focused on FRT methods. This is understandable as the aim is to stop a temporary fault becoming permanent, which would be unacceptable. Various fault ride through techniques are presented in the literature and are summarised as follows [56]–[61]:

- Power dissipation methods using DC chopper circuits
- Power reduction methods using fast communication to reduce WT power generation
- Power reduction methods using common variables such as frequency to reduce WT power generation (no fast communication)

2.6.1.1 Power dissipation methods using DC chopper circuits

One solution which has been applied in offshore HVDC transmission systems to date is the use of a DC chopper circuit located on the DC link [34]. Given a power imbalance due to an onshore fault, the excess energy can be dissipated as heat in the DC chopper circuit [29].

When applied to the HVDC link, the DC choppers must be rated to the MVA rating of the VSC. This requires a large amount of space which means they must be located at the onshore VSC as space required offshore is very expensive [35]

In [57], the DC choppers are applied to the DC links of the FRC-WTs. When the HVDC link voltage rises, a power reduction factor is sent to the FRC-WTs to activate the DC choppers. This is signalled either through fast communication or manipulation of voltage or frequency.

2.6.1.2 Power reduction methods using fast communication to reduce WT power generation

The active power output from the WTs can be reduced by using a fast communication system to send new active power set points. A system using a DC voltage droop to reduce the active power generated by the WTs was implemented in [56]. The WT active power output is reduced in two different ways and the performance compared.

One method applied the reduction factor to the torque set-point of the generator side converter of the FRC-WT. This results in an increase in speed of the WT rotors as less energy being transferred to the FRC DC link. This will cause a reduction in DC link voltage to which he grid side controller of the FRC-WT will respond by reducing active power output.

The other method applies the reduction factor from the HVDC link directly to the grid side controller of the FRC-WT. The active power set point is reduced which causes the FRC-WT DC link voltage to rise. The rise in the FRC-WT DC link voltage triggers another controller to reduce the power output from the generator side converter.

Both systems are shown to operate satisfactorily however the second method has a more immediate effect on the HVDC link voltage as it directly reduces the active power output from the WTs. Both systems are however completely dependent upon fast communication and it is shown that even a relatively small communication delay can result in an overvoltage on the HVDC link.

2.6.1.3 Power reduction methods using local variables to reduce WT power generation (no fast communication)

WTs installed in onshore transmission networks are designed with the capability to ride through voltage sags at their grid connection point [58]. If this capability is also added to offshore WTs connected to islanded offshore AC networks then it can be exploited to provide FRT following a fault affecting a HVDC link. This is achieved by reducing the voltage magnitude of the offshore AC network in response to a rise in the DC voltage of the HVDC link [56], [60]. The active power output from the FRC-WTs reduces with the reduction in AC voltage magnitude. The main drawback of this approach is that any piece of equipment connected to the offshore AC network will be affected by the voltage reduction, which depending on the equipment may or may not be an issue.

The offshore AC network frequency can also be used as a signal to reduce the WT generation. In [60], a frequency controller is added to the offshore VSC of a HVDC link. When a DC overvoltage is detected the frequency controller raises the frequency of the offshore AC network. The increase in frequency is detected by the FRC-WT using PLLs. A power reduction controller is applied to the grid side converter of the FRC-WT which reduces the active power from the WT in response to the increase in frequency. The system is shown to work however the response is slow and consequently DC choppers are still required in the HVDC link. The authors also highlight that the measuring frequency can be slow which is a potential drawback of the system.

2.6.2 Offshore transmission systems containing parallel HVDC links

If an offshore transmission system contains parallel HVDC links the situation is different. A permanent fault affecting one HVDC link should not affect the operation of another. Likewise, a fault occurring in the offshore AC network should not result in a total loss of infeed greater than the allowable limits. It is not clear that local protection methods alone can avoid this therefore some form of fault management is required.

In [40], the effects of a loss of one of the HVDC links are discussed and some control actions presented. It is discussed that through a combination of droop control and pre-

determined post-fault dispatch orders, a new steady state operating condition can be achieved. Although the proposition seems feasible it must be noted that no simulations were carried out to show this working. The authors do stress that the system has no means by which to reduce wind power generation. They suggest only that wind generation is curtailed pre-emptively to account for the possibility of a loss of one of the HVDC links. This would result in a large amount of lost earning potential which could render the project unfeasible.

In [62], a fault management strategy is developed for an offshore transmission system containing two parallel HVDC links. The system is based on the communication-less FRT method discussed in Section 2.6.1.3 and uses frequency to signal power reduction. The system is shown to cope with both a temporary and a permanent fault at the onshore interface point as well as a permanent DC fault on one of the HVDC links. The frequency modulation controllers appear to function adequately as no significant DC overvoltage is observed.

2.7   Optimal power flow in electric power systems

Power flow studies are an essential tool for the everyday planning of the electric power system. It provides a means to analyse the state of the power system for a given generation/load scenario. The network planner can use the analysis to identify any technical constraints on the power system, for example overloaded transmission lines or bus over-voltages [63].

Optimal power flow (OPF) was developed as an extension to the power flow problem by including economic objectives and analysis. Two main economic factors affect the operation of the electric power system including *economic dispatch* of power generation and *minimum-loss* delivery of the power to the loads. Both these factors can be solved using a suitable OPF study [63]. Therefore, OPF is an essential tool for the reliable and economic operation of the electric power system [64].

OPF studies also provide extended technical analysis of the electric power system through the management of technical constraints. A standard power flow can identify any active constraints in the network for a single generation/load scenario. An OPF can actively remove any technical constraints while also finding the optimum technically feasible economic solution [65].

2.7.1   OPF applied to the electric power system

In order to find the optimum technically feasible economic operating condition for a given power system, the OPF must execute a number of standard PF studies, each representing a different generator dispatch scenario. This is performed iteratively until the optimum solution is found. The standard PF requires the repeated inversion of a n by n matrix and therefore is relatively computationally expensive [64].

Owing to the complexity of the electric power system, OPF is applied to different hierarchical models which are valid for different time frames. One optimisation problem is applied to a high level model and once solved, the output is used as an input to another optimisation problem applied to a low level model [64].

High level models operate at discrete intervals of one hour or more and are applicable from at least 24 hours in advance. The objective of the OPF applied to the high level model is to determine the least expensive economic dispatch of power generators and is often referred to as Optimal Unit Commitment (UC) [64].

Low level models operate at discrete intervals ranging between 5 minutes and 1 hour. The objective of the OPF applied to the low level models is to determine a suitable set of control set points for generating and non-generating equipment which ensure the power system operates as reliably and economically as possible [64].

2.7.2   Solution algorithms for OPF

The OPF problem is a large highly constrained, non-linear and non-convex optimisation problem [66]. Various algorithms have been developed to tackle the OPF problem, varying in efficiency and suitability for a given application. OPF solution algorithms can be broadly grouped as *Conventional Methods* and *Intelligent Methods* [67].

Conventional methods are divided into sub-groups which include:

- Gradient method
- Newton method
- Linear programming method
- Quadratic programming method
- Interior point method

Intelligent methods are divided into sub-groups which include:

- Artificial neural networks

- Genetic Algorithms

- Particle swarm optimisation

- Ant colony algorithm

The conventional algorithms have proven to be very effective at solving the OPF problem [67]–[71]. However, they are all local optimisation techniques and therefore may get stuck at local minima, rather than finding the global optimal solution [67]. The suitability of each conventional method for a given OPF problem varies, with certain algorithms, such as the gradient method being more suitable for smaller well defined problems and other algorithms, such as the interior point method being more suitable for larger problems [67].

The intelligent algorithms overcome the local convergence problem as they search the global variable space [72]. They can also identify multiple optimal solutions and are therefore suitable for solving multi-objective OPF problems [67]. A potential drawback of the intelligent methods is the increased computational burden of searching the global variable space. Conventional methods may outperform intelligent methods provided the problem is well defined.

2.7.3 Novel applications of OPF

OPF can be used for many applications within the electric power system. Small onshore distribution networks called Islanded Microgrids (IMGs) share similar characteristics to offshore AC hubs as they are interfaced by VSCs and have little 'classical' inertia. OPF has been applied in IMGs for various applications. In [73], OPF is used to maximise the load applied to droop controlled IMGs while avoiding voltage collapse. An intelligent algorithm based on fuzzy logic control is used to identify the optimum operating point. This application is particularly interesting as two objective problems are specified including maximum load applied in the IMG and minimising the generation cost.

In [74], an OPF algorithm is applied to operate in a substation computer. A unique feature of this application is that it is applied in real-time generator control. The objective of the OPF is to minimise the cost of distribution generation in an 11 kV radial distribution network. Of specific interest to the work in this thesis is that the computation time of the OPF algorithm is shown to be in the region of $30 - 60$ ms.

2.8   Communication in offshore transmission systems

Offshore transmission systems rely upon communication for Supervisory Control and Data Acquisition (SCADA) and protection purposes. The communication system will be used by [75]:

- The wind turbine operator(s)
- The collection system operator(s)
- The offshore transmission system operator (OFTO)

Performance and functional requirements of the communication infrastructure vary according to the process using it. Communication systems are generally defined in terms of latency, bandwidth and reliability. The SCADA system requires the communication infrastructure to have a high bandwidth but low latency and high reliability are not so important. Conversely, the protection system requires low latency, high reliability and low bandwidth.

2.8.1   SCADA systems in offshore transmission systems

The SCADA system is relied upon to perform many functions, some of which include:

- Communicating dispatch orders to WTs and VSCs
- Communicating status updates of circuit breaker positions etc.
- Facilitating real time monitoring of electrical parameters throughout the network
- Logging events such as alarms or switching operations
- Remote monitoring and operation

The location of the offshore wind farms and transmission assets make access difficult. This increases the demand on the SCADA system as the functions it provides are essential for the normal operation of the system. The SCADA system must be designed for secure operation with high availability compared to a SCADA system applied within the onshore network.

The SCADA system is implemented using a redundant Local Area Network (LAN) topology, as shown in Figure 2.14 [75]. Using this topology minimises the risk of losing a communication route and maintains high availability.
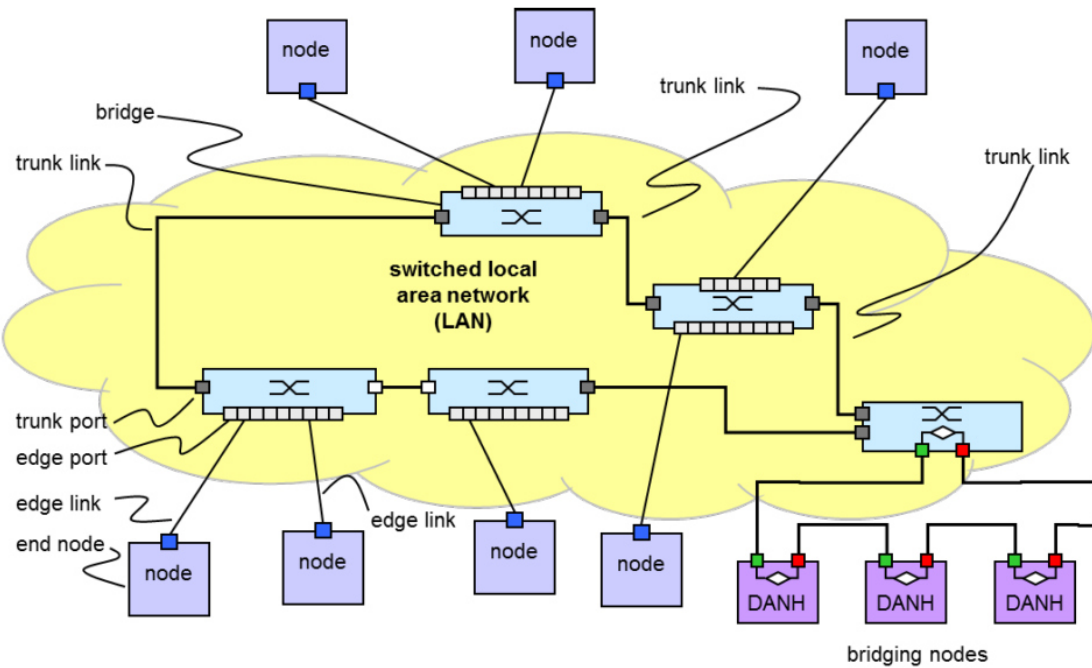
Figure 2.14 - Redundant LAN topology[76]

An Ethernet network consists of nodes and switches which are connected by point-point links. A bridge is a particular type of switch which is concerned with the receiving and forwarding of frames of data. The links between nodes and switches and between switches are implemented using either of two physical layers, copper and fibre and either of two bit rates 100 Mbit/s and 1 Gbit/s [76].

There are a range of protocols which can be used for the SCADA system e.g. IEC 61850, DNP3, Modbus, etc. IEC 61850 is particularly relevant as it provides for both SCADA functions and protection functions in the offshore network.

One LAN could be defined across a single point-point HVDC transmission system including the wind power plants. For communication between multiple transmission systems, as would be the case for an offshore AC hub, then gateways could be used to connect two LANs.

2.8.2   Communication delay in offshore transmission systems

For any control and/or protection architecture that relies upon communication infrastructure, the delay imposed by the finite speed of propagation through the system is of primary concern. In an Ethernet network, the delay is mainly due to the time taken for a frame of data to travel through a physical medium and the time taken to pass through bridges in the network.

2.8.2.1 Latency of physical paths

Table 2.1 presents the time taken for an IEEE 802.3 frame (single packet of data), as used by IEC 61850 to traverse various physical mediums [76].

Table 2.1 – Time taken for an IEEE 802.3 frame to traverse various physical mediums

Medium	Time to traverse a link
CAT-5 and CAT-6 cables	5.5 µs/km
Fibre optic cables	4.9 µs/km
Free air (wireless)	3.3 µs/km

Therefore a fibre optic link 150 km in length (which might be used to connect an onshore and offshore VSC platform for example) has a latency of 0.75 ms.

2.8.2.2 Bridge/Switch Latency

Bridges within an Ethernet network usually operate in a store and forward mode, which means the whole frame is received before it is forwarded. The maximum frame length of a packet of data sent using IEC 61850 is 1530 bytes and thus has 12,240 bits. On a bridge operating at 100 Mbit/s, this corresponds to a frame delay of 122.4 µs. Adding to this a typical bridge latency of 8 µs, the bridge hop latency is approximately 130 µs. To this value must be added the queuing latency, which depends upon the network load and whether any priority settings are applied. In IEC 61850, critical data can be assigned high priority and therefore can jump through the queue of data waiting to be sent on any bridge, thus the queuing delay can be minimised [76].

Assuming another 1530 byte frame is already present at a bridge with equally high priority (very low probability) when a new 1530 frame arrives, it must wait 130 µs before being processed. Therefore the maximum latency at single bridge is assumed to be 2 x 130 µs = 260 µs.

Figure 2.15 presents the communication involved following a fault occurring in an offshore transmission system.
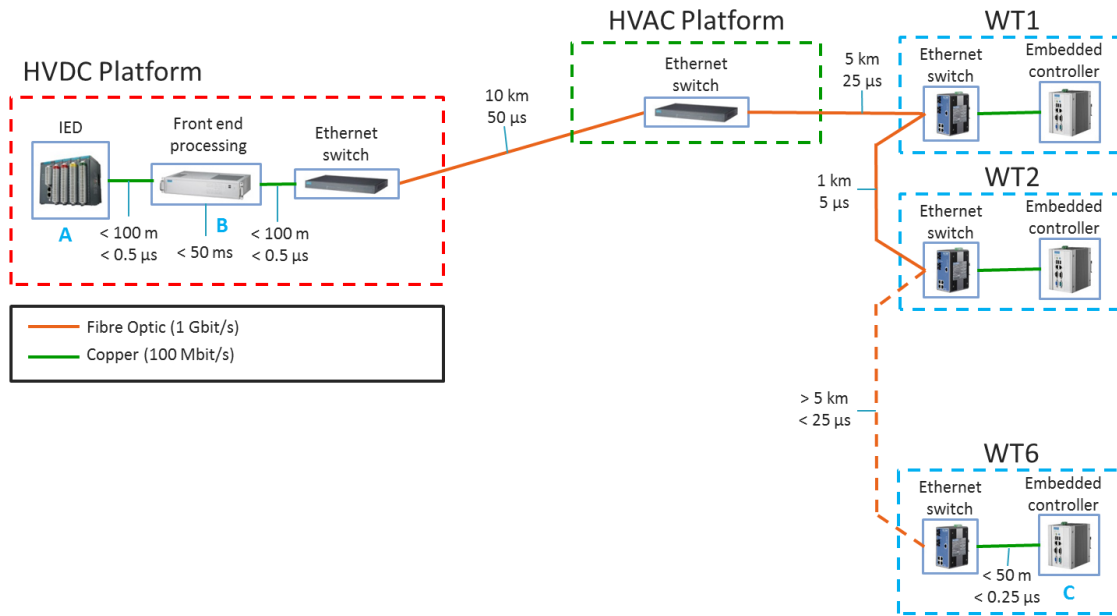
Figure 2.15 – Signal path and propagation delay of a frame of data sent between the VSC platform and WTs

Assuming a DC fault has occurred at IED (point A) on the HVDC platform will register an over-current and send a tripping signal to an appropriate breaker. This tripping signal is also sent to a processing unit (point B) which will decide what appropriate action to take in the rest of the network. Assuming it decides to reduce active power at all WFs, a signal must be sent to each individual WT to order it to reduce active power output. The longest latency is expected for the frame arriving at WT6 (point C), as it must travel along the Fibre optic cable embedded in the WT strings, hopping through the bridges while doing so. The total delay is calculated in Table 2.2.

Table 2.2 – Latency budget for communication of a single frame between the offshore VSC platform and WTs

Propagation event	Time (µs)
Trip signal from point A - B	
100 Mbit/s Ethernet (copper - 100m)	0.5
Dispatch orders point B - C	
Ethernet switch (HVDC)	260
1 Gbit/s Ethernet (Fibre - 10 km)	50
Ethernet switch (HVAC)	260
1 Gbit/s Ethernet (Fibre - 5 km)	25
Ethernet switch (WT1)	260
1 Gbit/s Ethernet (Fibre - 1 km)	5
Ethernet switch (WT2)	260
1 Gbit/s Ethernet (Fibre - 1 km)	5
Ethernet switch (WT3)	260
1 Gbit/s Ethernet (Fibre - 1 km)	5
Ethernet switch (WT4)	260
1 Gbit/s Ethernet (Fibre - 1 km)	5
Ethernet switch (WT5)	260
1 Gbit/s Ethernet (Fibre - 1 km)	5
Ethernet switch (WT6)	260
100 Mbit/s Ethernet (copper - 50m)	0.25
Total latency	**2180.75**

This analysis shows that when compared to the processing time required at B, which is likely to be in the region of 30-60ms as discussed in 2.7.3, the communication latency is relatively small.

3 Chapter 3 – Model of an offshore AC hub

3.1 Introduction

The offshore AC hub connects multiple HVDC VSCs and large numbers of FRC-WTs. Autonomous control of voltage, frequency and complex power is necessary to maintain stable operation of the network during changes in wind speed and dispatch orders. In addition, faults may lead to unacceptable operating conditions in the offshore AC hub. This could result in further outages as transmission and generation assets take protective action to avoid damage. This in turn could heavily impact the onshore MITS if left unmanaged. Before any suitable method of managing faults can be designed, the impact of faults in an offshore AC hub must be investigated and understood.

In this chapter, a model of the offshore AC hub is developed in SimPowerSystems[TM][1]. The model is modified to allow for investigation of the impact of faults in an offshore AC hub.

3.2 Changes in operating condition in an offshore AC hub

The main functions of an AC hub are to aggregate wind generation and provide interconnection between countries. Under normal operating conditions, the power generated by the wind turbines will be transferred to the onshore MITS and any remaining capacity will be used to transfer power between countries. This yields two operational variables: wind speed and electricity market conditions. Any power control philosophy implemented in an offshore AC hub must compensate for changes in wind power output and dispatch orders.

To maintain satisfactory operating conditions for power transfer, voltage and frequency must be maintained within tolerances. National Grid specifies voltage and frequency limits for offshore transmission systems in the System and Security of Supply Standard (SQSS) [77]. The relevant operational limits are shown in Table 3.1.

---

[1] SimPowerSystems[TM] is a suite of component libraries and analysis tools developed by MathWorks[®] in conjunction with Hydro-Québec of Montreal [105]. It is designed for use with the Simulink[®] simulation environment in MATLAB[®].

Table 3.1 – Operational voltage and frequency limits for offshore transmission systems [77]

Parameter	Minimum	Maximum	Units
Nominal Voltage			
Less than 400 kV down to 132 kV inclusive	-10	10	%
Less than 132 kV	-10	6	%
Nominal Frequency	49.5	50.5	Hz

Various faults can occur in an offshore AC hub and HVDC transmission links with a range of severity and likelihood of occurrence. The DC pole-pole fault as described in Chapter 2 of this thesis is one example. The impact of such a fault in a single point-to-point transmission system has been thoroughly explored in the literature. The salient feature of a DC pole-pole fault is a high fault current, fed by the AC network at either end of the transmission link [48].

The offshore AC hub has certain features that impose additional constraints on any fault management strategy. One feature is the lack of directly connected (i.e. not power electronic interfaced) rotating synchronous machines which typically make up a large proportion of generation capacity in onshore AC networks. The offshore AC hub is interfaced purely by VSCs, be it the FRCs in the WTs or the offshore VSCs of the HVDC links. This implies that there is no inertia, at least in the classical sense in which inertia is provided by the kinetic energy of a rotating mass. Another feature is the relatively low series impedance of the AC cables. A VSC will not provide anywhere near as much fault current as a synchronous machine. A single fault is therefore likely to severely impact the voltage profile of an offshore AC hub. If the voltage collapses throughout then power transmission is impossible. This gives rise to another concern: A loss of transmission capacity following a fault will lead to a sudden large, loss of infeed to the MITS. The effects of various fault outages must be fully defined before any form of fault management can be designed.

3.3   Modelling an offshore AC hub

3.3.1   Overview of the AC hub

The UK Crown Estate Round 3 zone known as Dogger Bank has been identified as a possible location of an offshore AC hub. This is because a large amount of wind generation is expected to be built there; hence aggregation of wind energy is required. Also, assuming an interconnection between Norway and the UK is to be built, it may be

more viable to route the interconnection via Dogger Bank, thus utilising previously installed assets and avoiding difficulties associated with locating onshore converter stations. Near-term development within the Dogger Bank zone is planned to take place within Tranche A in the form of three projects. Each project is expected to include up to 1200 MW of wind generation [78].

Figure 3.1 provides the assumed infrastructure development within Tranche A and Figure 3.2 shows the equivalent single line diagram. Each project uses a single point-to-point (P2P) VSC-HVDC link with a rating of 1200 MVA. A fourth point-to-point (P2P) VSC-HVDC link, also with a rating of 1200 MVA is included to provide interconnection between the UK and Norway. Connections between VSC-HVDC converter stations are made via AC cables thus forming the offshore AC hub.
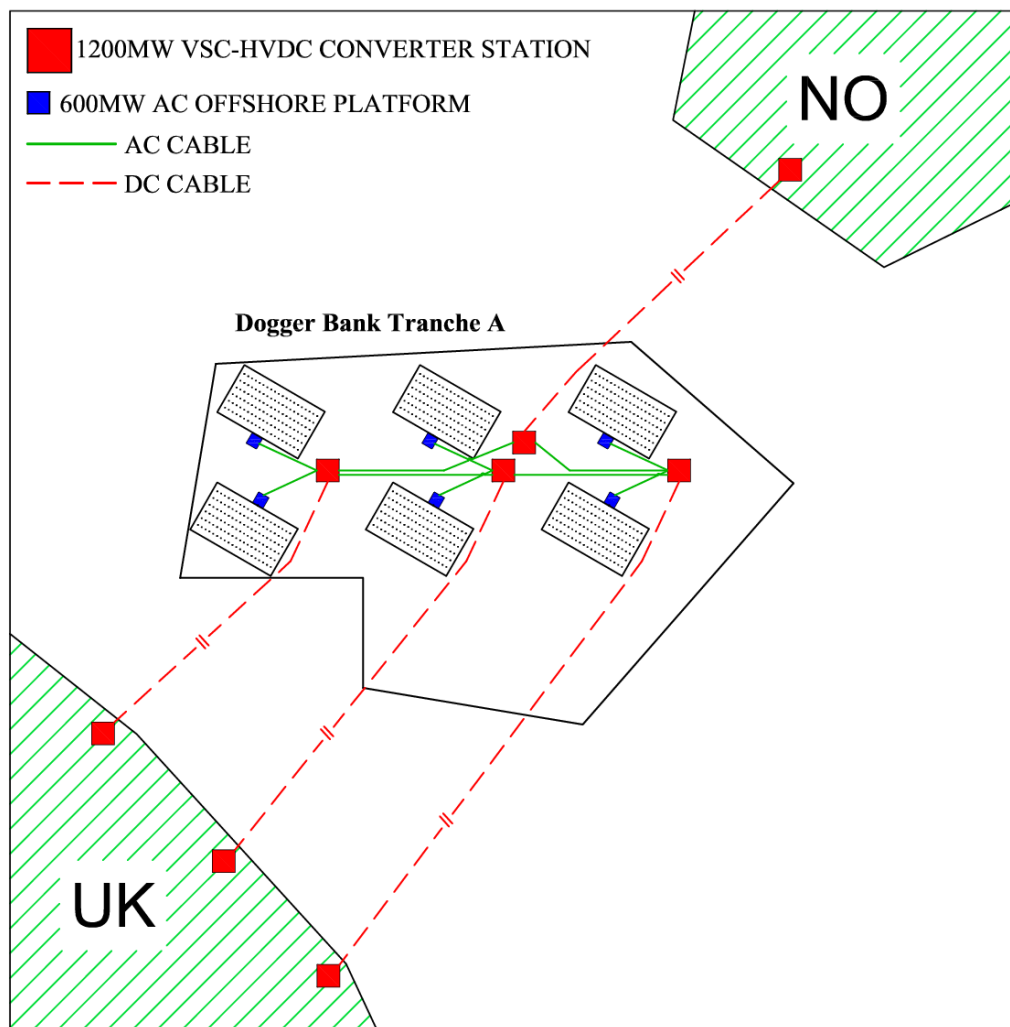
Figure 3.1 – Assumed infrastructure development in Dogger Bank Tranche A
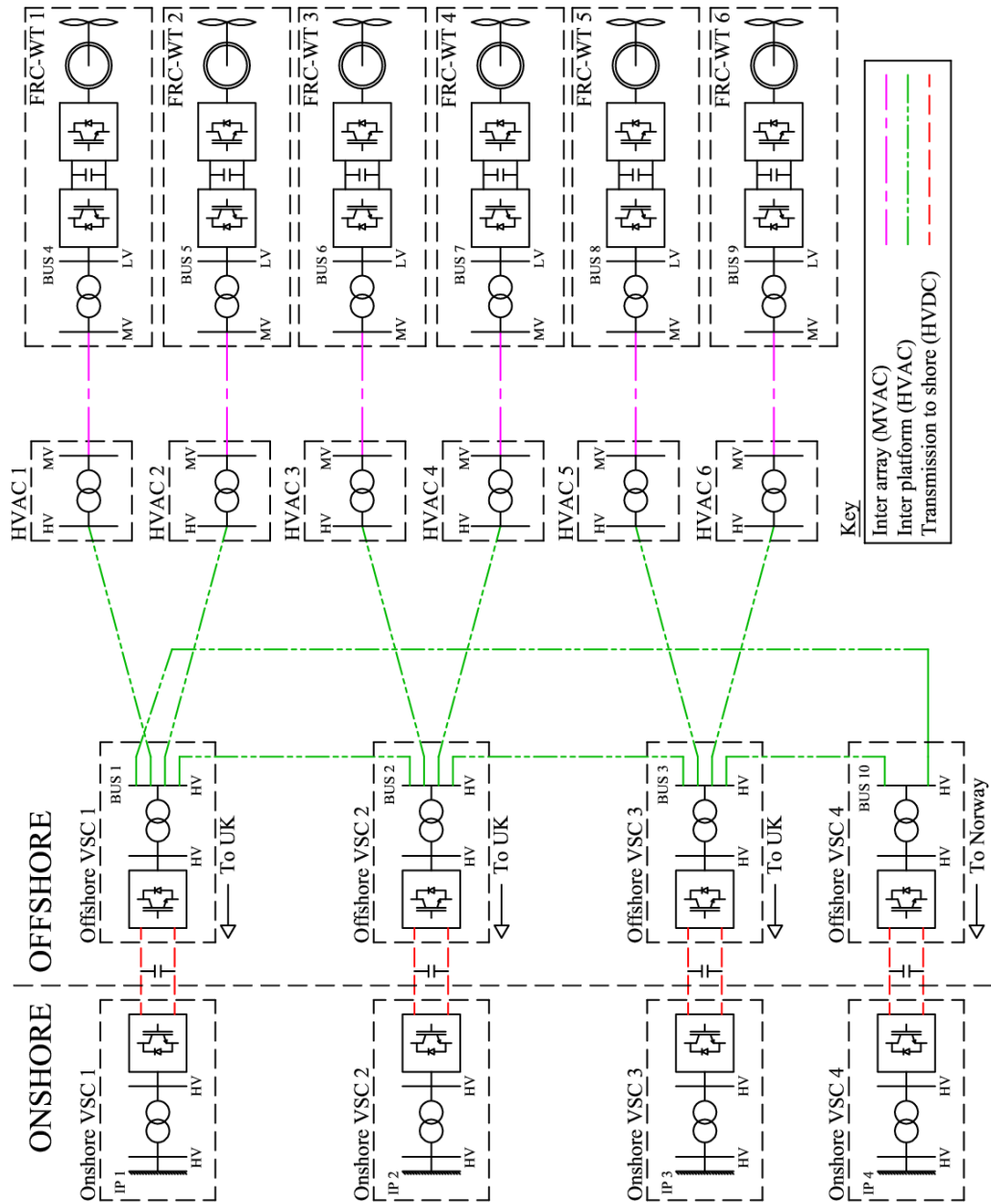
Figure 3.2 – Single line diagram of the infrastructure development at Dogger Bank

3.3.2 Wind array layout

The wind array layout is obtained through detailed analysis of system reliability, availability and maintenance of all equipment and optimisation of energy yields for the project in question. Obtaining the optimum wind farm layout is out of the scope of this thesis. However, it is reasonable to assume that any wind farm will attempt to minimise the inter array cable distances whilst maintaining suitable spacing between individual wind turbines to avoid the negative impacts of wind shadow.

As a general rule of thumb, a spacing of four times the wind turbine rotor diameter perpendicular to the prevailing wind direction and seven times the wind turbine rotor diameter along the prevailing wind direction is suitable [4]. Considering cable layout, it is reasonable to assume a radial cable layout configuration with the maximum number of wind turbines connected per string. A collector system voltage of 33 kV is assumed, along with a total generation per string of approximately 30 MW. Therefore, using 5 MW WTs, each string can connect up to six WTs. The RE Power 5M WT is one example of a commercially available 5 MW WT [79]. The rotor diameter of the 5M is 126 m. Figure 3.3 presents the assumed wind array layout based on the aforementioned design parameters including 120 5 MW WTs, and provides a maximum generation capacity of 600 MW.
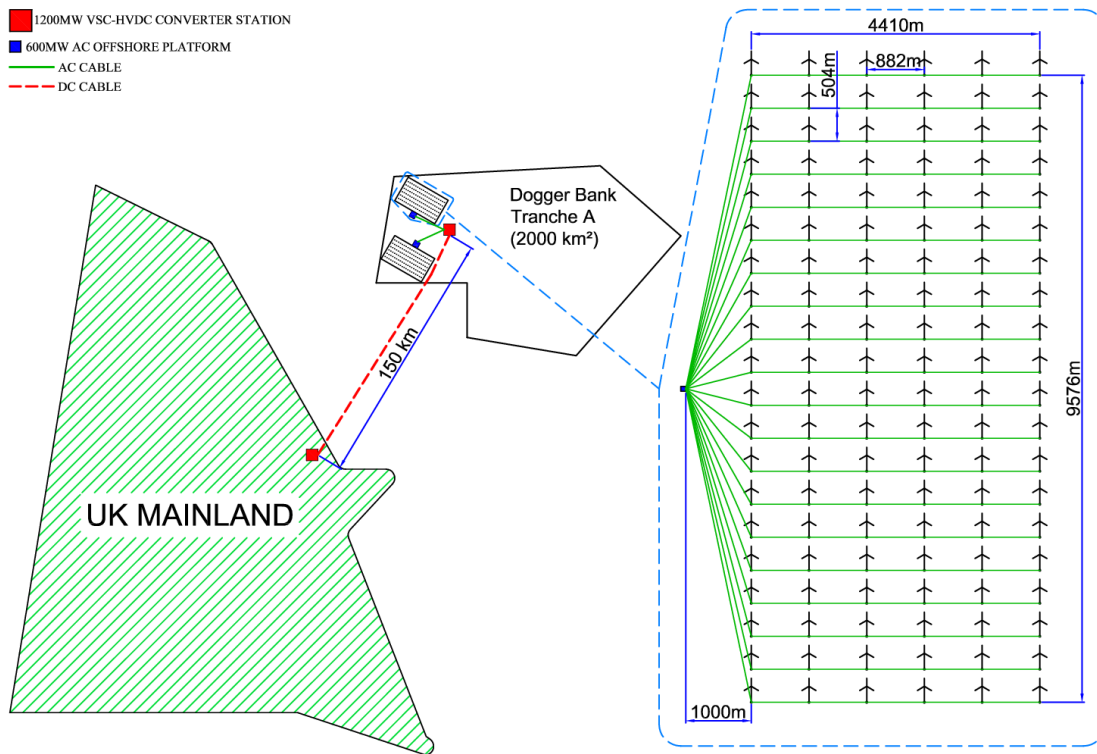
Figure 3.3 – Wind array layout in Dogger Bank tranche A

3.3.3 Cable sizing

All cables must be dimensioned for the nominal voltage, power level and the expected power factor as well any extra stresses imposed by faults. The relevant standard for calculating the maximum current carrying capacity of any AC cable is IEC 60287 which considers the losses and thermal resistance of the cable insulation and the surrounding

medium [80]. The necessary cable parameters were obtained from ABB's submarine cable systems brochure [18].

The conductor cross-sectional area must be specified for each section of the circuit according to the required power flow. It is assumed that the cables are all laid at a depth of 1 m and a 12 % de-rating factor is applied allowing for the cable sections located in J-tubes. It is assumed that the operating temperature of the conductors is 90 °C at nominal current.

3.3.3.1 Inter-array (MVAC)

It is assumed that all inter array MVAC cables are three-phase with copper conductors and a copper sheath. The maximum nominal voltage of the cables is assumed as 36 kV. Table 3.2 shows the assumed operating conditions of the inter array cabling and corresponding maximum current carrying capacity for a given cross sectional area.

Table 3.2 – MVAC submarine cable parameters

Parameters		Cable cross-sectional area (mm²)					Units
Symbol	Description	185	240	300	400	500	
R_{ac}	AC resistance	0.120	0.093	0.075	0.058	0.047	Ω/km
L	Inductance	0.390	0.380	0.360	0.350	0.340	mH/km
C	Capacitance	0.220	0.240	0.260	0.290	0.320	μF/km
W_d	Dielectric Loss	0.151	0.165	0.179	0.196	0.214	kW/km
$\lambda 1$	Loss factor for sheath and screen	0.327	0.419	0.515	0.665	0.799	-
$\lambda 2$	Loss factor for Armour, Reinforcement and Steel Pipes	0.142	0.185	0.230	0.303	0.367	-
$T1$	Thermal Resistivity between Conductor and Sheath	0.466	0.424	0.390	0.354	0.323	K.m/W
$T2$	Thermal Resistivity between Sheath and Armour	0.111	0.111	0.111	0.111	0.111	K.m/W
$T3$	Thermal Resistivity of Outer Covering	0.020	0.019	0.018	0.017	0.017	K.m/W
$T4$	External Thermal Resistance	0.396	0.391	0.387	0.382	0.376	K.m/W
I	Maximum current carrying capacity	488	544	595	660	712	A
I_n	Maximum current after 12% de-rating	429	479	524	581	626	A

The maximum apparent power capacity of the cable is given by (3.1),

$$S_{cable} = \sqrt{3}VI_n \tag{3.1}$$

A 400 mm² 33 kV inter array cable has a maximum apparent power capacity of 33.2 MVA. Assuming a 5 MW WT operates with a minimum power factor of 0.95, the apparent power is equal to 5.26 MVA. Therefore, as a first estimate, a 400 mm² cable can connect up to six WTs.

The actual apparent power capacity of the cable is reduced due to the increased charging current with increased cable length. The actual apparent power capacity of each cable is given by (3.2),

$$S_{cable} = \sqrt{3}VI_n \sqrt{1 - \left(\frac{\pi f C_c V l}{\sqrt{3}I_n}\right)^2} \tag{3.2}$$

Assuming the cable is installed between the first WT string and the HVAC platform, its length will be approximately 5 km. Applying (3.2) yields an actual apparent power capacity of 33.2 MVA. Therefore, it is realised that due to the short cable length, the maximum allowable current is equal to the cable ampacity. The 400 mm² conductor is considered as a suitable cable size for connecting a single WT string to the HVAC platform.

Further reductions in cable cross-sectional area could be made when progressing through the remainder of the wind array string. However, it is assumed that the same 400 mm² cable size is used for the remaining cable runs in each string.

3.3.3.2 Inter-platform (HVAC)

It is assumed that all inter platform HVAC cables are three-phase with copper conductors and a lead sheath. The maximum nominal voltage of the cables is assumed as 220 kV. Table 3.3 shows the assumed operating conditions of the inter platform cabling and corresponding maximum current carrying capacity for a given cross sectional area.

Table 3.3 – HVAC submarine cable parameters

Parameters		Cable cross-sectional area (mm²)			Units
Symbol	Description	630	800	1000	
R_{ac}	AC resistance	0.038	0.031	0.026	Ω/km
L	Inductance	0.410	0.400	0.380	mH/km
C	Capacitance	0.160	0.170	0.190	μF/km
W_d	Dielectric Loss	4.858	5.238	5.643	kW/km
$\lambda 1$	Loss factor for sheath and screen	0.288	0.362	0.441	-
$\lambda 2$	Loss factor for Armour, Reinforcement and Steel Pipes	0.424	0.496	0.586	-
$T1$	Thermal Resistivity between Conductor and Sheath	0.598	0.554	0.514	K.m/W
$T2$	Thermal Resistivity between Sheath and Armour	0.111	0.111	0.111	K.m/W
$T3$	Thermal Resistivity of Outer Covering	0.010	0.010	0.009	K.m/W
$T4$	External Thermal Resistance	0.321	0.316	0.313	K.m/W
I	Maximum current carrying capacity	808	873	924	A
I_n	Maximum current after 12% de-rating	711	768	813	A

The distance between each HVAC platform and corresponding HVDC platform is 10 km. For the 1000 mm² conductors, applying equation (3.2) yields an actual apparent power capacity of 309.5 MVA. The rated power of each WA is 600 MVA therefore, it is assumed that two 1000 mm² cables are suitable for interconnection between the WA HVAC platform and the HVDC platform.

To complete the AC-hub architecture, HVAC cables are required between HVDC platforms as is shown in Figure 3.2. It is assumed that given the failure of any single HVDC converter, sufficient onward transmission capacity is available through the connected HVAC cables up to the power rating of the HVDC platform (1200 MVA). As the AC-hub is arranged to form a ring, two HVAC circuits are present for each HVDC platform. Therefore, each circuit must be rated for at least 600 MVA.

The maximum distance between adjacent HVDC platforms is 20 km. For the 1000 mm² conductors, applying equation (3.2) yields an actual apparent power capacity of 308.4 MVA. Therefore, it is assumed that two 1000 mm² cables are suitable for each circuit between adjacent HVDC platforms.

3.3.3.3 Transmission to shore (HVDC)

As each HVDC link is of a symmetrical monopole configuration at least two cables are required, that is, at least one per pole. Due to the required cable length of 125 km and subsequent high cost of each cable, it is preferable that just one cable per pole is utilised. There is currently a strong incentive for manufacturers to improve HVDC XLPE cable technology as DC voltage levels increase to meet power ratings of one gigawatt and more, which, at the time or writing, is a typical rating specified for new projects. No cable manufacturers have published detailed cable data for these large capacity cables in the public domain (as they have done with lower capacity cables). ABB has published basic cable data for submarine XLPE cables, which was used as reference in this project [35].

A 2000 mm² copper conductor cable is selected for operation at ± 320 kV. This cable has an ampacity of 1953 A when close laid at a burial depth of 1 m. The AC resistance is 9 mΩ/km.

3.3.4 HVAC Platforms

The main functions of the HVAC platform include:

- To aggregate the power delivered from each of the 20 WT strings.
- To step up the voltage from 33 kV to 220 kV to allow for more efficient power transfer to the HVDC platform.
- To provide a basis from which to perform switching/isolation of WT strings.
- To provide an Operational & Maintenance (O&M) base for the wind farm.

3.3.4.1 HVAC Transformers

A key component of interest for modelling of the HVAC platform is the transformers. Various transformer arrangements may be adopted depending on redundancy, physical size/weight and mean time to repair requirements. In this study, it is assumed that two three phase YNyn0 transformers are installed in parallel, each with a nameplate rating of 400 MVA. Usually transformers can be temporarily overloaded; therefore N-1 redundancy can be achieved assuming a temporary rating of 150 % of the nominal rating of the transformer (100 % of the WA nominal power output) [34].

The leakage reactance of the transformers is of particular interest for modelling purposes. An increase in leakage reactance of the transformer is useful in limiting fault

currents but negatively impacts voltage regulation. A typical forced air-cooled transformer has a reactance of between 7 and 16 % at $V_{base} = 230$ kV [81].

The fault current provided by FRC-WTs is low compared to other forms of power generation as the current output is limited to 1.1 pu by the FRC during a fault. This would imply that a low leakage reactance would be sufficient and thus benefit voltage regulation. However, to achieve a lower leakage reactance a larger core is required which increases the weight of the transformer [82]. Increased weight is very costly in the design of an offshore platform. Therefore, there is strong incentive to reduce weight wherever possible. In addition, increased leakage reactance leads to increased reactive power consumption by the transformer under load, which can compensate for some of the reactive power generated by the MVAC and HVAC cables. As such, a higher value for the leakage reactance of 16 % was selected for each transformer. Assuming there are two in parallel, the equivalent leakage reactance is 8 %.

3.3.5 HVDC platform

The main functions of the HVDC platform include:

- To aggregate power delivered from each of the two WA HVAC platforms.
- To step up the voltage from 220 kV to a voltage more suitable for HVDC transmission to shore.
- To convert the AC waveform to DC to allow for more efficient power transfer to the MITS.
- To provide for HVAC interconnections to other HVDC platforms.

A diagram of the main electrical equipment located on the HVDC platform is shown in Figure 3.4. For modelling purposes, the components of interest include:

- The AC grid connection
- The converter transformers
- The VSC including:
  - Number of IGBTs and sub-modules
  - Sub-module capacitance
  - Arm reactor inductance
- DC chopper (onshore VSC only)

Figure 3.4 presents an overview of the key electrical equipment located on the HVDC platform.
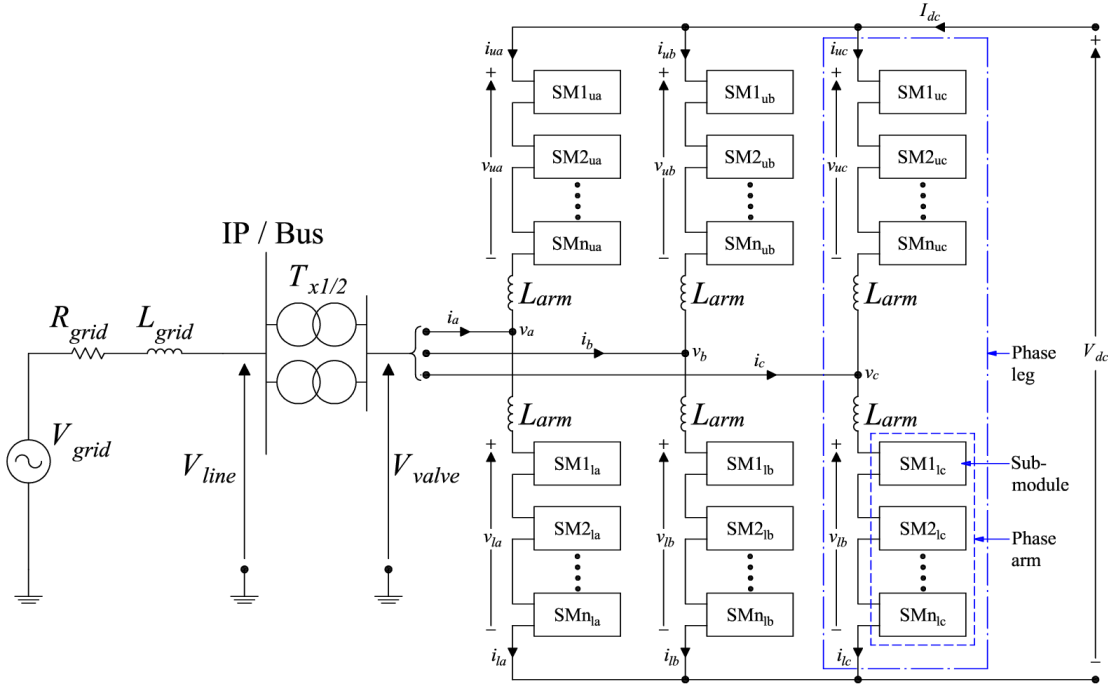
Figure 3.4 – Overview of the key electrical equipment located on the HVDC platform

3.3.5.1 Converter Transformers

As was the case with the HVAC platform, a number of transformer arrangements may be evaluated for any given project. In this study, it is assumed that two three phase YN0yn transformers are installed in parallel, each with a nameplate rating of 800 MVA. Again, N-1 redundancy and 150 % overload of the transformers is assumed.

As was the case for the transformers located on the HVAC platform, a higher leakage reactance is generally of benefit to reduce fault currents. However, voltage regulation is perhaps a more important consideration for the HVDC platform as too much voltage drop may reduce the PQ capability of the VSC. This can be offset to some extent with the use of variable taps on the winding of the transformers; however this additional complexity is not incorporated in the models presented in this thesis. In addition, as the MVA rating of the transformer increases, generally so does the leakage reactance [82]. This implies that a 20 % reactance value would be an appropriate value for each transformer. Assuming there are two in parallel, the equivalent leakage reactance is 10 %.

48

3.3.5.2   Voltage Source Converter

Number of IGBTs and sub-modules:

The VSC located on each offshore HVDC platform is assumed to be a Multi-Modular Converter (MMC). An overview of the MMC can be seen in Figure 3.4. Figure 3.5 presents a single sub-module as used in Siemens HVDC Plus, which is their variant of a MMC [83]. It consists of a single half-bridge arrangement and each switch consists of a single IGBT module and there is a single capacitor.
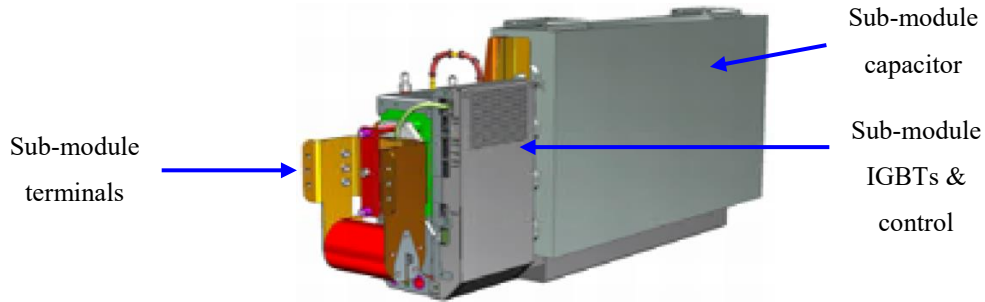
Figure 3.5 – A single sub-module as used in Siemens MMC [34]
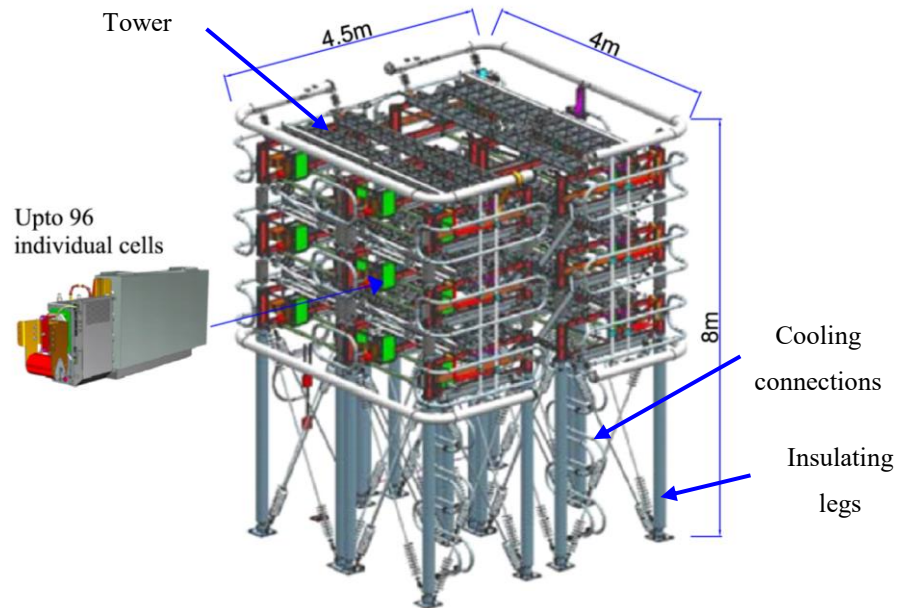
Figure 3.6 – Converter tower arrangement for Siemens HVDC Plus [34]

Figure 3.6 shows the module arrangement used within the MMC. A single module or converter tower, as it is referred to as by Siemens, contains three rows and four columns and each row consists of eight sub-modules, thus each module can contain up to 96 sub-modules [34].

The IGBT module rating was assumed to have a maximum collector-emitter voltage of 4.5 kV and maximum DC collector current of 2 kA. A reasonable operating voltage across each sub-module of 2 kV is selected. As each switch position consists of just one IGBT module, the voltage across each sub-module (V_{SM}) is 2 kV. Figure 3.7 presents the single line diagram of a sub-module.
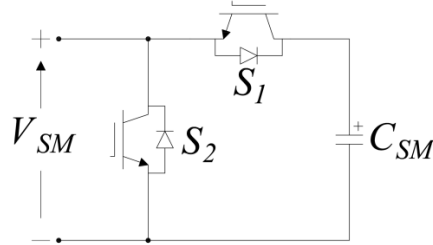
Figure 3.7 – Single line diagram of a single sub-module

S_1 and S_2 are the IGBTs located in each cell and C_{SM} is the cell capacitor. The total number of sub-modules required per phase arm is determined according to the maximum DC link voltage plus 10% additional sub-modules for redundancy, as given by (3.3).

$$N_{SM} = 1.1 \frac{V_{DC}}{V_{SM}}$$ (3.3)

Where V_{DC} is the DC link voltage, N_{SM} is the number of sub-modules per phase arm and V_{SM} is the cell voltage. Each module consists of up to 96 sub-modules therefore the number of modules required per phase arm (N_{mod}) is given by,

$$N_{mod} = \text{ceil}(\frac{N_{SM}}{96})$$ (3.4)

The number of IGBTs, sub-modules and converter modules required for the MMC is shown in Table 3.4.

Table 3.4 – MMC valve parameters

Parameters		Value
Symbol	Description	
N_{SM}	No. sub-modules per phase arm	352
N_{SM_mod}	No. sub-modules per module	88
N_{mod}	No. modules per arm	4
N_{IGBT}	Total No. IGBTs	4224

Sub-module capacitance:

The sub-module capacitance for the MMC is determined by the following equation [84]:

$$C_{SM} \geq \frac{|S|}{3\omega} \frac{1.22}{V_{DC}V_{SM}\Delta V}$$

(3.5)

The minimum sub-module capacitance to ensure the voltage ripple is less than 10% is 12.14 mF.

Arm reactor inductance:

The arm inductor is an important component in any VSC topology because it provides several key functions. One function of the arm inductor is to limit fault currents. In the event of a DC side fault, the VSC will act as an uncontrolled rectifier with current flowing through the free-wheeling diodes. Under these conditions the AC grid will feed the DC side fault until the AC breaker opens. The arm inductor of each phase arm is placed in series with the impedance of the transformer and AC grid impedance; the sum of which will limit the fault current. If the fault current is too large then the free-wheeling diodes in each IGBT module will be damaged. To protect the diodes a thyristor (T_1) is inserted in parallel to each sub-module as shown in Figure 3.8. When fired, most of the fault current will flow through the thyristor, which has a higher current rating than the anti-parallel diodes [85].
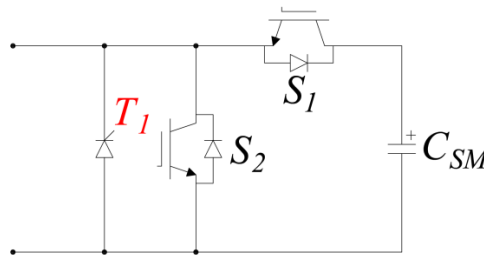
Figure 3.8 – Single line diagram of a MMC sub-module including a protective thyristor

Numerous sources in the literature have analysed DC pole-pole faults on HVDC links [49], [51], [86], [87]. The peak fault current on the AC-side ranges between 5 and 10 kA. Therefore, it is assumed that the maximum allowable peak fault current on the AC-side is ≤ 10 kA. The worst case peak fault current is given by (3.6),

$$I_{acfpm} = 2\frac{V_{ac}}{Z_T}\sqrt{2}$$

(3.6)

Rearranging equation (3.6) in terms of $|Z|$ and defining $I_{acfpm} = 10$ kA gives a required total impedance per phase Z_T. It is assumed that the fault current flows through 4 parallel arms with 4 arm reactors for 3 phases, as not all diodes are conducting at any one instant. Therefore, a total equivalent impedance for each phase is defined as [49]:

$$Z_{EQ} = Z_{grid} + Z_{tx} + \frac{3Z_{arm}}{4}$$

(3.7)

Assuming $Z_{EQ} = Z_T$ and rearranging equation (3.7) for Z_{arm} yields the required arm impedance to limit the peak fault current in the event of a DC pole-pole fault to 10 kA.

The grid impedance is determined from the assumed short circuit level (SCL) and X/R ratio as defined by:

$$Z_{grid} = R_{grid} + jX_{grid}$$

(3.8)

Where,

$$X_{grid} = \frac{V_{base}^2}{SCL}$$

$$R_{grid} = \frac{X_{grid}}{X/R}$$

The onshore SCL is assumed as 10 000 MVA. The offshore SCL is estimated as follows:

$$S_{grid\_SCL} = \sum S_{g\_max}$$

(3.9)

Where S_{g_max} is apparent power limit of each VSC and FRC-WT in the offshore network. Assuming that $S_{g\_max} = 1.1$ pu, $S_{grid\_SCL\_onsh} = 7920$ MVA. Using (3.8), Z_{grid} is determined for both the on and offshore interface points. Equation (3.7) is then applied to determine the necessary arm inductance both on and offshore, as summarised in Table 3.5.

Table 3.5 – Arm reactor inductance for VSCs

Parameters		Inductance (mH)
Symbol	Description	
L_{arm_onsh}	Onshore VSC arm reactor	145.0
L_{arm_offsh}	Offshore VSC arm reactor	132.0

3.3.5.3 DC Chopper

A DC chopper is a well proven method of avoiding an overvoltage in the DC link due to a power imbalance [56]. An overvoltage will arise in the event of more power being injected in to the DC link than is being extracted from the DC link. This could be due to an AC fault at the on or offshore interface point. The power imbalance between the on and offshore VSCs would cause the VSC sub-module capacitors to charge, possibly to damaging levels, if the power imbalance is not addressed. The DC chopper is able to address the power imbalance through dissipating the excess power as heat, thus avoiding the otherwise damaging overvoltage.

Figure 3.9 shows the DC chopper installed close to the onshore VSC. It is normal to install the DC chopper onshore as it avoids additional weight and space requirements for the offshore VSC platform which would be very expensive.
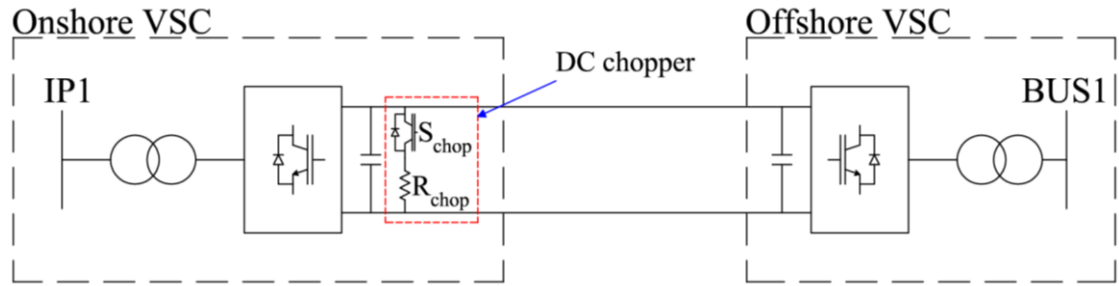
Figure 3.9 – DC chopper location on a HVDC link

The DC chopper consists of two main components, including a suitably dimensioned resistor bank and a semiconductor switch (normally a series connected string of IGBTs). The DC chopper must be able to absorb the excess energy for the duration of the power imbalance caused by a fault. Therefore, the power rating should be equivalent to the rating of the VSC-HVDC link. The duration of the power imbalance is the time taken until the fault is cleared, which could be up to 140 ms.

The power dissipated in the DC chopper resistor is given as:

$$P_{chopper} = \frac{\delta V_{dc}^2}{R_{chopper}} \qquad (3.10)$$

Where δ is defined as the duty ratio of the chopper circuit [29]. Under normal conditions, $\delta = 0$ therefore the chopper is switched off. Under fault conditions, the DC

voltage rises above the nominal value $V_{dc_{nom}}$. The duty cycle of the chopper is calculated as follows:

$$\delta = \begin{cases} 0 & V_{dc} < V_{dc\_thresh} \\ \dfrac{V_{dc} - V_{dc\_thresh}}{V_{dc\_max} - V_{dc\_thresh}} & \text{for } V_{dc\_thresh} < V_{dc} < V_{dc\_max} \\ 1 & V_{dc} > V_{dc\_max} \end{cases} \quad (3.11)$$

Where,

- V_{dc} is the measured DC voltage.
- V_{dc_thresh} is the threshold at which the DC chopper begins to operate.
- V_{dc_max} is the maximum allowed DC voltage

The required chopper resistance $R_{chopper}$ is calculated by re-arranging (3.10) assuming:

- δ is equal to 1
- V_{dc} is equal to $V_{dc_{max}}$ which is defined as $1.1 V_{dc}$
- $P_{chopper}$ is equal to 1.1 times the rated power of the DC link

The resistance of the chopper resistor is found as 375.5 Ω for the VSC-HVDC links.

3.3.5.4 Summary of HVDC platform electrical parameters including the MMC

Parameters		Value		Units
Symbol	Description			
-	Platform location	Offshore	Onshore	-
S_{VSC}	Rated Power	1200.0		MVA
S_{VSC_Tx}	Transformer rated power (each)	800.0		MVA
V_{line}	Transformer line-side AC voltage	220.0	400.0	kV
V_{valve}	Transformer valve-side AC voltage	333.0	333.0	kV
Z_{VSC_Tx}	Transformer Impedance	20.0		%
S_{grid_SCL}	Grid SCL	7920.0	10000.0	MVA
L_{grid}	Grid inductance	44.6	35.3	mH
R_{grid}	Grid resistance	0.3	0.2	Ω
L_{arm}	Arm reactor inductance	112.5	124.9	mH
R_{arm}	Arm reactor resistance	0.7	0.8	Ω
V_{DC}	DC bus voltage	640.0		kV
R_{chop}	DC chopper resistance	375.5		Ω
V_{SM}	Sub-module voltage	2.0		kV
C_{SM}	Sub-module capacitance	12.1		mF
N_{SM}	No. sub-modules per phase arm	2.0		-
N_{SM_mod}	No. sub-modules per module	88.0		-
N_{mod}	No. modules per arm	4.0		-
N_{IGBT}	Total No. IGBTs	4224.0		-

3.3.6 Fully Rated Converter Wind Turbines

The WTs use a PMSG connected to the offshore grid via a FRC as shown in Figure 3.10. A DC chopper is included to dissipate excess power from the Generator side converter should there be a fault in the offshore AC network. The applied chopper is the same as that applied to the HVDC links with the parameters adjusted accordingly.
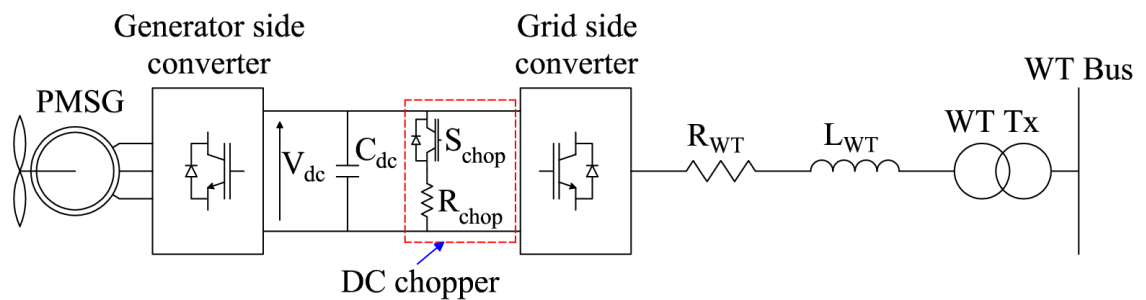
Figure 3.10 – Outline of the FRC-WT

The parameters used for the 5 MVA WT are obtained from [88]. The key parameters are summarised in Table 3.6.

Table 3.6 – List of FRC-WT parameters

Parameters		Value	Units
Symbol	Description		
S_{WT}	PMSG rated power	5.0	MVA
S_{WT_Tx}	Transformer rated power	5.0	MVA
$V_{HV/LV}$	Transformer HV/LV voltage	33 / 0.69	kV
L_{WT_Tx}	Transformer leakage inductance	0.1	pu
R_{WT_Tx}	Transformer winding resistance	0.0	pu
L_{WT}	Interface reactor inductance	0.2	mH
R_{WT}	Interface reactor resistance	0.5	mΩ
V_{dc}	DC-link voltage	1.5	kV
C_{dc}	DC-link capacitance	10.0	mF
R_{chop}	DC chopper resistance	18.8	mΩ

3.4 SimPowerSystems model of an offshore AC hub

A model of the offshore AC hub has been developed in the SimPowerSystems toolbox of MATLAB Simulink. The components are modelled in the natural (*abc*) reference frame. Each component is considered individually in order to determine how it should be modelled. The intention is to avoiding unnecessary model complexity that could generate complex high-order interactions that are not of immediate importance in this work, and/or would lengthen simulation times dramatically. In addition, hardware limitations must be considered to ensure the model does not become difficult to handle.

Figure 3.11 presents the single line diagram of the SimPowerSystems model. The following points summarise the key methods used to reduce model complexity:

- Averaged models are used to represent the VSCs and FRC-WTs.
- All 120 WTs in a single WA are modelled by a single equivalent WT model.
- Each FRC-WT does not include the wind turbine side converter of the FRC, the WTG and rotor. An equivalent DC source is used instead to represent the generated wind power.
- The MVAC cables between the first WT of each string and the HVAC platform are represented by a single equivalent cable model. The MVAC cables between FRC-WTs are neglected.
- The two transformers on the HVAC platform are modelled by a single ideal transformer model.

- The two transformers on the HVDC platform are modelled by a single ideal transformer model.
- Each HVAC cable circuit between the HVAC platform and the HVDC platform is represented by a single equivalent cable model.
- Each HVAC cable circuit between HVDC platforms is represented by a single equivalent cable model.
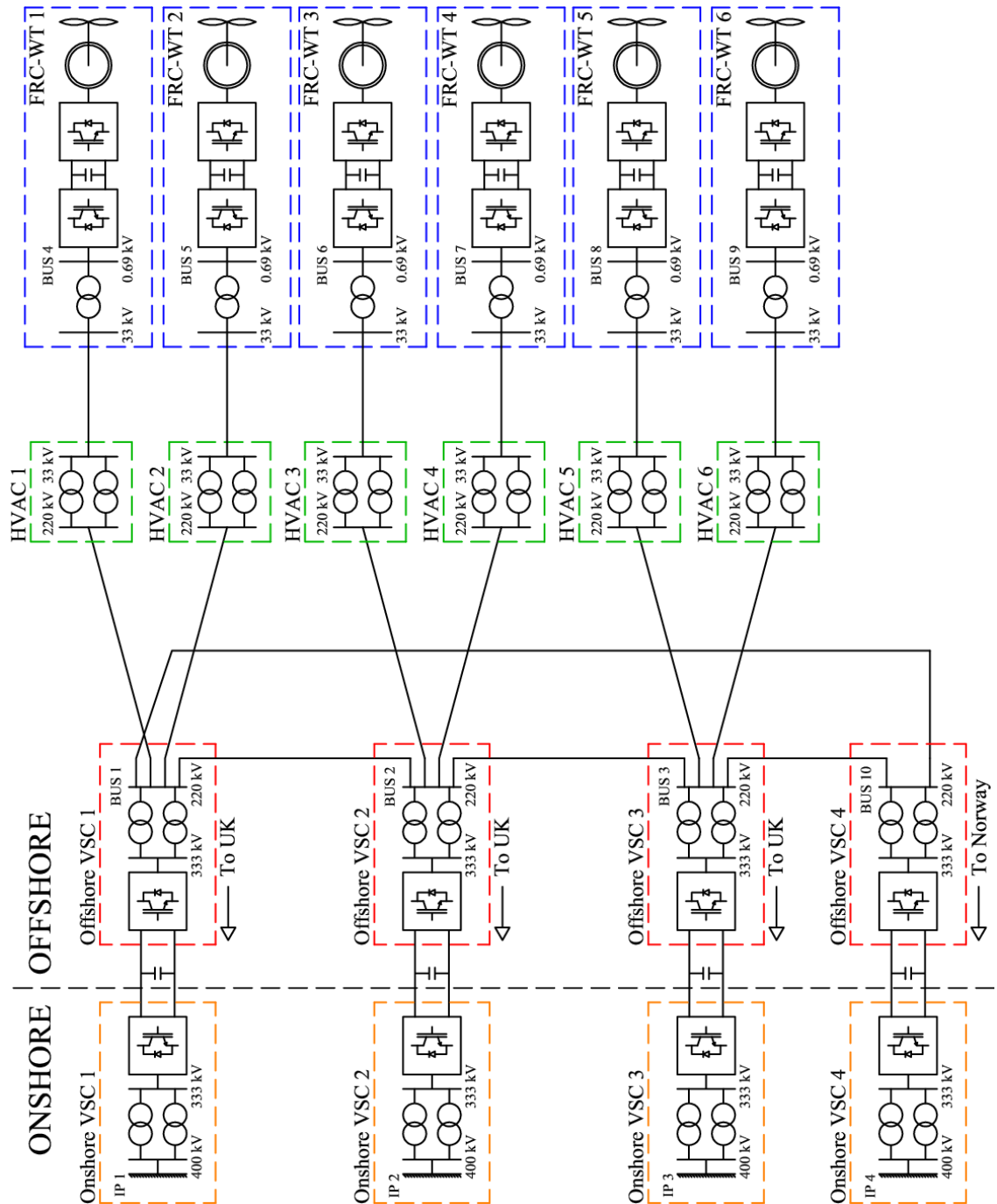
Figure 3.11 – Single line diagram of the offshore AC hub and HVDC links

3.4.1 Cable modelling

When modelling any transmission line, be it a cable or overhead line, four per unit length parameters are normally considered, resistance (Ω/km), inductance (mH/km), capacitance (μF/km) and conductance (S/km). If waveforms at higher frequencies than the fundamental are to be investigated (>5 times), frequency dependent models must be used, such as the Bergeron model [81].

For short overhead lines it is common to model the transmission line using just a series resistance and inductance. This is acceptable because the capacitance and conductance would be minimal for a short overhead line. For cables however, the capacitance is considerable even for short lengths and therefore must be considered.

If the length (l) of the line is much less than the wavelength (λ) of the voltage and current waveforms, then the nominal π equivalent circuit may be used, as shown in Figure 3.12. The approximation is valid if $l < 3000/f$ km (< 60 km at 50 Hz) for underground cables. If the cable length is to be above 60 km, then cascaded nominal π equivalent circuits can be used representing distributed sections of the line.
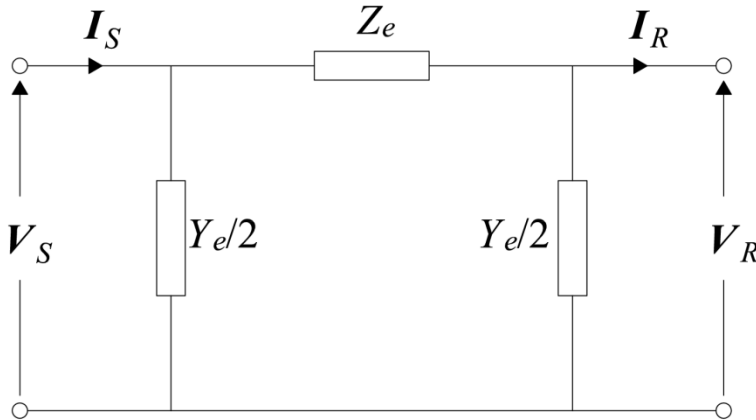
Figure 3.12 – Nominal π equivalent circuit

For a lossless transmission line the propagation constant (γ) is defined by

$$\gamma = j\beta = j\omega\sqrt{LC} \qquad (3.12)$$

If $\gamma l \ll 1$, which is likely for an electrically short transmission line, then the expressions for Z_e and Y_e may be approximated as follows,

$$\begin{aligned} Z_e &= Z_c \sinh(\gamma l) \\ &\approx Z_c(\gamma l) \end{aligned} \qquad (3.13)$$

58

$$\approx zl = Z$$

And,

$$\frac{Y_e}{2} = \frac{1}{Z_c}\tanh\left(\frac{\gamma l}{2}\right)$$

$$\approx \frac{1}{Z_c}\left(\frac{\gamma l}{2}\right) \tag{3.14}$$

$$\approx \frac{yl}{2} = \frac{Y}{2}$$

The inter platform HVAC cable whose parameters are defined in Table 3.3 has a propagation constant of 0.0027. Multiplying the propagation constant by the line length of 20 km gives $\gamma l = 0.053 \ll 1$. Therefore equations (3.13) and (3.14) are suitable to represent the total series impedance (zl) and total shunt admittance (yl) of the nominal π equivalent circuit. The nominal π equivalent circuit is used to represent all AC cable circuits in the AC hub model.

3.4.1.1 Inter-array equivalent cable model:

All 120 FRC-WTs located in a single wind array are aggregated into a single equivalent FRC-WT model. Therefore it is necessary to combine the cables serving each WT string in to a single equivalent cable model. The maximum length of cable between the HVAC platform and the first WT of each string is 5km. Therefore a nominal π equivalent circuit is suitable as shown in Figure 3.12. There are six FRC-WTs in each string and 24 strings per WA.

The first stage of aggregation is made by splitting the WA in to five sections, as illustrated in Figure 3.13. Each section consists of 24 FRC-WTs connected in parallel to a single bus with connection to the HVAC platform made via four parallel MVAC cables of equal length. The length of each set of MVAC cables in a section then varies according to the distance from the HVAC platform.
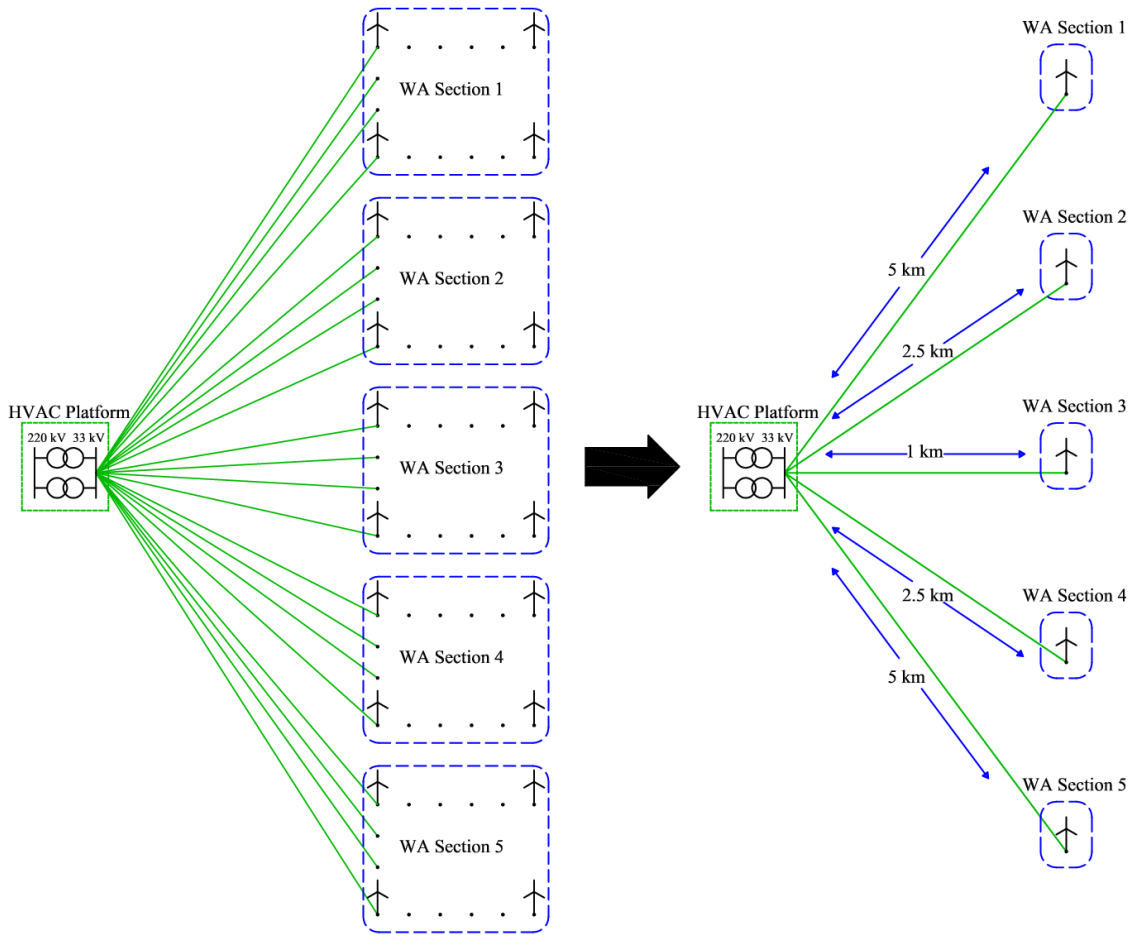
Figure 3.13 – Illustration of first stage of WA aggregation

The four parallel MVAC cables present in each section are then combined and represented by a nominal π equivalent circuit. The series impedance and shunt admittance of a single cable is determined by (3.13) and (3.14) respectively. The equivalent series impedance of four cables in parallel is calculated as:

$$Z_{e\_24} = \frac{Z_e}{4} = \frac{zl}{4} \tag{3.15}$$

The equivalent shunt admittance of four cables in parallel is calculated as:

$$\frac{Y_{e\_24}}{2} = 2Y_e = 2yl \tag{3.16}$$

Where l is the conductor length, z is the series impedance of a single cable per unit length and y is the shunt admittance of a single cable per unit length.

The second stage of aggregation is made though combining each of the five sections in to a single section representing the entire WA as illustrated in Figure 3.14.
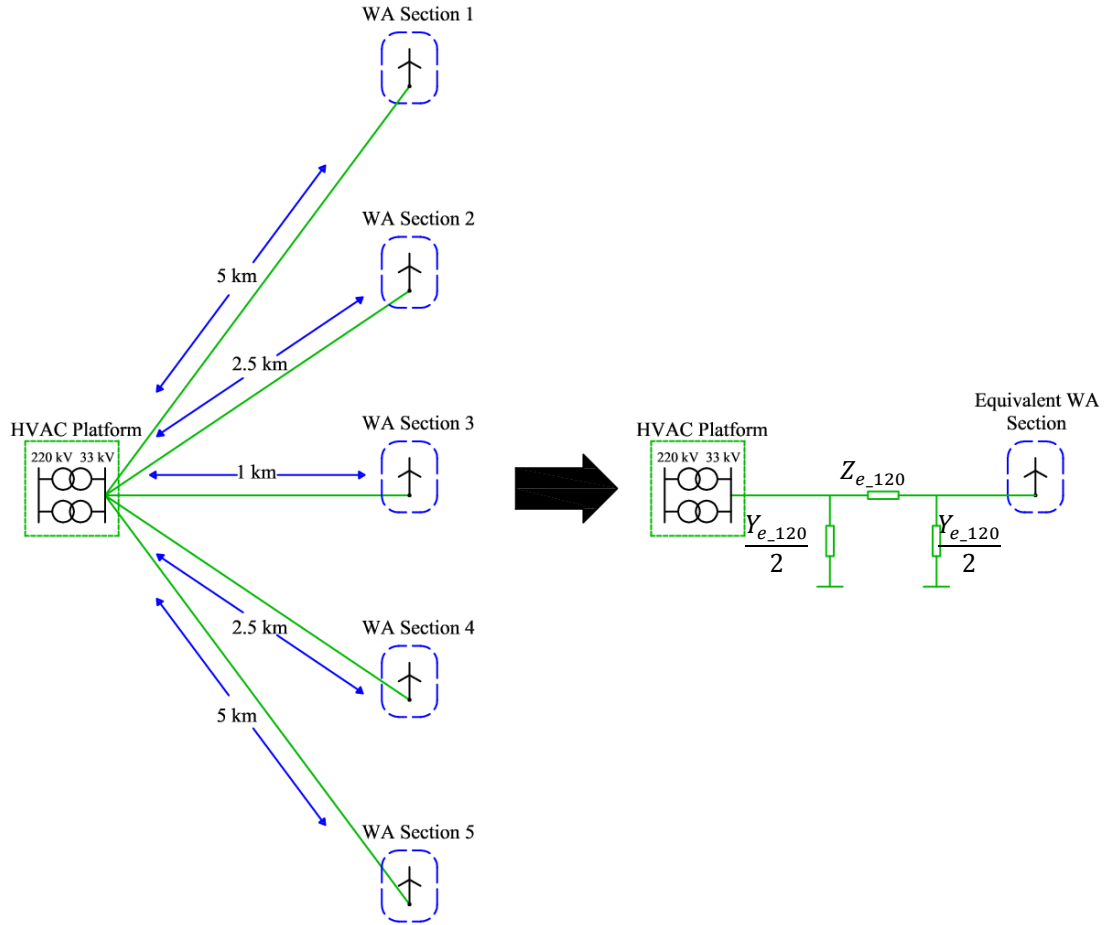
Figure 3.14 – Illustration of second stage of WA aggregation

Therefore, the final section consists of 120 WTs connected in parallel to a single bus with connection to the HVAC platform via a single equivalent cable model. The equivalent series impedance and equivalent shunt admittance of the five equivalent cable section models is calculated using (3.17) and (3.18) respectively.

$$Z_{e\_120} = \frac{1}{\sum \dfrac{4}{zl_n}} \tag{3.17}$$

$$Y_{e\_120} = \sum_{n=1}^{N} 2yl_n \tag{3.18}$$

Where l_n is the length of each section n. The equivalent cable model parameters for the inter-array MVAC cables are given in Table 3.7.

3.4.1.2 Inter-platform equivalent cable model:

As discussed in section 3.3.3.2, each HVAC platform is connected to the HVDC platform via two 300 MVA HVAC cables. The length of each cable is 10 km, therefore

again a nominal π equivalent circuit is used, as shown in Figure 3.12. An equivalent cable model is developed by halving the series impedance and doubling the shunt admittance of a single cable length.

The same method is used to determine the equivalent cable model of the HVAC cables strung between HVDC platforms. Again there are two 300 MVA HVAC cables per circuit, albeit the cables are 20 km in length. The equivalent cable model parameters for the inter-platform HVAC cables are given in Table 3.7.

3.4.1.3 Transmission to shore (HVDC) equivalent cable model:

Two HVDC cables connect the on and offshore platforms of each HVDC link as was discussed in section 3.3.3.3. As shown in Figure 3.15, an equivalent series resistance at each end of the cable is used to represent the total series resistance of the cable.
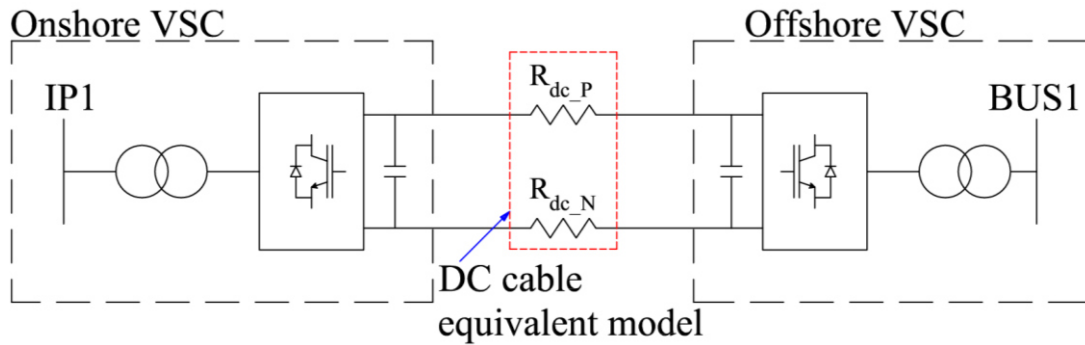
Figure 3.15 – Equivalent cable model of the HVDC cables

In order to perform a detailed analysis of DC fault response, the longer line length of the HVDC cables dictates that frequency dependent distributed parameter models should be used [45]. However, capturing a detailed DC fault response is not the aim of this thesis. The impact of a DC fault on the offshore AC-hub is of interest in this thesis. Therefore, the use of a basic DC cable model was considered as sufficient.

3.4.1.4 Summary of cable model parameters

Table 3.7 presents the equivalent cable parameters for each cable section used in the SimPowerSystems model.

Table 3.7 – Equivalent cable model parameters

Parameters		Value	Units
Symbol	Description		
	Inter-array cable (33 kV):		
R_{33}	Series resistance	65.00	mΩ
L_{33}	Series inductance	39.79	µH
$Y_{33}/2$	Shunt capacitance	0.15	µF
	Inter-platform cable (220 kV, 10km):		
R_{220_10}	Series resistance	132.50	mΩ
L_{220_10}	Series inductance	1.89	mH
$Y_{220\_10}/2$	Shunt capacitance	1.89	µF
	Inter-platform cable (220 kV, 20km):		
R_{220_20}	Series resistance	265.00	mΩ
L_{220_20}	Series inductance	3.79	mH
$Y_{220\_20}/2$	Shunt capacitance	3.79	µF
	HVDC cable (320 kV, 150km):		
$R_{DC\_P/N}$	Series resistance	1.35	Ω

3.4.2 HVAC Platforms

The key electrical components of the HVAC platform is the transformers, as shown in Figure 3.16.
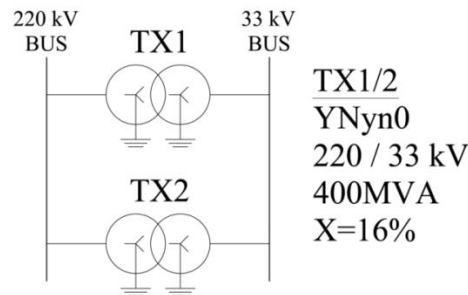
Figure 3.16 – Transformer arrangement on the HVAC platform

A single ideal transformer model is used to represent the two transformers located on the platform. The transformer model is shown in Figure 3.17.
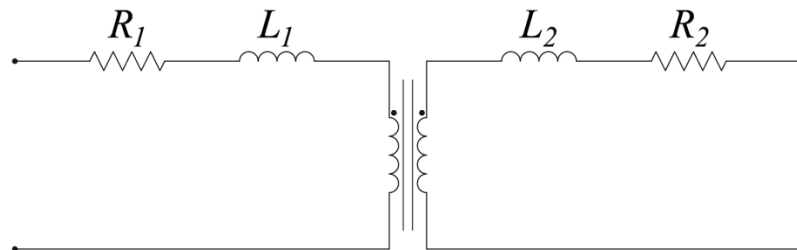
Figure 3.17 – Ideal transformer model

The parameter values for the equivalent linear transformer model are listed in Table 3.8.

Table 3.8 – Equivalent transformer model parameters for the HVAC platform

Parameters		Value	Units
Symbol	Description		
R_1	HV winding series resistance	96.80	mΩ
L_1	HV winding series inductance	15.41	mH
R_2	LV winding series resistance	2.18	mΩ
L_2	LV winding series inductance	0.35	mH

3.4.3   HVDC Platforms

The VSCs located on each offshore HVDC platform are assumed as Multi-Modular Converters (MMC). A single line diagram of a MMC is shown in Figure 3.18. The number of individual sub-modules in the MMC was calculated in section 3.3.5.2, hence there are 4224 IGBTs in each MMC complete with anti-parallel diodes. In the offshore AC hub, there are in total 8 VSCs and therefore there are 33792 IGBTs in total (not including FRC-WTs).
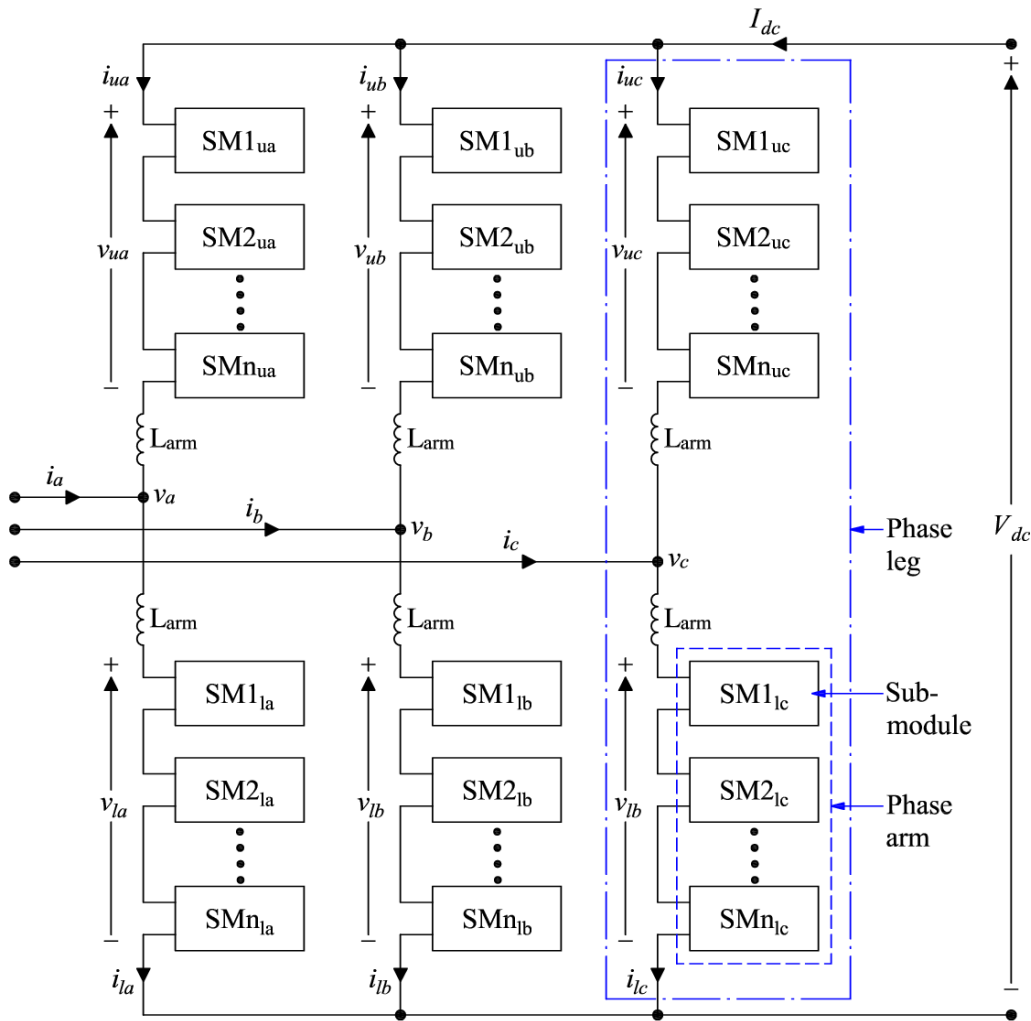
Figure 3.18 – Single line diagram of the MMC topology

In [86], MMC models with varying levels of detail are simulated under normal and fault operational conditions. There is a trade-off to be made between model accuracy and computational effort. The choice of which model to use is therefore a question of which model provides sufficient accuracy for the analysis to be carried out with the least computational effort.

The analysis carried out in this thesis is split into two areas:

1. **Normal operation** - Analysis of changes in voltage, current and complex power in response to changes in dispatch orders and wind power output.
2. **Operation under fault** - Analysis of the impacts of faults on the voltage/current and complex power.

3.4.3.1 VSC model under normal operation

For the first point of analysis, an averaged model [89] of a MMC, as shown in Figure 3.19, can provide a sufficient level of detail and also requires the least computational effort. The AC side of the averaged model includes six equivalent voltage sources representing each phase arm of the MMC. On the DC side an equivalent current source represents the combined current flowing through each phase leg. A single equivalent capacitance is placed on the DC side to represent the sub-module capacitors.
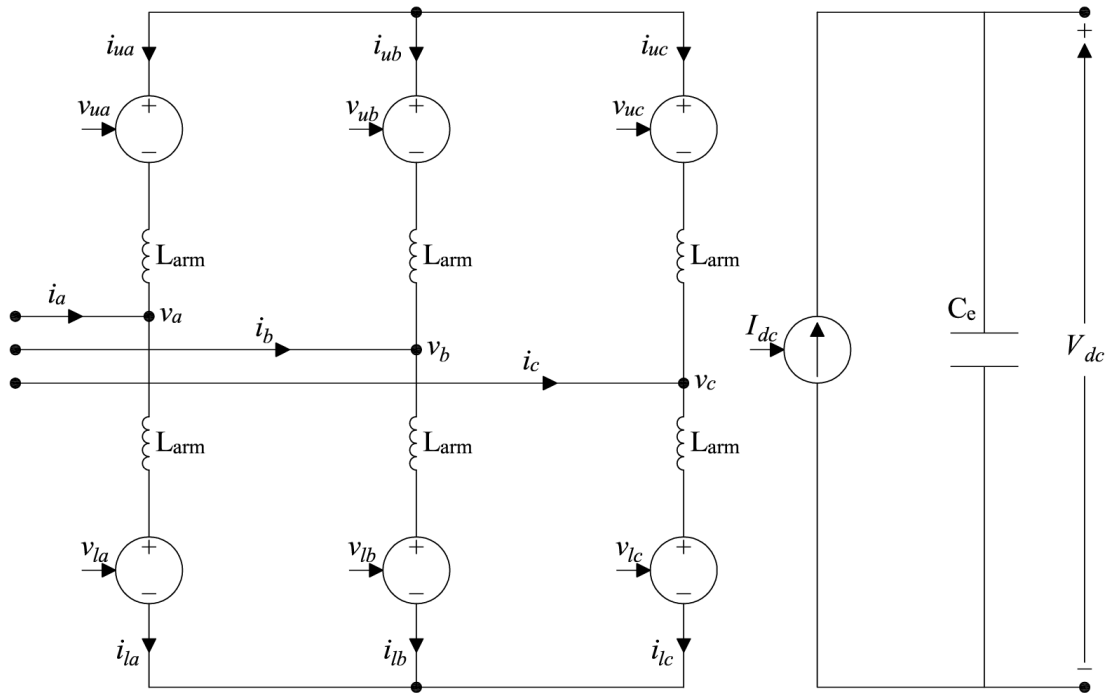
Figure 3.19 – Averaged model of a MMC

65

The voltage across each phase arm v_{uj} is equal to the sum of the sub-module voltages present in each arm. The average model assumes that the voltages across each sub-module are perfectly balanced. Therefore no circulating current is present and consequently, circulating current suppression controllers are not required.

From Figure 3.19 the voltage across the upper and lower phase arms are defined as:

$$v_{uj} = \frac{V_{dc}}{2} - L_{arm}\frac{di_{uj}}{dt} - v_j \tag{3.19}$$

$$v_{lj} = \frac{V_{dc}}{2} - L_{arm}\frac{di_{lj}}{dt} + v_j \tag{3.20}$$

Where $j = a, b, c$. The upper and lower arm currents are defined as:

$$i_{uj} = \frac{I_{dc}}{3} - \frac{i_j}{2} \tag{3.21}$$

$$i_{lj} = \frac{I_{dc}}{3} + \frac{i_j}{2} \tag{3.22}$$

Combining (3.19)-(3.22) yields:

$$v_{uj} = v_{refj} + \frac{V_{dc}}{2} \tag{3.23}$$

$$v_{lj} = -v_{refj} + \frac{V_{dc}}{2} \tag{3.24}$$

Where,

$$v_{refj} = \frac{v_{uj} - v_{lj}}{2} \tag{3.25}$$

The voltage reference v_{refj} is provided by the MMC control loops. The arm voltages are then determined using (3.23) and (3.24). The power balance between the AC and DC side is maintained exactly and is described by

$$P_{ac} = P_{dc} \tag{3.26}$$

$$\sum_{j=a,b,c} v_{refj} i_j = V_{dc} I_{dc} \tag{3.27}$$

Therefore the dc current can be defined as:

$$I_{dc} = \frac{\sum_{j=a,b,c} v_{refj} i_j}{V_{dc}} \tag{3.28}$$

Assuming all sub-modules have the same voltage V_{SM}, the equivalent capacitor C_e is determined as a function of the sub-module capacitance as defined by (3.29) [85].

$$C_e = \frac{6C_{SM}}{N_{SM}} \tag{3.29}$$

3.4.3.2   VSC model for operation under fault

For the second point of analysis, more detailed models are normally required to capture the voltage and current perturbations occurring within the MMC [86]. However, the available computing resources for this project are limited and the increased computational effort required for the detailed models would exceed these limits. To overcome this issue, a modified average model capable of reproducing fault behaviour to sufficient levels of accuracy was developed.

In [86], modifications to the average model are made in an attempt to produce a fault response that agrees with more detailed simulations. The authors show that even once modified, the average model fails to produce a valid fault response. The authors conclude that this is because the arm inductances are bypassed during the fault and therefore do not impede the fault current. The results confirm this as a large transient fault current is observed.

To overcome this, further modifications to the average model are required. The modifications to account for faults with the VSC operating under normal conditions is shown in Figure 3.20. The key modifications to the averaged model include:

- Six parallel diodes to represent the free-wheeling diodes that would be present in each sub-module. These are inserted when the IGBTs are blocked by opening switch $K1_{u/lj}$ and closing switch $K2_{u/lj}$ for each phase j where $j = a, b, c$.
- A diode on the DC link to insure that the current flows in the correct direction in the event of a fault. This is inserted at the time the fault is initiated by opening switch $K1_{dc}$ and closing switch $K2_{dc}$.
- A switch to isolate the equivalent capacitance of the DC link. The switch $K3_{dc}$ opens when the IGBTs are blocked.
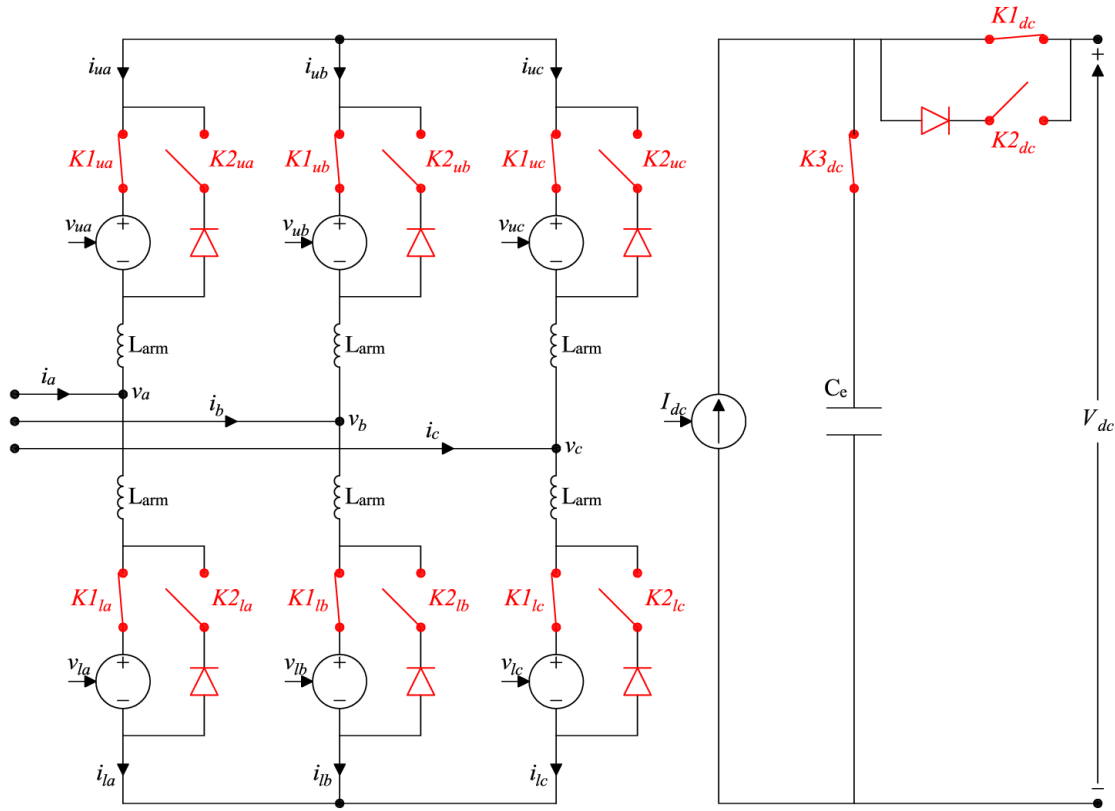
Figure 3.20 – Averaged model with the additional modifications, operating under normal conditions

Figure 3.21 shows the operation of the VSC when subject to a pole-pole fault on the DC side. The DC fault is applied on both the AC and DC side of the averaged model, with the same fault impedance Z_{fault}. The fault current in the AC side $I_{dcf(ac)}$ is used as a signal to the equivalent current source on the DC side, causing the DC fault current $I_{dcf(dc)}$ to flow. The DC voltage is therefore a product of the DC fault contributions from each VSC terminal across the fault impedance Z_{fault}.
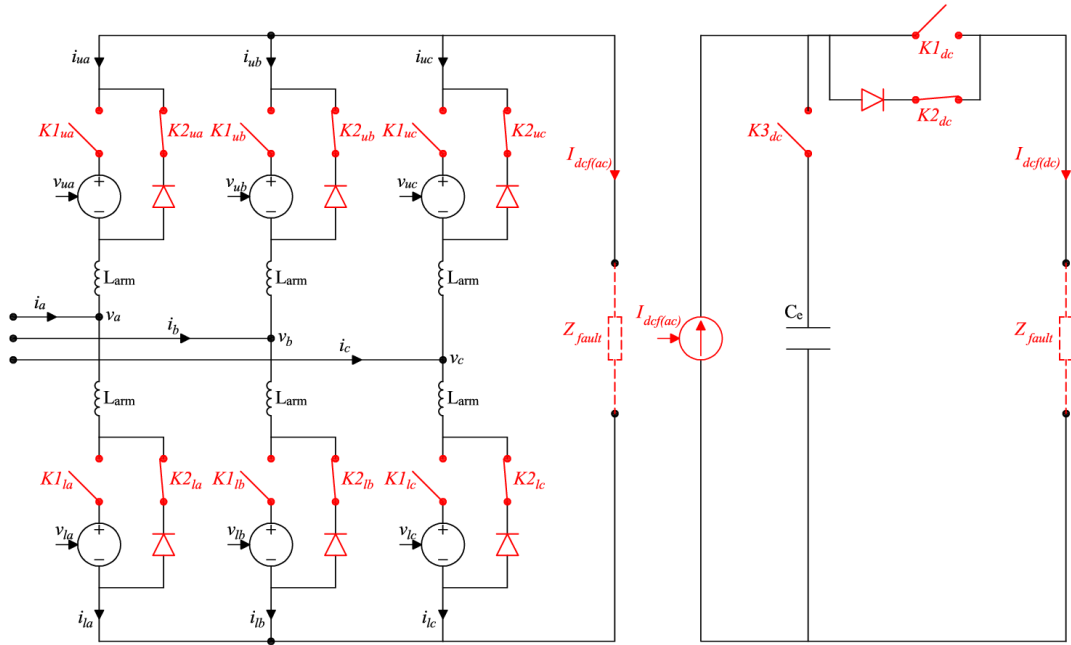
Figure 3.21 – Averaged model with additional modifications operating under fault operating conditions

3.4.3.3 Converter transformer

As was discussed in section 3.3.5.1, two parallel three-phase transformers are required for each VSC, as shown in Figure 3.22. Again, an ideal transformer model is used to represent the transformer as shown in Figure 3.17.
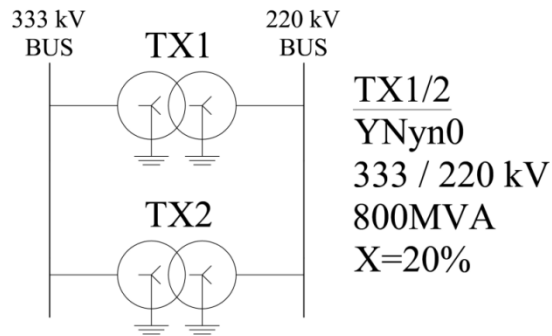
Figure 3.22 – Transformer arrangement on the HVDC platform

The parameter values for the equivalent ideal transformer model are listed in Table 3.9.

Table 3.9 – Equivalent transformer model parameters for the HVDC converter transformers

Parameters		Value	Units
Symbol	Description		
	Offshore HVDC Transformer model (333 / 220 kV)		
R_1	HV winding series resistance	138.61	mΩ
L_1	HV winding series inductance	22.06	mH
R_2	LV winding series resistance	60.50	mΩ
$L2$	LV winding series inductance	9.63	mH
	Onshore HVDC Transformer model (400 / 333 kV)		
$R1$	HV winding series resistance	138.61	mΩ
$L1$	HV winding series inductance	22.06	mH
$R2$	LV winding series resistance	200.00	mΩ
$L2$	LV winding series inductance	31.83	mH

3.4.4 Wind Turbines

All 120 FRC-WTs located in a single WA are aggregated into a single equivalent FRC-WT model. The aggregation of the inter-array cables, as was described in Section 3.3.3.1 means that the WTs are connected in parallel to a single bus. Therefore, the single equivalent WT model must represent 120 WTs in parallel. This is achieved by increasing the apparent power base from 5 MVA to 600 MVA and modifying the WT parameters listed in Table 3.6 accordingly.

To reduce the computational burden further, the turbine blades and hub, PMSG and generator side converter of the FRC are replaced by an equivalent current source. This is placed on the DC link as shown in Figure 3.23.
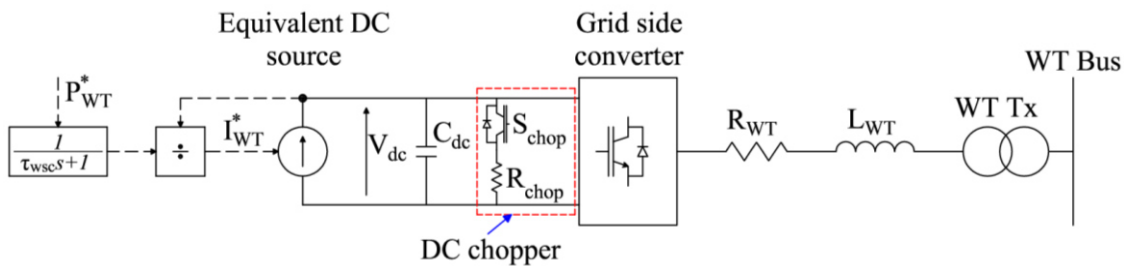
Figure 3.23 – Equivalent model of the FRC-WT

The generator side converter maintains optimal torque according to the rotor speed to extract maximum power from the wind [89]. The regulation of the torque is achieved through vector control which has a time constant τ_{wsc} of approximately 10 ms. A current reference for the DC current source I_{WT}^* is determined from the specified wind power input P_{WT}^* and the DC voltage. The power reference is passed through a first-

order transfer function with $\tau_{wsc} = 10$ ms to account for the response characteristic of the vector control loop.

4 Chapter 4 – Managing planned and unplanned changes in operating condition in an offshore AC hub

4.1 Introduction

The offshore AC hub connects multiple HVDC VSCs and large numbers of FRC-WTs. Autonomous control of voltage, frequency and complex power is necessary to maintain stable operation of the network during changes in wind speed and dispatch orders. In addition, faults may lead to unacceptable operating conditions in the offshore AC hub. This could result in further outages as transmission and generation assets take protective action to avoid damage. This in turn could heavily impact the onshore MITS if left unmanaged. Before any suitable method of managing faults can be designed, the impact of faults in an offshore AC hub must be investigated and understood.

In this chapter, control systems which are developed for point-to-point HVDC transmission links are extended to account for parallel operation in an offshore AC hub. In particular, master-slave and droop control schemes are implemented and compared on a model of the offshore AC hub developed in SimPowerSystems^{TM} [2]. The impact of three different faults in an offshore AC hub are presented.

4.2 Design of control systems for FRC-WTs and VSCs

The control systems used in the FRC-WTs and VSCs are implemented in the synchronous (dq) reference frame as was discussed in Section 2.4. It is important that each of the control loops are properly tuned to ensure satisfactory operation. In this section, the design criteria for each control loop are discussed. Confirmation that each control loop meets the design criteria is made through analysis of the bode diagram and step response of the open and closed loop transfer functions.

---

[2] SimPowerSystems^{TM} is a suite of component libraries and analysis tools developed by MathWorks® in conjunction with Hydro-Québec of Montreal [105]. It is designed for use with the Simulink® simulation environment in MATLAB®.
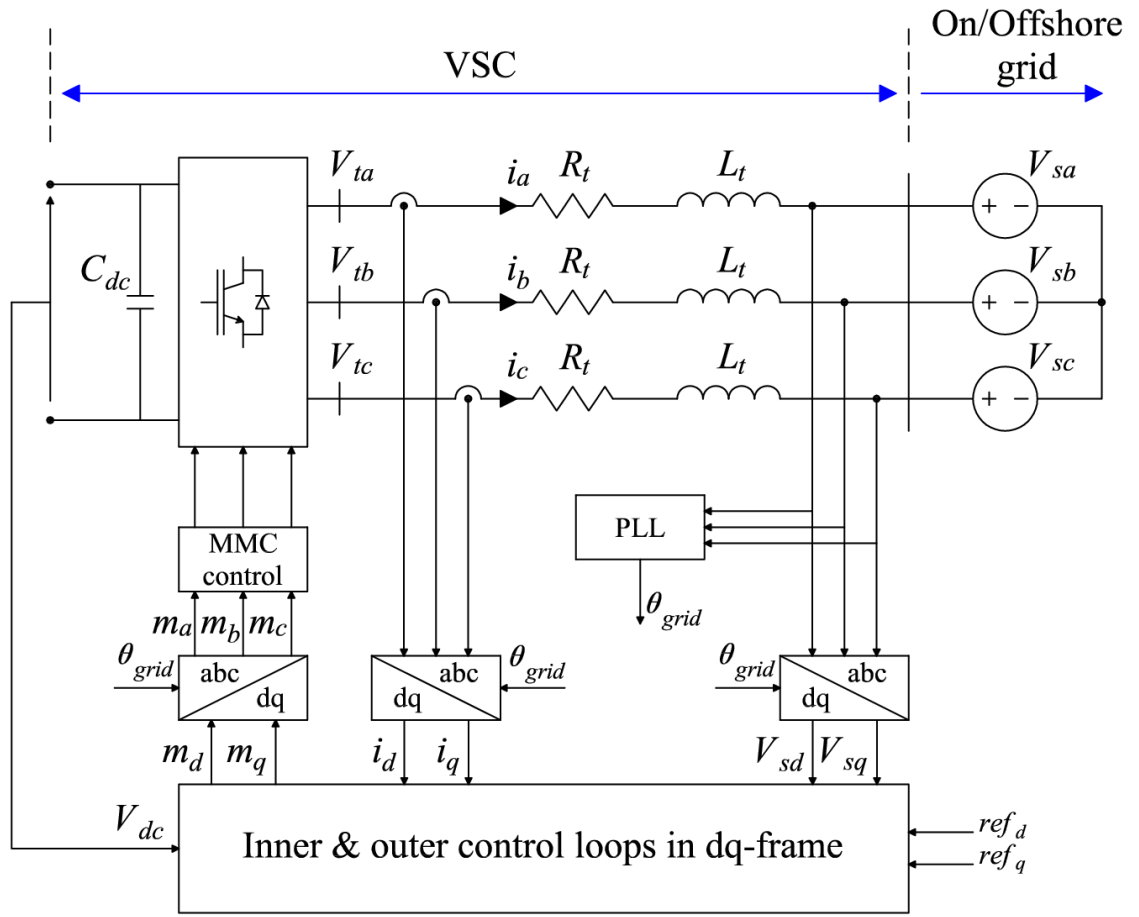
Figure 4.1 – Control overview of the VSC

As seen in Figure 4.1, the VSC as seen from the AC side appears as a voltage source which drives a current in to the offshore grid. V_t is the voltage produced at the VSC valve terminals and for each phase is described as:

$$V_{ta} = R_t i_a + L_t \frac{di_a}{dt} + V_{sa} \tag{4.1}$$

$$V_{tb} = R_t i_b + L_t \frac{di_b}{dt} + V_{sb} \tag{4.2}$$

$$V_{tc} = R_t i_c + L_t \frac{di_c}{dt} + V_{sc} \tag{4.3}$$

To convert from the natural reference frame to the synchronous reference frame, the Park transformation is used as described by (4.4).

$$
\begin{bmatrix} V_{sd} \\ V_{sq} \\ V_{so} \end{bmatrix} = \frac{2}{3} \begin{bmatrix} \sin(\omega t) & \sin\left(\omega t - \frac{2\pi}{3}\right) & \sin\left(\omega t + \frac{2\pi}{3}\right) \\ \cos(\omega t) & \cos\left(\omega t - \frac{2\pi}{3}\right) & \cos\left(\omega t + \frac{2\pi}{3}\right) \\ \frac{1}{2} & \frac{1}{2} & \frac{1}{2} \end{bmatrix} \begin{bmatrix} V_{sa} \\ V_{sb} \\ V_{sc} \end{bmatrix} \quad (4.4)
$$

Equations (4.1)-(4.3) written in the synchronous reference frame are given by:

$$
V_{td} = R_t i_d - \omega L_t i_q + L_t \frac{di_d}{dt} + V_{sd} \quad (4.5)
$$

$$
V_{tq} = R_t i_q + \omega L_t i_d + L_t \frac{di_q}{dt} + V_{sq} \quad (4.6)
$$

Where ω is the frequency of the synchronous reference frame, V_{sd} and V_{sq} are the grid voltages in the synchronous reference frame, V_{td} and V_{tq} are the converter voltages in the synchronous reference frame and i_d and i_q are the currents flowing into the grid in the synchronous reference frame. R_t and L_t represent the equivalent resistance and reactance between the VSC and the grid.

Equations (4.5) and (4.6) show that it is possible to manipulate the current flowing into the grid at the interface point through adjustment of the converter voltage angle and magnitude or, equivalently V_{td} and V_{tq} in the synchronous reference frame. This forms the basis of the vector control schemes implemented for each VSC as described in the following sections.

4.2.1 Phase Locked Loop (PLL) design

A PLL is required for all VSCs which are not participating in frequency control. The PLL operates by regulating V_{sq} to zero, which in turn ensures that $V_{sd} = \hat{V}_s$. The compensator design of the PLL follows the procedure defined in [89]. The schematic diagram of the PLL is shown in Figure 4.2.
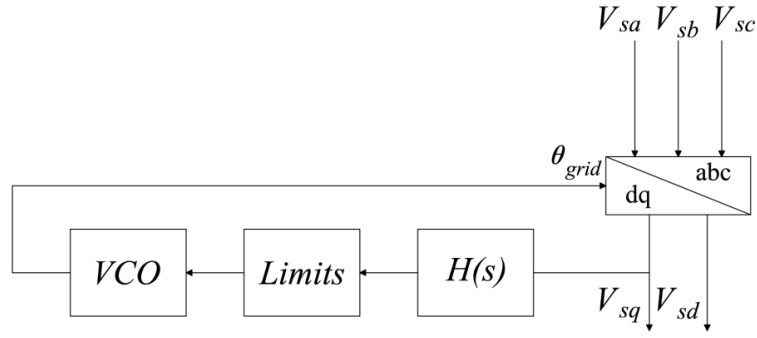
Figure 4.2 – Schematic diagram of the PLL

The control block diagram of the PLL is given in Figure 4.3.
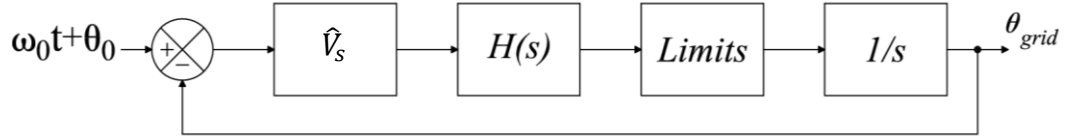
Figure 4.3 – Control block diagram of the PLL

The input to the PLL includes a ramp term $\omega_0 t$ therefore, the open loop transfer function of the block diagram in Figure 4.3 must include at least two poles at $s = 0$ to ensure zero steady state error. One integral already exists, therefore, $H(s)$ must include one pole at $s = 0$. To eliminate the double frequency ripple produced by the dq transform in the presence of negative sequence components, $H(s)$ must include a complex conjugate pair of zeros at $s = \pm j2\omega_0$. In addition, to ensure that the loop gain magnitude continues to drop with a slope of -40dB/decade for $\omega > 2\omega_0$, a double real pole at $s = -2\omega_0$ is included in $H(s)$ [89]. Therefore,

$$H(s) = \left(\frac{h}{\widehat{V}_s}\right) \frac{s^2 + (2\omega_0)^2}{s(s + 2\omega_0)^2} F(s) \qquad (4.7)$$

$\widehat{V}_s$ is the nominal peak magnitude of V_s which is assumed as 1pu as the voltage is scaled to accept a per-unit voltage. $F(s)$ is the normal compensator transfer function with no zero at $s = 0$. Based on the control block diagram presented in Figure 4.3, the open loop transfer function $G(s)$ is given by (4.8):

$$G(s) = h \frac{s^2 + (2\omega_0)^2}{s^2(s + 2\omega_0)^2} F(s) \qquad (4.8)$$

Assuming a gain crossover frequency ω_c of 25 Hz and a phase margin of 60° is required, if $hF(s) = 1$, the phase of the open loop transfer function $G(s)$ is equal to

$-208°$. Therefore, to achieve the desired phase margin, $F(j160)$ must add $92°$ to $\angle G(j160)$. As the required phase advance is large, $F(s)$ includes two cascaded lead compensators, each to provide approx. $46°$ at ω_c. Therefore,

$$F(s) = \left(\frac{s + (\rho/\alpha)}{s + \rho}\right)\left(\frac{s + (\rho/\alpha)}{s + \rho}\right) \qquad (4.9)$$

Where,

$$\rho = \omega_c\sqrt{\alpha} \qquad (4.10)$$

$$\alpha = \frac{1 + \sin\delta_m}{1 - \sin\delta_m} \qquad (4.11)$$

Where the phase of each lead compensator δ_m is set equal to $46°$. The open loop frequency response of the PLL is shown in Figure 4.4.
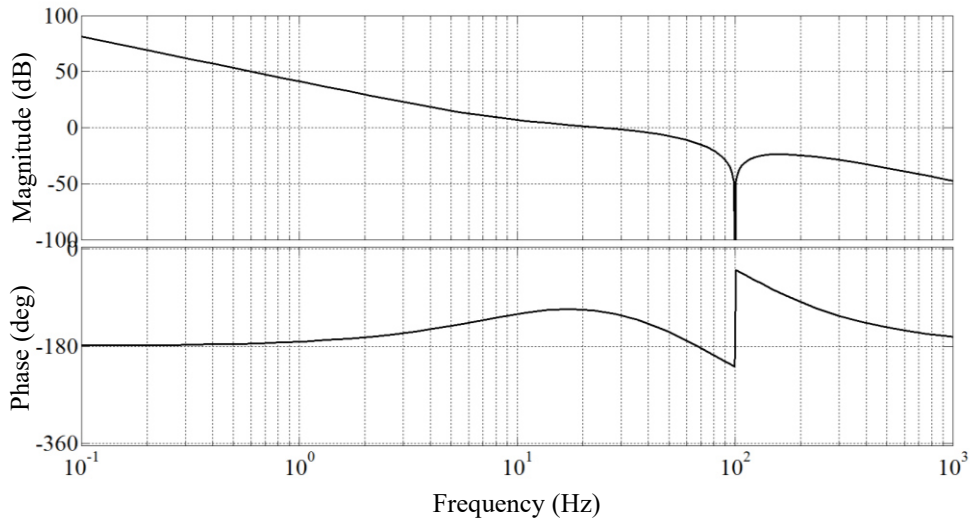
Figure 4.4 – Open loop frequency response of the PLL

From Figure 4.4 it can be seen that the phase margin is $60°$ as was specified in the design. In addition, when $\omega > \omega_c$ the slope of $|G(s)|$ is -40 dB/decade which provides sufficient attenuation to harmonics that may be present in V_s. Figure 4.5 shows the response of the PLL when V_s is subject to a change in frequency. At $t = 0.25$ s, ω_0 is increased from 50 to 51 Hz.
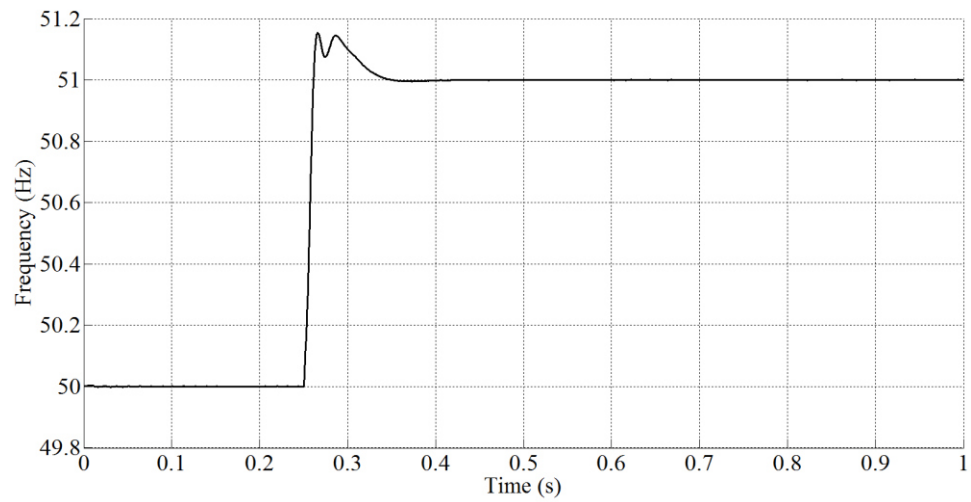
Figure 4.5 – Response of the PLL to a step change in frequency

4.2.2   On/Offshore VSCs

4.2.2.1   Inner control loop – Current control

The block diagram of the inner current control loops are shown in Figure 4.6.

Figure 4.6 – Control overview of the inner current control loop

PI compensators $k_d(s)$ and $k_q(s)$ are used in the d-axis and q-axis inner current control loops respectively, in order to eliminate steady state offset. Each PI compensator is represented by the following transfer function:

$$k_d(s) = k_q(s) = \frac{k_p s + k_i}{s} \qquad (4.12)$$

The plant through which the current is being controlled includes the series impedance of the arm reactors and converter transformer. Hence, the plant is represented by a first order transfer function,

$$G_{pl}(s) = \frac{i_d(s)}{V_d(s)} = \frac{1}{L_t s + R_t} \qquad (4.13)$$

Where L_t and R_t are the combined series inductance and resistance of the arm reactors and converter transformer. If the voltage feed-forward and cross-coupling terms are

treated as disturbances and are neglected, the inner current control loop can be represented by the simplified control block diagram as shown in Figure 4.7.
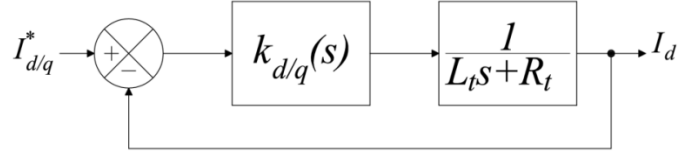
Figure 4.7 – Inner current control loop block diagram

The zero of the PI compensator can effectively cancel the plant pole assuming the PI compensator parameters are chosen as [89]:

$$k_p = \frac{L}{\tau_i} \tag{4.14}$$

$$k_i = \frac{R}{\tau_i} \tag{4.15}$$

The transfer function of the inner current control loop becomes:

$$\frac{I_d(s)}{I_d^*(s)} = \frac{1}{\tau_i s + 1} \tag{4.16}$$

Where τ_i is the time constant of the inner current control loop. The time constant is the time taken for the response to reach 63% of its final value [90]. The time constant of the inner current control loops is typically selected in the range of $0.5 - 5$ ms [89]. The closed loop bandwidth of the inner current control loops expressed in rad/s is defined as $1/\tau_i$.

The time constant is selected as 1 ms and the controller gains are chosen using (4.14) and (4.15) accordingly. The closed loop bandwidth of the inner current control loops is approximately 160 Hz (1000 rad/s). To confirm the parameter selection is correct, a bode diagram and step response of the inner current control loops is shown in Figure 4.8 and Figure 4.9.
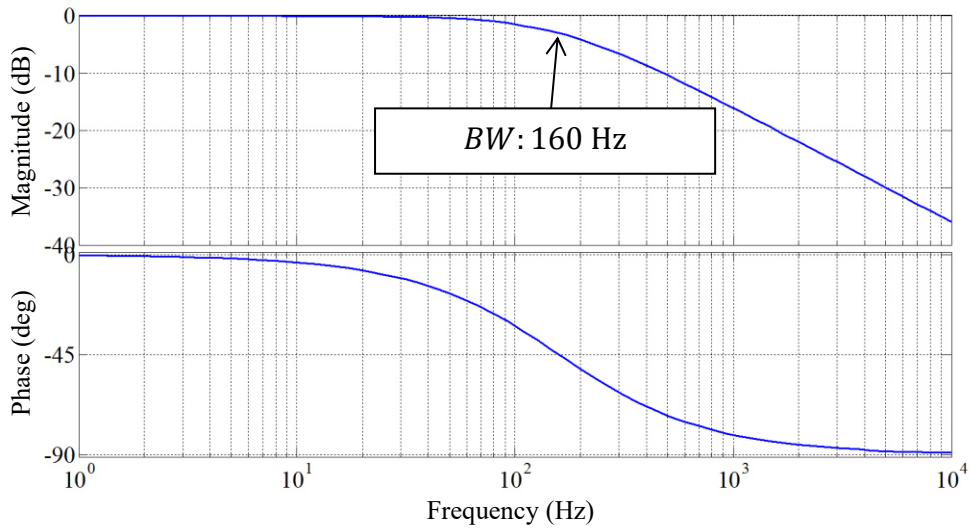
Figure 4.8 – Closed loop response of the inner current control loop
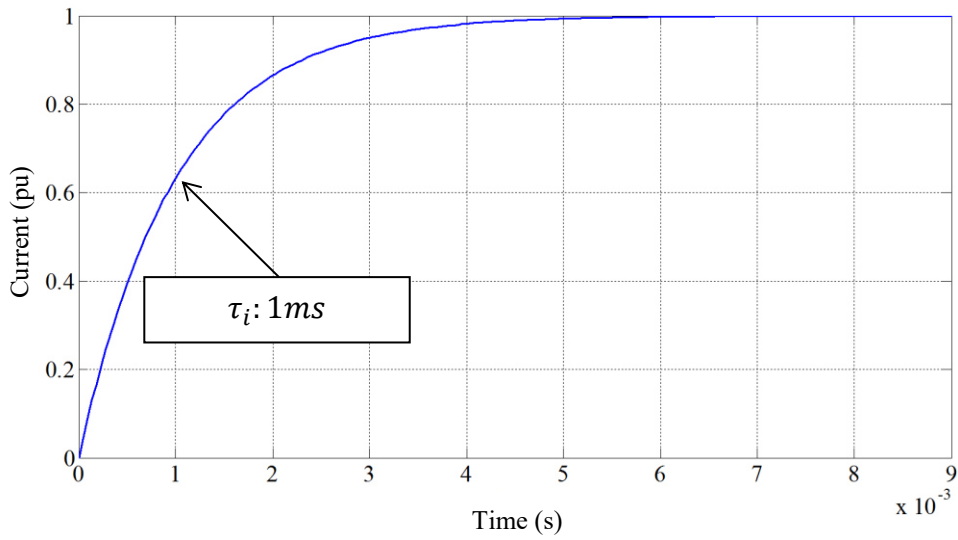
Figure 4.9 – Step response of the inner current control loop

From the bode diagram, it can be seen that the frequency at which the gain is -3 dB is 160 Hz, which is the bandwidth of the system. From the step response, the time constant is found to be 1 ms which matches the design time constant. The gains for the inner current control loop are defined in Table 4.1

Table 4.1 – Inner current control loop parameters

Inner control loop	k_p	k_i
Offshore VSC	100	985
Onshore VSC	107	1063

4.2.2.2 Outer control loops – Voltage Control

The objective of the outer loop of the VSC when operating in voltage control mode is to maintain V_{sd} and V_{sq} by providing a current reference I_d^* and I_q^* respectively. The voltage is being controlled across a load as seen from the converter transformer line side bus. The load itself is of a high order, non-linear and is influenced by other active sources in the AC hub. Therefore, the design of the control scheme is not a straightforward task.

For two-level VSCs, it is common to define the filter capacitance as the controlled plant for the outer voltage control loop [89]. In the literature, this capacitance is used as a means to decouple the voltage dynamic at the connection point from the rest of the system. An MMC produces far less harmonic content and in most cases, under normal THD limits of $< 1 \%$, no filter capacitance is included. Therefore, the VSC model does not include any filter capacitance and the decoupling is not performed. The block diagram of the outer voltage control loops are shown in Figure 4.10.

Figure 4.10 – Control overview of the outer voltage control loop

PI compensators $k_{do}(s)$ and $k_{qo}(s)$ are used to eliminate steady state offset.

$$k_{do}(s) = k_{qo}(s) = \frac{k_{po}s + k_{io}}{s} \qquad (4.17)$$

To tune the PI compensators suitable gains must be found which ensure the AC voltage is controlled with minimal overshoot and zero steady state error. In addition, the outer loop should be considerably slower than the inner loop to avoid undesirable interaction [91]. As the voltage dynamic at the connection point is not decoupled, a direct analytical approach to determining controller gains was not taken. Instead, suitable gains were identified through observing the performance of the outer voltage control loop in response to a step input using a range of controller gains.

The step response was applied to a single offshore VSC located at bus 1. The load on the single VSC was assumed as all cables and transformers in the AC hub but not

including the other offshore VSCs and the FRC-WTs. Instead, an open circuit was left in place of each VSC or FRC-WT position as illustrated in Figure 4.11.
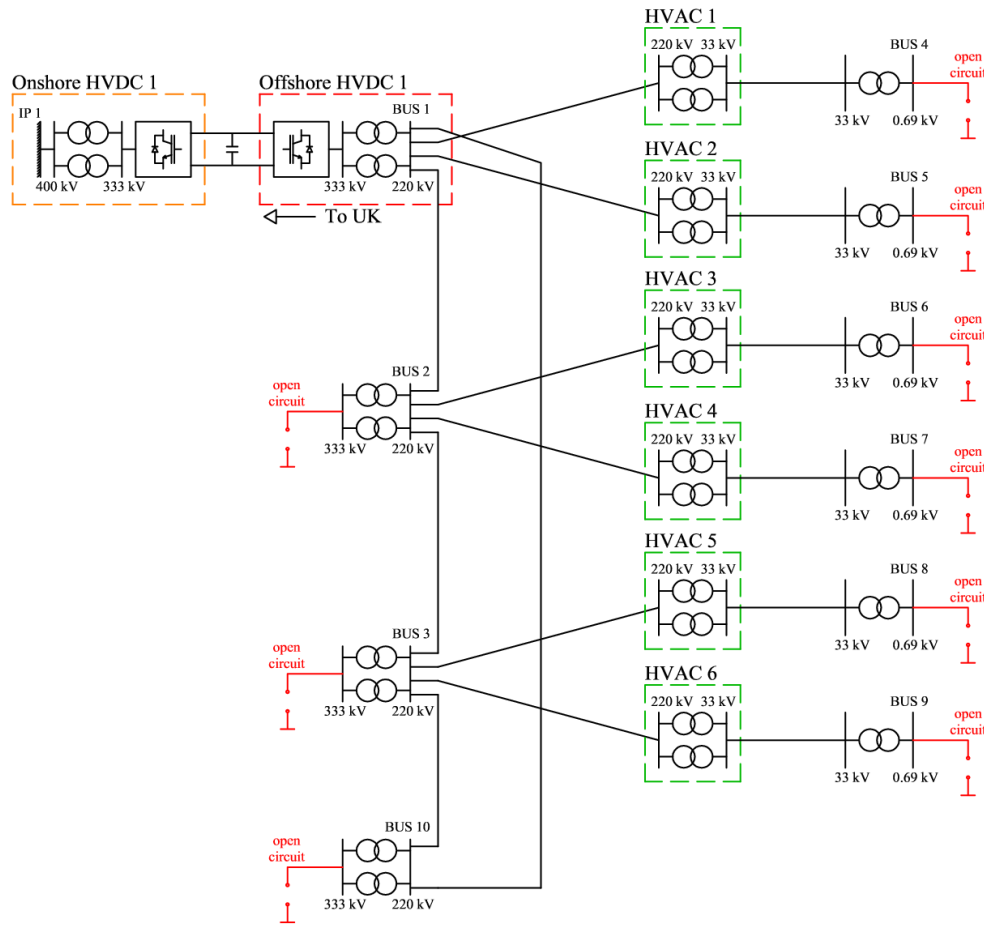
Figure 4.11 – Model used for control tuning of the outer voltage control loop

The design criteria for the voltage controller were specified as follows:

- Closed loop response should have zero steady state error
- The maximum percent overshoot (OS %) of the step response should be less than 20 %.
- The settling time (T_s) should be less than 0.4 s.

The percent overshoot is defined as the amount that the response surpasses the steady-state or final value, expressed as a percentage of the final value. The settling time is defined as the time taken for the response to reach and stay within 2 % of its final value [90].

Figure 4.12 shows the step responses of the d-axis voltage control loop with a range of proportional (k_{po}) and integral (k_{io}) gains for $k_{do}(s)$. The percent overshoot and settling time for each response are presented in Table 4.2.
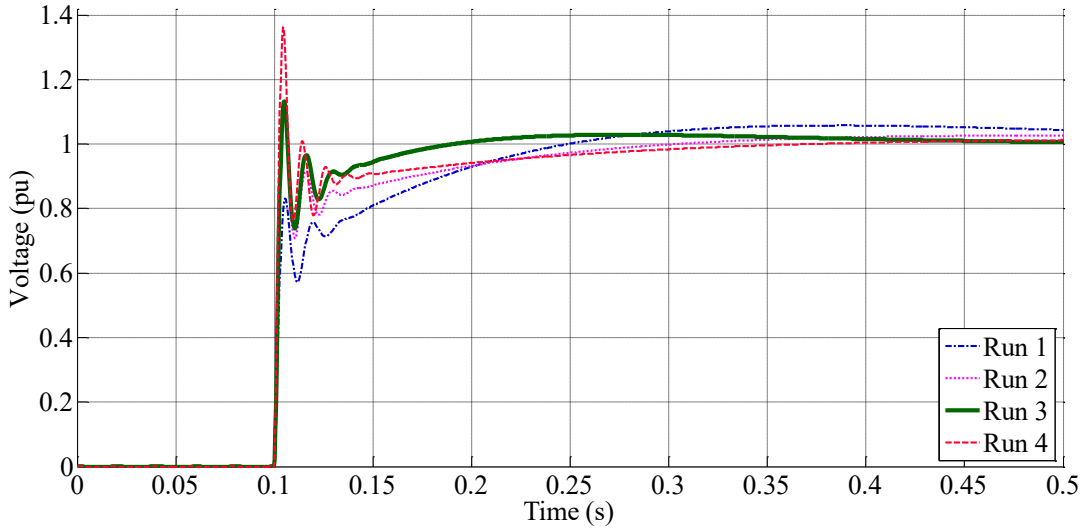
Figure 4.12 – Step response of the d-axis control loop

Table 4.2 – Control gains used for each plot in Figure 3.32

Run	k_{po}	k_{io}	OS %	T_s
1	0.010	0.10	5.80	0.54
2	0.015	0.10	11.55	0.53
3	0.015	0.20	13.40	0.27
4	0.020	0.10	36.33	0.19

From the data presented in Table 4.2 runs 1 & 2 have an acceptable level of overshoot however the settling time is too long. Run 4 has an acceptable settling time however the overshoot is too large. This is expected due to the increase in k_{po}. Finally run 3 has both an acceptable overshoot and acceptable settling time according to the design criteria. Therefore, the gains for both the d-axis and q-axis PI compensators $k_{do}(s)$ and $k_{qo}(s)$ were selected according to run 3.

4.2.2.3 Outer control loops – Active/Reactive Power Control

A schematic of the outer power control loop is provided in Figure 4.13. The objective of the outer loop of the VSC when operating in power control mode is to maintain active and reactive power by providing suitable current references to the inner current control loop.
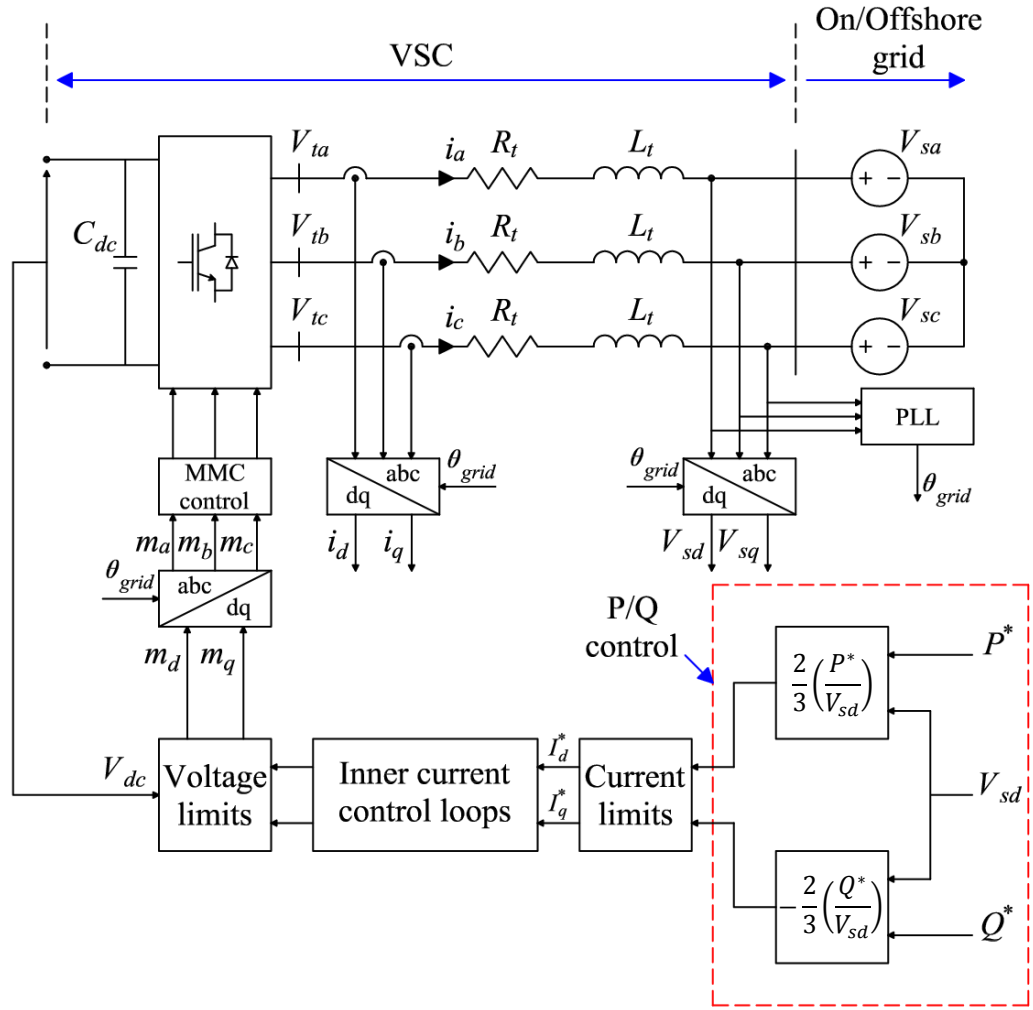
Figure 4.13 – Control overview of the outer power control loop

The active and reactive power in the synchronous reference frame is described by (4.18) and (4.19) respectively.

$$P = \frac{3}{2}\left(V_d I_d + V_q I_q\right) \tag{4.18}$$

$$Q = \frac{3}{2}\left(V_q I_d - V_d I_q\right) \tag{4.19}$$

As described in section 4.2.1, the PLL ensures that $V_{sq} = 0$. In doing so the reference frame is aligned with the grid voltage vector V_s and therefore can be defined as:

$$V_s = V_{sd} + j0 \tag{4.20}$$

Assuming the PLL has ensured the reference frame with the grid voltage, (4.13) and (4.14) become:

$$P = \frac{3}{2}(V_{sd}I_d) \tag{4.21}$$

$$Q = -\frac{3}{2}(V_{sd}I_q) \tag{4.22}$$

Therefore, by re-arranging (4.21) and (4.22), the d and q-axis current references (I_{dref} and I_{qref}) are defined according to the active and reactive power references (P^* and Q^*) respectively, as shown in (4.23) and (4.24) [89].

$$I_d{}^* = \frac{2}{3}\left(\frac{P^*}{V_{sd}}\right) \tag{4.23}$$

$$I_q{}^* = -\frac{2}{3}\left(\frac{Q^*}{V_{sd}}\right) \tag{4.24}$$

4.2.2.4 Outer control loops – V_{DC}/Q control

A schematic of the DC voltage/reactive power control loop is provided in Figure 4.14. This control scheme is used for the onshore VSC of each HVDC link. The main objective of the d-axis outer control loop is to maintain the nominal DC link voltage V_{DC}. This is achieved by the varying I_d^* to the inner d-axis control loop as necessary to export active power equal to the amount injected in to the DC link by the offshore VSC, minus losses. The main objective of the q-axis outer control loop is to maintain the reactive power output of the VSC to the reactive power set point Q^*. This is achieved by varying I_q^* to the inner q-axis control loop as dispatched.

DC Voltage control:

Again, it is important that the inner loop operates faster than the outer loop to ensure that there is no undesired interaction between the two [91].
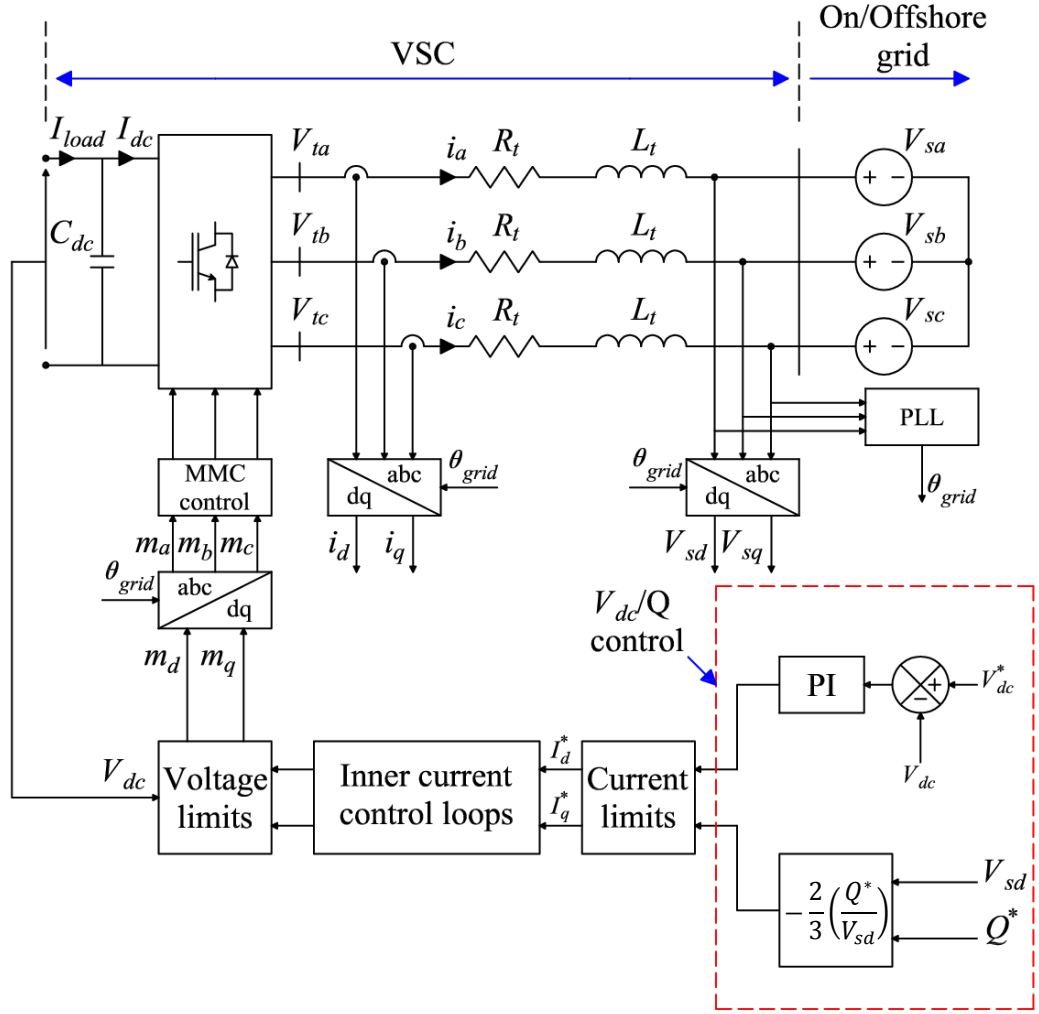
Figure 4.14 – Control overview of the outer DC voltage/reactive power control loops

Assuming the VSC is lossless, the power balance between the AC and DC side of the VSC is given by:

$$P = \frac{3}{2}\left(Vt_d I_d + V_{tq} I_q\right) = V_{dc} I_{dc} \qquad (4.25)$$

The current flowing in the DC link is defined by:

$$I_{dc} = C_{dc}\frac{dV_{dc}}{dt} + I_{load} \qquad (4.26)$$

Where C_{dc} is the DC link capacitance, V_{dc} is the DC link voltage, I_{dc} is the DC link current and I_{load} is the load current on the DC side as shown in Figure 4.14. Assuming the PLL ensures that $V_{sq} = 0$, hence V_{sd} is aligned with phase A (V_{sa}), (4.25) becomes:

$$P = \frac{3}{2}(V_d I_d) = V_{dc} I_{dc} \qquad (4.27)$$

87

Finally, inserting (4.26) in to (4.27) and re-arranging, the plant dynamics for the outer DC voltage control loop are given by:

$$C\frac{dV_{dc}}{dt} = \frac{3}{2}\frac{V_d}{V_{dc}}I_d - I_{load} \tag{4.28}$$

Now V_d can be expressed in terms of the DC link voltage and the modulation index of a given phase (M_a) as shown in (4.29).

$$V_d = M_a\frac{V_{dc}}{2} \tag{4.29}$$

Therefore, by inserting (4.29) in to (4.28), the DC link voltage can be expressed as:

$$C\frac{dV_{dc}}{dt} = \frac{3M_a}{4}I_d - I_{load} \tag{4.30}$$

Based on (4.30), a transfer function for the plant with the d-axis current (I_d) as an input and the DC voltage (V_{dc}) as an output can be defined:

$$\frac{V_{dc}(s)}{I_d(s)} = \frac{3}{4}\frac{M_a}{Cs} \tag{4.31}$$

Again, a PI compensators $k_{do}(s)$ *is* used to eliminate steady state offset. The transfer function for the PI compensator is shown in (4.30).

The design criteria for the voltage controller were specified as follows:

- The closed loop bandwidth should be approximately 10 times less than the inner current control loop
- The open loop response should have a phase margin of at least 60°
- Closed loop response should have zero steady state error
- The maximum percent overshoot ($OS\%$) of the step response should be less than 20 %.

Suitable gains for the PI compensator $k_{do}(s)$ was found through analysis of the bode and step response. Figure 4.15 shows the open and closed loop frequency response of the d-axis DC voltage control loop with the chosen gains $k_{po} = 0.023$ and $k_{io} = 0.684$.
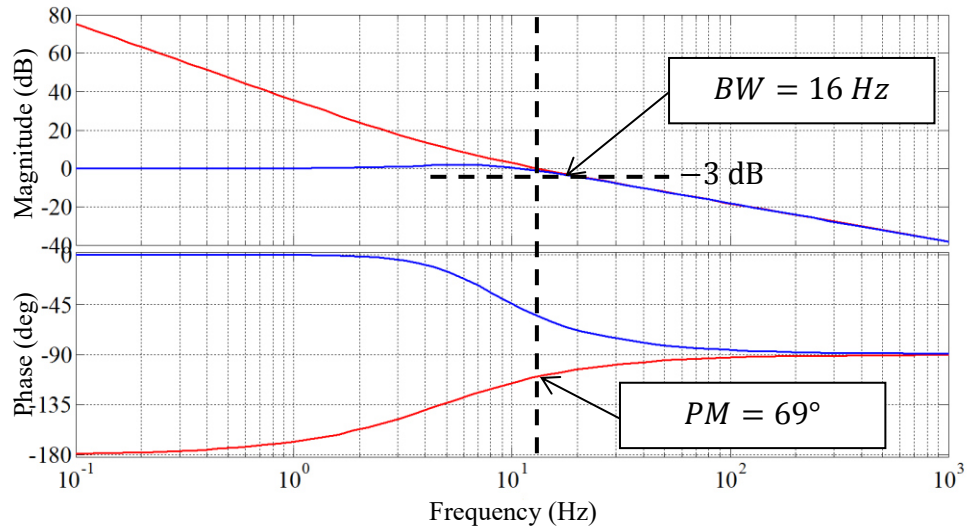
Figure 4.15 – Open and closed loop frequency response of the outer DC voltage control loop

From Figure 4.15, it can be seen that the magnitude of the closed loop response passes through -3 dB at 16 Hz. This represents the bandwidth of the outer DC voltage control loop and satisfies the design criteria as it is 10 times less than the bandwidth of the inner current control loop defined in section 4.2.2.1. Also in Figure 4.15 it can be seen that the phase of the open loop response is $-111°$ when the magnitude is 0 dB. The phase margin (PM) is equal to $180° - 111° = 69°$. Therefore, the phase margin is also within the design specification.
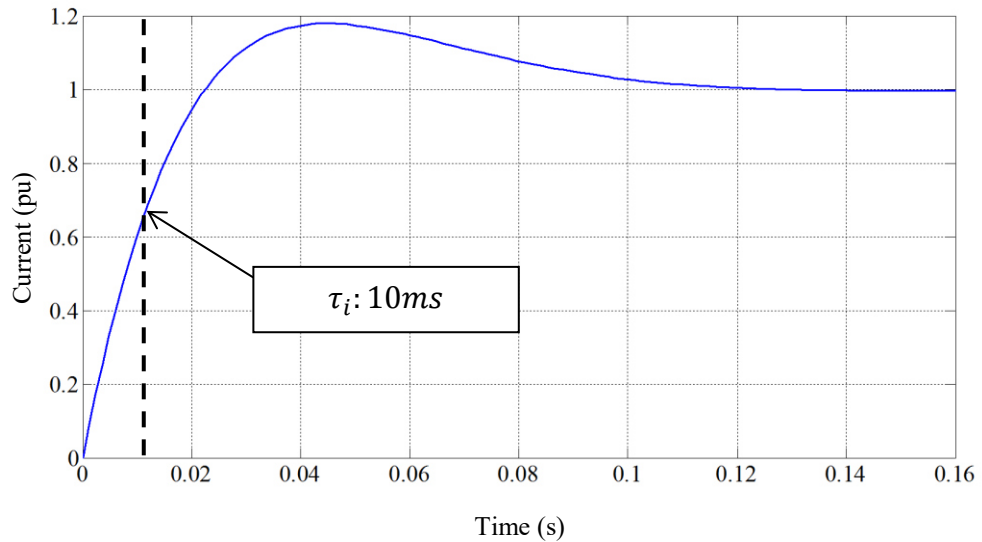
Figure 4.16 – Step response of the outer DC voltage control loop

Figure 4.16 shows the closed loop step response of the outer DC voltage control loop. Zero steady-state error can is observed as is a percent overshoot of less than 20 %. Therefore, the response satisfies all the design criteria.

Reactive Power control:

The reactive power control loop for the onshore VSC is achieved using the same configuration as described for the reactive power control loop of the offshore VSC. Equation (4.22) shows that the reactive power of the onshore VSC can be controlled through adjustment of I_q. Therefore $I_q{}^*$ is determined from Q^* using (4.31).

4.2.3 Grid side converter of FRC-WTs

The inner control loop of the grid side converter has the same configuration as that used for the inner current control loop of the VSCs. Therefore, the same approach is taken to define the PI compensators and thus tune the control loops. The parameters used for the inner control loop of the FRC-WT grid side converter are described in Table 4.3.

The FRC-WT grid side converter maintains the DC link voltage under fluctuating wind power outputs. Therefore, the same outer control loops that were used for the onshore VSC is applied for the FRC-WT grid side converter. The main objective of the d-axis outer control loop is to maintain the nominal DC link voltage V_{DC}. This is achieved by the varying I_{dref} to the inner d-axis control loop as necessary to export active power equal to the amount injected in to the DC link by the FRC-WT wind turbine side converter, minus losses. The main objective of the q-axis outer control loop is to maintain the reactive power output of the FRC-WT grid side converter to the reactive power set point Q^*. This is achieved by the varying I_q^* to the inner q-axis control loop as dispatched. The parameters used for the outer control loop of the FRC-WT grid side converter are described in Table 4.3

Table 4.3 – Control loop parameters of the FRC-WT

Parameters		Value
Symbol	Description	
k_p	Inner loop proportional gain	0.0017
k_i	Inner loop integral gain	0.0042
k_{po}	Outer loop proportional gain	170.0
k_{io}	Outer loop integral gain	852.0

4.3 Control of voltage, frequency and complex power under normal operating conditions

As described in section 2.4, the control of voltage and frequency in an offshore AC network connected to the MITS via a single HVDC link falls to the offshore VSC. The offshore VSC operates with the AC voltage/frequency control scheme as defined in section 4.2.2.2. As additional HVDC links are included in the offshore network it is necessary to co-ordinate the control of voltage, frequency and complex power flow between the offshore VSCs. Two prominent control concepts are identified in the literature and compared for application in the offshore AC hub. Each concept is described in section 4.3.1 & 4.3.2. The results are presented and discussed for each control scheme operating under changes in normal operating conditions in sections 4.3.4 & 4.3.5.

4.3.1 The Master-Slave control strategy

Using the master-slave control strategy, one VSC is defined as the master converter, and the others are defined as slave converters. The master converter uses voltage/frequency control as defined in section 4.2.2.2. As the voltage magnitude and angle are held constant at the master converter's bus, it can be described as the slack bus within the system, generating or absorbing complex power as necessary. The slave converter uses active/reactive power control as defined in section 4.2.2.3 and therefore the power orders are dispatched. Each slave converter uses a PLL to synchronise with the voltage waveform produced by the master converter as defined in section 4.2.1. Figure 4.17 highlights which converter is defined as the master and which are defined as slave converters.
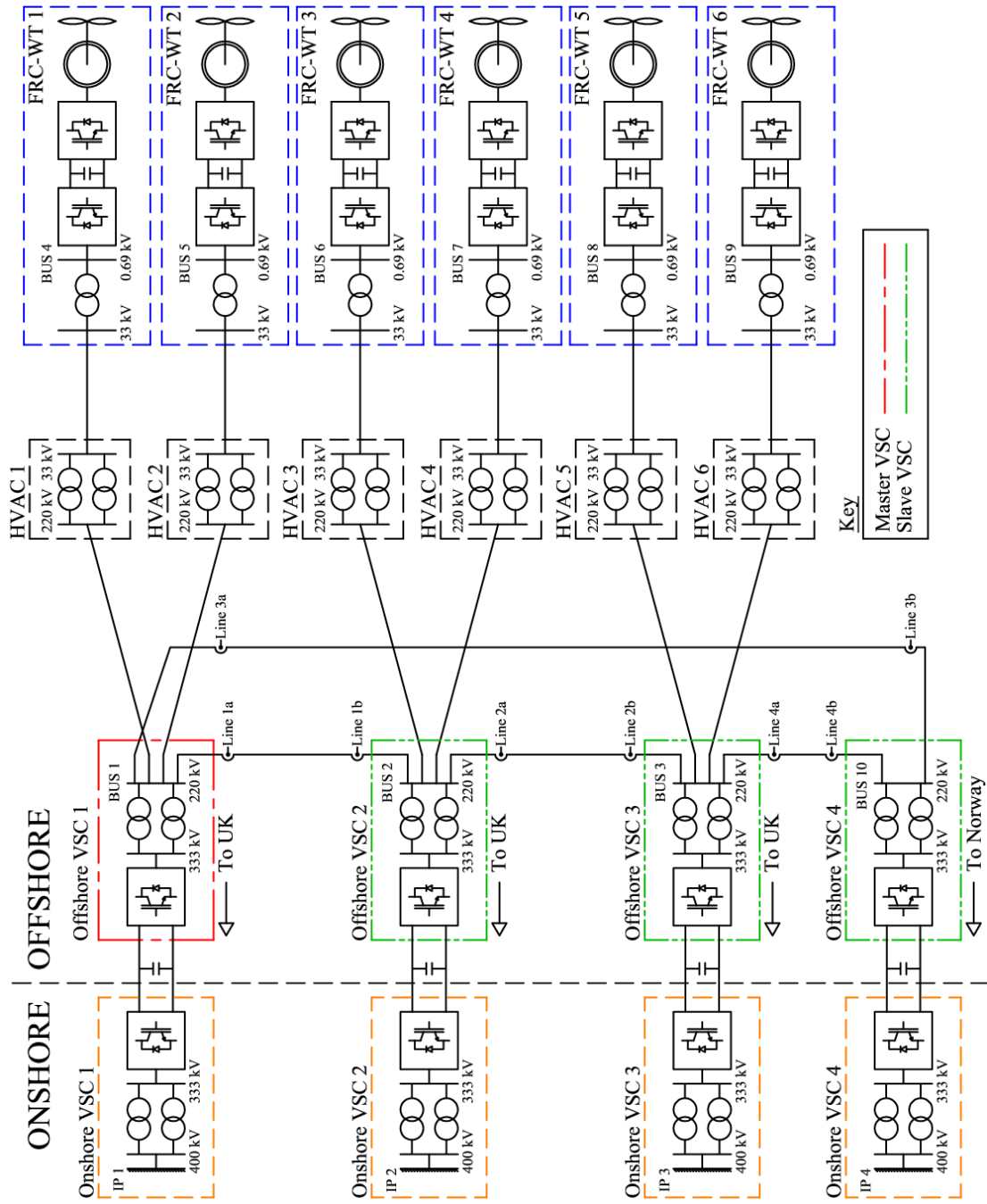
Figure 4.17 – Overview of the AC hub using the master-slave control strategy

4.3.2 The Droop control strategy

Using the droop control strategy, the offshore VSCs 1, 2 and 3 all participate in maintaining voltage and frequency within the network. This implies that complex power is automatically shared amongst the three converters. Each droop converter uses voltage/frequency control as defined in section 4.2.2.2. However, rather than ω being fixed at ω_n, it is drooped against P_s according to the droop gain m_p as given in (4.32) [92].

$$\omega = \omega_n - m_p P_s \qquad (4.32)$$

In addition, rather than V_{sd}^* being fixed at the nominal voltage V_n, it is drooped against Q_s according to the droop gain n_q as given in (4.33) [92].

$$V_{sd}^* = V_n - n_q Q_s \qquad (4.33)$$

The droop gains are specified as given in (4.34) and (4.35).

$$m_p = \frac{\omega_{max} - \omega_{min}}{P_{max}} \qquad (4.34)$$

$$n_q = \frac{V_{sd(max)} - V_{sd(min)}}{Q_{max}} \qquad (4.35)$$

The offshore VSC connected to bus 10 uses active/reactive power control as specified in section 4.2.2.3. The FRC-WTs connected to buses $4 - 9$ use DC voltage/reactive power control as specified in section 4.2.2.4. Figure 4.19 highlights which converters are defined as the droop converters within the offshore AC hub. The droop characteristics are shown in Figure 4.18.
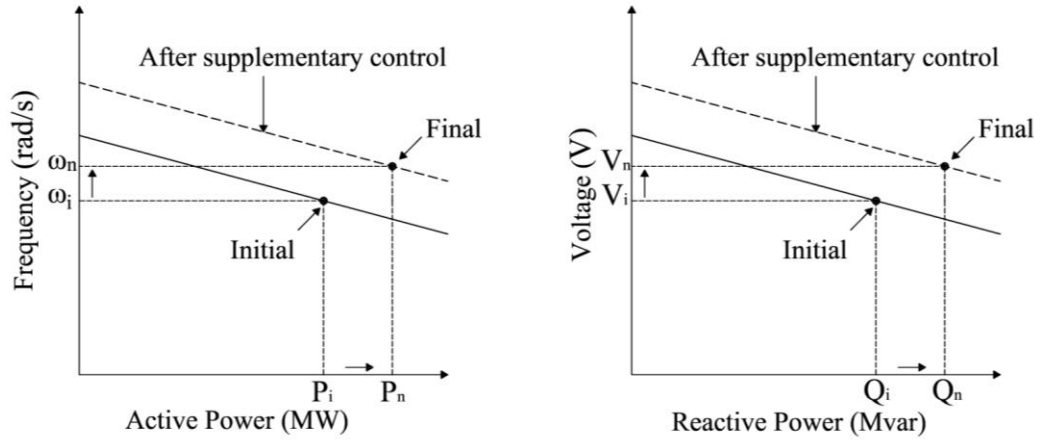
Figure 4.18 – Droop characteristics

Figure 4.19 – Overview of the AC hub using the droop control strategy

4.3.3   Initial steady state operating condition

Before a change in dispatch order or wind generation power output is applied the system is in steady state. The active power output from the FRC-WTs is 3.75 MW and is consistent across all WAs. The HVDC link which is connected to Norway is importing 800 MW in to the offshore AC hub. The three HVDC links which are connected between the offshore AC hub and the UK MITS are absorbing active power.

94

When the master-slave control strategy is implemented, the offshore VSCs designated as slave converters each absorb 1200 MW. The master VSC is effectively the slack bus, therefore it absorbs both active and reactive power as necessary to maintain the voltage and frequency in the offshore AC hub. With reference to Figure 4.17 the initial conditions when using the master-slave control strategy are shown in Table 4.4. The apparent power base is 1200 MVA.

Table 4.4 – Initial conditions when using the master-slave control strategy

Bus	V (pu)	δ (°)	P (pu)	Q (pu)
1	1.000	0.000	-0.779	-0.334
2	1.002	-0.390	-1.002	0.000
3	1.004	-0.251	-1.002	0.000
4	1.008	9.734	0.373	0.000
5	1.008	9.734	0.373	0.000
6	1.010	9.296	0.373	0.000
7	1.010	9.296	0.373	0.000
8	1.012	9.397	0.373	0.000
9	1.012	9.397	0.373	0.000
10	1.006	0.414	0.664	0.000

When the droop control strategy is implemented, all three HVDC links connected between the offshore AC hub and the UK MITS share the transfer of active and reactive power equally between them. With reference to Figure 4.19 the initial conditions when using the droop control strategy are shown in Table 4.5.

Table 4.5 – Initial conditions when using the droop control strategy

Bus	V (pu)	δ (°)	P (pu)	Q (pu)
1	1.013	0.000	-0.928	-0.125
2	1.011	-0.181	-0.928	-0.114
3	1.013	0.000	-0.928	-0.125
4	1.020	9.667	0.373	0.000
5	1.020	9.667	0.373	0.000
6	1.019	9.507	0.373	0.000
7	1.019	9.507	0.373	0.000
8	1.020	9.667	0.373	0.000
9	1.020	9.667	0.373	0.000
10	1.016	0.538	0.664	0.000

4.3.4 Change in dispatch orders

A change of dispatch orders is a routine operation for power systems responding to changing load and market conditions. The rate at which a typical generator responds to a dispatch order is limited to 50 MW/min in the MITS [55]. This limit is imposed to

ensure the safe and reliable operation of the transmission system under normal operating conditions. In the event of unacceptable frequency conditions on the MITS, generating units or interconnectors may be expected to respond dynamically to provide support. The VSC is able to ramp up or down its power output much more quickly than traditional rotating generators. In [93], the VSC is shown to achieve full power reversal in a matter of seconds to aid system stability.

For the AC hub under consideration in this study, one likely scenario is that it becomes favourable to export power to Norway. To simulate this event, a new dispatch order is sent to the offshore VSC which is connected to bus 10. The offshore VSC connected to bus 10 is part of the HVDC link connected between the offshore AC hub and Norway.

At $t = 0.2$ s, the active power reference to the offshore VSC at bus 10 begins to ramp from generating 800 MW to absorbing 800 MW. To compare the dynamic performance of each control philosophy, a higher ramp rate than would otherwise be chosen for a dispatch order was selected. An active power ramp rate of 400 MW/s is assumed and therefore the ramp finishes at $t = 4.2$ s.

Figure 4.20 presents the change in active power through each offshore VSC bus using the master-slave control strategy (top graph) and droop control strategy (bottom graph). The active power through bus 10 ramps from generating 0.66 pu (800 MW) to absorbing 0.66 pu (800 MW) as specified by the dispatch command.
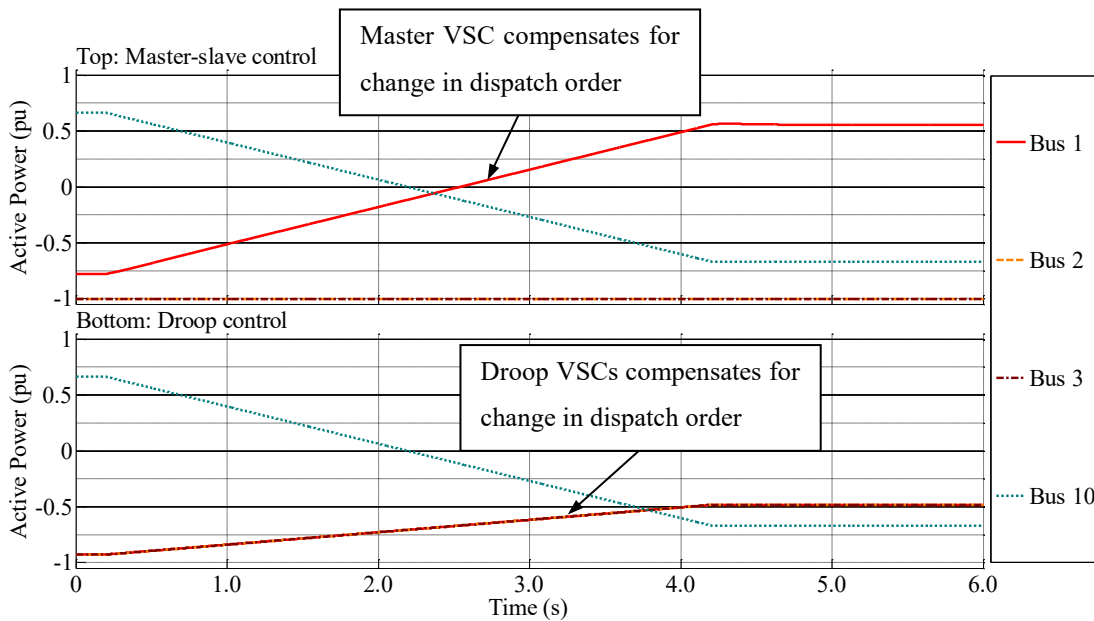
Figure 4.20 – Active power at each offshore VSC bus following a change in dispatch order

In the top graph of Figure 4.20 the active power through bus 1 ramps from absorbing 0.78 pu to generating 0.57 pu of active power. This is expected as the offshore VSC connected to bus 1 is designated as the master converter. The offshore VSCs connected to bus 2 & 3 are both designated as slave VSCs. This is reflected in the result as the active power through bus 2 & 3 is constant throughout the change in dispatch order as they both absorb 1 pu.

In the bottom graph of Figure 4.20 the active power through bus 1, 2 & 3 is equal and ramps from absorbing 0.93 pu to absorbing 0.48 pu of active power. This is expected as the offshore VSCs connected to bus 1, 2 & 3 participate in droop control and have equal droop gains.

Figure 4.21 presents the change in voltage magnitude at each HV bus using the master-slave control strategy (top graph) and droop control strategy (bottom graph).
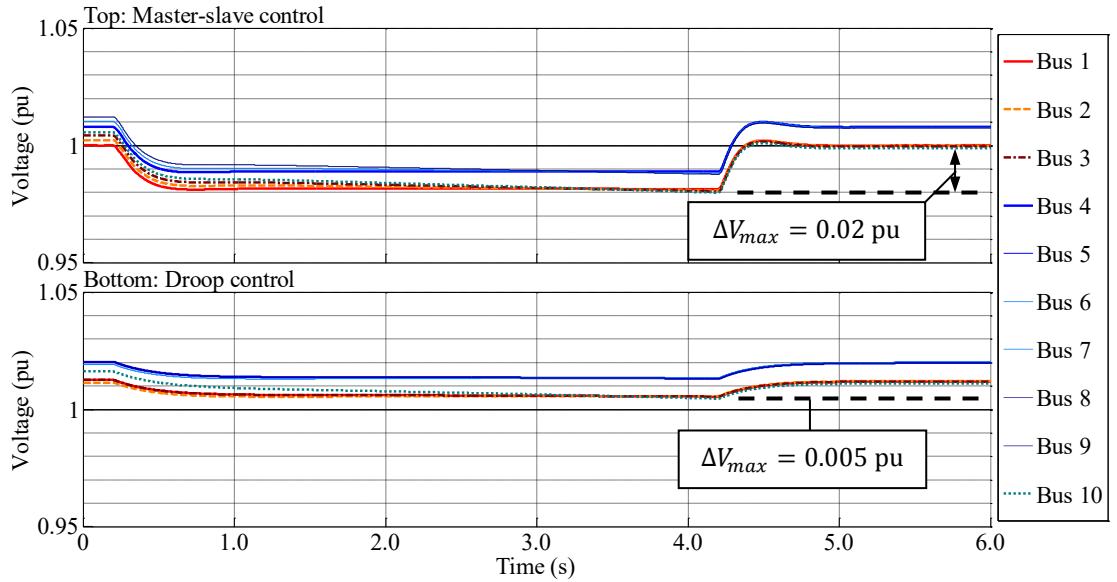
Figure 4.21 – Voltage magnitude at each offshore bus following a change in dispatch order

In the top graph of Figure 4.21, it can be seen that before the change in dispatch ($t < 0.2$ s) the voltage magnitude at bus 1 is constant at 1 pu. This is expected as the offshore VSC connected to bus 1 is designated as the master converter and controls the voltage magnitude to 1 pu. The voltage magnitude at the other buses is > 1 pu but still well within the operating limits listed in [77]. This correctly reflects the capacitive nature of the offshore network where those buses farthest from bus 1 have the highest voltage magnitude. During the transition to the new dispatch order ($t = 0.2 \rightarrow 4.2$ s)

the voltage magnitude at bus 1 drops to 0.98 pu before recovering to 1 pu once the transition is finished ($t > 4.2$ s). This deviation is considered as acceptable as the voltage magnitude remains well within limits.

In the bottom graph of Figure 4.21, it can be seen that before the change in dispatch ($t < 0.2$ s) the voltage magnitude at bus 1,2 & 3 is constant at 1.01 pu. A small offset of 0.01 pu is present from the nominal voltage magnitude. This is a result of the proportional only action of the droop control loops. This can be corrected through a small reduction of the nominal voltage reference of the droop control loops. During the transition to the new dispatch order ($t = 0.2 \to 4.2$ s) the voltage magnitude at bus 1 drops marginally by 0.005 pu before recovering to 1.01 pu once the transition is finished ($t > 4.2$ s). This deviation is considerably less than that observed when using the master-slave control strategy. This is because the change in active power is shared among three VSCs.

Figure 4.22 presents the change in line currents through the interconnecting HVAC cables using the master-slave control strategy (top graph) and droop control strategy (bottom graph).
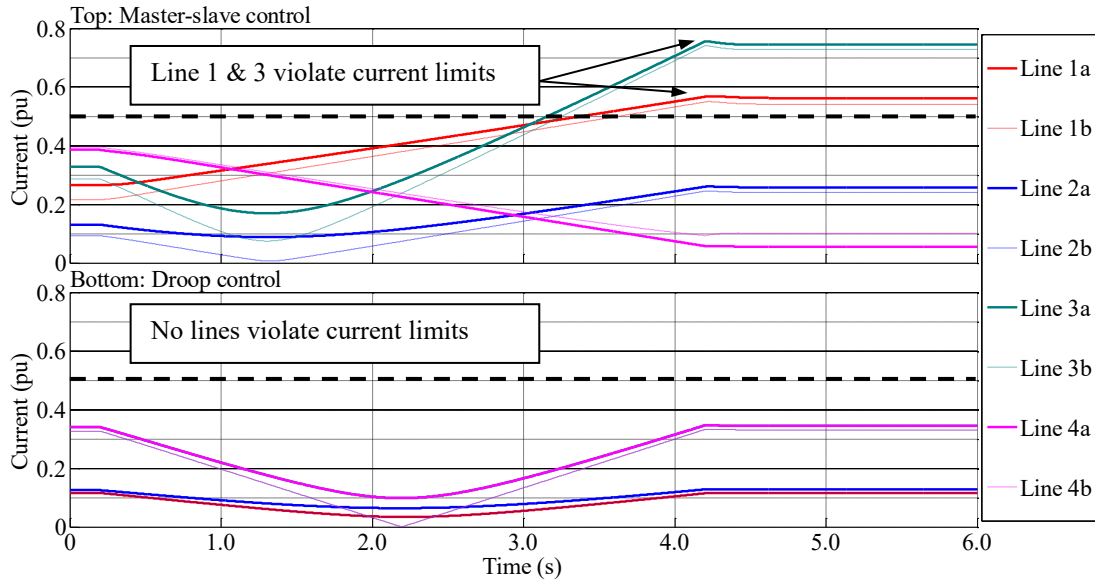
Figure 4.22 – Line current magnitude through each inter-platform HVAC cable following a change in dispatch order

In the top graph of Figure 4.22, it can be seen that before the change in dispatch ($t < 0.2$ s) the current magnitude through all cables is well below the nominal current carrying capacity of the cable which is 0.5 pu. During the transition to the new dispatch

order ($t = 0.2 \to 4.2$ s) the current magnitude through Line 1 & 3 increases beyond 0.5 pu and the current magnitude through line 4 reduces. This is an unacceptable operating condition as lines 1 & 3 are overloaded. It is caused by the increase in power flow between bus 10 and bus 1 and reduction in power flow between bus 10 and bus 3. This could be corrected by adjustment of the dispatch orders to the slave VSCs to avoid constraining power flow.

When using the droop control strategy (bottom graph), the same problem is not apparent. This is because the droop control scheme automatically balances the power flow through the VSCs. The power flow between bus 10 and bus 1 & 3 is equal and therefore the current is shared equally between lines 3 & 4.

In conclusion, the results presented in Figure 4.20, Figure 4.21 and Figure 4.22 show that both the master-slave and droop control schemes can successfully manage the voltage, current and complex power flow in the offshore AC hub, following a change in dispatch orders. However, the droop control scheme is able to automatically balance active power flow through the participating VSCs which helps to avoid violating network constraints.

4.3.5   Change in wind power output

Changes in wind speed throughout the Dogger Bank zone will cause the power output from the wind turbines to vary continually. It is important that the AC hub control system philosophy is able to maintain control of voltage, frequency and complex power given the fluctuating power input from the WTs. The power reference to each equivalent WT (P_{WT}^*) is varied according to a variable wind speed input (v_{WT}^*) to simulate the effect of variable wind speed in the Dogger Bank zone.

The mechanical power extracted by a WT rotor is described by the following equation [94]:

$$P_m = \frac{1}{2}\rho A_r C_p(\lambda, \theta)v_w^3 \tag{4.36}$$

Where ρ is the air density in kg/m^3, A_r is the rotor swept area in m^2, C_p is the power coefficient which is dependent on the tip speed ratio λ and the pitch angle θ, and v_w is the wind speed in m/s. The wind power input P_{WT}^* to the FRC-WT is assumed to equal the mechanical power input P_m. Given the WT parameters used in this study as

specified in [79], (4.33) was rearranged for C_p, which is equal to 0.3 at the nominal power output and wind speed. With C_p fixed at 0.3, the mechanical power input to the FRC-WT was determined from the wind speed using (4.33).

The wind power input P_{WT}^* to the WT will not change immediately with changes in wind speed v_{WT}^* due to the inertia of the turbine blades, hub and PMSG. To simulate this inertia, a first-order transfer function is inserted with time constant τ_{WT}. In [88], the effective inertia constant for a 5 MW FRC-WT is 2.7 s. Therefore, τ_{WT} was assumed equal to 3 s.

v_{WT}^* is generated separately for each WT equivalent model and consists of three components including average wind speed, a gust and turbulence [94]. The average wind speed $v_{WT\_av}^*$ is consistent across all WAs and is assumed as 10 m/s. A wind gust $v_{WT\_gst}^*$ is represented using the following equation [94],

$$v_{WT\_gst}^* = A_{gst}\left[1 - \cos\left(2\pi\left(\frac{t}{D_{gst}} - \frac{T_{s\_gst}}{D_{gst}}\right)\right)\right] \qquad (4.37)$$

Where A_{gst} is the amplitude of the gust [m/s], D_{gst} is the duration of the gust [s] and T_{s_gst} is the starting time of the gust. A_{gst} and D_{gst} are assumed equal across all WAs. T_{s_gst} is staggered across all WAs to represent a gust of wind moving through the Dogger bank zone.

Turbulent wind is simulated according to a turbulent wind model as described in [95]. The turbulent wind is determined by passing white noise through an appropriate shaping filter. The amplitude of the turbulent component is equal for all WAs and is up to 20 % of the average wind speed. The white noise generator of each turbulence model is seeded with a different integer for each WA.

Figure 4.23 presents the variable wind speed reference v_{WT}^* applied to each FRC-WT equivalent model.
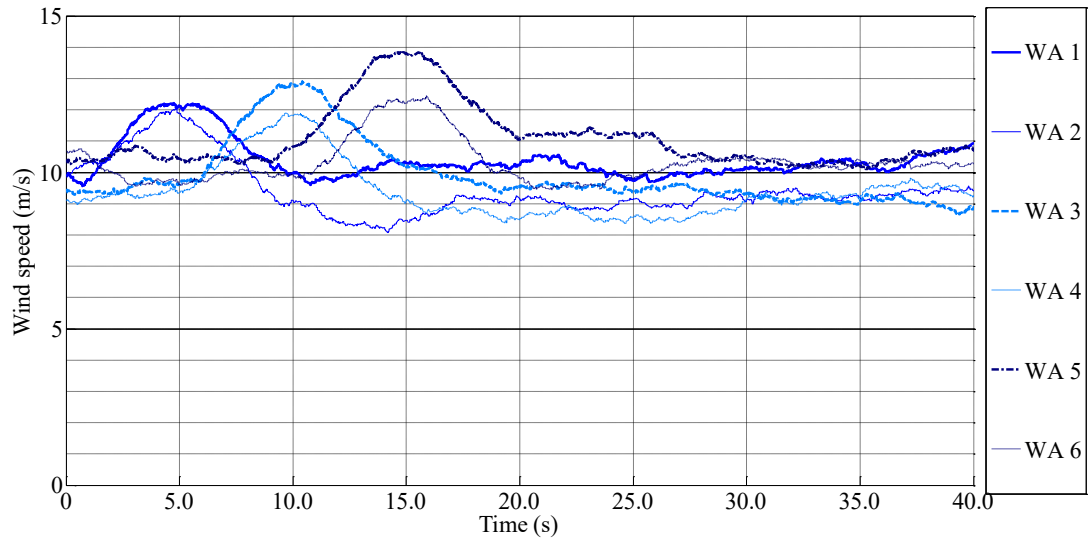
Figure 4.23 – Variable wind speed across all WAs

Figure 4.24 presents the change in active power generated at each WT bus using the master-slave control strategy (top graph) and droop control strategy (bottom graph). It can be seen in the top and bottom graph of Figure 4.24 that the FRC-WTs operating under the master-slave and droop control schemes respectively, operate satisfactorily. Note that although both graphs in Figure 4.24 look identical, the voltage profile in each simulation is different.
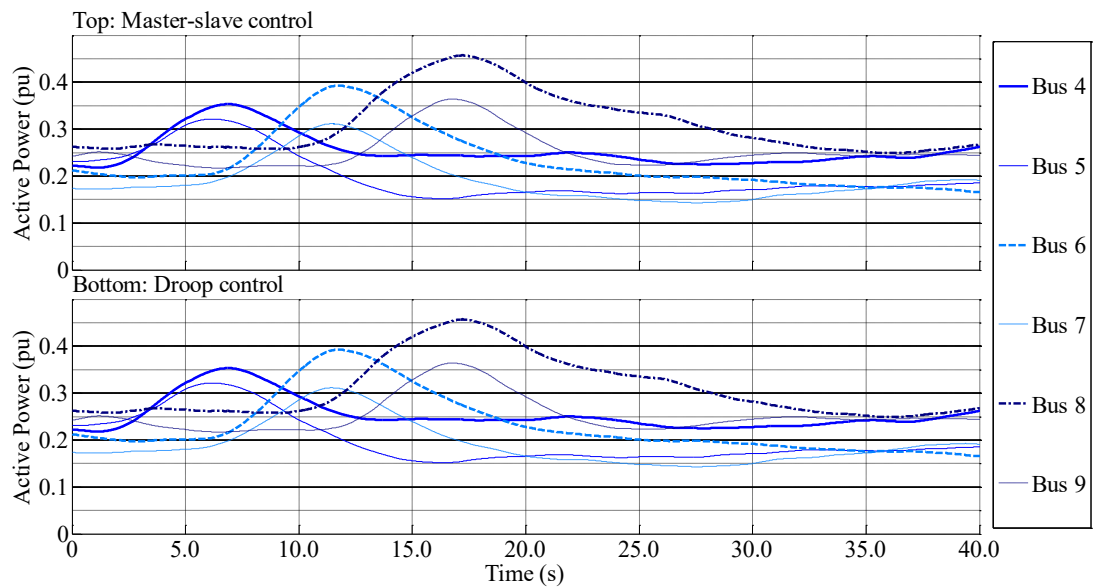
Figure 4.24 –Active power generation at each FRC-WT bus with variable wind speed

Figure 4.25 presents the change in active power through each offshore VSC bus using the master-slave control strategy (top graph) and droop control strategy (bottom graph).
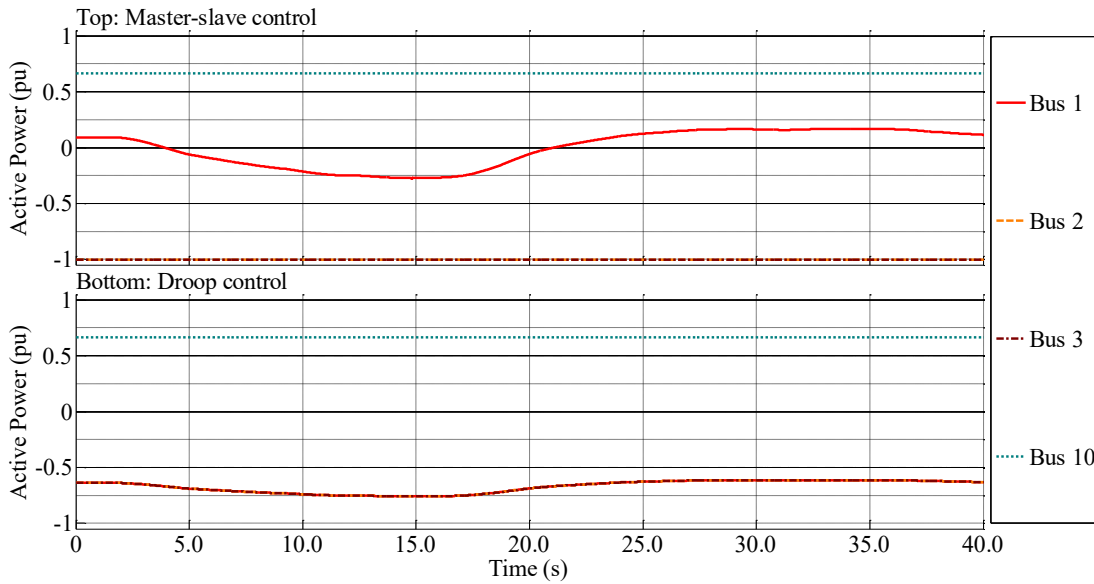
Figure 4.25 – Active power at each offshore VSC bus with variable wind speed

In the top graph of Figure 4.25 the active power through bus 1 varies according to the WA active power input. As the offshore VSC connected to bus 1 is designated as the master converter, it is solely responsible for responding to changes in WA output. The offshore VSCs connected to bus 2, 3 and 4 are designated as slave VSCs. This is reflected in the result as the active power through bus 2, 3 & 4 is constant.

In the bottom graph of Figure 4.25 the active power through bus 1, 2 & 3 is equal and varies according to the WA active power input. This is expected as the offshore VSCs connected to bus 1, 2 & 3 participate in droop control and have equal droop gains. The offshore VSC connected to bus 4 is designated as slave VSCs and therefore the active power through bus 4 remains constant.

Figure 4.26 presents the change in voltage magnitude at each bus using the master-slave control strategy (top graph) and droop control strategy (bottom graph).
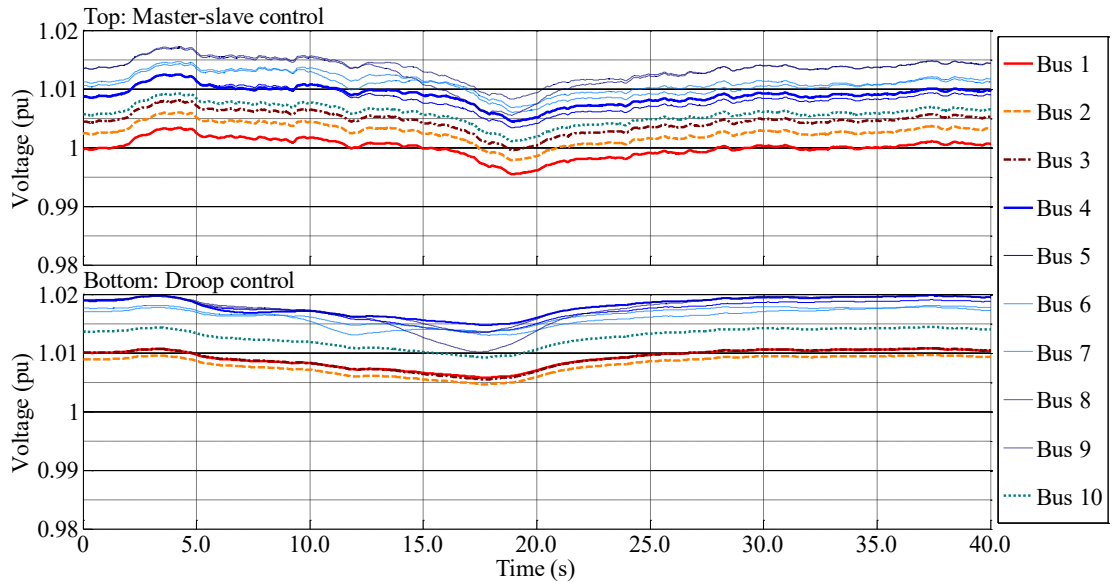
Figure 4.26 – Voltage magnitude at each offshore bus with variable wind speed

In Figure 4.26 it can be seen that the voltage magnitude varies with the change in wind power input. When comparing the master-slave and droop control strategies it can be seen that the master-slave strategy exhibits a less smooth response compared to the droop control strategy. The deviation seen in both strategies is considered as acceptable as the voltage magnitude remains well the statutory limits defined in [77]. The deviation that is apparent is caused by the varying reactive power flow in the network. Figure 4.27 presents the change in reactive power through each offshore VSC bus using the master-slave control strategy (top graph) and droop control strategy (bottom graph).
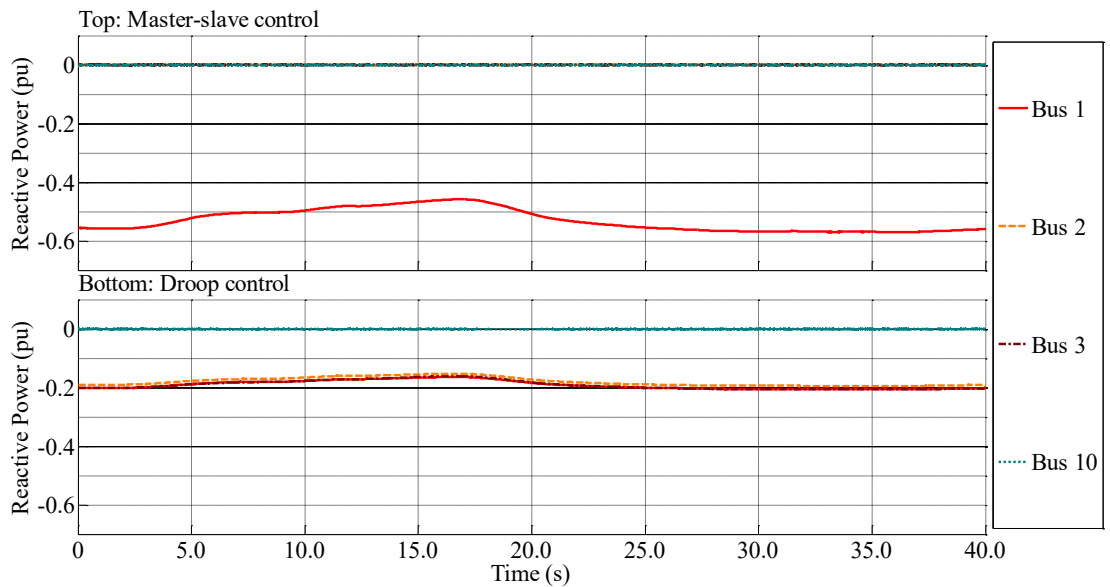
Figure 4.27 – Reactive power at each offshore VSC bus with variable speed

In the top graph of Figure 4.27, the reactive power through bus 1 varies according to the WA active power input. As the wind power input increases, the reactive power absorbed by the master VSC decreases. As more current flows through the offshore AC cables and transformers, the series I^2X reactive power loss increases and partially compensates the reactive power generated by the shunt capacitance of the AC cables, thus relieving the burden on the VSC. For the droop control strategy, the change in reactive power flow through is distributed amongst three offshore VSCs and therefore the change in reactive power flow is less for any single offshore VSC.

In conclusion, the results presented in figures 3.44 to 3.48 show that both the master-slave and droop control schemes can successfully manage the voltage, current and complex power flow in the offshore AC hub with varying wind power input. However, the droop control scheme is able to automatically balance reactive power consumed by the participating VSCs which improves the smoothness of the voltage profile across the network.

4.4 Impact of fault outages in the offshore AC hub

The master-slave and droop control schemes are designed for use under normal operating conditions such as a change in dispatch order or wind speed. Under abnormal operating conditions, e.g. due to a fault, the control schemes could fail to maintain adequate control of voltage, frequency and complex power.

Failure to maintain voltage, frequency and complex power to nominal levels for a short time period is permissible, provided the following conditions are met:

- The maximum withstand levels of all equipment are not exceeded.
- The duration a given parameter differs from its nominal operating range is not sufficient to damage any equipment.
- The system returns to an acceptable operating condition following clearance of the fault.
- The fault does not affect the onshore MITS beyond the limits stipulated by the SQSS standard.

The behaviour of an offshore AC hub during a fault depends on the type and location of the fault. In order to determine the implications of a fault on the operating condition of the offshore AC hub, three separate faults are applied to the offshore AC hub. The droop control scheme is selected as the AC hub control strategy. The fault scenarios include:

- A DC pole to pole fault on one of the HVDC links connected to the UK MITS.
- A 3-phase fault occurring on one of the HVAC bus bars within the offshore AC hub.
- A 3-phase fault occurring on one of the HVAC cables which interconnect two adjacent HVDC platforms.

4.4.1 DC pole-pole fault

The DC pole-pole fault is a severe fault affecting the HVDC system and possibly the wider offshore network. In a symmetrical monopole VSC, as used in this study, it is characterised by a high fault current between the poles on the DC side [76]. A DC pole-pole fault is applied to HVDC link 1 of the AC hub model to study the implications on the AC hub and MITS.

At $t = 0.1$ s, a DC pole-pole fault is applied at the midpoint of the cable of HVDC link 1. After 1 ms, the VSC equivalent cell capacitors are isolated, the equivalent arm voltage sources are isolated and the diodes are inserted to simulate blocking of the IGBTs in the on and offshore VSCs. The AC CBs open to isolate the faulted HVDC link from the MITS and the offshore AC hub. The three-phase AC CB model provided in SimPowerSystems was used in the AC hub model. The model is capable of breaking the fault current at the next zero crossing after a trip signal is received. Modern high-speed CBs are able to break the current in two cycles of the fundamental current waveform, while discrimination and selection of the correct protective action can be achieved within a single cycle [63]. Therefore, the trip signal is sent to the appropriate CBs after 60 ms and the current flow is broken at the next zero crossing for each phase.

As shown in Figure 4.28, the DC link voltage of VSC1 drops rapidly. This is followed by a fault current contribution from the offshore VSC of approximately 2.5 pu as shown in Figure 4.29.
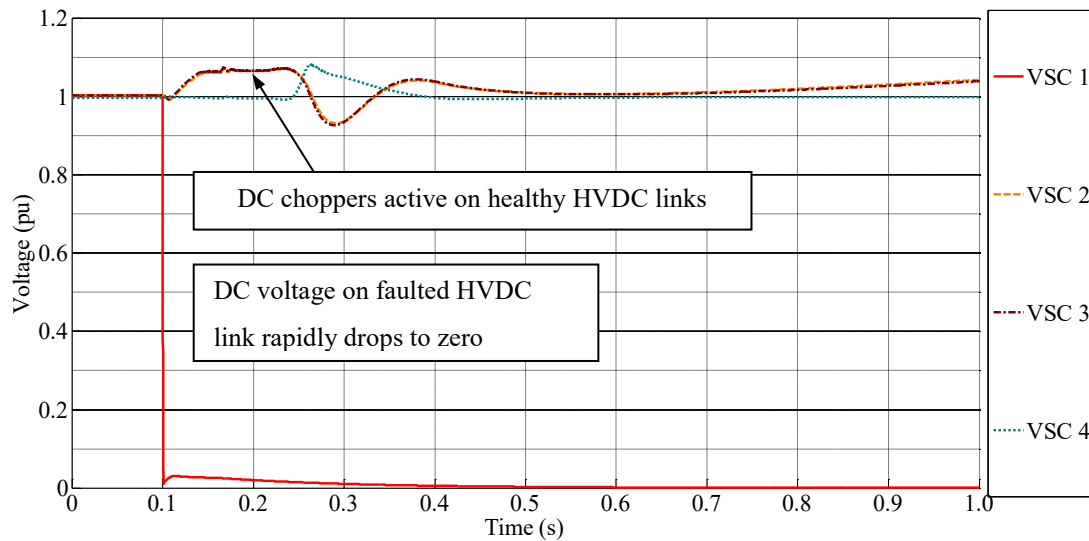
Figure 4.28 – DC link voltage across each HVDC link following a DC pole-pole fault
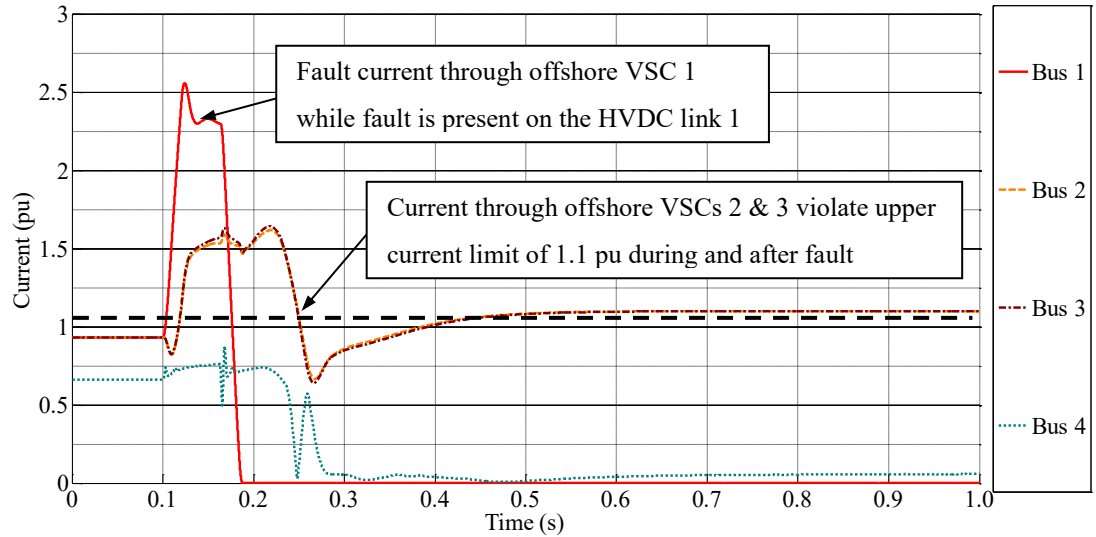
Figure 4.29 – Current magnitude through each offshore VSC bus following a DC pole-pole fault

From Figure 4.28 and Figure 4.29, the extent of the impact on the other healthy HVDC links is clearly apparent. Figure 4.28 shows the DC voltage of HVDC links 2 & 3 rise quickly following the fault. This is due to an increase in current in to the HVDC links from the offshore VSC, as can be seen in Figure 4.29. The DC link voltage of HVDC links 2 & 3 does not go above the upper voltage limit as it is managed by the DC chopper. The current through the VSCs does however increase beyond the upper current limit of the offshore VSCs which is 1.1 pu. This suggests the healthy offshore VSCs are unable to control the fault current during and after the occurrence of the fault.

Figure 4.30 shows the voltage magnitude at the AC buses throughout the AC hub. The voltage magnitude across all buses drops initially until the AC breaker isolates the faulted HVDC link. After the AC breaker is opened, the voltage magnitude drops further initially before rising to approximately 1.3 pu after 275 ms. This level of voltage magnitude violates the upper voltage limit of the offshore AC network of 1.1 pu. This implies that the remaining healthy offshore VSCs operating under droop control are unable to maintain control of the voltage magnitude following clearance of the fault.
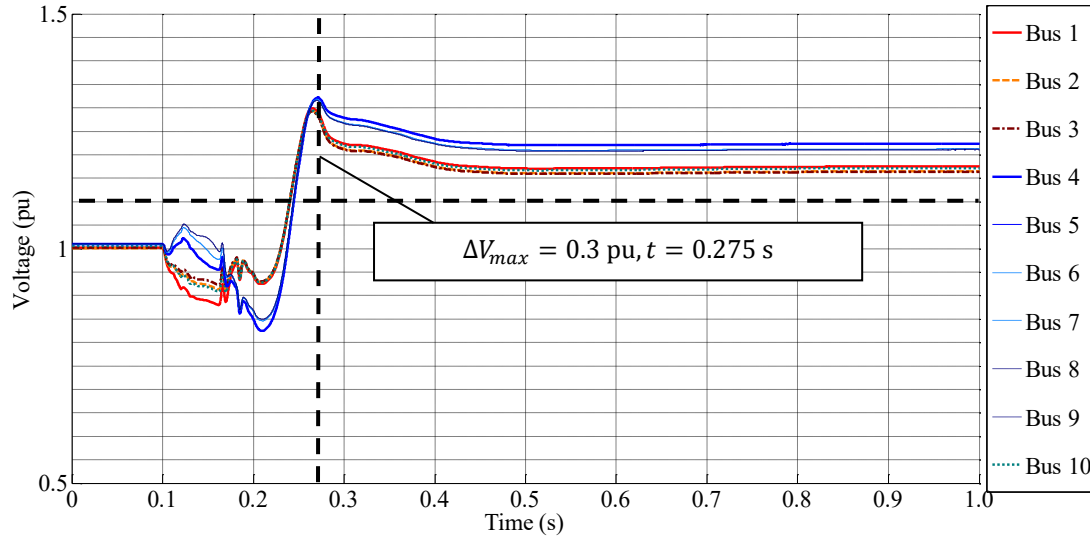
Figure 4.30 – Voltage magnitude at each offshore bus following a DC pole-pole fault

Figure 4.31 shows the active power infeed at the onshore interface points of each onshore VSC. Loss of infeed from the faulted HVDC link (VSC 1) is expected and observed as it will no longer be able to transfer active power once the AC CBs are opened. Until the CBs are opened, a significant active power oscillation is observed from onshore VSC 1. This oscillation may severely impact the MITS.

Onshore VSCs 2 & 3 initially increase their output up to 1.1 pu. This is a result of the increase in DC link voltage as observed in Figure 4.28. The onshore VSCs are tasked with maintaining DC link voltage therefore to address any overshoot they must export more active power. The infeed is approximately constant throughout the fault duration but significantly reduces after approximately 275 ms. This is after the fault is cleared and coincides with the peak in AC voltage magnitude observed in Figure 4.30.
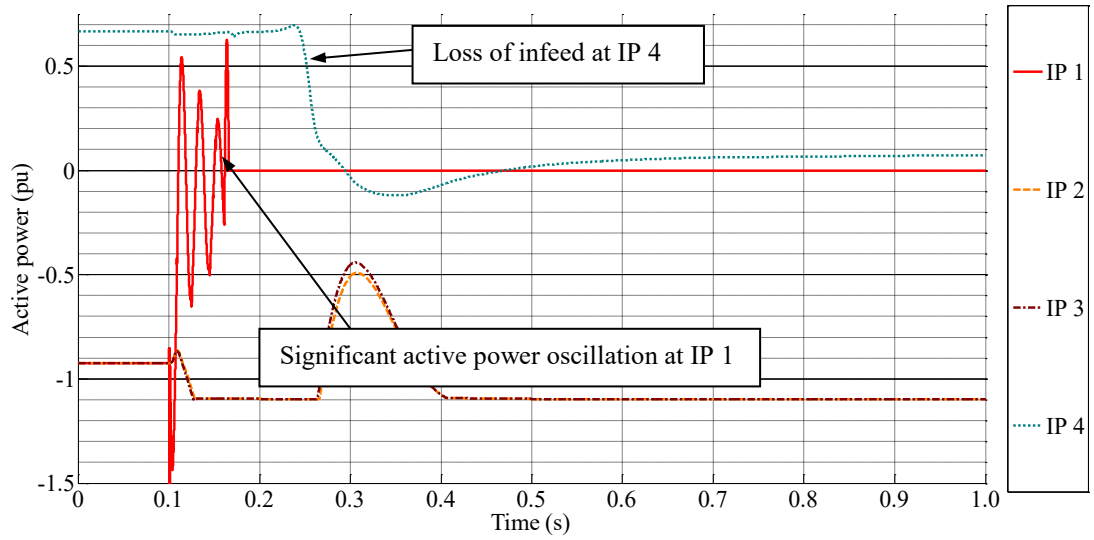
Figure 4.31 – Active power infeed at each onshore interface point following a DC pole-pole fault

In conclusion, the results presented in figures 4.28 to 4.31 confirm that the impact of a DC pole-pole fault on a single HVDC link greatly affects the offshore AC hub and MITS. The excess current through the healthy offshore VSCs cannot be tolerated for the duration it is experienced and therefore are likely to shut down. In addition, the voltage profile offshore is unacceptable after the fault is cleared. This is due to a power imbalance in the network. Finally, the MITS may be affected by significant power oscillations and loss of infeed above that stipulated in [96].

4.4.2 3ph fault on an offshore bus

The 3ph fault occurring on an offshore bus is an unlikely but severe fault that could affect the entire AC hub. The offshore AC cables have a relatively low series impedance therefore the fault is expected to impact the voltage profile across the entire network. A 3ph fault is applied to bus 3 of the AC hub model to study the implications on the AC hub and MITS. A double bus-bar arrangement is assumed for each bus therefore it is assumed that the faulted section can be isolated without influencing the topology of the AC hub.

At $t = 0.1$ s, a 3ph fault is applied to bus 3. The fault impedance was assumed as very small ($Z_f = 1$ mΩ) to give the worst case scenario. At $t = 0.16$ s the AC CBs open to isolate the faulted section of bus-bar and the remaining healthy bus-bar is utilised. Figure 4.32 shows the voltage magnitude at the AC buses throughout the AC hub.
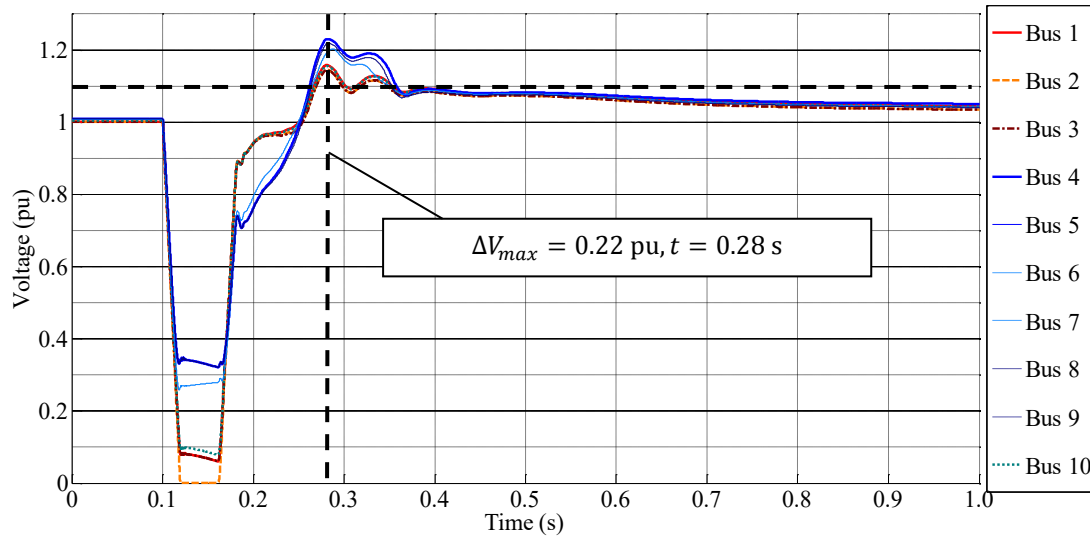
Figure 4.32 – Voltage magnitude at offshore VSC buses following a 3ph fault on an offshore bus

The voltage magnitude at bus 3 drops rapidly to zero. The voltage magnitude at the other buses drop to less than 0.5 pu, with those buses farthest from the faulted bus suffering the smallest reduction in voltage magnitude. The voltage magnitude at all buses begins to rise once the AC breaker isolates the faulted bus section after 60 ms. After the AC breaker is opened, the voltage magnitude at all buses above the upper voltage limit of the offshore AC network of 1.1 pu. When $t > 0.35$ s the voltage magnitude at all buses drops below the upper voltage limit and returns to a steady state condition.
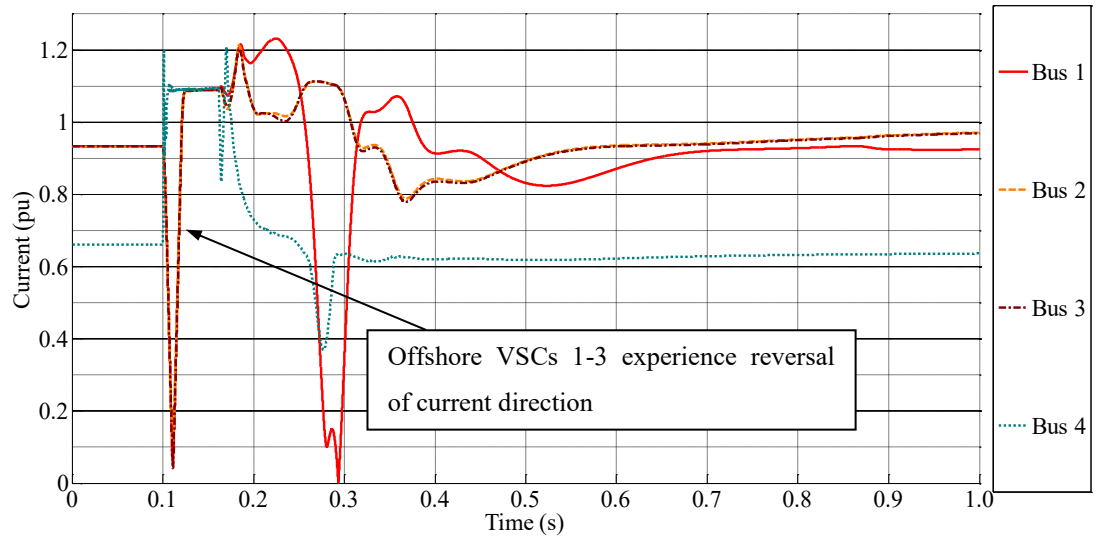
Figure 4.33 – Current magnitude through each offshore VSC bus following a 3ph fault on an offshore bus

Figure 4.33 shows the current magnitude flowing through the offshore VSCs. Immediately after the fault, offshore VSCs 1, 2 & 3 experience a reduction in current magnitude followed by an increase up to the current limit. Offshore VSC 4 experiences an immediate increase in current magnitude. This difference can be explained by considering the pre-fault condition. Offshore VSCs 1, 2 & 3 are all absorbing active power from the AC hub before the fault as can be seen in Figure 4.34. During the fault they supply reactive power to the fault as shown in Figure 4.35. Therefore the current must first change direction which explains the initial reduction in current magnitude seen in Figure 4.33.

It should be noted that the dynamic shown in Figure 4.33 after re-closing the breaker ($t > 0.16$ s) is heavily dependent upon the controller action present in each VSC. The healthy VSCs would trip given the excessive post-fault current magnitude.

111
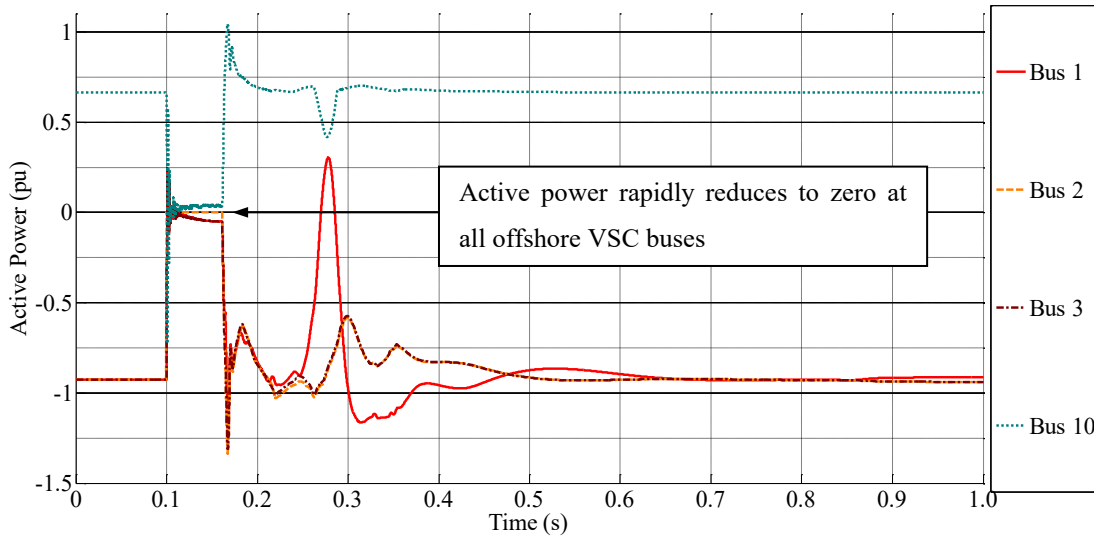
Figure 4.34 – Active power through each offshore VSC bus following a 3ph fault on an offshore bus
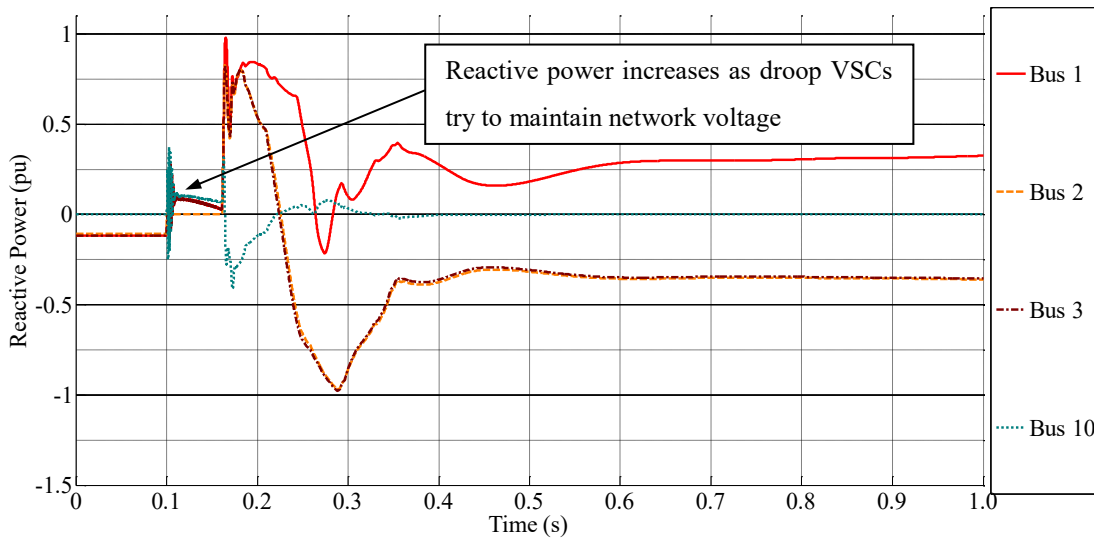
Figure 4.35 – Reactive power through each offshore VSC bus following a 3ph fault on an offshore bus

From Figure 4.34 it can be seen that the active power through the each VSC returns to the pre-fault active power flow after approximately 0.7 s. However, the reactive power flow through offshore VSCs 1, 2 & 3 differs to the pre-fault reactive power flow. VSCs 2 & 3 are absorbing reactive power while VSC 1 is generating reactive power. This leads to the undesirable steady-state condition where the droop VSCs work against each other rather than sharing the reactive power load. This is a new stable but undesirable operating point.

112

In conclusion, the results presented in Figures 4.32 to 4.35 show that the impact of a 3ph fault on a single bus affects the offshore AC hub and MITS. The over-voltage following clearance of the fault at all buses in the AC hub, although short-lived is not acceptable. Two of the offshore VSCs experience an over-current above the current limit. The voltage profile and active power flows suggest the system will return to an acceptable steady state condition. However, closer observation of the reactive power flow through offshore VSC 1 reveals that it differs to that of offshore VSC 2 & 3. All participating droop VSCs have the same droop gains and therefore should share the reactive power demand equally.

4.4.3 3ph fault on an offshore HVAC cable

The 3ph fault occurring on an offshore HVAC cable is a more likely event than a bus fault due to the relatively high probability, for example, of damage being caused by a ship's anchor. It is also a severe fault that could affect the entire AC hub. A 3ph fault is applied to line 2 of the AC hub model to study the implications on the AC hub and MITS. It is assumed that the entire circuit (including two parallel 3ph cables) is damaged and therefore must be removed from service.

At $t = 0.1$ s, a 3ph fault is applied at the midpoint of line 2. The fault impedance was assumed as very small ($Z_f = 1$ mΩ) to give the worst case scenario. At $t = 0.16$ s the AC CBs open to isolate the faulted cable circuit. Figure 4.36 shows the voltage magnitude at the AC buses throughout the AC hub.
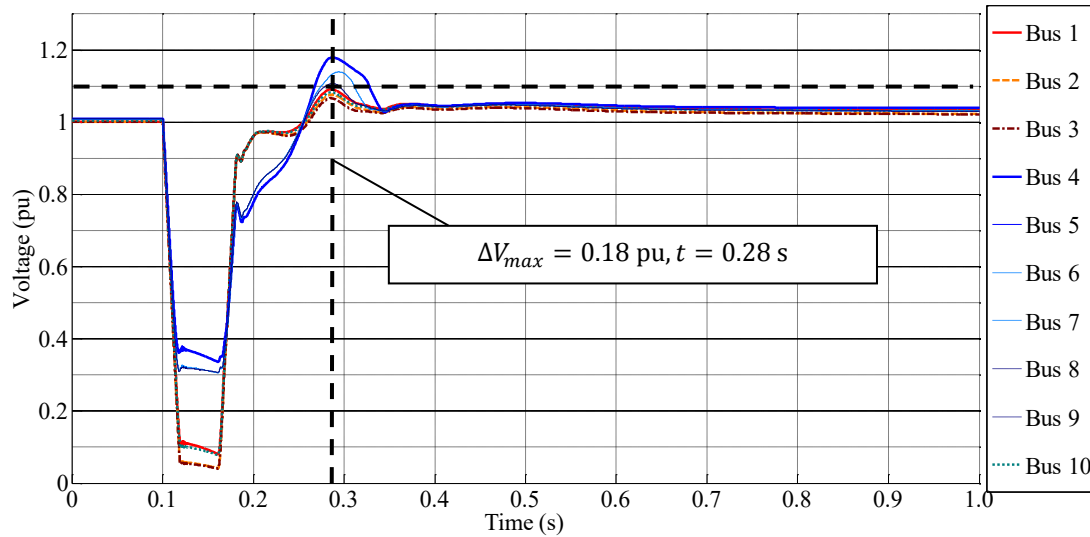
Figure 4.36 – Voltage magnitude at each offshore bus following a 3ph fault on an offshore HVAC cable

A similar result is observed as was presented for the 3ph fault at bus 3. However for the 3ph cable fault, the voltage magnitude does not reach zero at any bus because there is always some cable impedance between the fault location and any given source. The voltage magnitude at all buses drops to less than 0.5 pu, with those buses farthest from the faulted bus suffering the smallest reduction in voltage magnitude. The voltage magnitude at all buses begins to rise once the AC breaker isolates the faulted bus section after 60 ms. After the AC breaker is opened, the voltage magnitude at the FRC-WT buses (4–9) briefly rise above the upper voltage limit of the offshore AC network of 1.1 pu.

Figure 4.37 shows the active power infeed to the MITS. The infeed from all onshore VSCs reduces to zero during the fault. The infeed from the onshore VSCs 1, 2 & 3 goes positive which implies that the HVDC links are absorbing power from the MITS. Once the fault is cleared, the infeed returns to the pre-fault steady state condition.

114
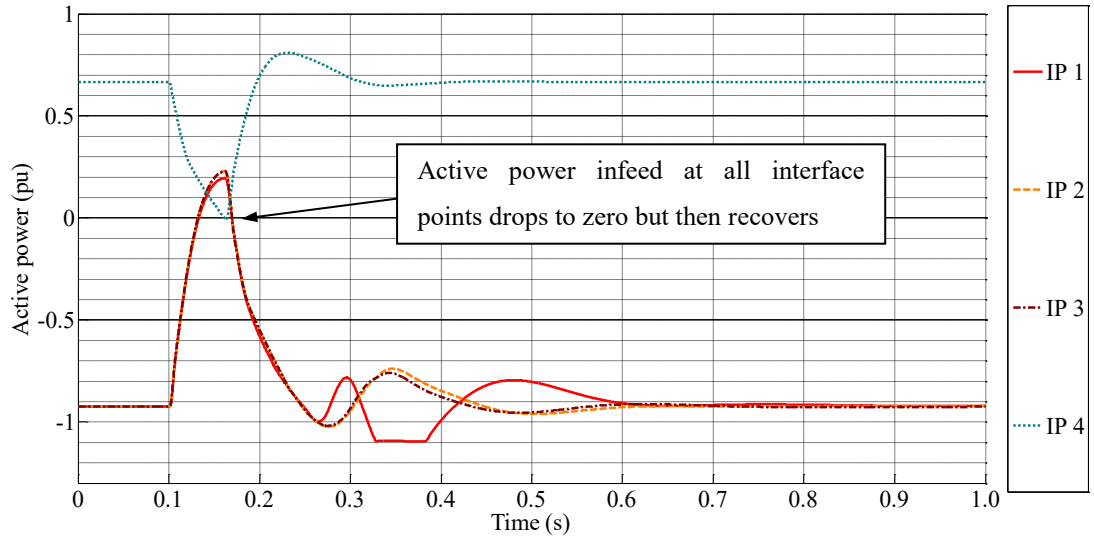
Figure 4.37 – Active power infeed at each onshore VSC interface point following a 3ph fault on an offshore HVAC cable

Figure 4.38 shows the reactive power flow through the offshore VSCs. Again, the droop controlled VSCs do not share the reactive power load equally following clearance of the fault.
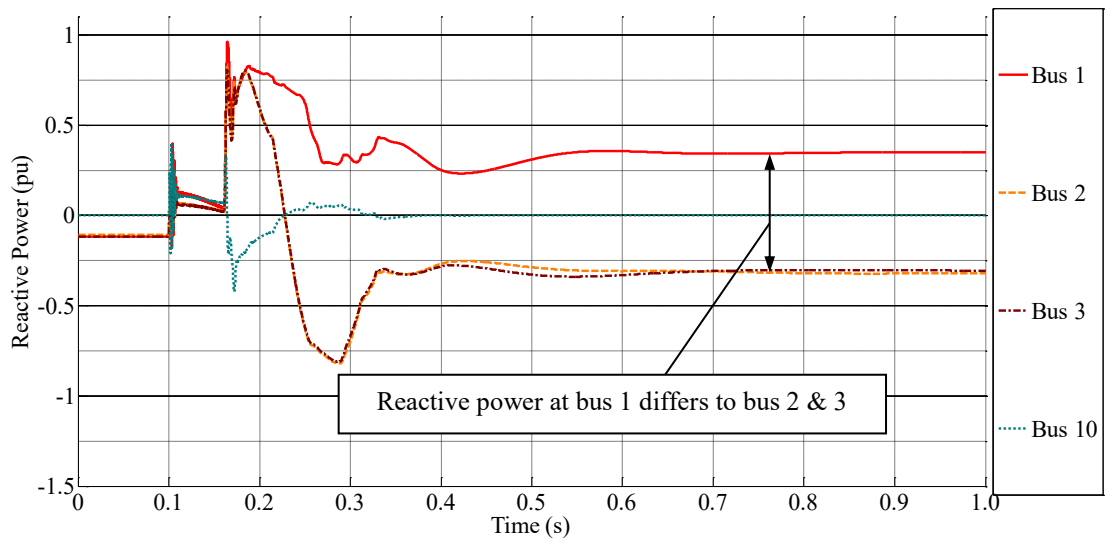
Figure 4.38 – Reactive power at each offshore VSC bus following a 3ph fault on an offshore HVAC cable

In conclusion, the results presented in Figures 3.55 to 3.57 show that the impact of a 3ph fault on HVAC cable circuit affects the offshore AC hub and MITS. The over-voltage following clearance of the fault at all buses in the AC hub, although short-lived is not acceptable. The active power infeed is restored to pre-fault levels following

clearance of the fault. Again, the reactive power flow through offshore VSC 1 reveals that it differs to that of offshore VSC 2 & 3. Again all participating droop VSCs have the same droop gains and therefore should share the reactive power demand equally.

5 Chapter 5 – Control systems for managing faults in an offshore AC hub

5.1 Introduction

Faults lead to unacceptable operating conditions in the offshore AC hub. This was proven in chapter 3 where it was shown that equipment operating limits were violated, the post-fault steady-state reactive power flow was undesirable and the loss of infeed to the MITS was too great during and after a DC pole-pole fault occurred. If an offshore AC hub is to be built in practice, these issues must be addressed. In this chapter, two fault management systems are applied to the offshore AC hub. The performance of each fault management system is compared given three different faults scenarios.

Various fault management systems for offshore hubs have been identified in the literature [56]–[60], [97]. These systems primarily address power imbalance and ride-through of faults occurring at the onshore IP and across the poles of the HVDC links. The systems identified are de-centralised, therefore a number of controllers operate independently acting only on information available locally (voltage, frequency). This negates the requirement for low latency communication infrastructure, for application in the offshore AC hub. The result of the combined effort of de-centralised controllers located at each VSC and FRC-WT is to effectively manage certain faults that could arise in the particular test networks that are presented (e.g. ref [62] using two VSC and two FRC-WT).

A centralised fault management system is presented in this chapter for comparison with the de-centralised fault management system. The centralised system has a single central controller which gathers information about the network in real-time and issues necessary instructions to local controllers should a fault occur. Applied to the offshore AC hub, the central controller could reside on any of the offshore HVDC platforms and the local controllers are the control loops of each VSC and FRC-WT.

The main potential disadvantage of the centralised fault management technique is its reliance on low latency communication infrastructure, which is not required by decentralised controllers. The centralised fault management system uses an online optimal power flow (OPF) algorithm to determine a new steady state post fault operating condition. The main advantage, as will be shown later in this chapter, is that the centralised controller is able to minimise the detrimental impacts of a range of faults in a complex offshore hub through fast provision of an acceptable post-fault operating condition.

5.2 De-centralised fault management system

A de-centralised fault management system is described in [62]. The system regulates power balance in an offshore transmission system in response to faults at the onshore IP and on the HVDC links. It achieves this by varying the operating frequency of the offshore AC grid. Local controllers use the change in operating frequency (as measured locally), to signal a reduction in power output and hence correct any power imbalance which is present as a result of a fault. A key benefit of this system is that it does not rely upon low-latency communication between onshore and offshore controllers.

Other fault management systems are presented in the literature. However, the system presented in [62] is most interesting as the authors have applied it to an offshore transmission system which could be considered as a small AC hub. The offshore transmission system considered in [62] is presented in Figure 5.1.
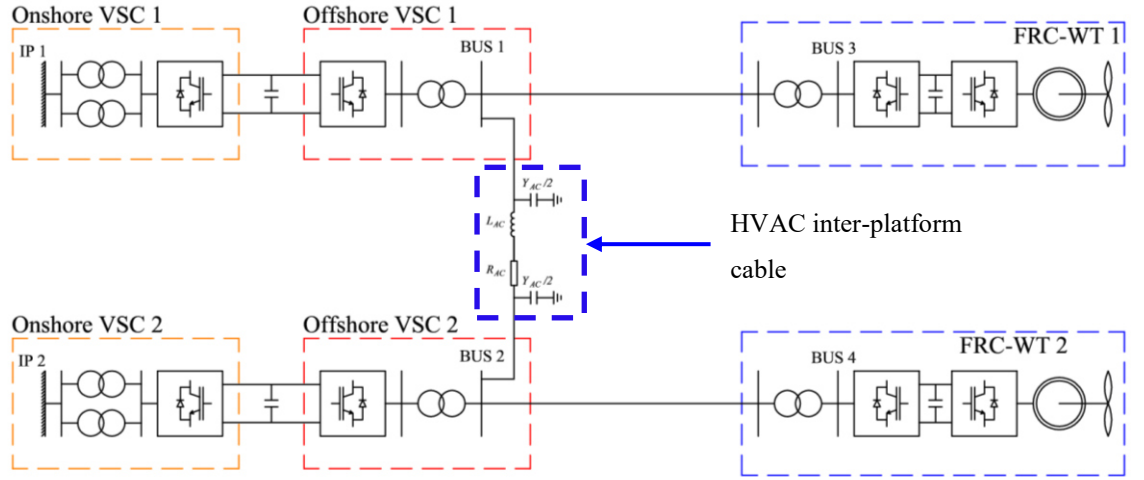
Figure 5.1 – Offshore network configuration used in [62]

As seen in Figure 5.1, the offshore network consists of two HVDC links and two offshore WAs. Each WA is represented by a single equivalent FRC-WT model. Each FRC-WT is connected to an offshore VSC. The offshore VSCs are connected together by a single HVAC cable which is represented by a nominal π-section. It is the HVAC cable that is of key significance as it forces the otherwise separate offshore HVDC converters and WAs to share a common operating frequency. The authors implement a droop control strategy to allow both offshore VSCs to participate in managing voltage and frequency in the offshore network.

In chapter 3, a model of an offshore AC hub was developed in SimPowerSystems as shown in Figure 5.2.
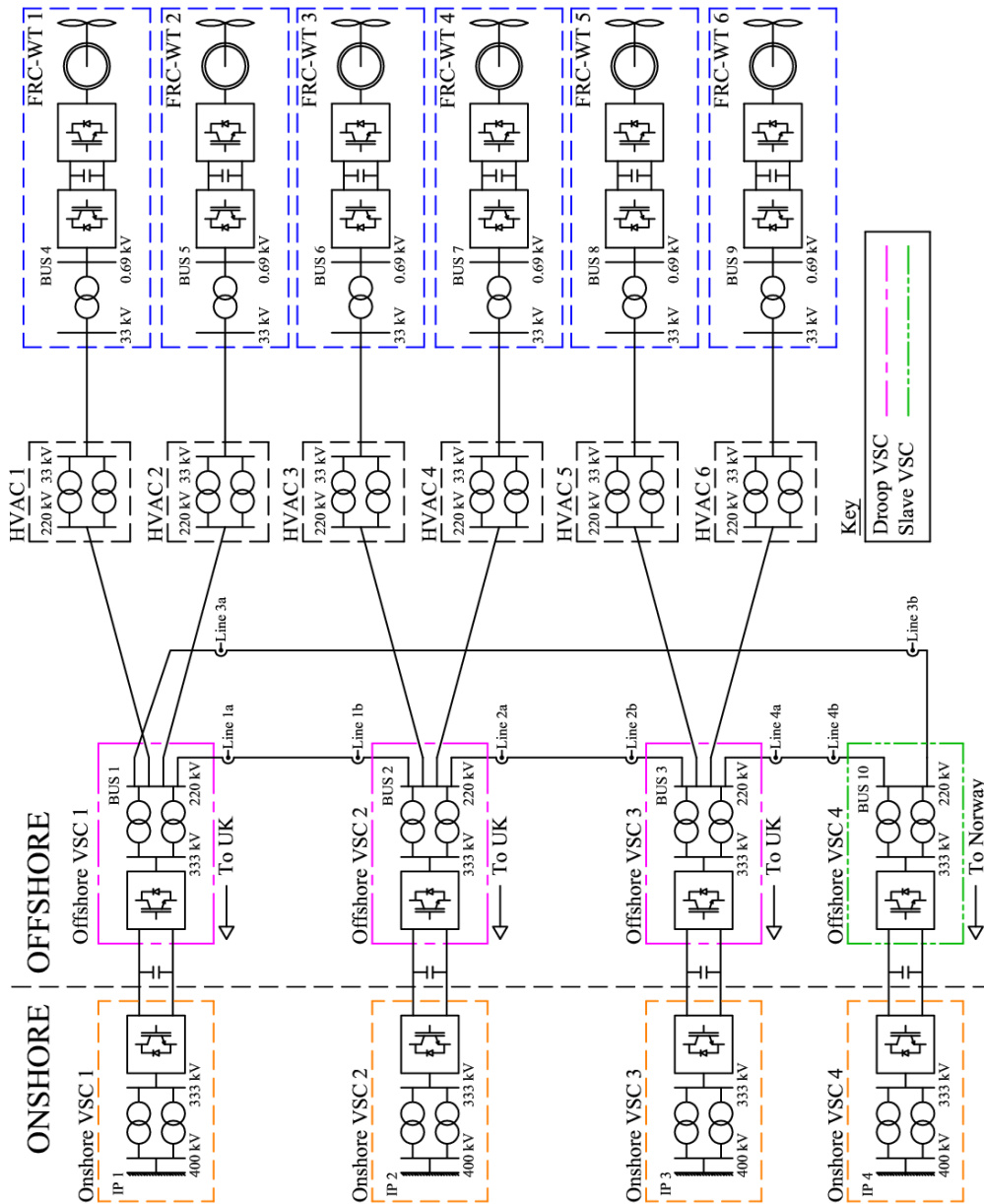
Figure 5.2 – Single line diagram of the offshore AC hub and HVDC links

The model was implemented using the droop control strategy as presented in Chapter 4 of this thesis. The offshore AC hub model developed is considerably larger than that presented in [1] and Figure 5.1 as it contains four HVDC links and six WAs instead of two HVDC links and two WAs. In addition, the model is more complex as it represents the AC cable sections right up to the first WT of each string.

When there is more than one HVDC link operating in parallel, as is the case in an offshore AC hub, a fault in one of the HVDC links reduces the active power

through the faulted link to zero. Two possible outcomes exist following the occurrence of a fault in one of the HVDC links, which depend on the pre-fault operating conditions:

1. If the amount of active power generated in the offshore AC hub is *less* than the available onward transmission capacity of the remaining healthy HVDC links, then the active power must be re-directed through those links.

2. If the amount of active power generated in the offshore AC hub is *greater* than the available onward transmission capacity of the remaining healthy HVDC links, then a power imbalance will exist. This power imbalance must be corrected by reducing generation in order to avoid overloading transmission assets and causing loss of infeed to the MITS.

The first outcome is actioned by the droop control applied to each participating offshore VSC. The reduction in active power through the faulted HVDC link causes the active power through the remaining healthy HVDC links to increase. The frequency produced by the remaining healthy offshore VSCs increases as they absorb more active power as determined by the droop characteristic.

The second outcome cannot be remedied by the droop control alone. Additional control action is required to reduce the active power generated by the FRC-WTs and dispatch controlled VSC. To implement the de-centralised fault management system defined in [62], two key additions were made to the AC hub model including:

- A frequency modulation controller on each offshore VSC participating in droop control (offshore VSCs 1-3).
- A power reduction controller on each FRC-WT and each power dispatch controlled offshore VSC (offshore VSC 4).

5.2.1 Frequency modulation controller

The frequency modulation controller implemented on each offshore VSC participating in droop control is shown in Figure 5.3.
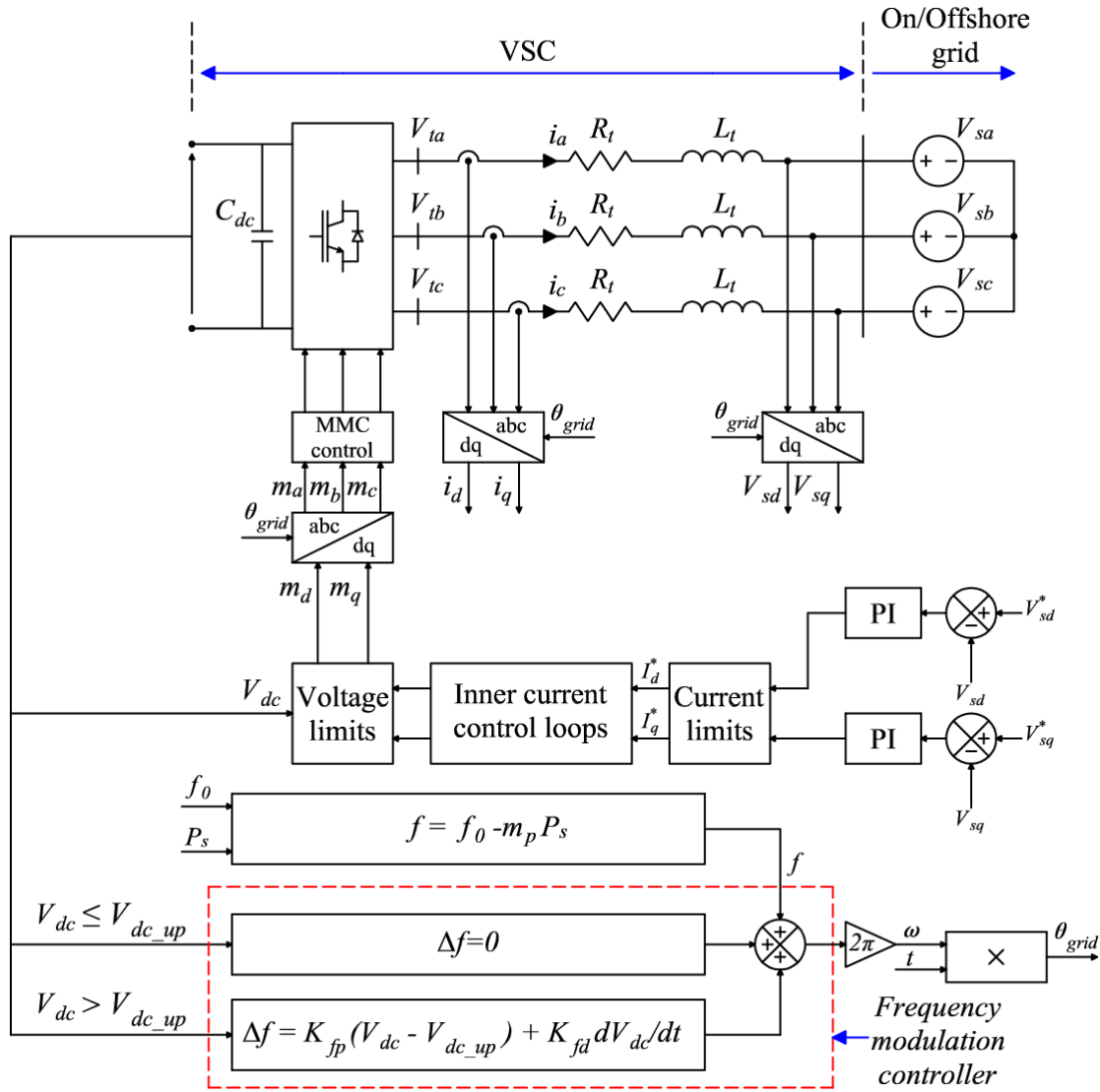
Figure 5.3 – Frequency modulation controller applied to droop controlled offshore VSCs

Under normal operating conditions the DC voltage is below the DC voltage upper limit V_{dc_up}. If a fault occurs which causes a power imbalance between the onshore and offshore VSCs then the DC voltage will rise above the DC voltage upper limit. The frequency modulation controller is then activated and a transient frequency adjustment Δf is made according to (5.1).

$$\Delta f = K_{fp}(V_{dc} - V_{dc\_up}) + K_{fd}\frac{dV_{dc}}{dt} \qquad (5.1)$$

Where K_{fp} and K_{fd} are the proportional and derivative gains respectively. The parameters used to for the frequency modulation controller are shown in Table 5.1.

Table 5.1 - Frequency modulation controller parameters

Parameters		Value	Units
Symbol	**Description**		
V_{dc}	Nominal DC voltage	640.0	kV
V_{dc_up}	Upper DC voltage limit	653.0	kV
K_{fp}	Proportional gain	0.80	pu
K_{fd}	Derivative gain	0.01	pu

The power reduction controller implemented on each FRC-WT and dispatch controlled offshore VSC is shown in Figure 5.4.
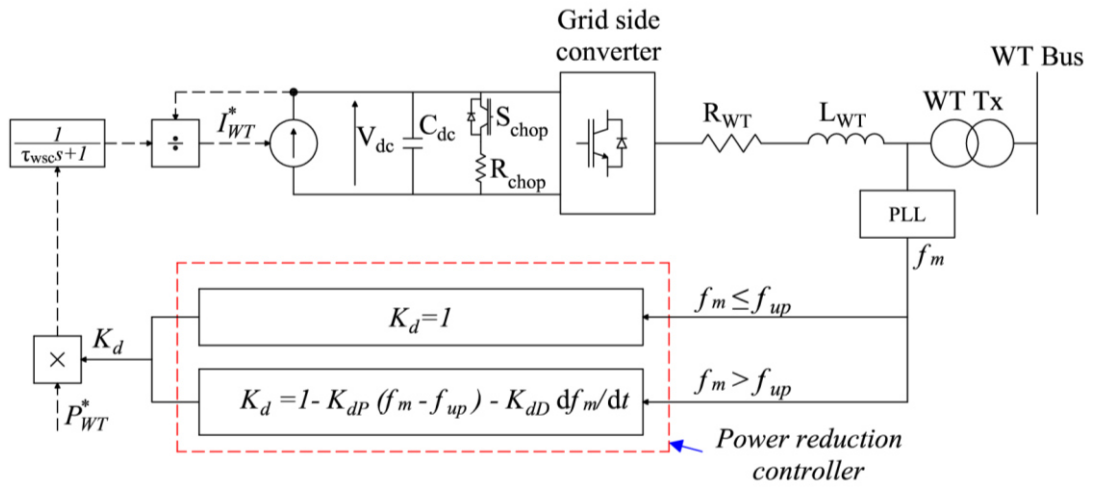
Figure 5.4 – Power reduction controller applied to each dispatch controlled offshore VSC and FRC-WT

Under normal operating conditions the offshore AC grid frequency f_m as measured by the FRC-WT PLL is below the upper frequency limit f_{up}. If a fault occurs which results in an increase in DC voltage on the HVDC link, the offshore grid frequency will increase above f_{up} and the power reduction controller will be activated. The power reduction controller reduces the active power reference P_{WT}^* by multiplying it by the reduction factor K_d which is determined by (5.2).

$$K_d = 1 - K_{dP}(f_m - f_{up}) - K_{dD}\frac{\mathrm{d}f_m}{\mathrm{d}t} \qquad (5.2)$$

Where K_{dP} and K_{dD} are the proportional and derivative gains respectively. The parameters used to for the power reduction controller are shown in Table 5.2.

Table 5.2 – Power reduction controller parameters

Parameters		Value	Units
Symbol	**Description**		
f_m	Nominal frequency	50.0	Hz
f_{up}	Upper frequency limit	50.5	Hz
K_{dP}	Proportional gain	0.40	pu
K_{dD}	Derivative gain	0.02	pu

5.2.2 Test of frequency modulation and power reduction method:

To test the performance of the de-centralised method, a DC pole-pole fault was applied to HVDC link 1. Figure 5.5 presents the AC voltage magnitude across all HVAC buses.
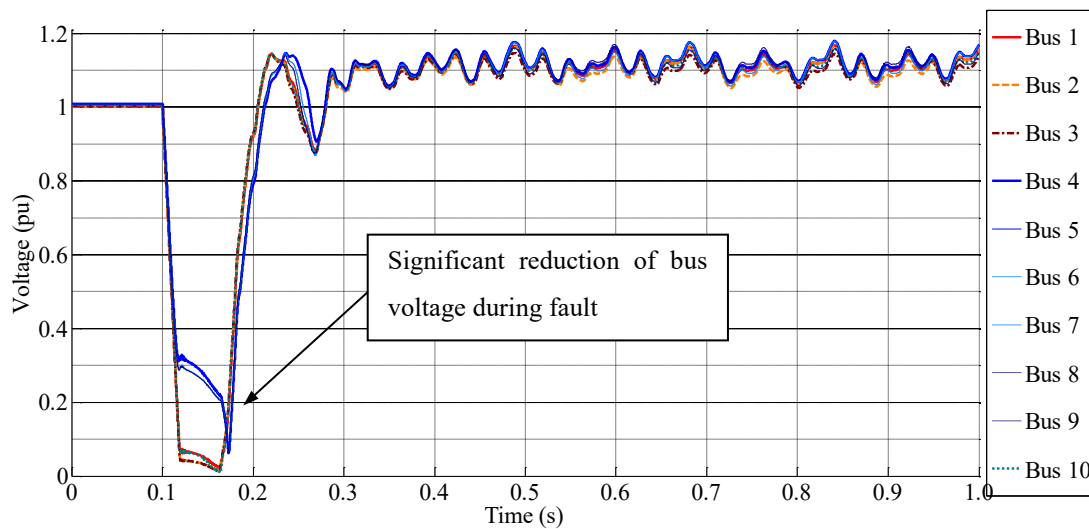
Figure 5.5 - Voltage magnitude at each offshore bus following a DC pole-pole fault

The voltage across all HVAC buses reduces significantly during the fault. The voltage reduction is in fact greater than the response with no fault management method as was shown in Chapter 4. This suggests that this fault management method can actually increase the severity of the fault.

Figure 5.6 shows the DC voltages across the HVDC links. The voltages measured at offshore VSC 2 & 3 increase above 1.1 pu which is the upper DC voltage limit. In addition, a voltage oscillation due to an exchange of energy between HVDC link 2 & 3 is observed when $t > 0.5$ s.
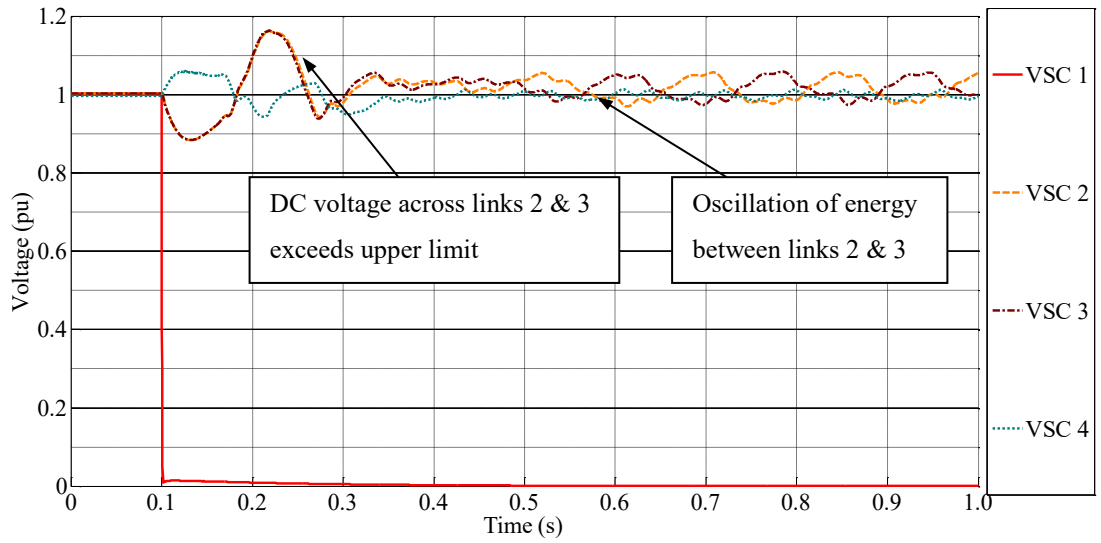
Figure 5.6 – Voltage across each HVDC link following a DC pole-pole fault

Figure 5.7 shows the active power delivered at the FRC-WT buses. The active power output reduces to zero throughout the duration of the fault, which is due to the collapse in voltage. Again, considerable oscillation is present after the fault, however it can be seen that the active power output reduces following the fault. This shows that the power reduction controllers are operating, albeit less than satisfactorily due to the oscillation.

Figure 5.7 – Active Power at each FRC-WT bus following a DC pole-pole fault

125

Figure 5.8 shows the frequency measured at each offshore VSC bus. It can be seen that both VSC 2 and VSC 3 produce a frequency that increases then decreases. In addition, an oscillatory behaviour is observed between the two as when one increases the other does not. This suggests there is a problem associated with the frequency modulation controllers hunting against one another. This also explains why there is an exchange of energy between HVDC links 2 & 3 as was highlighted in Figure 5.6.
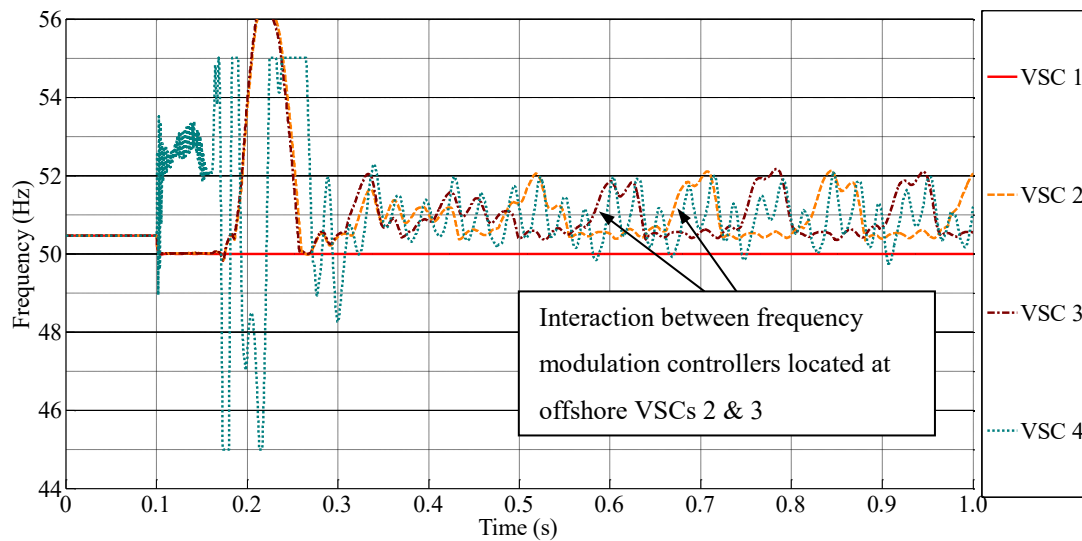
Figure 5.8 – Frequency at each offshore VSC bus following a DC pole-pole fault

The PLLs located at the FRC-WTs and dispatch controlled offshore VSC attempt to replicate the frequency produced by the droop controlled offshore VSCs by locking on to the phase of the local voltage measurement. The frequency produced by the PLLs at the FRC-WTs is shown in Figure 5.9.
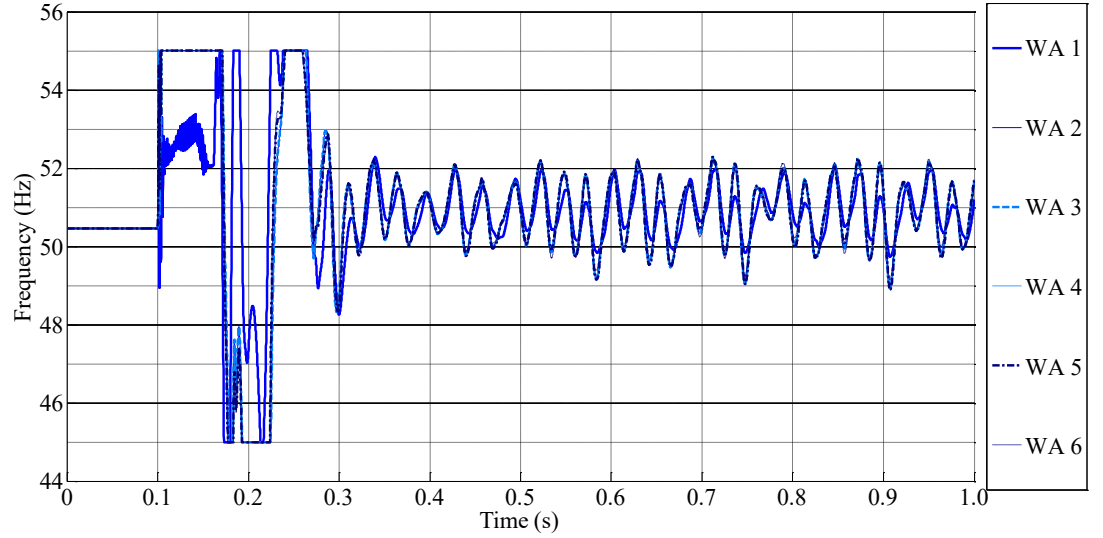
Figure 5.9 - Frequency at each FRC-WT bus following a DC pole-pole fault

As can be seen in Figure 5.9, the frequency as measured at the FRC-WTs contains considerable oscillation. The performance of the PLL will strongly affect the performance of the power reduction controller, which explains the results seen in Figure 5.7. The PLL provides the frequency measurement f_m from which the power reduction acts upon. From Figure 5.9 it can be seen that for the 200 ms following the occurrence of the fault, the PLL swings between the upper and lower saturation limits which are set at 55 Hz and 45 Hz respectively.

In a bid to improve the performance of the de-centralised method, the gains and thresholds of the frequency modulation and power reduction controllers were adjusted but without alteration to the system architecture. A trial and error method was used to try and improve the performance, which is the same method used in [62]. Unfortunately, a set of gains which improved the response of the controllers could not be found.

5.2.3   Modifications to de-centralised method

For the system to function correctly, two issues must be overcome. Firstly, the low frequency oscillatory interaction between the droop controlled offshore VSCs must be addressed. Secondly, the performance of the power reduction controllers must be improved.

127

The frequency modulation controller was modified by replacing the PD controller with a PI controller. The power reduction controller was modified to dampen the response by introducing a frequency threshold and upper limit, as well as a first-order low-pass filter. In addition, the derivative action was removed. The power reduction factor is determined by (5.3):

$$K_d = \begin{cases} 1 & f_m < f_{thresh} \\ 1 - \dfrac{f_m - f_{thresh}}{f_{up} - f_{thresh}} & \text{for } f_{thresh} < f_m < f_{up} \\ 0 & f_m > f_{up} \end{cases} \quad (5.3)$$

Where,

- f_m is the frequency measured by the PLL.
- f_{thresh} is the threshold at which the frequency modulation controller begins to operate.
- f_{up} is the maximum allowed DC voltage

The modifications to the power reduction controller are highlighted in Figure 5.10.
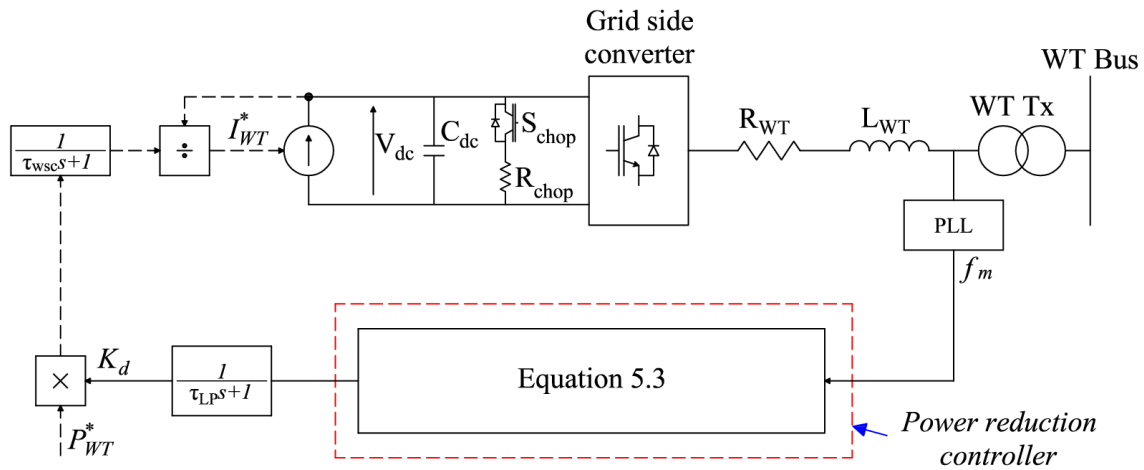
Figure 5.10 – Modified power reduction controller

The new parameters for both the frequency modulation controller and power reduction controller are shown in Table 5.3.

Table 5.3 – Updated frequency modulation and power reduction control parameters

Parameters		Value	Units
Symbol	Description		
Frequency modulation controller:			
V_{dc}	Nominal DC voltage	640.0	kV
V_{dc_up}	Upper DC voltage limit	653.0	kV
K_{fp}	Proportional gain	0.80	pu
K_{fi}	Integral gain	12.80	pu
Power reduction controller:			
f_m	Nominal frequency	50.0	Hz
f_{thresh}	Frequency threshold	50.5	Hz
f_{up}	Upper frequency limit	52.0	Hz
T_{LP}	Low-pass filter time constant	0.05	s

5.2.4 Re-test following modifications to de-centralised method

Again, a DC pole-pole fault is applied to HVDC link 1. Figure 5.11 shows the voltage magnitude at the HVAC buses throughout the AC hub. The voltage magnitude across all buses drops initially on occurrence of the fault. However, the magnitude only drops to approximately 0.85 pu. The maximum voltage is slightly higher than the upper voltage limit at 1.12 pu.
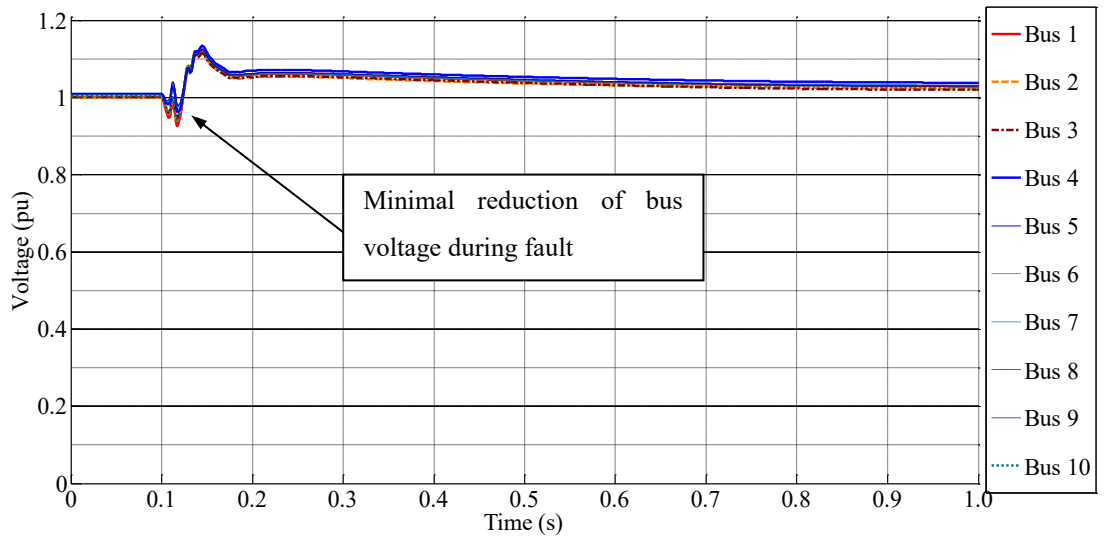
Figure 5.11 - Voltage magnitude at each offshore bus following a DC pole-pole fault

As shown in Figure 5.12, the DC link voltage of VSC1 drops rapidly. The voltage across the healthy HVDC links remain below the upper DC voltage limit. It is important to note that DC choppers are not used in this simulation.
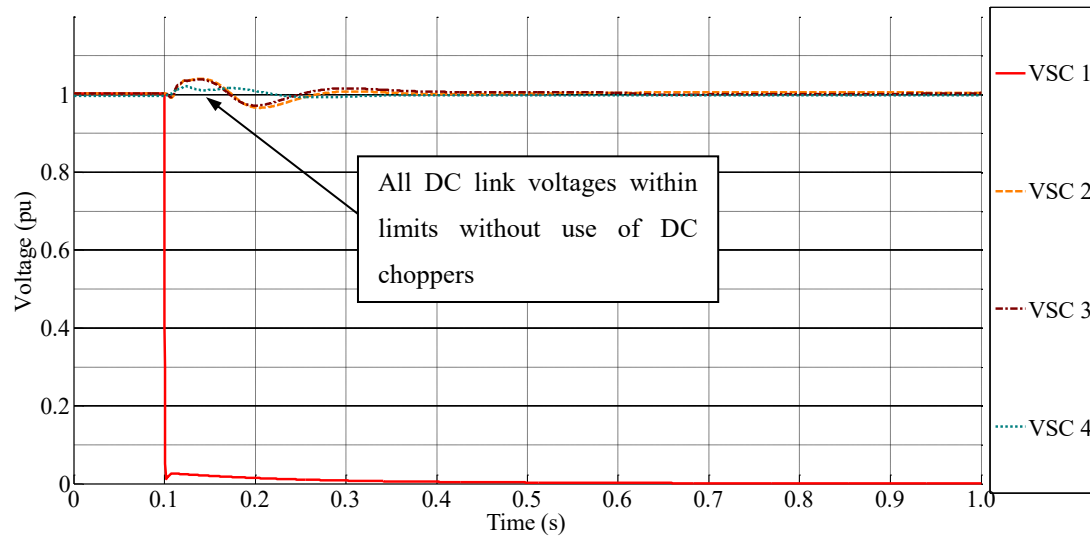
Figure 5.12 - Voltage across each HVDC link following a DC pole-pole fault

The active power flowing through the offshore VSCs is shown in Figure 5.13. The active power through the offshore VSC connected to bus 1 reduces to zero as expected due to the fault. The active power through the offshore VSCs connected to bus 2 & 3 increases to compensate. The active power through the offshore VSC connected to bus 10 reduces, which confirms the power reduction controller is operating.
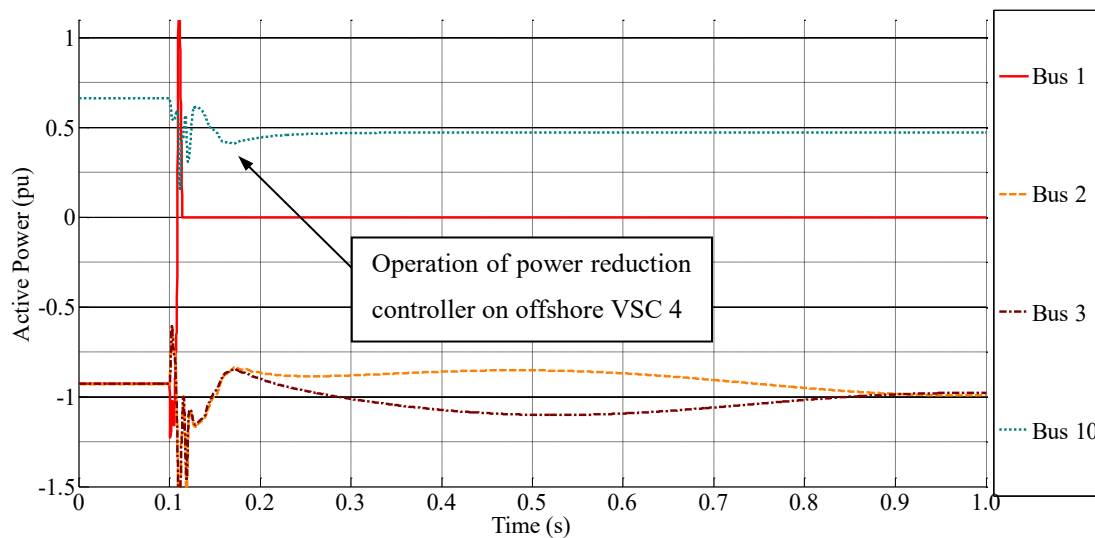
Figure 5.13 – Active power through each offshore VSC bus following a DC pole-pole fault

130

Figure 5.14 shows the active power through the FRC-WT buses. Again, the operation of the power reduction controllers is validated by the reduction in active power transfer through all buses.
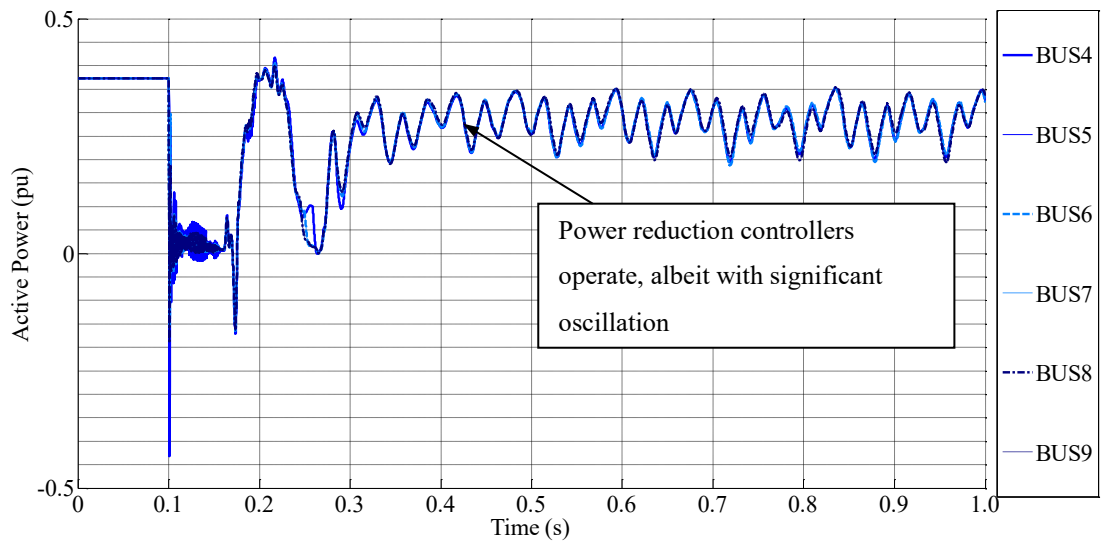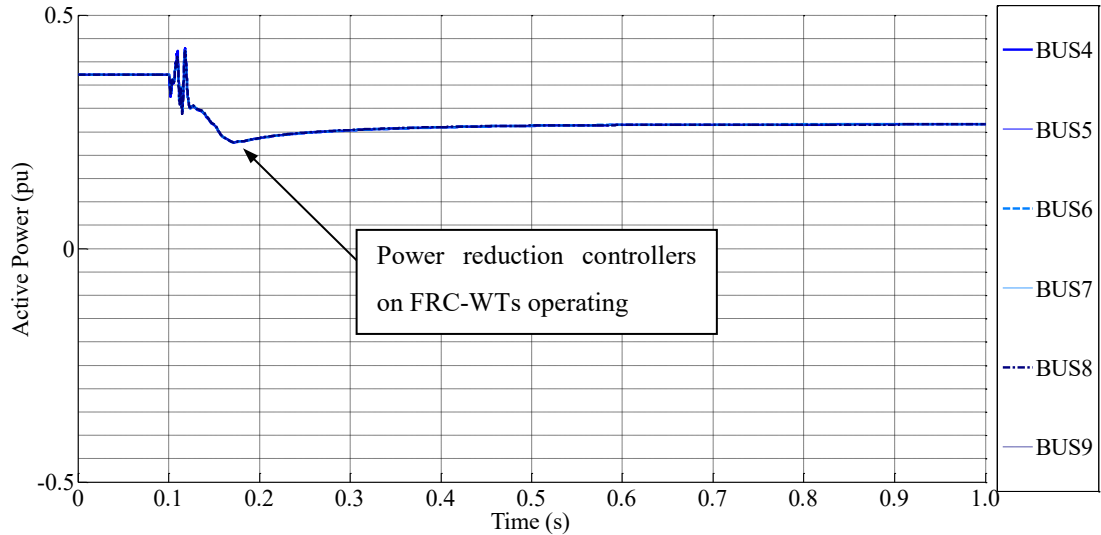

Figure 5.14 - Active power through each FRC-WT bus following a DC pole-pole fault

Figure 5.15 shows the frequency at each offshore VSC. The frequency of VSC 1 drops to the nominal frequency as the active power reduces to zero due to the fault. The frequency at VSC 2 and 3 increases due to the rise in DC link voltage, confirming that the frequency modulation controllers are operating. The frequency at VSC 4 is determined by a PLL and oscillates between its limits during the fault before settling to a steady state condition.
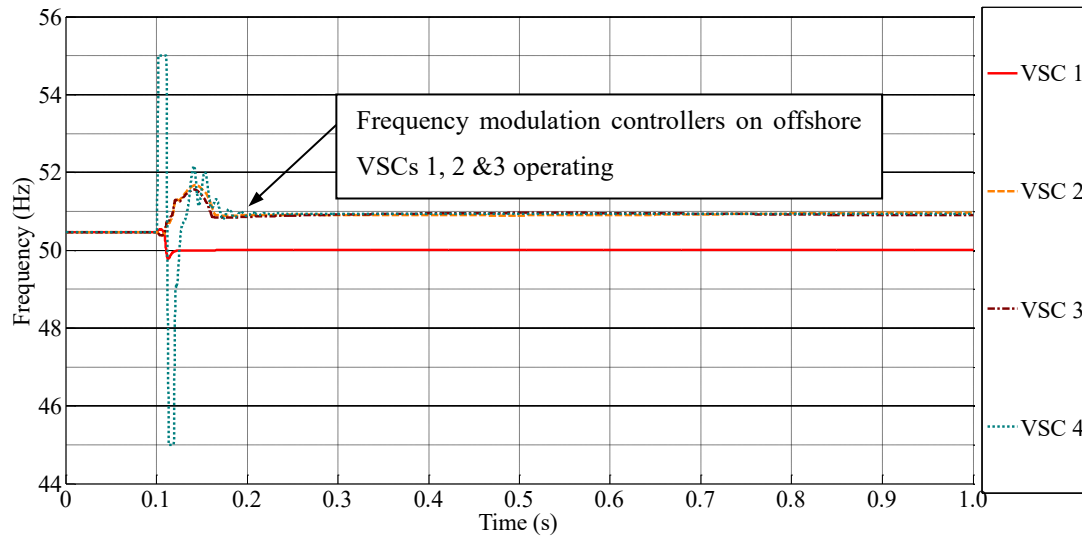
Figure 5.15 - Frequency at each offshore VSC bus following a DC pole-pole fault

The frequency as measured by each of the FRC-WTs is shown in Figure 5.16. As was the case for VSC 4, the frequency oscillates between its limits during the fault and then the oscillation decays once the fault is cleared. The new steady-state operating frequency is just below 51 Hz.
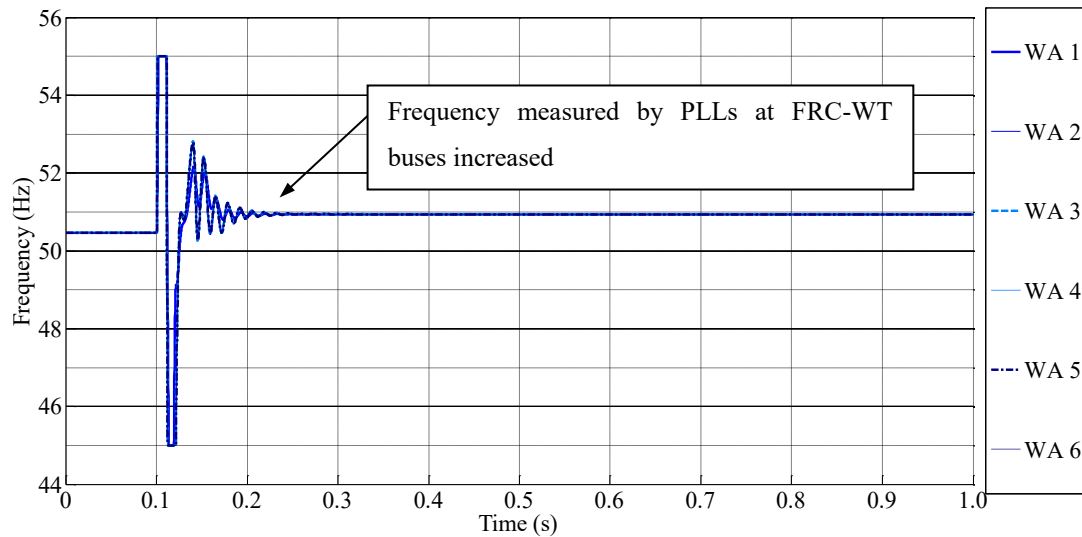
Figure 5.16 - Frequency at each FRC-WT bus following a DC pole-pole fault

5.3 Centralised fault management system

A centralised fault management system is now developed and is referred to as the *AC-hub controller*. Figure 5.17 presents a simplified block diagram of the AC hub controller. The AC hub controller continually monitors the network and acts only when a fault is present. The controller pre-configures and executes an online OPF algorithm to calculate new dispatch orders for the post-fault condition. It is expected that the AC hub controller operates in a small amount of time i.e. less than 100 ms to ensure the impact of the fault on both the on and offshore network is minimised.
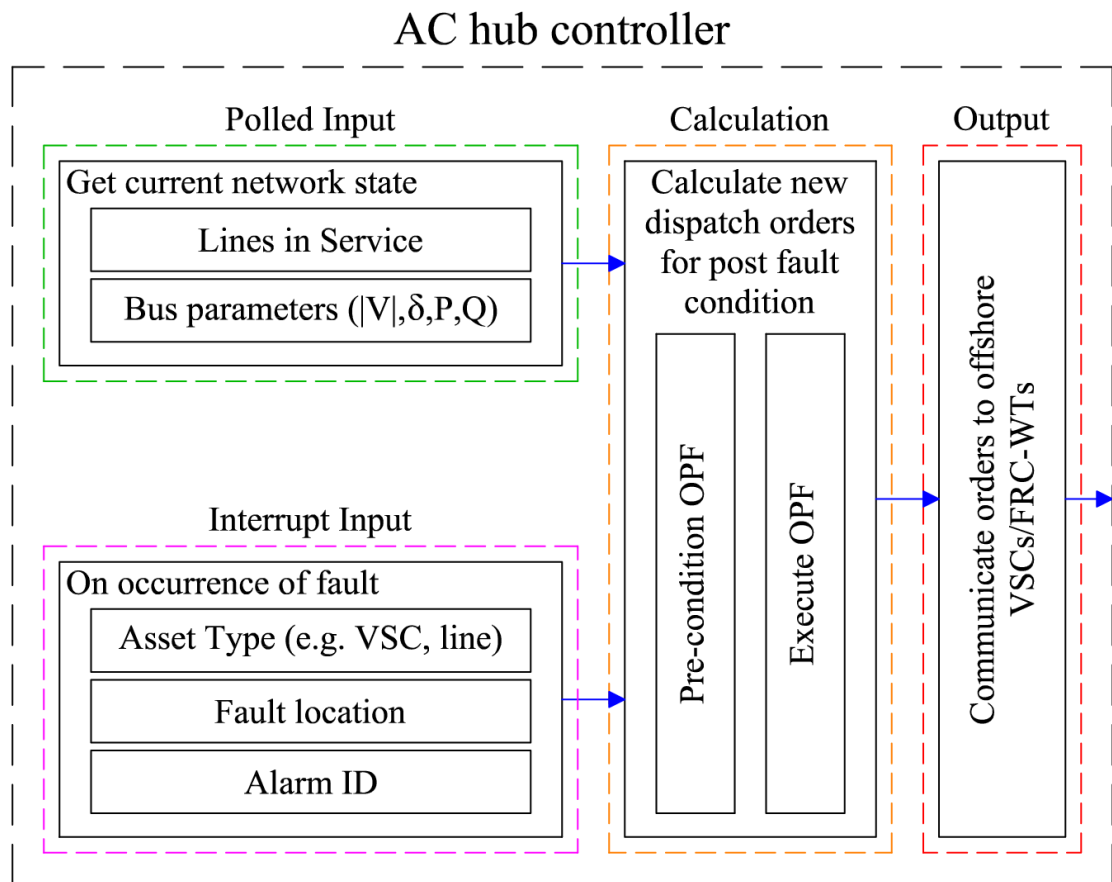
Figure 5.17 – Simplified functional diagram of the AC hub controller

5.3.1 Representation of the offshore AC hub

It is important that a feasible post-fault operating condition is found as quickly as possible. It is expected that the new orders are ready for dispatch as soon as the fault has been cleared. To that end, a simple 10 bus representation of the AC hub network is used. The single line diagram (SLD) of the electrical network used for

the OPF algorithm is given in Figure 5.18. The voltage base is 220 kV and the apparent power base is 1200 MVA.
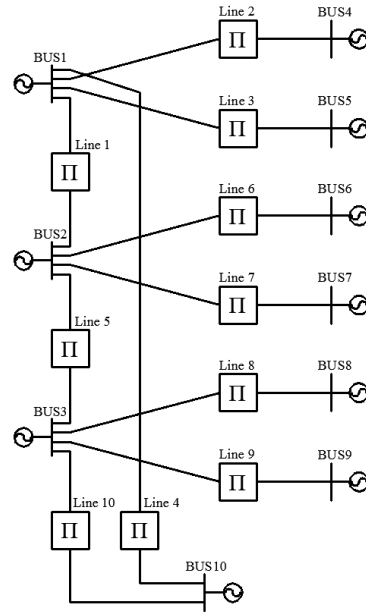
Figure 5.18 – Single line diagram of offshore AC hub as used in OPF

Each offshore VSC including the converter transformers are replaced by a voltage source at the respective offshore AC bus (buses 1, 2, 3 and 10). Each equivalent FRC-WT representing a single WA is replaced by a voltage source at the respective offshore AC bus (buses 4-9). The impedance of all electrical components between each offshore bus is combined into an equivalent π-section.

Buses 1, 2 and 3 are droop controlled generator buses which collectively maintain voltage and frequency while distributing active (P_g) and reactive (Q_g) power generation between them as determined by their respective droop gains. Buses 4 to 10 are considered as generator buses which are available for dispatch.

5.3.2   Functional description of the AC hub controller

The internal functional layout of the AC hub controller is presented in Figure 5.19.
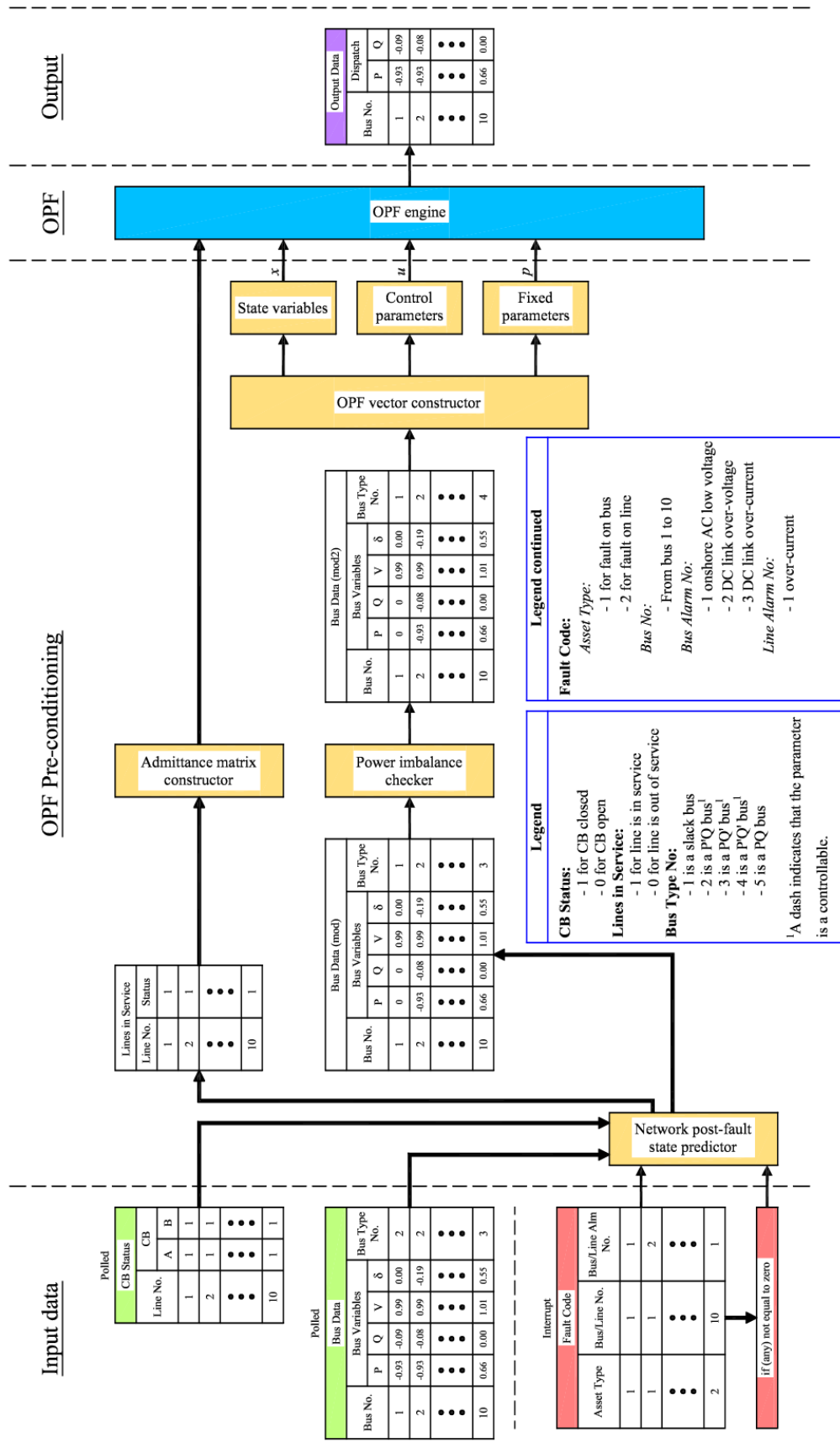
Figure 5.19 - AC hub controller functional diagram

135

5.3.2.1 Input data

The input data to the AC hub controller consists of two types. One type is polled data obtained through the SCADA system and the other is data which will trigger an immediate action by the algorithm, i.e. is event driven.

Polled data: One aspect of the polled data is the CB status of each line present in the network. The CB status is used to determine the network configuration as lines are switched in or out under planned operating conditions.

Another aspect of the polled data is the parameter values at each bus which are described as bus data. An example of the bus data is given in Table 5.4 and includes active and reactive power, voltage magnitude and voltage angle at each bus.

Table 5.4 – Bus data table

Bus No.	P (pu)	Q (pu)	V_{mag} (pu)	V_{ang} (°)	*Bus type*
1	-0.9557	-0.1020	1.0002	0.0000	4
2	-0.9557	-0.1019	0.9990	-0.1824	4
3	-0.9557	-0.1020	1.0002	0.0000	4
4	0.3750	0.0000	1.0079	10.1295	5
5	0.3750	0.0000	1.0079	10.1295	5
6	0.3750	0.0000	1.0067	9.9716	5
7	0.3750	0.0000	1.0067	9.9716	5
8	0.3750	0.0000	1.0079	10.1295	5
9	0.3750	0.0000	1.0079	10.1295	5
10	0.6667	0.0000	1.0038	0.5449	5

An additional column is included in the bus data table called bus type. Each bus is defined a bus type number according to the way the OPF algorithm must treat each parameter at each bus. Each parameter can be either fixed, controllable or a state variable. For example, a slack bus will have fixed voltage magnitude and angle but variable active and reactive power. Table 5.5 is used as a reference to determine the appropriate bus number where: x is a state variable, u is a control parameter and p is a fixed parameter.

Table 5.5 – Bus parameter configuration look up table

Bus type	P	Q	V_{mag}	V_{ang}	Description
1	x	x	p	p	Slack bus
2	u	p	x	x	P'Q bus[1]
3	p	u	x	x	PQ' bus[1]
4	u	u	x	x	P'Q' bus[1]
5	p	p	x	x	PQ bus

[1]A dash indicates that the parameter is a controllable.

Trigger data: The trigger data stops the normal polling action of the AC hub controller and triggers the pre-configuration process. The trigger data consists of a table from which a fault code is read if any of the data in the table is non-zero. It is assumed that a fault occurring anywhere in the network is assigned a code defined as follows:

- Asset Type:
  - 1 for fault on bus
  - 2 for fault on line
- Bus No:
  - From bus 1 to 10
- Bus Alarm No:
  - 1 onshore AC low voltage
  - 2 DC link over-voltage
  - 3 DC link over-current
- Line Alarm No:
  - 1 over-current

For example, a DC link over-current occurring on HVDC link 3 at bus 3 would have the fault code [1 3 3].

5.3.2.2 OPF pre-conditioning

The OPF pre-conditioning phase analyses the input data and configures it appropriately for input into the OPF algorithm.

Network post-fault state predictor: The first stage of the pre-conditioning phase is to predict the effect of the fault according to the fault code on the post-fault network state. This process is described in the flow chart in Figure 5.20.

If the fault present is related to a generator bus, then the objective of the function is to decide whether to force the active and/or reactive power to zero. The decision is made by comparing the fault code to a look up table which is pre-defined with the appropriate action. The modification is achieved by modifying P and Q in the bus data table to zero and setting the bus type number to 5 which defines P and Q as fixed parameters.

If the fault present is related to a line, then the objective of the function is to decide whether to take the line out of service. Again, the decision is made by comparing the fault code to a look up table which is pre-defined with the appropriate action, assuming that line is already in service. A new table is then created defining those lines in service according to the CB status and any post-fault modification if necessary.
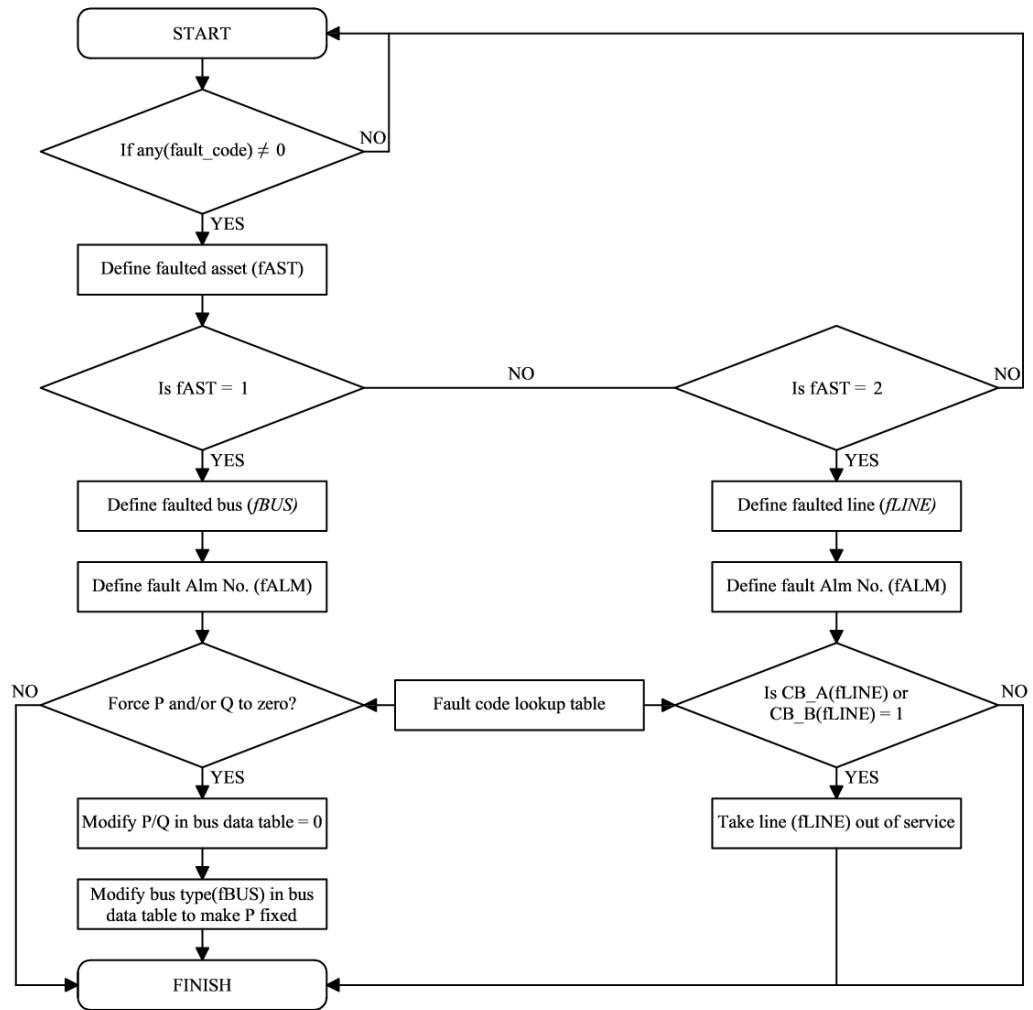
Figure 5.20 – Flow diagram of the network post-fault state predictor

Admittance matrix constructor: The main objective of this function is to populate an admittance matrix according to the predicted post-fault network state. This process is described in the flow chart in Figure 5.21.

139
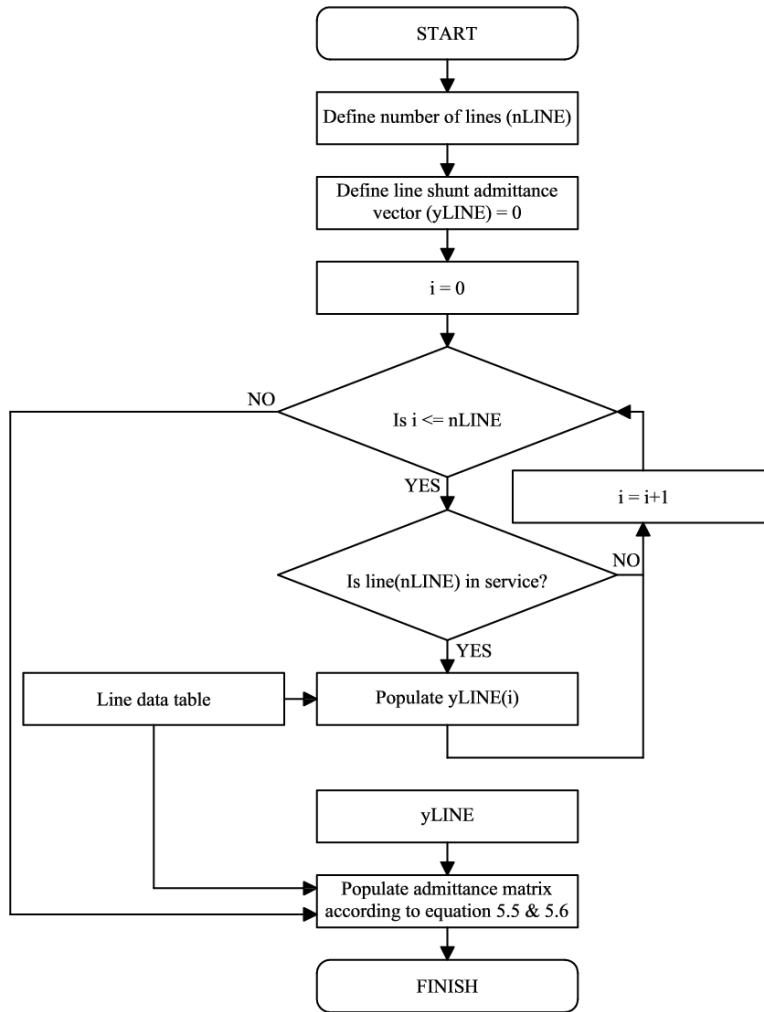
Figure 5.21 – Flow diagram of the admittance matrix constructor

The function inputs include a table showing lines in service and a line data table. Table 5.6 presents the line data covering the entire network. The function extracts the necessary line data from Table 5.6 according to which lines are in service.

The admittance of each branch of the network between bus m and bus n is defined by:

$$Y_a = Y_{mn} = G_{mn} + jB_{mn} \qquad (5.4)$$

To construct the admittance matrix, the function uses the following equations:

For off diagonal elements,

$$Y_{mn} = -Y_a \ (m \neq n) \qquad (5.5)$$

140

For diagonal elements,

$$Y_{mm} = \sum_{1}^{n} Y_{mn} + Y_{sh_m} \qquad (5.6)$$

Table 5.6 - Line data for offshore AC hub as used in OPF

Line No.	From bus m to bus n		Series Z(pu)		Series Y(pu)		Shunt Y(pu)	
	Bus_m	Bus_n	R	X	G	B	$Y/2_m$	$Y/2_n$
1	1	2	0.0066	0.0296	7.1475	-32.1989	0.0482	0.0482
2	1	4	0.0578	0.4734	0.2540	-2.0816	0.0497	0.0037
3	1	5	0.0578	0.4734	0.2540	-2.0816	0.0497	0.0037
4	1	10	0.0066	0.0296	7.1475	-32.1989	0.0482	0.0482
5	2	3	0.0066	0.0296	7.1475	-32.1989	0.0482	0.0482
6	2	6	0.0578	0.4734	0.2540	-2.0816	0.0497	0.0037
7	2	7	0.0578	0.4734	0.2540	-2.0816	0.0497	0.0037
8	3	8	0.0578	0.4734	0.2540	-2.0816	0.0497	0.0037
9	3	9	0.0578	0.4734	0.2540	-2.0816	0.0497	0.0037
10	3	10	0.0066	0.0296	7.1475	-32.1989	0.0482	0.0482

Power-imbalance checker: The objective of this function is to evaluate the balance of active power within the network. This process is described in the flow chart in Figure 5.22.
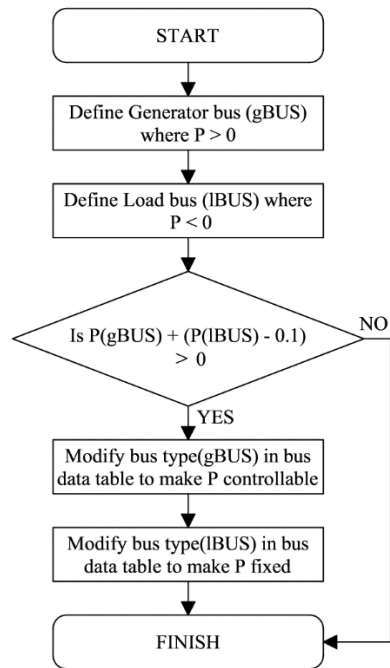
Figure 5.22 – Flow diagram of the power-imbalance checker

Assuming a VSC is absorbing active power in the network, following a fault it may no longer be able to do so. This will cause a power imbalance as the amount of generation is greater than the load. To correct the power imbalance the amount of generation must be reduced. The OPF algorithm will only reduce the active power generation at a given bus if the active power parameter at that bus is set as a controllable parameter c. This is achieved by modifying the bus type number in the bus data table.

To avoid unnecessary loss of infeed to the onshore transmission system, the buses with healthy offshore VSCs connected to them must ensure that the maximum capacity is used. To do this, the function identifies those buses which appear as a healthy load in the offshore AC hub and sets the active power parameter at that bus as fixed to the maximum. This is achieved by modifying the bus type number in the bus data table.

OPF vector constructor: The main objective of this function is to create three vectors of parameters including:

- $[x]$ is a vector of variable parameters
- $[u]$ is a vector of control parameters
- $[p]$ is a vector of fixed parameters

This process is described in the flow chart in Figure 5.23. The function first identifies the bus type parameter located in the bus data table, which may or may not have been modified according to the network state and fault present. The bus type parameter is then compared to Table 5.5 to determine which vector to insert each of the bus parameters.
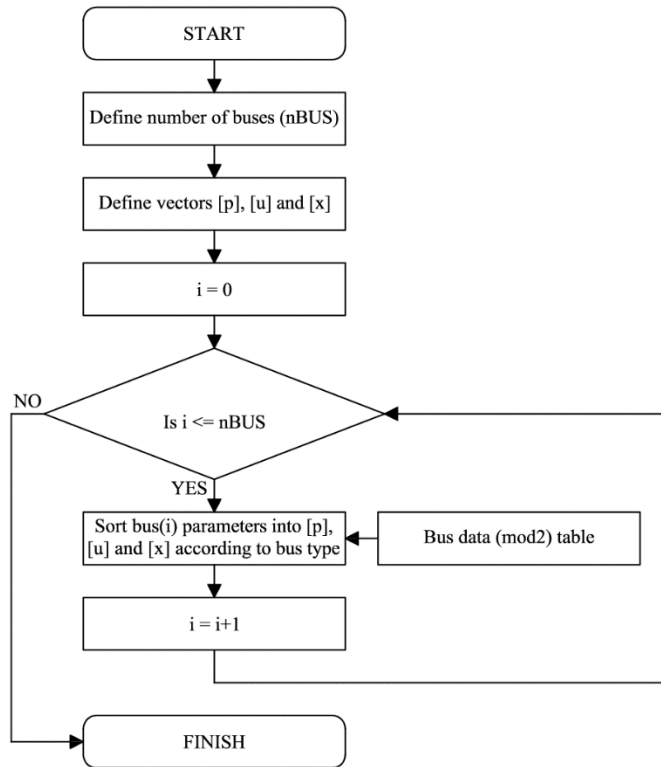
Figure 5.23 – Flow diagram of the OPF vector constructor

5.3.2.3 Optimal power flow algorithm

The post-fault operating condition is found using a classical optimal power flow (OPF) method known as the gradient method. In this application, the gradient method is an extension of the Newton-Raphson power flow method as defined in [68]. The method used is described in Appendix A. The objective of the Newton-Raphson power flow is to solve a set of non-linear power flow equations for a given network. The key information obtained from the power flow is the voltage magnitude, voltage angle and complex power generation/demand at each bus [81].

Generalised OPF formulation:

The generalised optimal power flow problem subject to equality and inequality constraints is as follows:

Objective function:

143

$$f = \sum_{i=1}^{N} P_i + \sum_{j=1}^{M} w_j \tag{5.7}$$

Subject to,

Equality constraints:

$$
\begin{aligned}
g_p &= P_i - P_{i,sch} \\
&= \sum_{n=1}^{N} |Y_{in} V_i V_n| \cos(\theta_{in} + \delta_n - \delta_i) - \left(P_{gi} - P_{di}\right) \\
&= 0
\end{aligned} \tag{5.8}
$$

$$
\begin{aligned}
g_q &= Q_i - Q_{i,sch} \\
&= -\sum_{n=1}^{N} |Y_{in} V_i V_n| \sin(\theta_{in} + \delta_n - \delta_i) - \left(Q_{gi} - Q_{di}\right) \\
&= 0
\end{aligned} \tag{5.9}
$$

Inequality constraints:

w_{iV}

$$
= \begin{cases}
K_{iV}{}^{min}\left(V_i{}^{min} - V_i\right)^2 \cdot \operatorname{sgn}\left(V_i{}^{min} - V_i\right) \le 0 \; ; & V_i < V_i{}^{min} \\
0 \; ; & V_i{}^{min} \le V_i \le V_i{}^{max} \\
K_{iV}{}^{max}(V_i - V_i{}^{max})^2 \cdot \operatorname{sgn}(V_i - V_i{}^{max}) \le 0 \; ; & V_i > V_i{}^{max}
\end{cases} \tag{5.10}
$$

W_{iIf}

$$
= \begin{cases}
K_{iIf}\left(Y_a(V_m - V_n) - I_f{}^{max}\right)^2 \cdot \operatorname{sgn}\left(I_f - I_f{}^{max}\right) \le 0 \; ; & I_f > I_f{}^{max} \\
0 \; ; & 0 \le I_f \le I_f{}^{max}
\end{cases} \tag{5.11}
$$

W_{iIt}

$$
= \begin{cases}
K_{iIt}(Y_a(V_n - V_m) - I_t{}^{max})^2 \cdot \operatorname{sgn}(I_t - I_t{}^{max}) \le 0 \; ; & I_t > I_t{}^{max} \\
0 \; ; & 0 \le I_t \le I_t{}^{max}
\end{cases} \tag{5.12}
$$

W_{iMVA}

$$
= \begin{cases}
K_{iMVA}\left(\left(P_i{}^2 + Q_i{}^2\right) - (S_i{}^{max})^2\right)^2 \cdot \operatorname{sgn}(S_i - S_i{}^{max}) \le 0 \; ; & S_i > S_i{}^{max} \\
0 \; ; & 0 \le S_i \le \; .
\end{cases} \tag{5.13}
$$

Variable limits:

$$P_{gi}{}^{min} \leq P_{gi} \leq P_{gi}{}^{max}, \ P_{gi} \in [u] \qquad (5.14)$$

$$Q_{gi}{}^{min} \leq Q_{gi} \leq Q_{gi}{}^{max}, \ Q_{gi} \in [u] \qquad (5.15)$$

And where,

$[x]$ is a vector of variable parameters

$[u]$ is a vector of control parameters

$[p]$ is a vector of fixed parameters

Applied OPF formulation:

The objective of the OPF algorithm is to find a feasible post-fault operating condition which is defined as there being no violation of constraints in the network. The objective function therefore becomes only to minimise the sum of the constraint penalties as given in (5.16).

$$f = \sum_{j=1}^{M} w_j \qquad (5.16)$$

A detailed description of the applied OPF formulation is shown in Appendix A.

5.3.2.4 Output

The output of the AC hub controller is a set of power dispatch orders for the dispatch-able offshore VSCs and FRC-WTs (This does not include the healthy VSCs which are droop controlled).

5.3.3 Test of AC hub controller algorithm

The algorithm has been tested in response to a change in network state following a DC pole-pole fault. The original network parameters for the pre-fault condition are shown in Table 5.7.

Table 5.7 - Pre-fault bus data

Bus No.	P (pu)	Q (pu)	V_{mag} (pu)	V_{ang} (°)	Bus type
1	-0.9557	-0.1020	1.0002	0.0000	4
2	-0.9557	-0.1019	0.9990	-0.1824	4
3	-0.9557	-0.1020	1.0002	0.0000	4
4	0.3750	0.0000	1.0079	10.1295	5
5	0.3750	0.0000	1.0079	10.1295	5
6	0.3750	0.0000	1.0067	9.9716	5
7	0.3750	0.0000	1.0067	9.9716	5
8	0.3750	0.0000	1.0079	10.1295	5
9	0.3750	0.0000	1.0079	10.1295	5
10	0.6667	0.0000	1.0038	0.5449	5

The DC pole-pole fault on HVDC link 1 will stop the offshore VSC at bus 1 from transferring power. This is represented by reducing the allowable active and reactive power transfer through bus 1 to zero. Table 5.8 presents the bus data from a load flow analysis following occurrence of the fault.

Table 5.8 - Bus data following occurrence of a fault

Bus No.	P (pu)	Q (pu)	V_{mag} (pu)	V_{ang} (°)	Bus type
1	0.0000	0.0000	1.0042	0.0000	5
2	-1.4311	-0.1418	0.9973	-1.1690	4
3	-1.4311	-0.1418	0.9973	-1.1842	4
4	0.3750	0.0000	1.0120	10.0475	5
5	0.3750	0.0000	1.0120	10.0475	5
6	0.3750	0.0000	1.0049	9.0209	5
7	0.3750	0.0000	1.0049	9.0209	5
8	0.3750	0.0000	1.0049	9.0050	5
9	0.3750	0.0000	1.0049	9.0050	5
10	0.6667	0.0000	1.0043	-0.0458	5

As can be seen in Table 5.8, the active and reactive power through buses 2 and 3 increases to compensate for the reduction in active and reactive power in bus 1. This results in the inequality constraints W_{2MVA} and W_{3MVA} being violated. The OPF algorithm must take action to remove the constraint violation.

In order to remove the constraint violation present at buses 2 and 3, the active power generation in the AC hub must be reduced. To achieve this, the algorithm identifies all those buses that are generating active power, which includes buses 4 – 10. The active power generation at each of the generator buses is identified as a control parameter hence $P_{g4:10}$ becomes an element of $[u]$. Once pre-configured,

the algorithm executes and produces a new table of bus data representing the post-fault operating condition with no active constraints as shown in Table 5.9.

Table 5.9 - Post-fault bus data

Bus No.	P (pu)	Q (pu)	V_{mag} (pu)	V_{ang} (°)	Bus type
1	0.0000	0.0000	1.0193	0.0000	5
2	-0.9550	-0.2934	1.0120	-0.7559	4
3	-0.9550	-0.2934	1.0119	-0.6990	4
4	0.2014	0.0000	1.0283	5.2050	2
5	0.2014	0.0000	1.0283	5.2050	2
6	0.2188	0.0000	1.0211	4.9841	2
7	0.2188	0.0000	1.0211	4.9841	2
8	0.2207	0.0000	1.0210	5.0911	2
9	0.2207	0.0000	1.0210	5.0911	2
10	0.6472	0.0000	1.0191	0.1638	2

The OPF algorithm has reduced the active power output of the wind generation at buses 4 - 9 and also the imported power at bus 10 in order to correct the power imbalance in the offshore network. In addition, the reactive power absorbed by buses 2 and 3 has increased, mainly because the active power transfer through the HVAC cables has reduced which results in less compensation from those cables. The new power references are then calculated and passed to the relevant HVDC converters and wind turbine generators.

5.3.4 Physical implementation of the centralised fault management system

The method described above requires reliable, low latency connections in order to collect bus data and communicate the triggering signals required for proper operation of the AC hub controller. In a future offshore AC hub, it is reasonable to assume that each HVDC platforms, offshore AC platform and wind turbines would be connected via a fibre optic communication medium that is integral to the electrical power cables. This ensures that the physical communication 'backbone' has low latency, i.e. capable of supporting communications over a timeframe shorter than a typical fault (<50ms). An estimation of the propagation delay of each fibre optic link in the offshore AC hub is shown in Figure 5.24. The speed of light in optical fibre is approximately 70 % of the speed of light in air, due to refraction of light in glass (i.e. a refractive index of 1.468) [98].
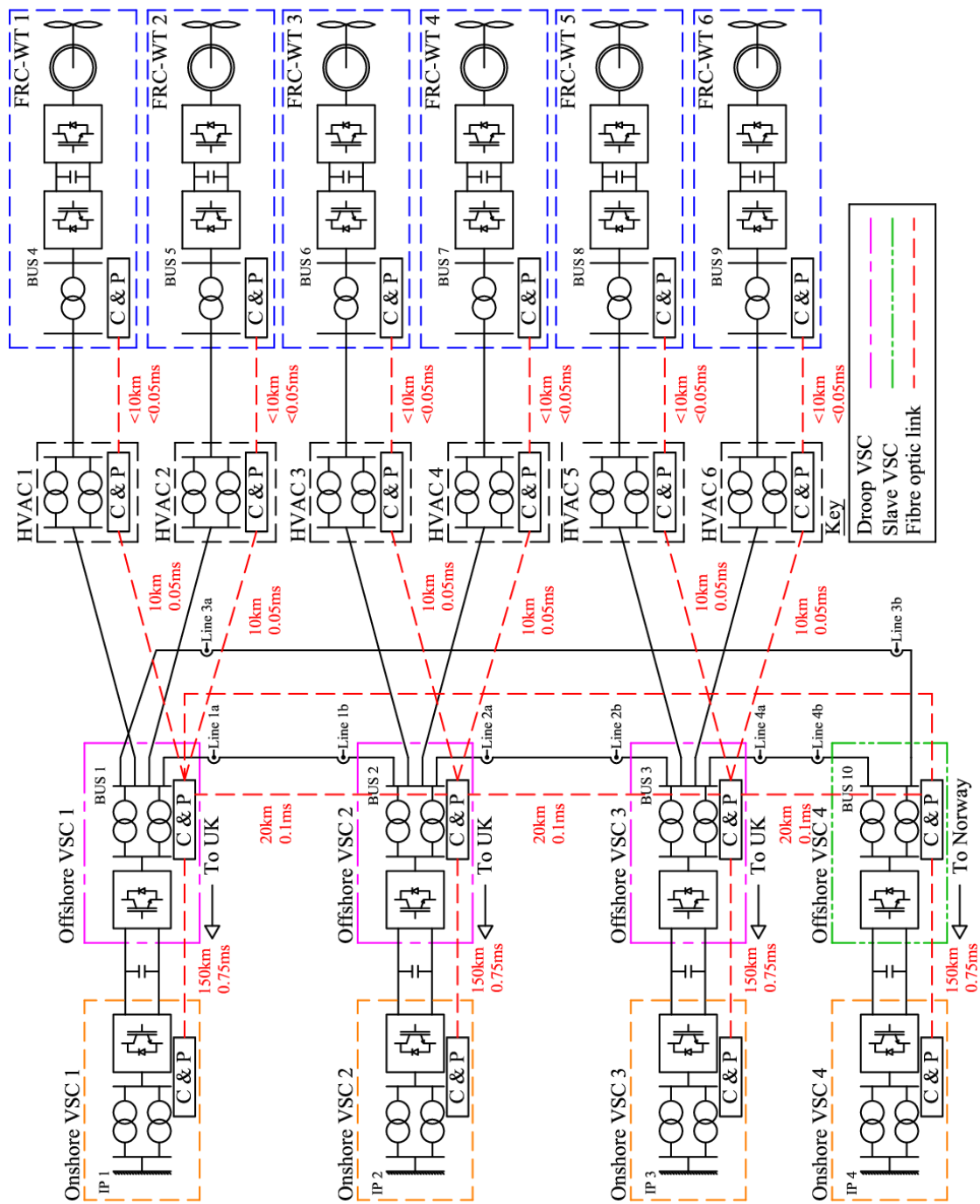
Figure 5.24 – Fibre optic links in the offshore AC hub including distance and propagation delay

Typically, fibre optic communications are implemented over secure digital hierarchy (SDH) networks for protection and control purposes [98]. One common example from present-day offshore HVDC platforms is in differential protection, where a dedicated fibre is used to allow two relays to communicate over a long distance [54].

IEC 61850 is implemented in more modern substations. IEC 61850 is an international standard which covers digital communications within the substation [76]. As part of IEC 61850, a protocol known as GOOSE (Generic Object Oriented Substation Events) is specified. The GOOSE protocol spans the process bus which provides for communication between Intelligent Electronic Devices (IEDs) i.e. relays, and the station bus which communicates across the whole substation and is concerned with the SCADA system. The GOOSE protocol is implemented over a high speed Ethernet network. The GOOSE protocol specifies that packets must be communicated within 4 ms. The GOOSE protocol also allows for communication between substations which are geographically remote, again achieved over SDH fibre networks. This lends itself to the offshore AC hub which will consist of multiple offshore substations [76].

It is likely that redundant AC hub controllers will be present to guard against a single point of failure. However, only one AC hub controller should be operational in the AC hub network at any one time and so appropriate failover algorithms would need to be implemented to ensure a smooth transition between controllers.

5.4 Comparison of centralised and de-centralised fault management systems

To compare the performance of the de-centralised and centralised fault management systems described in 5.2 and 5.3, two fault scenarios are applied to the offshore AC hub (the bus bar fault is omitted as it has similar fault characteristics to the cable fault). The fault scenarios include:

- A DC pole to pole fault on one of the HVDC links connected to the UK MITS.
- A 3-phase fault occurring on one of the HVAC cables which interconnect two adjacent HVDC platforms.

Failure to maintain voltage, frequency and complex power to nominal levels for a short time period is permissible, provided the following conditions are met:

- The maximum withstand levels of all equipment are not exceeded.

- The duration a given parameter differs from its nominal operating range is not sufficient to damage any equipment.

- The system returns to an acceptable operating condition following clearance of the fault.

- The fault does not affect the onshore MITS beyond the limits stipulated by the SQSS standard.

5.4.1 DC pole-pole fault

A DC pole-pole fault is applied to HVDC link 1 of the AC hub model to study the implications on the AC hub and MITS. At $t = 0.1$ s, a DC pole-pole fault is applied at the midpoint of the cable of HVDC link 1. After 1 ms, the VSC equivalent cell capacitors are isolated, the equivalent arm voltage sources are isolated and the diodes are inserted to simulate blocking of the IGBTs in the on and offshore VSCs. The AC CBs open after approximately 60 ms to isolate the faulted HVDC link from the MITS and the offshore AC hub.

As shown in Figure 5.25, the DC link voltage of VSC1 drops rapidly. The voltage across the healthy HVDC links in both systems increases but remains below the upper DC voltage limit of 1.1 pu. However, for the de-centralised method the DC choppers were not used. This shows that the de-centralised system is able to manage the DC voltage during the fault. The centralised method cannot respond to the rise in DC voltage during the fault. Therefore, DC choppers must still be relied upon during the fault.
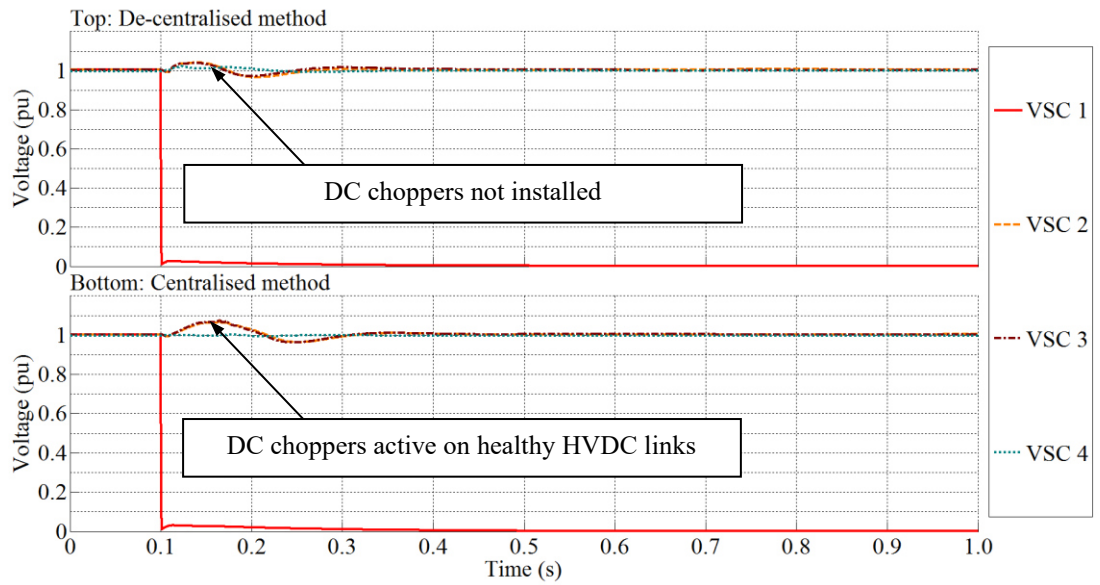
Figure 5.25 - Voltage across each HVDC link following a DC pole-pole fault

Figure 5.26 shows the voltage magnitude at the HVAC buses throughout the AC hub. In both cases the voltage magnitude across all buses drops initially on occurrence of the fault. However, the magnitude only drops to approximately 0.85 pu. The maximum voltage in both cases is slightly higher than the upper voltage limit at 1.12 pu. The voltages return to a steady-state condition once the fault is cleared.
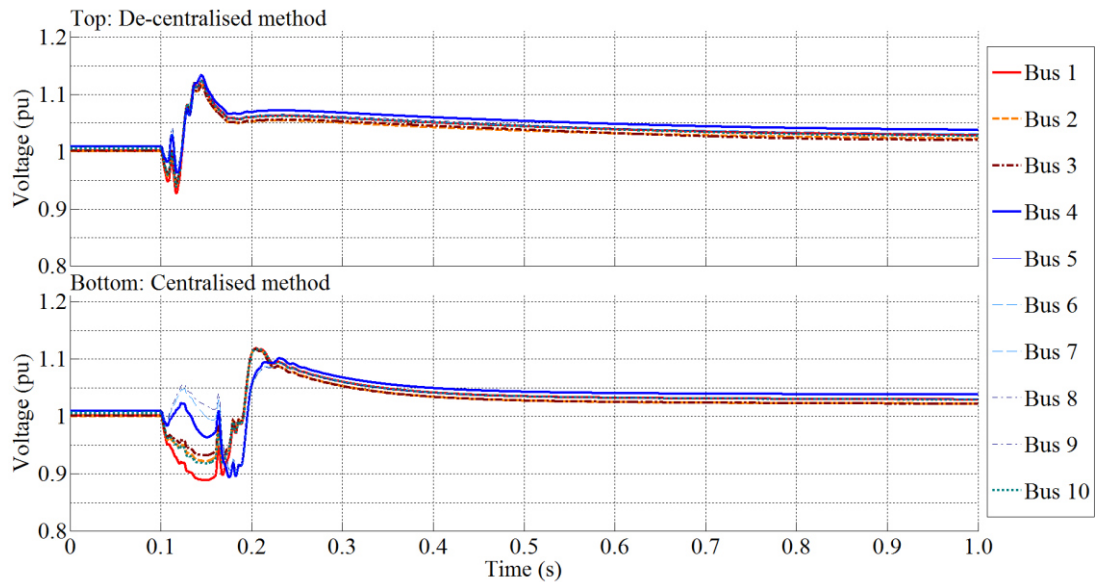
Figure 5.26 - Voltage magnitude at each offshore HVAC bus following a DC pole-pole fault

Figure 5.27 shows the current flowing through the offshore VSCs. The fault current fed through the faulted offshore VSC bus (bus 1) is 1.5 pu when using the

de-centralised system and 2.6 pu when using the centralised system. In addition, when using the de-centralised system, the maximum current through the healthy VSC buses (2, 3 & 4) remains below the converter current upper limit of 1.1 pu both during and after the fault. When using the centralised system, the maximum current through the healthy VSC buses is 1.5 pu during the fault but returns below the upper limit once new orders are dispatched.
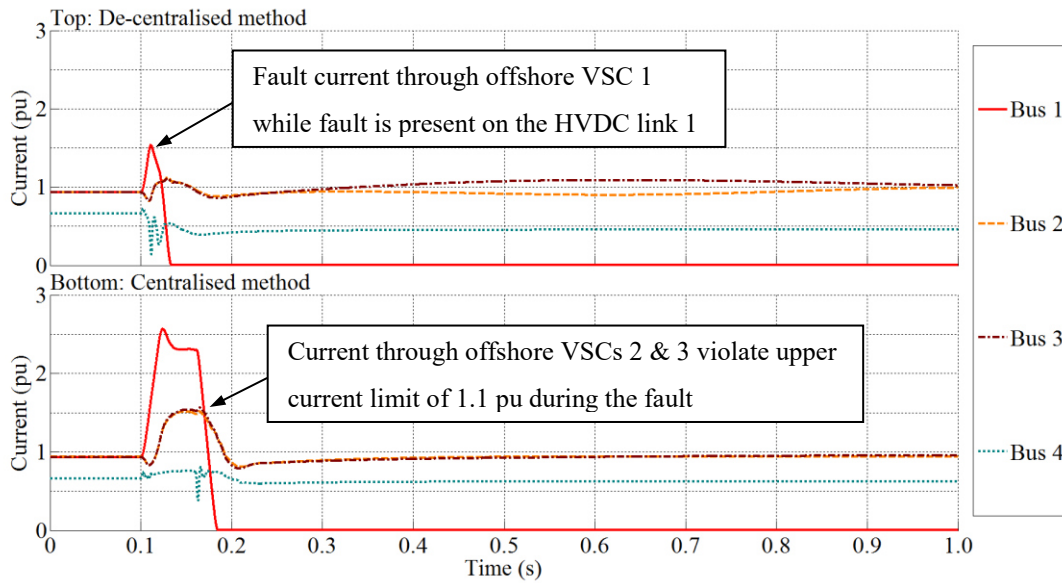
Figure 5.27 – Current through each offshore VSC following a DC pole-pole fault

Figure 5.28 shows the active power generated at the WT buses. When using the de-centralised system, the operation of the power reduction controllers during the fault is clearly apparent as the active power produced by the FRC-WTs reduces before the fault is cleared at $t = 4.16$ s. The active power produced by the FRC-WTs remains roughly constant during the fault but reduces once new dispatch orders are received.
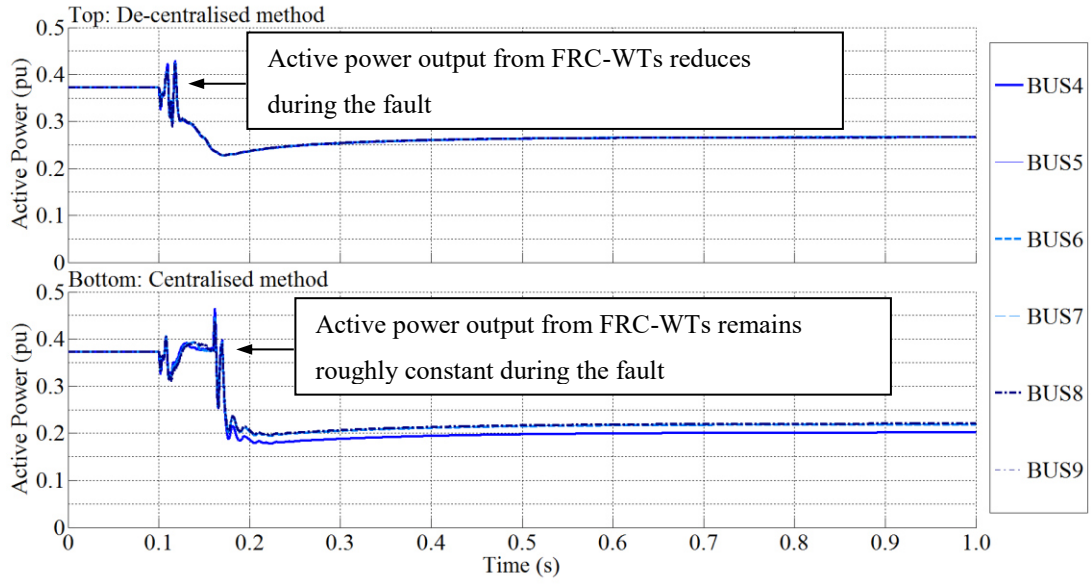
Figure 5.28 – Active power through each FRC-WT bus following a DC pole-pole fault

Figure 5.29 shows the re-active power generated at the WT buses. In both cases, the reactive power output increases for a period then decreases for a period before returning to zero. When comparing the two results it can be seen that the period for which the re-active power deviates from zero is much less when using the de-centralised system.
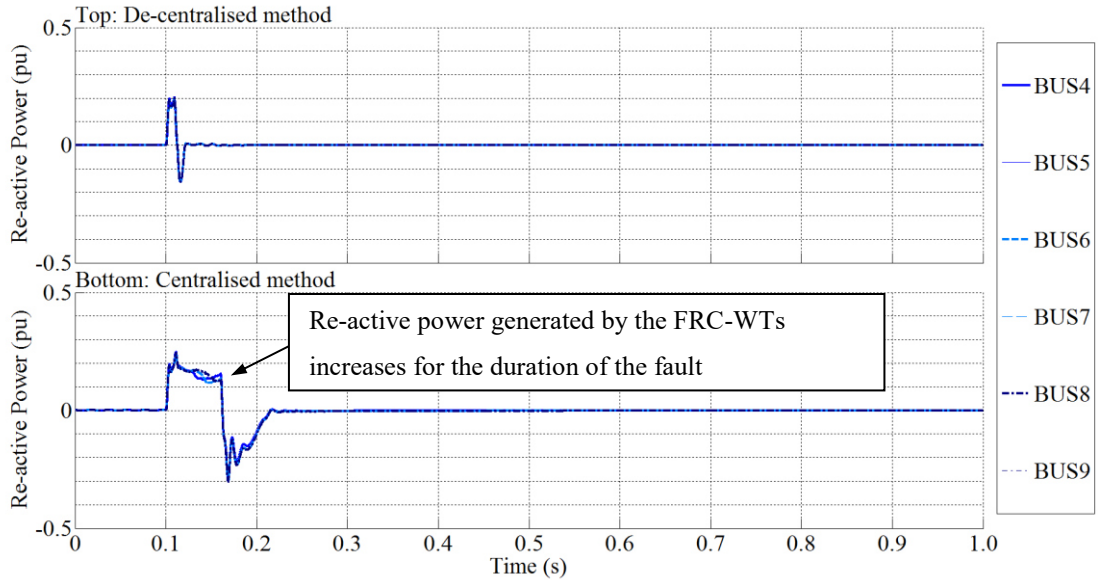
Figure 5.29 –Re-active power through each FRC-WT bus following a DC pole-pole fault

When using the centralised system, the increased active and re-active power contribution from the FRC-WTs during the fault explains why there is a

significantly higher fault current through VSC 1 compared to when using the de-centralised system, as was shown in Figure 5.27.
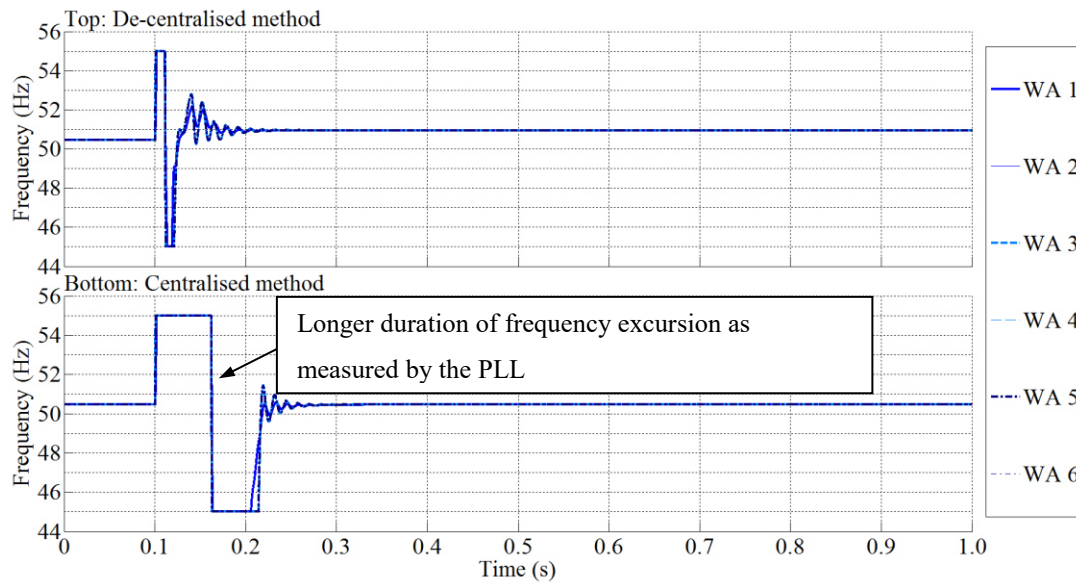
Figure 5.30 – Frequency at each FRC-WT bus following a DC pole-pole fault

Figure 5.30 shows the frequency as measured by the PLL at each WT bus. A swing in the measured frequency is observed, although again, as was the case with the re-active power, the duration of the swing is considerably larger when using the centralised system. This change in frequency is a result of the PLL losing a lock on the phase as it changes during the fault.

It is apparent that the centralised system is not able to perform as well as the de-centralised system because no action is taken throughout the duration of the fault. The power reduction applied during the fault by the de-centralised system prevents the healthy VSCs being overloaded. It also enables the PLLs located at the FRC-WT buses to regain phase lock in a shorter period.

5.4.2   3ph fault on an offshore HVAC cable

At $t = 0.1$ s, a 3ph fault is applied at the midpoint of line 2. The fault impedance was assumed to be effectively zero ($Z_f = 1$ mΩ) to give the worst case scenario. At $t = 0.16$ s the AC CBs open to isolate the faulted cable circuit. Figure 5.31 shows the voltage magnitude at the AC buses throughout the AC hub.

154
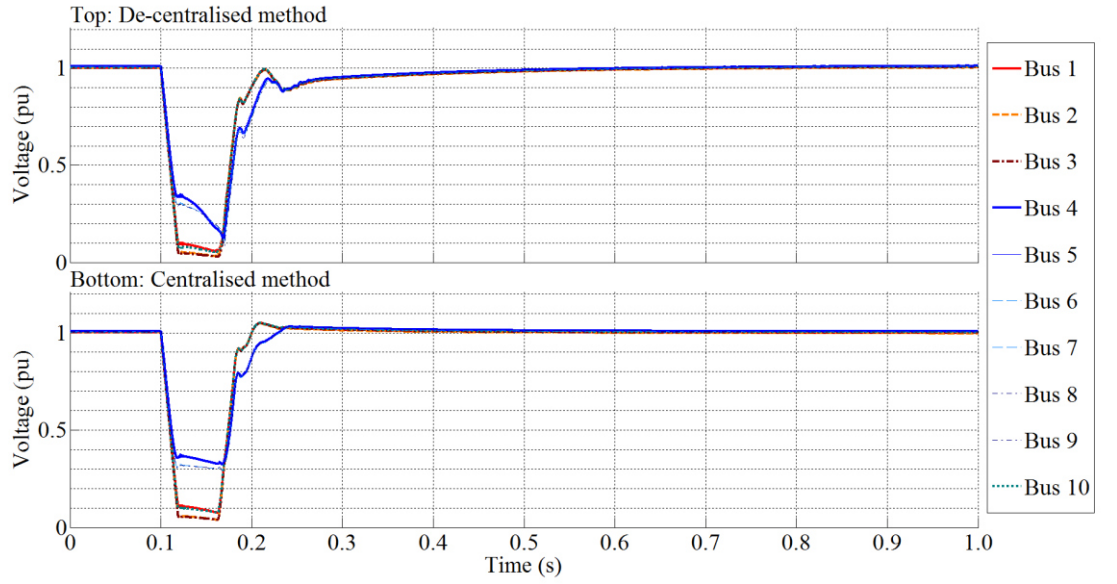
Figure 5.31 – Voltage magnitude at each offshore HVAC bus following a 3ph cable fault

In both cases, the voltage magnitude drops below 0.5 pu on occurrence of the fault, before recovering to nominal levels once the AC CBs are opened and the fault is isolated. The results of both cases differ to that presented in Chapter 4 as the voltage magnitude does not exceed the upper voltage limit of 1.1 pu.

Figure 5.32 presents the active power flowing through each offshore VSC bus. It can be seen that when using the de-centralised method, the active power generated at bus 10 reduces significantly once the faulted line is isolated. In addition, the active power absorbed at buses 1,2 and 3 reduces to approximately 0.25 pu. When using the centralised system, the active power through the offshore VSC buses returns to the pre-fault amount once the faulted line is isolated.
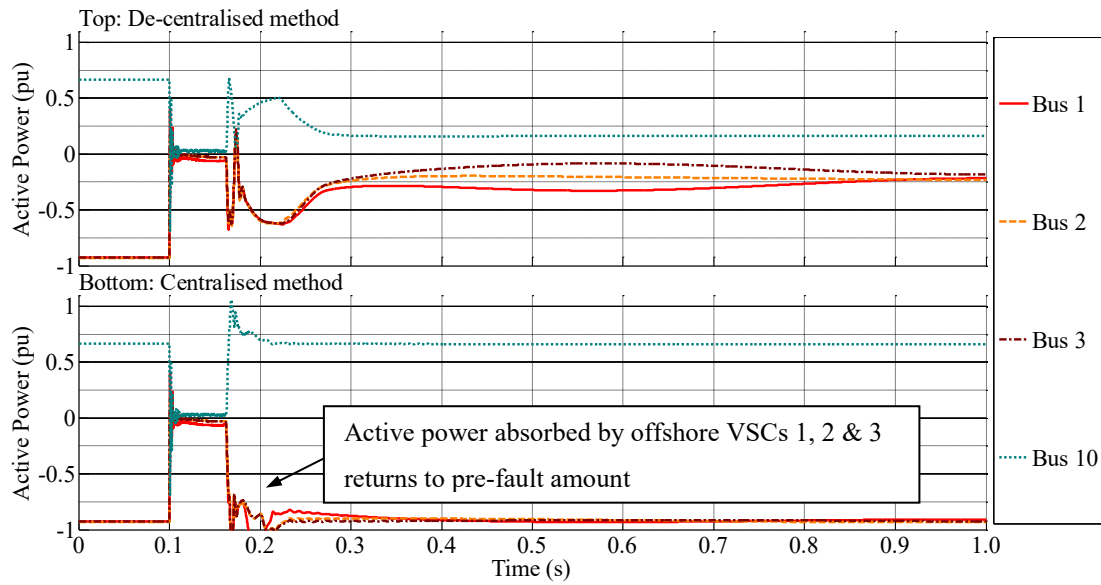
Figure 5.32 – Active power through each offshore VSC bus following a 3ph cable fault

The reduction of active power absorbed by offshore VSCs 1, 2 and 3 is explained by the change in active power generated at the FRC-WT buses, as shown in Figure 5.33. When using the de-centralised system, the post-fault generation reduces to 0.1 pu. When using the centralised system, the post-fault generation returns to the pre-fault amount, that being 0.375 pu.
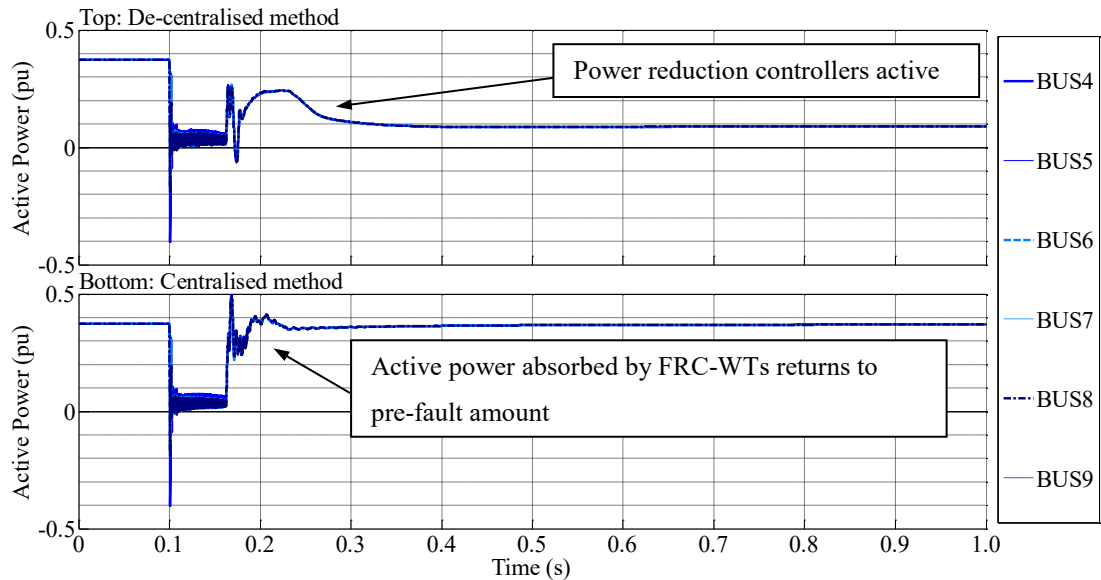
Figure 5.33 - Active power through each FRC-WT bus following a 3ph cable fault

Therefore, if less power is being generated by the FRC-WTs and VSC 4 (connected to bus 10), then the droop controlled VSCs (connected to buses 1, 2

156

and 3) will export less power to the MITS. This is confirmed in Figure 5.34 where it can be seen that less active power is exported at the onshore IPs.
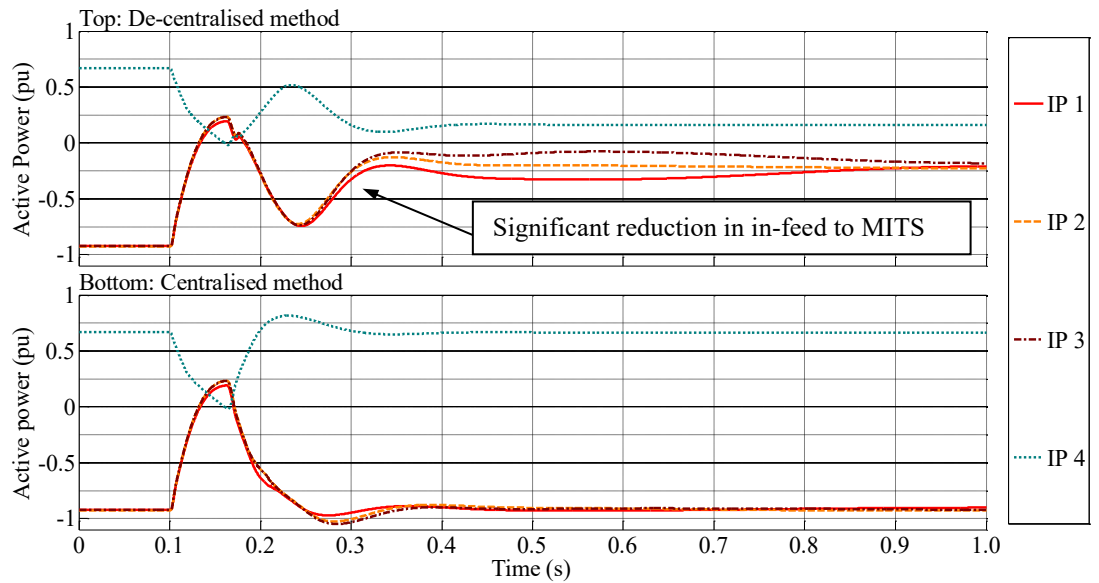
Figure 5.34 - Active power through each onshore interface point following a 3ph cable fault

The reason for the reduction in power output from the FRC-WTs and VSC 4 is the operation of the power reduction controllers. Figure 5.35 shows the frequency produced by each offshore VSC. During the fault, the frequency at VSC 1, 2 and 3 reduces to the nominal frequency. This is expected as the active power absorbed reduces during the fault. After the faulted line is isolated, when using the de-centralised system, a large increase in the frequency produced by VSC 1, 2 and 3 is observed. This suggests that the frequency modulation controllers are operating.

157
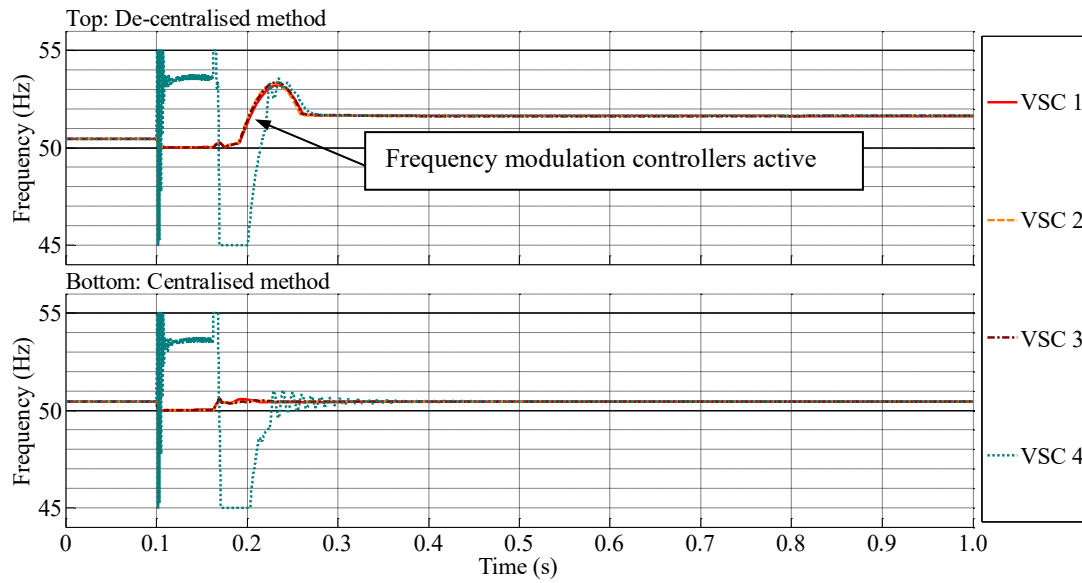
Figure 5.35 – Frequency at each offshore VSC bus following a 3ph cable fault

Figure 5.36 shows the DC link voltages as measured at each offshore VSC. The action of the frequency modulation controllers is justified as the DC link voltage at VSC 1, 2 and 3 can be seen to rise above the nominal DC voltage level immediately after the faulted line is isolated by the AC breakers. The DC voltage returns to the nominal DC voltage level however, the integral component of the frequency modulation controller is increased. The output of the integrator remains non-zero for the remainder of the test which explains the increased steady-state frequency observed in Figure 5.35.
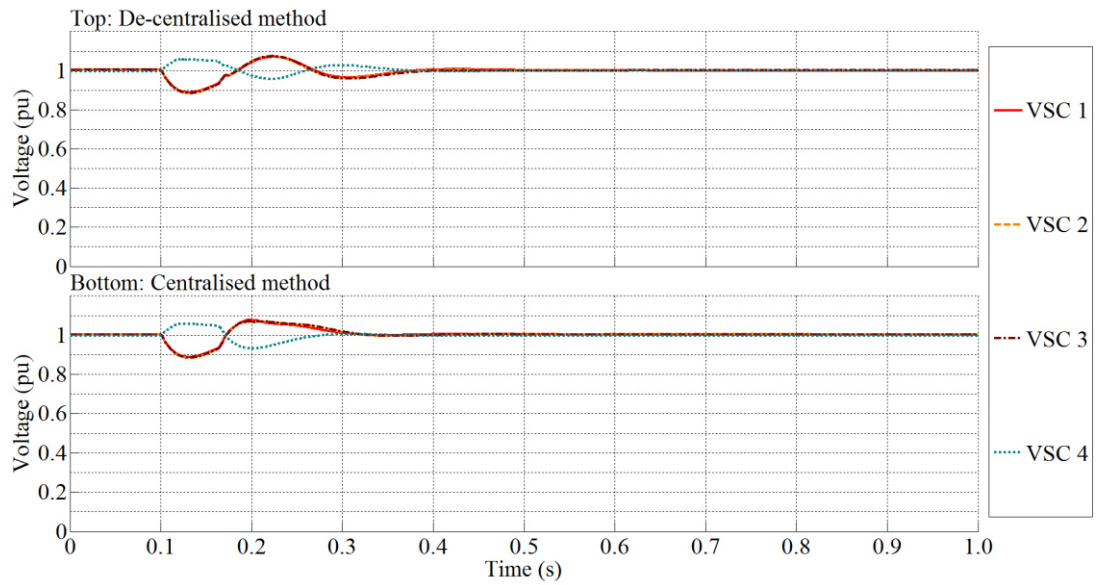
Figure 5.36 – Voltage across each HVDC link following a 3ph cable fault

The test is re-run but with the integral gain K_{fi} of the frequency modulation controllers set to zero. Figure 5.37 shows the active power flowing through the offshore VSC buses. As can be seen the active power returns to the pre-fault condition once the faulted line has been isolated, albeit more slowly compared to when using the centralised controller.
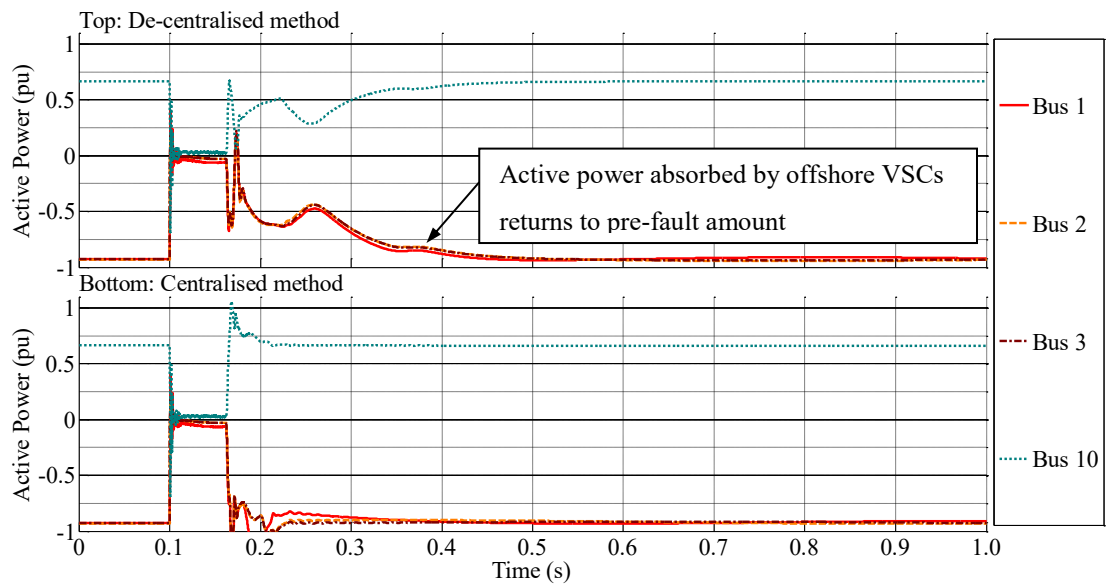
Figure 5.37 - Active power through each offshore VSC bus following a 3ph cable fault with no integral component in frequency modulation controllers

Figure 5.38 shows the frequency produced by each offshore VSC. The frequency produced by VSC 1, 2 and 3 increases once the faulted line is isolated but returns

159

to the nominal frequency after that. This suggests the frequency modulation controllers are operating to manage the excess DC voltage.
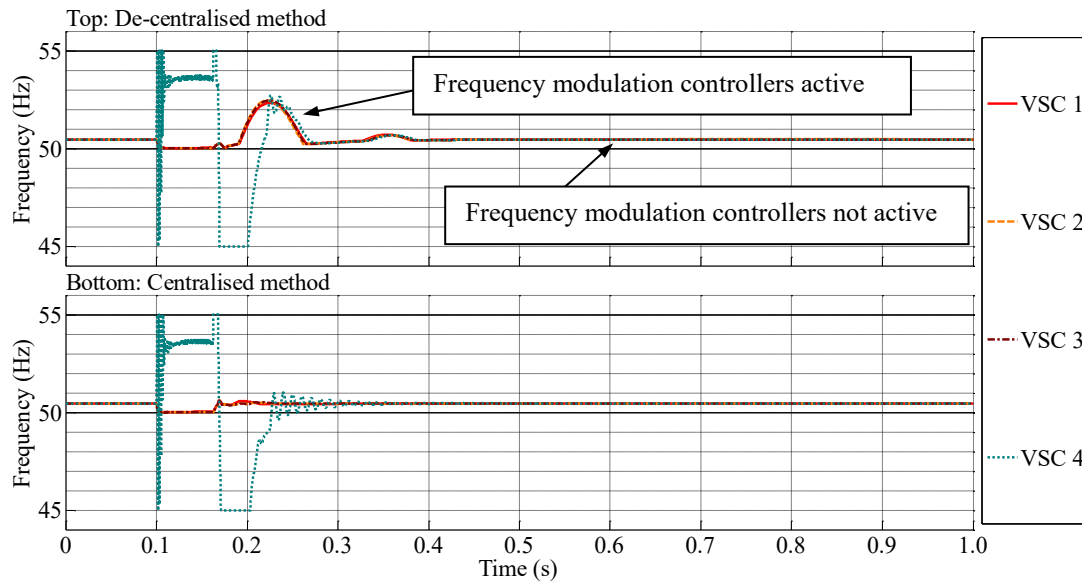
Figure 5.38 – Frequency at each offshore VSC bus following a 3ph cable fault with no integral component in frequency modulation controllers

5.4.3 Discussion of results

It is important to note that a 3ph fault on a HVAC cable was not simulated in [62]. Nonetheless, it is a fault which could occur and therefore the system must be able to cope with such a fault should it arise.

The difference between the DC pole-pole fault and the 3ph HVAC cable fault is that a power imbalance exists only for the DC fault. The faulted cable offshore does not cause a permanent power imbalance.

The de-centralised method is shown to work effectively in the event of a DC pole-pole fault, which corrects power imbalance. However, during a fault when no power imbalance is present, the de-centralised system actually exacerbates the problem. This suggests that the de-centralised system requires some form of selectivity to ensure that it only operates to correct power imbalance in the network and prevent over-voltage in the HVDC links.

The centralised method has access to much more information about the network state. Therefore, it can act in an appropriate way to ensure that the network remains in a feasible operating condition post-fault with minimal loss of infeed to

160

the MITS. The main drawback of the centralised scheme is that it cannot act during the fault to prevent excessive fault currents. Therefore DC choppers are still required to operate to maintain the DC link voltage. However, it is likely that DC choppers would still be installed using the de-centralised method in case the local frequency modulation controller fails.

The ideal system would incorporate elements of both schemes. The de-centralised controllers could act quickly to correct any power imbalance. The centralised system could act to ensure the post-fault condition does not violate constraints and provide some form of selectivity to the de-centralised method i.e. restrain operation when there is no power imbalance present.

6 Chapter 6 – Experimental validation of control systems for managing faults in an offshore AC hub

6.1 Introduction

This chapter presents the validation of the AC hub controller developed in Chapter 5 using an experimental test setup consisting of a Real Time Digital Simulator (RTDS) and a real time platform applied in a hardware-in-the-loop configuration. The AC hub model developed in Chapters 3 & 4 was implemented on the RTDS. The centralised fault management system called the AC hub controller was implemented on the real time platform which is a dSPACE DS1103 unit. Analogue and digital signals are used to exchange data between the RTDS and dSPACE unit. A DC pole-pole fault is applied to HVDC link 1 of the offshore AC hub model and the simulation and experimental results are compared.

6.2 Hardware in the loop configuration

Figure 6.1 shows the hardware in the loop configuration.
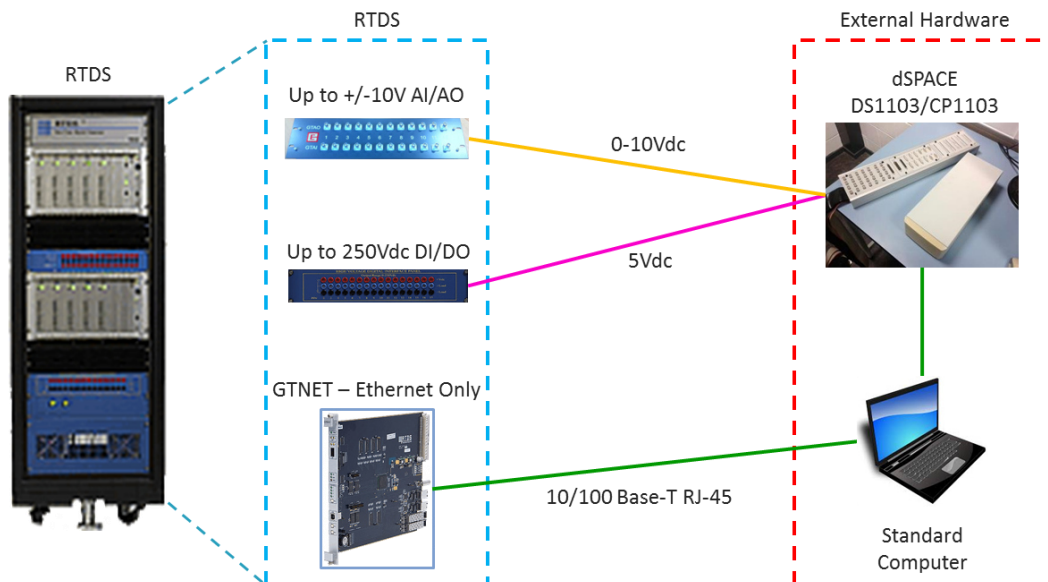
Figure 6.1 – Hardware in the loop configuration

6.2.1 Using the Real Time Digital Simulator for validation of the AC hub controller

The Real Time Digital Simulator (RTDS), as shown in Figure 6.2, is a power system simulator which can perform electromagnetic transient simulations in real time [99]. The RTDS is able to achieve real-time operation using a high speed digital architecture while maintaining a small time step, usually 50 µs. Nodal analysis is performed at each time-step to determine the network state using Dommel's solution algorithm as described in [100].
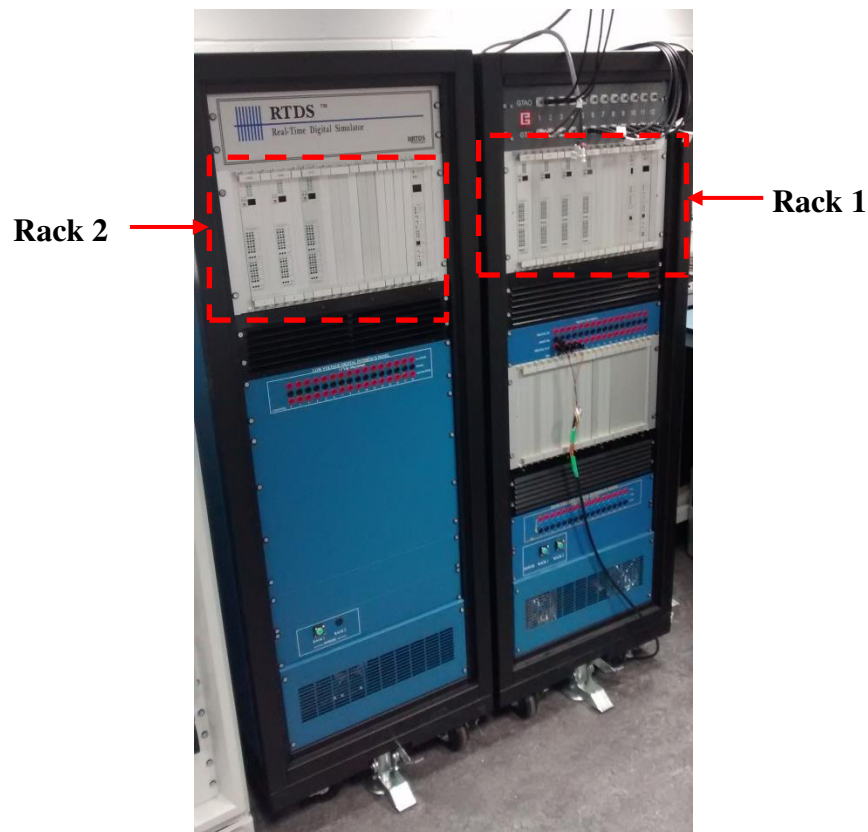
Figure 6.2 – Two rack RTDS connected in point-point configuration

A model was designed, implemented and analysed on the RTDS using a graphical user interface called RSCAD©. In this chapter, the implementation of the AC hub model developed in Chapters 3 & 4 on the RTDS using RSCAD is presented. Due to the number of nodes present in the AC hub model, the model was implemented across two RTDS racks as highlighted in Figure 6.2.

Table 6.1 provides an overview of the cards used in a RTDS rack.

Table 6.1 – Overview of the cards used in the RTDS

RTDS Component	Description
GPC card	Giga-processor card: Used to solve the equations representing the power system and control system components which are modelled on the RTDS.
PB5 card	PB5 processor card: An updated version of the GPC card. It is more powerful and allows for twice as many nodes when present in a rack when compared to a GPC card.
GTNET	GTNET Network interface card: Used to interface various network protocols with RTDS simulator (GSE, SV, DNP3, PMU).
GTWIF	GTWIF Workstation interface card: Used to interface with a user's computer workstation running the RSCAD software. It also performs synchronisation with other racks and communicates between other cards and racks. There is one GTWIF card per rack.

Rack 1 consists of one PB5 processor card, three GPC processor cards, a GTNET card and a GTWIF card. Rack 2 consists of two PB5 cards, one GPC card and a GTWIF card. The processor cards perform the high speed computations necessary for real-time operation. The PB5 card is a more recent upgrade of the GPC card which allows for more nodes on a given power system solution. The GTNET card is a card specifically designed for interfacing with the RTDS using industry standard communication protocols such as DNP3. The GTWIF card provides for an interface between the RTDS and the host computer workstation. It also manages communications between the other cards on a rack and allows for point-point connection between two racks.

To allow for hardware in the loop testing, Analogue Input/Output (AI/AO) cards are located within each RTDS cabinet. Interface panels which are connected to the AI/AO cards are located on the front of the RTDS to allow for straightforward access. These were used to connect to the dSPACE unit which provides a platform for the AC hub controller algorithm.

6.2.2 Using the dSPACE unit for validation of the AC hub controller

The dSPACE DS1103 real time computer, as shown in Figure 6.3 was used in the experimental set up. This real time computer is used by industry as a rapid prototyping platform. The DS1103 is capable of real-time operation and has enough input/output channels for the application in hand.

CP1103 interface board

DS1103 real-time computer

Figure 6.3 – dSPACE real time computer and input/output board

The DS1103 has a separate input/output board called a CP1103 board to allow for straightforward access to input/output channels. The CP1103 is shown in Figure 6.3.

The DS1103 is fully programmable from the Matlab command line or from the Simulink environment. Real-time applications running on the dSPACE DS1103 are interfaced directly with Matlab, therefore data acquisition and control actions can be performed in real-time. In addition, algorithms written in Matlab script can be downloaded, providing they are embeddable in C code. The AC hub controller developed in Simulink was implemented directly on to the DS1103 as a real-time or as-fast-as-possible application. Note that the DS1103 will run as fast as possible, as opposed to real time, when the execution of the downloaded script cannot be completed in a single time step.

Once the real-time application is loaded on to the DS1103, it is managed from a software program called ControlDesk®. ControlDesk provides an environment from which to load and operate the real-time applications. It also provides an environment from which to visualise data in real-time [101].

6.2.3 Hardware interfaces

As described in Chapter 5, the AC hub controller requires the following communication interfaces:

- **Ethernet** – This is required for the SCADA interface which is used for updating the pre-fault network state. The SCADA interface to the RTDS is provided by the GTNET card. A standard PC is used to interface with the GTNET card.

- **Digital Input/Output** – This is required to signal that a fault is present in the offshore AC hub. The GTFPI board on the RTDS is used to provide 5 V (OUTPUT 'HIGH') signals which are interfaced directly with digital inputs on the CP1103 board. A 4-bit word is used to relay the fault code which indicates the fault type and location.

- **Analogue Input/Output** – This is required to communicate the post-fault dispatch orders from the AC hub controller to the RTDS. The CP1103 board is used to output 0-10 V analogue signals to the GTAO/GTAI front panel interface board on the RTDS. The signals are sampled and held at the instant the AC hub controller provides an output. They are then scaled to per-unit to provide references for the FRC-WTs and offshore VSCs.

6.2.4 Software interfaces

Figure 6.4 shows the software architecture of the hardware-in-the-loop configuration.

166
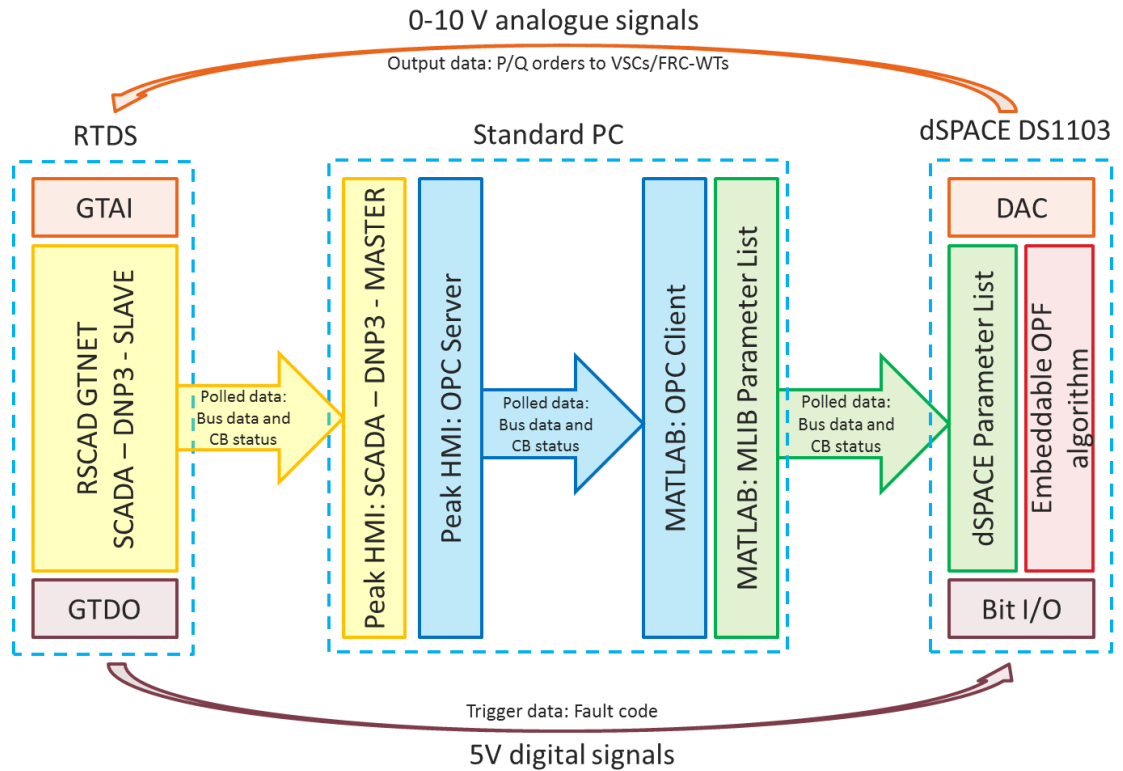
Figure 6.4 – Diagram of the software interfaces between the RTDS and dSPACE equipment
The AC hub controller requires that the bus and line data be continually updated for the OPF algorithm to function effectively.

The SCADA system is implemented using DNP3 (Distributed Network Protocol), which was developed specifically for data acquisition and control in in the electric utility industry [102]. The GTNET card located in rack 1 of the RTDS is set up with DNP3 firmware and is designated as a DNP3 slave device. Communication is made via Ethernet to the host workstation. A software package called PeakHMI is used to act as the DNP3 master device.

To transfer data from PeakHMI to the dSPACE unit the data must first be published using the OPC (OLE for Process Control) standard. OPC is an open source standard for the secure and reliable exchange of data between devices from different vendors [103]. PeakHMI is designated as an OPC server and publishes the data to any OPC clients that are connected.

The data published by the OPC server is input in to Matlab using the OPC toolbox. The OPC toolbox allows data to be read, written and logged from

devices configured as OPC servers [104]. A script is run which configures Matlab as an OPC client and continually reads the data published by the OPC server.

Once the data is present in Matlab it must be written to the real-time application running on the dSPACE board. This is achieved using an interface library called MLIB, which is one of the dSPACE control libraries installed on Matlab. The data is continually written to the real-time application as it becomes available on the OPC server.

6.3   Implementation of offshore AC hub model on RSCAD

The AC hub model developed in SimPowerSystems was implemented on the RTDS. The AC hub model implemented on the RTDS would ideally be an exact representation of the model implemented on SimPowerSystems. However, certain constraints are present which prevent an exact replication of the SimPowerSystems model on the RTDS. The main constraint was the available hardware resource in the RTDS, which determines the maximum number of nodes.

The model was drafted in RSCAD using components from the pre-installed component libraries. Components are split up in to two groups: *power system components* and *control components*. If a required component is not present in the pre-installed libraries then it is possible for a user to construct and implement new components using the component builder tool.

The component builder tool was used extensively to create new control components. The component builder tool includes a facility to import models from Simulink. This requires that the Simulink model is first compiled into a C code. The Simulink Coder toolbox was used to do this. The inner and outer control loops defined in Chapter 4 were implemented using the component builder tool, an example of which are those used in the offshore VSC control loops, as shown in Figure 6.5.
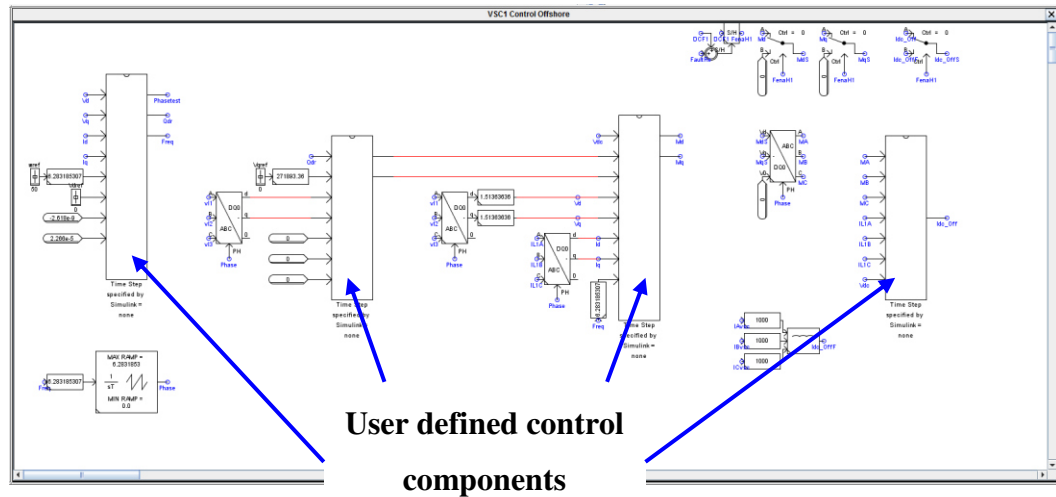
Figure 6.5 – RTDS user components implemented within offshore VSC control

The point of interconnection between power system components is referred to as a node. A branch is a passive element such as a resistor, inductor, capacitor or some combination thereof which connects two nodes [99]. Figure 6.6 shows the interconnection of two three phase transformers (power system components) via a nominal pi-section (branch), with the six nodes highlighted.
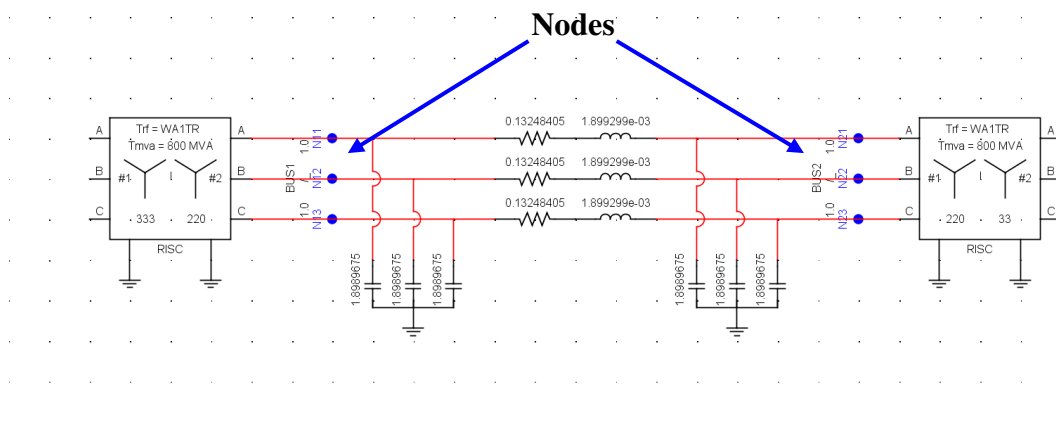
Figure 6.6 – Interconnection and node placement example using RSCAD

A subsystem is defined as a network configuration including power system components, branches and nodes, whose mathematical solution is solved independently. It may only represent a portion of the power system but can be linked to another subsystem using travelling wave transmission lines. The maximum number of nodes per subsystem when a rack contains a PB5 processor card is 144 (older GPC processor cards allow for only 66 nodes per subsystem). Each rack consists of at least one PB5 processor card and therefore up to 144 nodes may be present on each rack [99].

6.3.1 Modification to representation of inter-platform cables

Due to the nodal requirements of the AC hub model it was partitioned in to two subsystems, with one subsystem per rack. Figure 6.7 shows how the AC hub model was implemented across two racks.
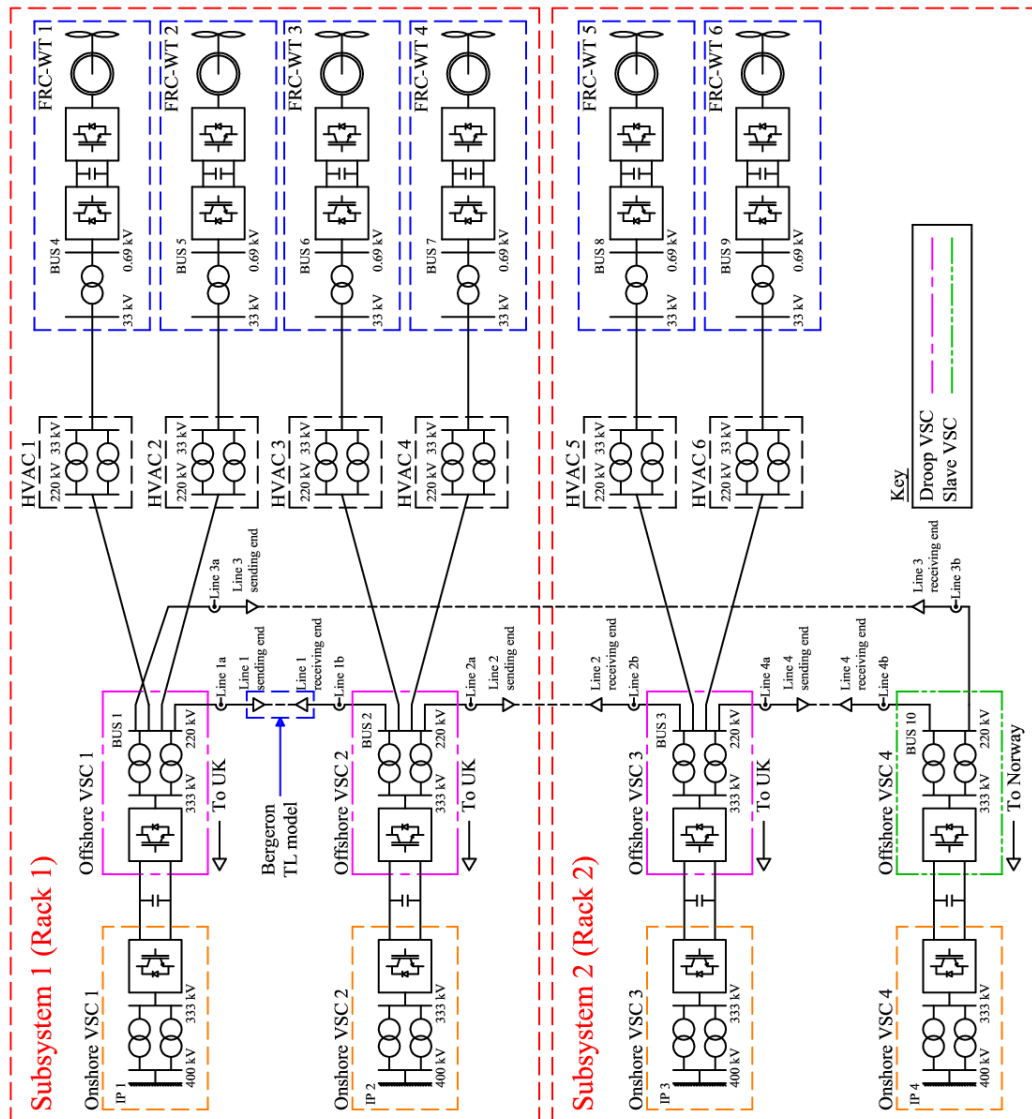
Figure 6.7 – Partitioning of the AC hub model on the RTDS

As can be seen, the two racks are interconnected using travelling wave transmission line models. These transmission lines coincide with the inter-platform HVAC cables, which are modelled in SimPowerSystems using equivalent pi-sections. Equivalent pi-section models are not travelling wave based models and so a Bergeron model is used instead. Basic RLC data is required for

the Bergeron model. The cable data defined in Chapter 3 is adapted accordingly and is listed in Table 6.2.

Table 6.2 – HVAC platform-platform cable data for modelling in RSCAD

Description	Value	Units
Design Frequency	50	Hz
Line Length	20	km
Positive sequence series resistance	0.013	Ω/km
Positive sequence series inductive reactance	0.060	Ω/km
Positive sequence shunt capacitive reactance	0.008	MΩ*km
Zero sequence series resistance	0.053	Ω/km
Zero sequence series inductive reactance	0.239	Ω/km
Zero sequence shunt capacitive reactance	0.034	MΩ*km

6.3.2 Modification to reduce required number of nodes

Following examination of the AC hub model for implementation on the RTDS, it became clear that the maximum number of nodes would be exceeded should an exact replication of the SimPowerSystems model be implemented. To reduce the number of nodes, the VSC averaged model is modified.

The original model used in the SimPowerSystems model used 13 nodes. Figure 6.8 shows the VSC averaged model which uses just 9 nodes. As there are 8 VSCs present in the AC hub (not including FRCs), the total saving in use of nodes is 32, which is significant.
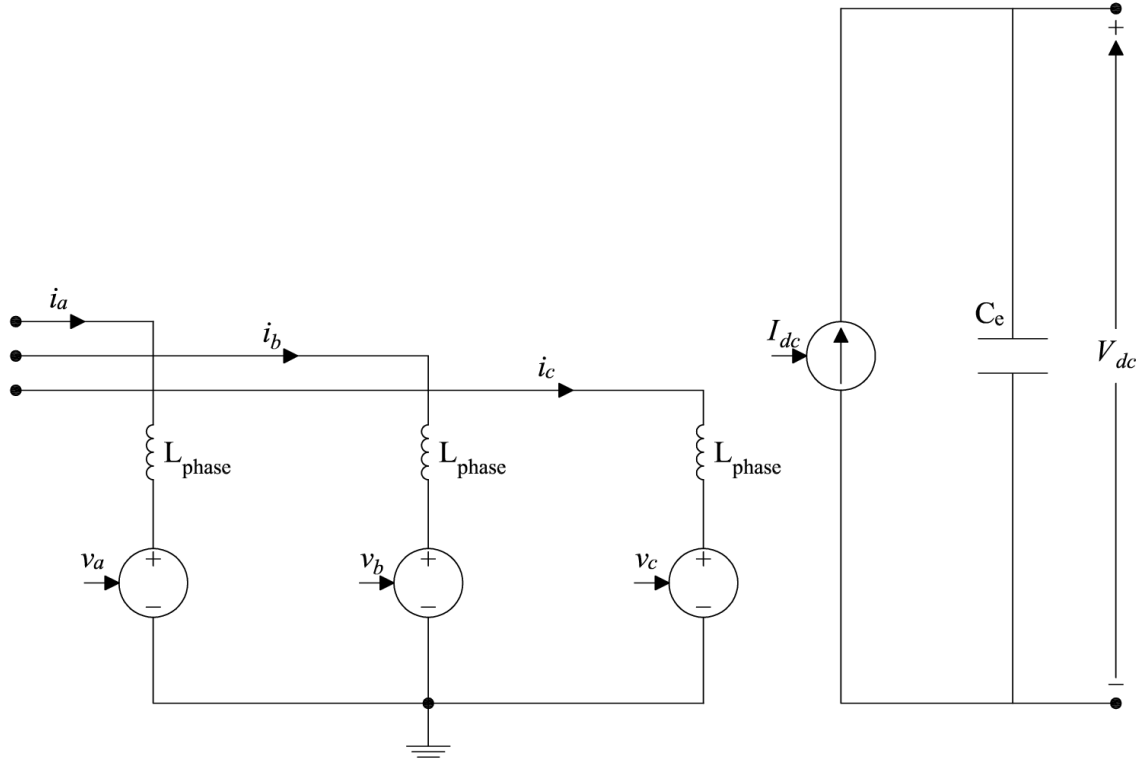
Figure 6.8 – Simplified averaged VSC model implemented on the RTDS

The reduced node model shown in Figure 6.8 omits some detail that was contained in the original model. The most significant change in detail is that now the inductors appear as phase inductors, rather than arm inductors. A suitable phase inductance must be applied which represents the original arm inductance. In Chapter 3, an equivalent impedance Z_{EQ} is calculated to limit the peak fault current in the event of a DC pole-pole fault to 10 kA.

$$Z_{EQ} = Z_{grid} + Z_{tx} + \frac{3Z_{arm}}{4} \qquad (6.1)$$

The equivalent impedance includes the sum of the grid impedance, the transformer impedance and the arm impedance. It is assumed that the fault current flows through 4 parallel arms with 4 arm reactors for 3 phases, as not all diodes are conducting at any one instant. However, given the circuit presented in Figure 6.8, it is assumed that the fault current flows through the phase legs impeded only by the phase inductance. Therefore, assuming that:

$$Z_{phase} = \frac{3Z_{arm}}{4} \qquad (6.2)$$

To achieve the same equivalent impedance it is assumed that:

$$Z_{phase} = Z_{EQ} - Z_{grid} - Z_{tx}$$

In normal operation, an equivalent current source on the DC side represents the combined current flowing through each phase leg. During a fault, the VSC acts as an uncontrolled diode bridge. Therefore, when a fault occurs, the dc current in the event of a fault I_{dcf} is determined according to a full wave rectifier block from the RSCAD component library. The component uses (6.3) to determine I_{dcf} from the AC currents.

$$I_{dcf} = \max(abs(i_{af}), abs(i_{bf}), abs(i_{cf})) \qquad (6.3)$$

During the fault, the equivalent voltage sources are set equal to zero. The phase inductance used in the on and offshore VSCs is shown in Table 6.3.

Table 6.3 – Phase inductance values for the on and off-shore VSCs

Parameters		Inductance (mH)
Symbol	Description	
L_{ph_onsh}	Onshore VSC phase reactor	93.7
L_{ph_offsh}	Offshore VSC phase reactor	84.4

6.4 Implementation of the OPF algorithm on dSPACE and interface with the RTDS:

The AC hub controller developed in Simulink was implemented directly on to the DS1103 as a real-time (or as-fast-as-possible) application. The AC hub controller itself is an algorithm written in Matlab script. The script was implemented in Simulink using a number of user defined function blocks.

To enable the AC hub controller to be run on the DS1103, all code specified in the user-defined function blocks must be embeddable in C code. The Matlab Coder toolbox was used to embed the functions into C. The Simulink model was then built in to a target file and downloaded on to the DS1103.

The OPF algorithm is triggered by the occurrence of a non-zero on any of the fault status digital inputs. The inputs are then read and a fault code is produced. The fault code is then used to pre-configure the OPF algorithm. Once the algorithm is pre-configured, the OPF is run. Once completed, new dispatch orders appear at the analogue outputs.

The time taken for the algorithm to run is not directly known as it depends on the particular fault and network configuration. A number of tests were run to identify the OPF algorithm execution times on the dSPACE computer. Figure 6.9 summarises the time taken for new dispatch orders to appear at the analogue outputs of the CP1103 board following different code sequences applied at the digital inputs.
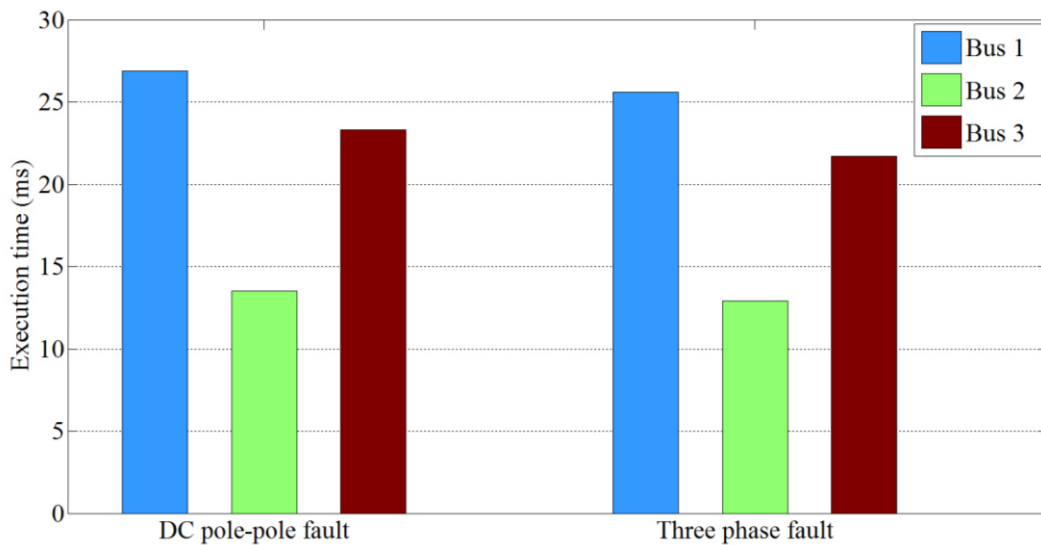
Figure 6.9 - OPF execution times with varying location and fault type

As can be seen from Figure 6.9, there is a correlation between the execution time and the location of the fault. The algorithm is able to provide a new set of dispatch orders following faults affecting bus 2 more quickly than those affecting buses 1 and 3. This can be attributed to the network configuration. Should a fault occur which forces the active and reactive power through bus 2 to reduce to zero, then the active and reactive power must be re-distributed between bus 1 and 3. As the network configuration is symmetrical about bus 2, the impedance alone will act to share complex power between the healthy offshore VSCs. The OPF

174

algorithm will then be left with less active constraints to remove and thus a solution can be found with fewer iterations and thus is produced more quickly.

The analogue outputs are read by the OPF algorithm after a pre-determined delay following occurrence of the fault. The delay is assumed as 70 ms which is 10 ms after the fault is cleared. This is considered a feasible time for the signals to be communicated to the FRC-WTs and offshore VSCs based on the analysis presented in Chapter 2.

6.5 Experimental results

A DC pole-pole fault is applied to HVDC link 1 of the AC hub model to study the implications on the AC hub and MITS. At $t = 0.1$ s, a DC pole-pole fault is applied at the midpoint of the cable of HVDC link 1. The AC CBs open after approximately 60 ms to isolate the faulted HVDC link from the MITS and the offshore AC hub.

As shown in Figure 6.10, the DC link voltage of VSC1 drops rapidly. The voltage across the healthy HVDC links in both systems increases but remains below the upper DC voltage limit of 1.1 pu. The result from the RTDS shows the DC voltage of HVDC links 2 & 3 remain above the nominal voltage level for 200 ms after the occurrence of the fault. However, the result from SimPowerSystems shows the DC voltage of HVDC links 2 & 3 remains above the nominal voltage level for just 120 ms after the occurrence of the fault. As the control system on both systems is identical, this would suggest that more energy is present in HVDC links 2 & 3 from the RTDS result.
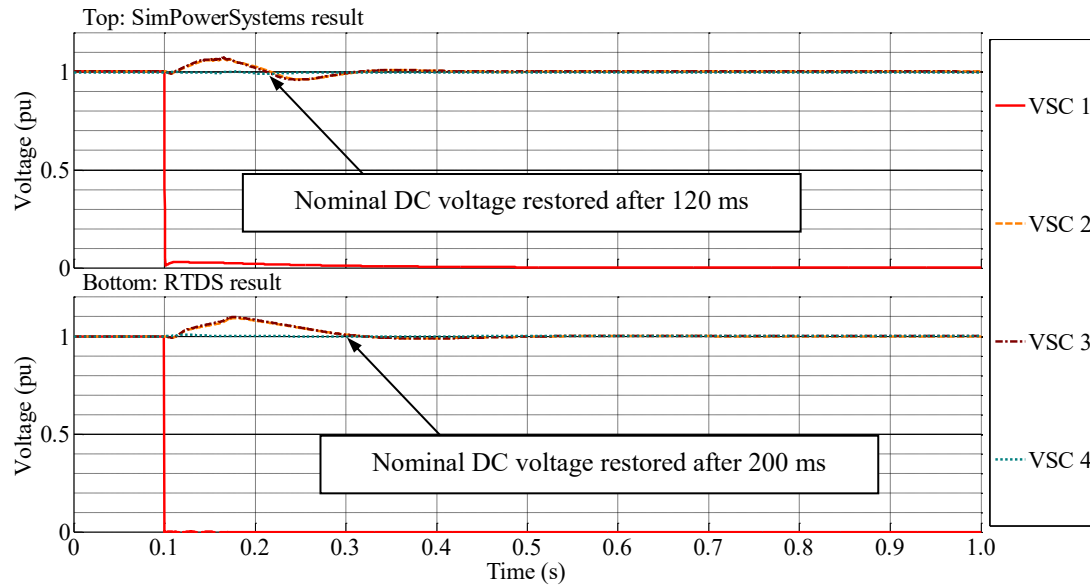
Figure 6.10 - Voltage across each HVDC link following a DC pole-pole fault

Figure 6.11 shows the voltage magnitude at the HVAC buses throughout the AC hub. The maximum voltage observed from the RTDS result is 1.35 pu, which is significantly higher than the maximum of 1.12 pu observed from the SimPowerSystems result. It is possible that a voltage of 1.35 pu will cause surge arresters to conduct. If surge arresters were present on the system and did conduct, the result would differ significantly to that presented due to the non-linear response of the surge arrester. The voltages return to a steady-state condition once the fault is cleared.
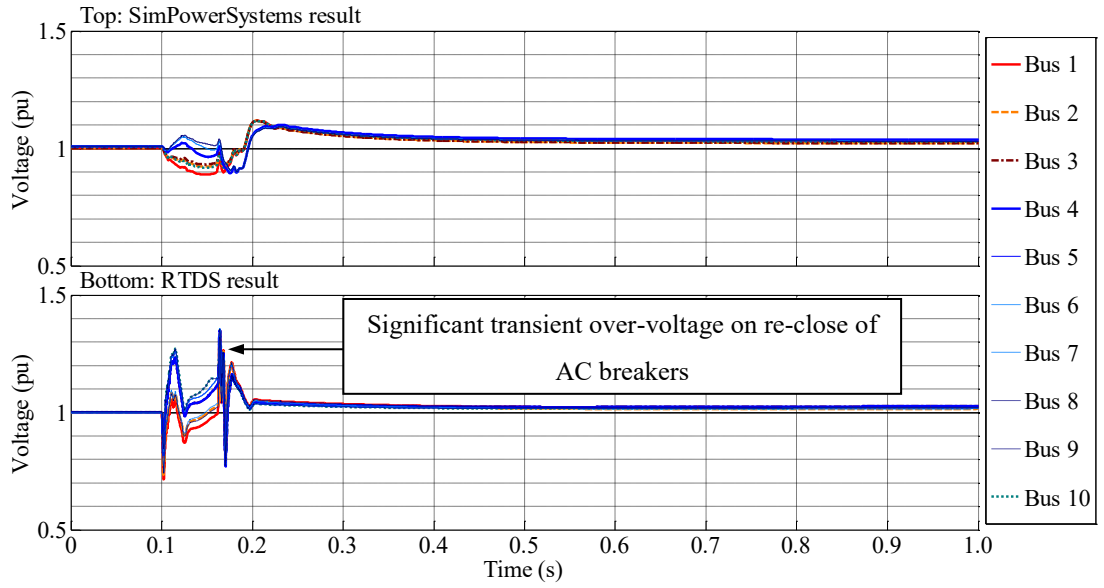
Figure 6.11 - Voltage magnitude at each offshore HVAC bus following a DC pole-pole fault

Figure 6.12 shows the current flowing through the offshore VSCs. The SimPowerSystems result shows the maximum fault current magnitude fed through the faulted offshore VSC bus (bus 1) is 2.6 pu. The RTDS result shows the maximum fault current magnitude fed through the faulted offshore VSC bus (bus 1) is 3.9 pu.
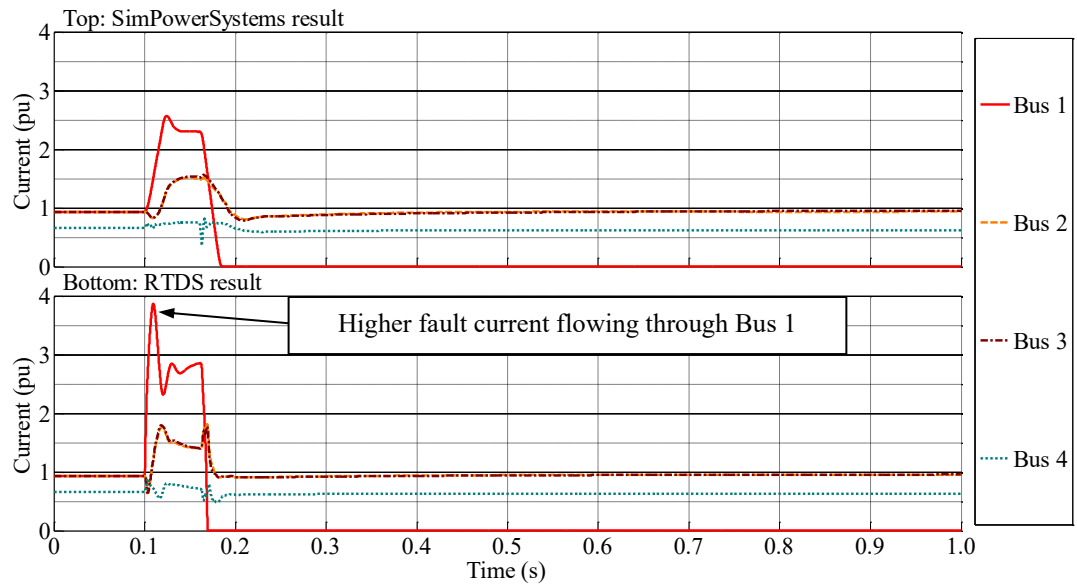
Figure 6.12 - Current through each offshore VSC following a DC pole-pole fault

The current magnitude through offshore VSCs 2 & 3 is similar in both results, albeit that the maximum current magnitude is exceeded during the fault. In steady-state, both systems are seen to have a similar response.

Figure 6.13 shows the active power flowing through the offshore VSC buses. The results are comparable from both systems. The only significant difference between the two is a transient change in active power immediately after the fault, as highlighted.
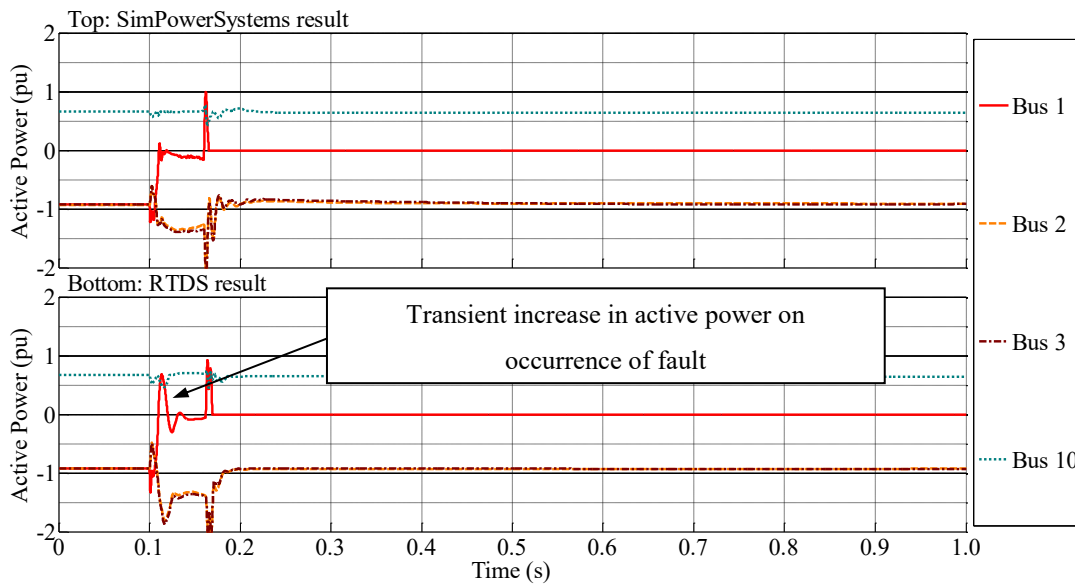
Figure 6.13 - Active power through each offshore VSC bus following a DC pole-pole fault

Figure 6.14 shows the re-active power flowing through the offshore VSC buses. The maximum re-active power absorbed at the faulted bus (1) from the SimPowerSystems result is 3 pu. The maximum re-active power absorbed at the faulted bus (1) from the RTDS result is 4 pu. This explains why the current magnitude through offshore VSC 1 is greater in the RTDS result. The reactive power through the non-faulted buses (2, 3 & 4) during the fault is similar in both systems. Therefore, the increased reactive power absorbed through bus 1 is not generated at buses 2, 3 & 4. Other sources in the offshore AC hub must be providing the reactive power generation. The steady-state reactive power through the offshore VSC buses is similar in both results.
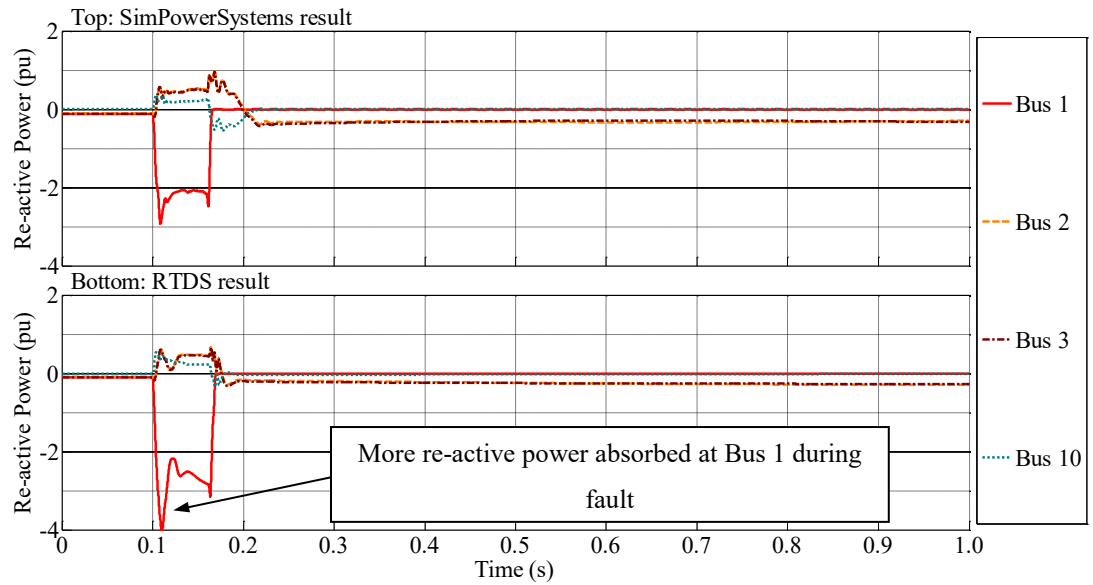
Figure 6.14 – Re-active power through each offshore VSC bus following a DC pole-pole fault

Figure 6.15 shows the active power through the FRC-WT buses. Again the results are comparable from both systems. The only significant difference between the two is a transient change in active power immediately after the fault, as highlighted.
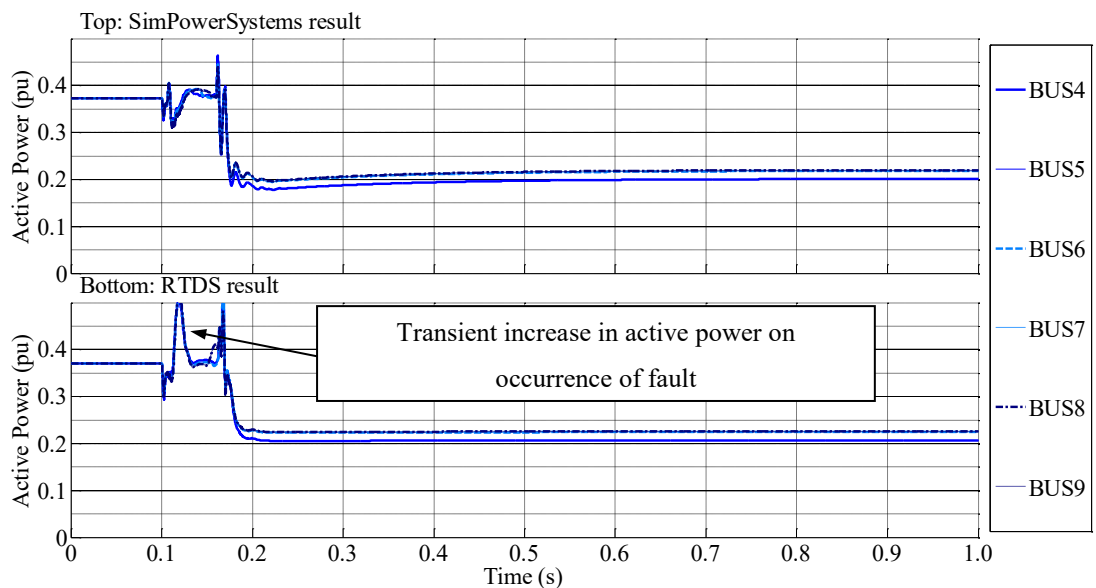
Figure 6.15 - Active power through each FRC-WT bus following a DC pole-pole fault

Figure 6.16 shows the re-active power through the FRC-WT buses. The maximum re-active power injected at the FRC-WT buses from the SimPowerSystems result is 2.5 pu. The maximum re-active power injected at the

FRC-WT buses from the RTDS result is 4 pu. Therefore, regarding the RTDS results, it can be seen that the additional re-active power absorbed by the faulted offshore VSC is provided by the FRC-WTs. The steady-state reactive power through the offshore VSC buses is similar in both results.
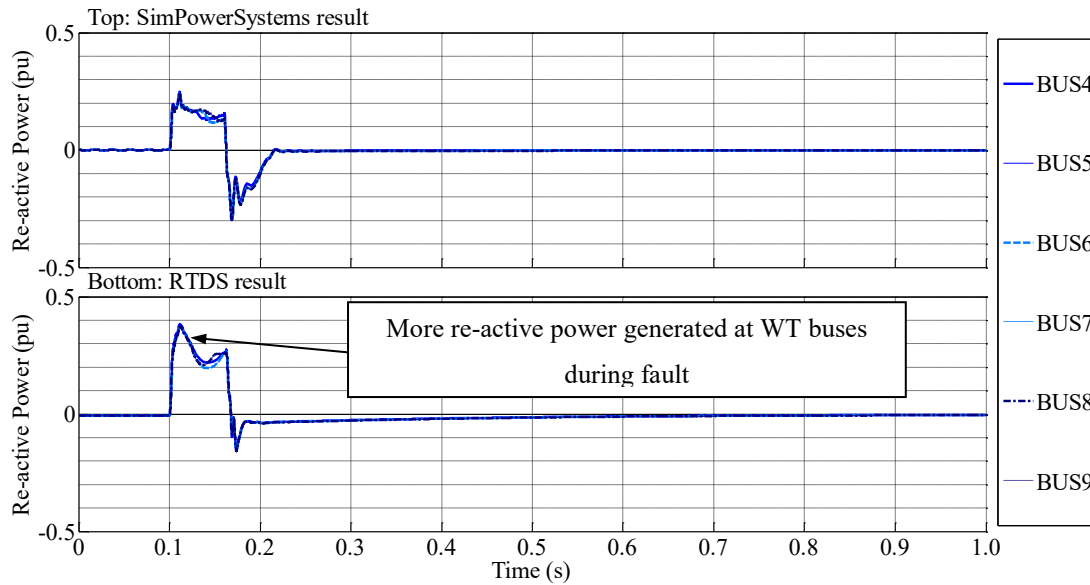
Figure 6.16 – Re-active power through each FRC-WT bus following a DC pole-pole fault

Figure 6.17 shows the active power delivered to the MITS at the IP of each HVDC link. The dynamics seen in both results are the same. The active power through IP1 oscillates during the fault before dropping to zero once the AC breakers are opened. The active power delivered to the MITS by the healthy VSCs connected to IP 2 & 3 increases during the fault before returning to the pre-fault condition. This is desirable as it helps to reduce the loss of infeed to the MITS.
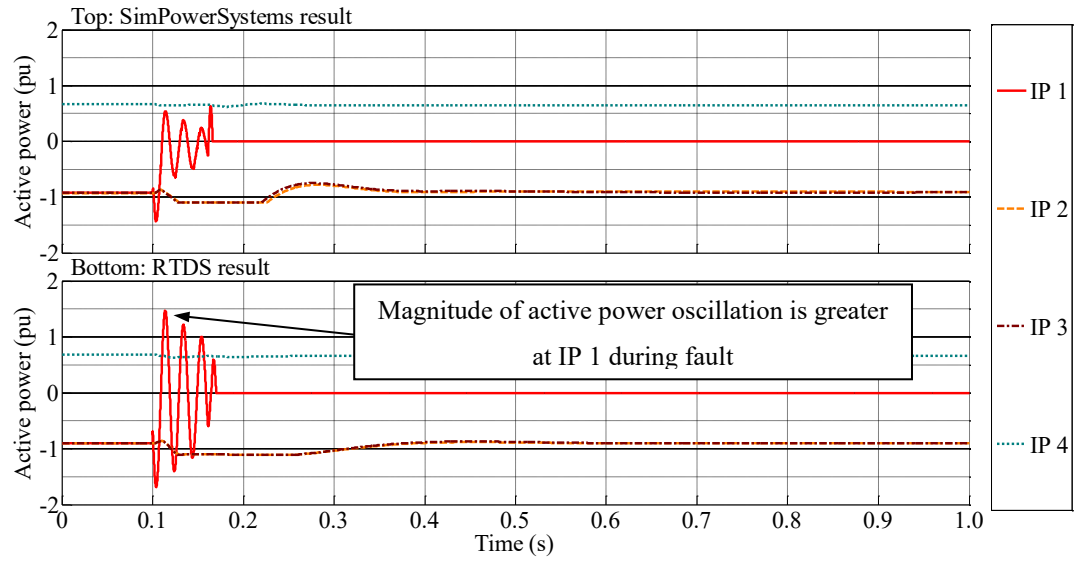
Figure 6.17 - Active power through each onshore interface point following a DC pole-pole fault

The difference in magnitude of the active power oscillation of onshore VSC 1 (the faulted HVDC link) seen in Figure 6.17 is explained when looking at the three-phase current, as shown in Figure 6.18. The peak current through the faulted onshore VSC (1) from the SimPowerSystems result is 7.5 kA. The peak current magnitude through the faulted onshore VSC (1) from the RTDS result is 10 kA.
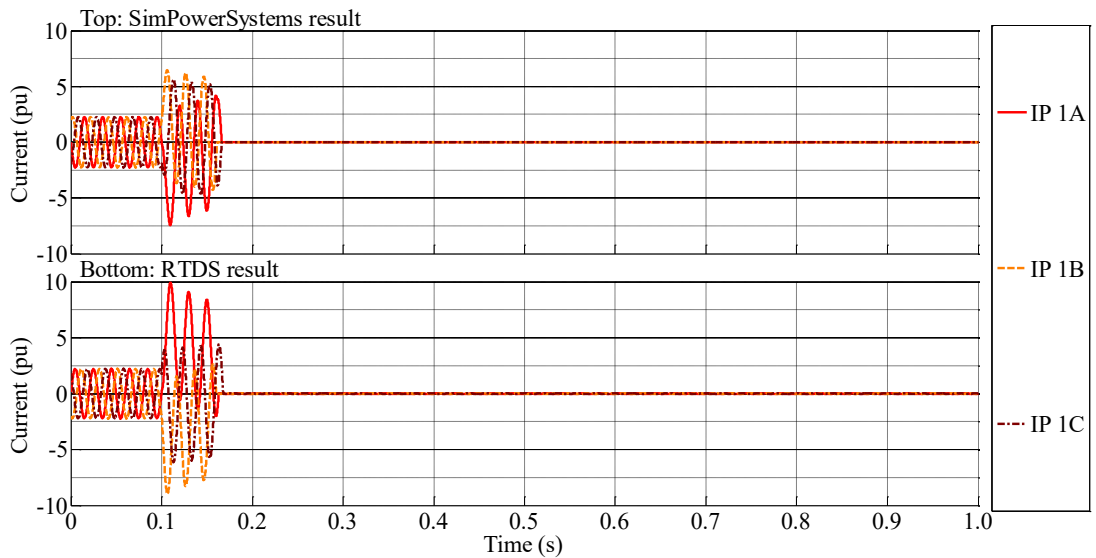
Figure 6.18 – Fault current measured at onshore IP 1 (Faulted HVDC link)

6.5.1 Discussion of results

It is apparent that the current flowing through both the on and offshore VSCs of the faulted HVDC link is greater in the RTDS result than the SimPowerSystems result. In fact, the peak current magnitude through the faulted onshore VSC (1) from the RTDS result of 10 kA is equal to the maximum design current of the VSC as discussed in Chapter 3. Therefore, the peak current magnitude observed in the SimPowerSystems result is less than expected.

In the design phase, the peak current magnitude was determined as:

$$I_{acfpm} = 2\sqrt{2}\,\frac{V_{ac}}{Z_{EQ}} \qquad\qquad (6.4)$$

Therefore I_{acfpm} is determined according to a single AC side voltage source V_{ac} and an equivalent impedance Z_{EQ}. For the VSC model applied in the RTDS, (3.6) determines the peak current magnitude exactly as the VSC valve voltage is set to zero and the DC fault impedance is not apparent on the AC side of the VSC.

In the SimPowerSystems model, (3.6) is not accurate in determining I_{acfpm}. This is because the voltage across the VSC valve stack is not always zero due to the operation of the anti-parallel diodes and therefore a voltage is produced which opposes the fault current. In addition, the DC side fault impedance is represented on the AC-side as discussed in Chapter 3 which will also impede the fault current.

It would have been possible to modify the arm reactance of the VSCs implemented on the RTDS to reduce the fault current to that seen on the SimPowerSystems model, which is considered as more realistic. However, this would have required the re-tuning of all the control loops of those converters which will have altered the system dynamic response.

In addition, re-arranging (3.6) to determine an equivalent impedance of the VSC model for a given peak fault current will always yield a larger than necessary impedance. This is because (3.6) represents the worst case scenario when the DC fault impedance is zero and the voltage across the VSC valve stacks are zero.

Therefore, the result seen from the RTDS represents the worst case scenario with the highest permissible fault current.

As side from the difference in fault current, the results are very similar. In both cases, a new post-fault operating point is identified and communicated to the offshore VSCs and FRC-WTs. All offshore VSCs and FRC-WTs are able to adopt the new operating condition with no violation of network constraints once the fault is cleared. The loss of infeed to the MITS is restricted to the loss of a single link in both results.

7 Chapter 7 – Conclusions and Further Work

7.1 Conclusions

7.1.1 Managing planned changes in operating condition in an offshore AC hub

It is widely anticipated that by 2050, significant investment in energy infrastructure will result in the development of a pan-European Supergrid. The offshore AC hub has been identified as a feasible infrastructure solution for implementation in a future pan-European Supergrid.

A model of the offshore AC hub has been developed in SimPowerSystems$^{\text{TM}}$ using the round three offshore wind development zone Dogger Bank, as a case study. Dynamic models of the VSCs and FRC-WTs are implemented using averaged models. Appropriate modifications to these models are made to properly represent the impact of faults. Vector control loops are implemented for control of local variables, which are tuned using formal control design techniques.

Two common control philosophies, master-slave and droop control, which are developed for point-to-point HVDC transmission links are extended to account for parallel operation in the offshore AC hub. It is shown that both the master-slave and droop control schemes can successfully manage the voltage, current and complex power flow in the offshore AC hub following a change in dispatch orders and with varying wind power input.

Having compared the control philosophies, it is shown that the droop control strategy is able to maintain tighter control of the voltage and current profile throughout the offshore AC hub, well within the limits set in National Grids SQSS. This is because it is able to automatically balance complex power between participating VSCs.

7.1.2 Impacts of faults in an offshore AC hub

Three fault scenarios occurring in an offshore AC hub are simulated using the SimPowerSystems model. This includes:

- A DC pole to pole fault on one of the HVDC links connected to the UK MITS
- A 3-phase fault occurring on one of the HVAC bus bars within the offshore AC hub
- A 3-phase fault occurring on one of the HVAC cables which interconnect two adjacent HVDC platforms.

The impact of a DC pole-pole fault on a single HVDC link greatly affects the offshore AC hub and MITS. Excess fault current is shown to flow through healthy offshore VSCs which is likely to cause damage. In addition, the post-fault voltage profile was unacceptable due to power imbalance. Finally, the DC fault results in a significant loss of infeed to the MITS.

The impact of a 3ph fault on a single bus or HVAC cable circuit negatively affects the offshore AC hub and MITS. A significant over-voltage following clearance of the fault occurs which is beyond maximum equipment ratings. Once the fault is cleared, the system is shown to operating within acceptable limits, although the ability of the droop VSCs to share reactive power is impeded.

Based on the above outcomes it is concluded that additional action is required to manage the impacts of these faults if the offshore AC hub is to be a feasible offshore infrastructure solution.

7.1.3 Control systems for managing faults in an offshore AC hub

A de-centralised fault management system detailed in the literature has been implemented in the offshore AC hub model. The offshore AC hub model described in this thesis is larger and more complex than the model implemented in the literature.

Having applied a DC pole-pole fault with the de-centralised fault management system in operation, it was shown to function unsatisfactorily by worsening the

185

impact of the fault. Changes were made to the de-centralised method which allowed it to function correctly.

A novel centralised fault management method has been developed using an online OPF algorithm, called the AC hub controller. The online OPF is implemented using a gradient method solution algorithm. The algorithm is shown to be able to calculate a new post-fault operating condition, following an unplanned network event.

Two fault scenarios are used to compare the performance of each fault management strategy including:

- A DC pole to pole fault on one of the HVDC links connected to the UK MITS.
- A 3-phase fault occurring on one of the HVAC cables which interconnect two adjacent HVDC platforms.

The de-centralised method is shown to work effectively in the event of a DC pole-pole fault, which corrects power imbalance. However, during a 3ph fault, when no power imbalance is present, the de-centralised system actually exacerbates the problem. The centralised method is shown to operate satisfactorily following both faults, albeit that it relies more heavily on DC choppers to manage the fault current during the fault. It is concluded that the ideal system would incorporate elements of both schemes.

7.1.4 Experimental validation of centralised fault management systems applied in an offshore AC hub

An experimental platform has been developed to test the novel control system as hardware in the loop with an RTDS. The results from the SimPowerSystems model and from the RTDS are compared and generally show good agreement. A discrepancy in fault current is identified, however on closer inspection it is shown that this discrepancy is due to a modelling compromise because of hardware constraints with the RTDS.

The validity of the result is maintained as it is proven that the result from the RTDS is a worst case scenario. All offshore VSCs and FRC-WTs are able to

adopt a new operating condition with no violation of network constraints once the fault is cleared. The loss of infeed to the MITS is restricted to the loss of a single link in both results.

7.1.5 Main contributions of thesis

- To **design a suitable control system for operating an offshore AC hub under planned changes in operating conditions**. This was achieved through the implementation of both master-slave and droop control schemes.

- To **identify the implications of various faults in an offshore AC hub**. Faults were shown to heavily impact the offshore AC hub and cause significant loss of infeed to the MITS.

- To **design a suitable control system to manage the impacts of faults in an offshore AC hub**. A novel fault management system using an online OPF algorithm has been presented. It is compared with a de-centralised method adapted from the literature.

- To **design and build an experiment using hardware in the loop to demonstrate and validate the novel control system for managing the impact of faults in an offshore AC hub**. The novel fault management system was successfully implemented on a real time control platform as hardware-in-the-loop with a Real Time Digital Simulator (RTDS).

7.1.6 Main achievements of research

This research has resulted in the following achievements:

A presentation and poster was delivered to describe and compare topologies for the offshore node to industry professionals at the *CIGRE-UK conference*, 2012. It was titled: "Counting the number of IGBTs in competing offshore hub designs,".

A conference paper was written comparing the performance of two control philosophies applied in the offsore AC hub. The reference is as follows:

- J. Stevens and D. Rogers, "Control of multiple VSC-HVDC converters within an offshore AC-hub," in *2013 IEEE Energytech, Energytech 2013*, 2013, no. 11220744.

In addition, simulation results of this research were presented to industrial partners including Ove Arup & Partners ltd, National Grid and Alstom Grid. Also, presentations of the ongoing research were made to research peers at the annual university HVDC colloquium.

7.2 Further Work

Given the research outcomes of this thesis and building upon the work carried out, further progress on this line of research can be readily made. These possible avenues of research are listed below.

7.2.1 Combine the de-centralised and centralised fault management systems

It was identified in Chapter 5 of this thesis that both the de-centralised and centralised fault management systems have advantages. The de-centralised system was shown to operate during a DC link fault, thus managing fault current. A key benefit of the centralised system is its decision making ability, where it was shown to be able to distinguish whether or not a power imbalance is present in the offshore AC hub. In addition, it was shown that it could ensure the post-fault operating condition did not violate any network constraints.

It is proposed that these two systems be combined in to a single fault management solution. The de-centralised system could act during the fault to minimise fault current. The centralised system could then decide upon the appropriate action to take once the fault is cleared and then provide a suitable post-fault solution. To some extent, the communication requirements of the centralised system may be relaxed as the online OPF need only indicate to the de-centralised system whether to take action or not, with new orders issued after a short period.

7.2.2 Use of Particle Swarm Optimisation as solution algorithm for OPF

The solution algorithm used to solve the OPF within the AC hub controller was based on the gradient method. This was shown to give satisfactory results by removing any violation of constraints. One possible solution algorithm is particle swarm optimisation (PSO). This has some advantages over gradient method if larger networks were to be considered. In addition, if an objective function designed to optimise the post-fault network state (as opposed to only removing any violation of constraints), this could yield further scope and advantages for the centralised system.

8 References

[1]   UK Government, *Climate Change Act 2008*. 2008.

[2]   Decc, "The UK Renewable Energy Strategy," Department of Energy and Climate Change, 2009.

[3]   E. E. A. Technical, *Europe's onshore and offshore wind energy potential*, vol. 6, no. 6. Office for Official Publications of the European Communities, 2009.

[4]   National Grid, "Offshore Development Information Statement," 2010.

[5]   B. R. Andersen, "HVDC transmission-opportunities and challenges," *AC DC Power Transm. 2006. ACDC 2006. 8th IEE Int. Conf.*, pp. 24–29.

[6]   M. P. Bahrman, "HVDC transmission overview," in *2008 IEEE/PES Transmission and Distribution Conference and Exposition*, 2008, pp. 1–7.

[7]   N. Flourentzou, V. G. Agelidis, and G. D. Demetriades, "VSC-Based HVDC Power Transmission Systems: An Overview," *IEEE Trans. Power Electron.*, vol. 24, no. 3, pp. 592–602, Mar. 2009.

[8]   T. J. Hammons, V. F. Lescale, K. Uecker, M. Haeusler, D. Retzmann, K. Staschus, and S. Lepy, "State of the Art in Ultrahigh-Voltage Transmission," *Proc. IEEE*, no. 99, pp. 1–31, 2011.

[9]   The Energy and Climate Change Committee, "House of Commons Energy and Climate Change Committee A European Supergrid," 2011.

[10]   Friends of the Supergrid, "Position paper on the EC Communication for a European Infrastructure Package," Brussels, 2010.

[11]   OffshoreGrid, "OffshoreGrid : Offshore Electricity Infrastructure in Europe Offshore Electricity," 2011.

[12]   EWEA, "Oceans of Opportunity," 2009.

[13]   S. Gordon, "Supergrid to the rescue," *Power Eng.*, vol. 20, no. 5, pp. 30–33.

[14]   The European Parliament, "Guidelines for trans-European energy infrastructure," *Off. J. Eur. Union*, vol. 2013, no. 347, pp. 39–75, 2013.

[15]   ENTSO-E, "e-Highway 2050," 2013. [Online]. Available: http://www.e-highway2050.eu/e-highway2050/. [Accessed: 06-Jul-2015].

[16]   ENTSO-E, "The North Seas Countries' Offshore Grid Initiative (NSCOGI)," 2015. [Online]. Available: https://www.entsoe.eu/about-entso-e/system-development/the-north-seas-countries-offshore-grid-initiative-nscogi/Pages/default.aspx. [Accessed: 06-Jul-2015].

[17]   R. King, "Electrical Transmission Systems for Large Offshore Wind Farms," Cardiff University, 2011.

[18]   ABB, "XLPE Submarine Cable Systems Attachment to XLPE Land Cable Systems - User ´ s Guide."

[19]   D. Van Hertem, M. Ghandhari, and M. Delimar, "Technical limitations towards a SuperGrid — A European prospective," in *2010 IEEE International Energy Conference*, 2010, pp. 302–309.

[20]   I. M. de Alegría, J. L. Martín, I. Kortabarria, J. Andreu, and P. I. Ereño, "Transmission alternatives for offshore electrical power," *Renew. Sustain. Energy Rev.*, vol. 13, no. 5, pp. 1027–1038, Jun. 2009.

[21]   J. Arrillaga, Y. H. Liu, and N. R. Watson, *Flexible Power Transmission: The HVDC Options [Hardcover]*. Wiley-Blackwell, 2007.

[22]   ABB Semiconductors Ltd, "Phase Control Thyristor." Switzerland, pp. 1–7, 2014.

[23]   P. Kundur, *Power System Stability and Control*. McGraw-Hill Professional, 1994.

[24]   "ABB Xiangjiaba - Shanghai - ABB HVDC Reference Projects in Asia (HVDC References)." [Online]. Available: http://www.abb.com/industries/ap/db0003db004333/148bff3c00705c5ac12 5774900517d9d.aspx. [Accessed: 12-Sep-2012].

[25]   M. M. C. Merlin, T. C. Green, S. Member, P. D. Mitcheson, D. R. Trainer, R. Critchley, W. Crookes, and F. Hassan, "The Alternate Arm Converter : A New Hybrid Multilevel Converter With DC-Fault Blocking Capability," *IEEE Trans. Power Deliv.*, vol. 29, no. 1, pp. 310–317, 2014.

[26]   B. Jacobson, P. Karlsson, G. Asplund, L. Harnefors, and J. Tomas, "VSC-HVDC Transmission with Cascaded Two-Level Converters," Ludvika, Sweden, 2010.

[27]   P. Kundur, N. J. Balu, and M. G. Lauby, *Power system stability and control*. McGraw-Hill, 1994.

[28]   ABB, "BorWin1 | References - HVDC | ABB," 2015. [Online]. Available: http://new.abb.com/systems/hvdc/references/borwin1. [Accessed: 06-Jul-2015].

[29]   L. Livermore, "Integration of Offshore Wind Farms Through High Voltage Direct Current Networks," Cardiff University, 2013.

[30]   D. Van Hertem and M. Ghandhari, "Multi-terminal VSC HVDC for the European supergrid: Obstacles," *Renew. Sustain. Energy Rev.*, vol. 14, no. 9, pp. 3156–3163, Dec. 2010.

[31]   S. De Boeck, P. Tielens, W. Leterme, and D. Van Hertem, "Configurations and earthing of HVDC grids," in *2013 IEEE Power & Energy Society General Meeting*, 2013, pp. 1–5.

[32]   J. Häfner and B. Jacobson, "Proactive Hybrid HVDC Breakers - A key innovation for reliable HVDC grids," in *The electric power system of the future - Intergrating supergrids and microgrids.*, 2011.

[33]   TenneT, "Offshore projects," 2015. [Online]. Available: http://www.tennet.eu/de/en/grid-projects/offshore-projects.html. [Accessed: 08-Jul-2015].

[34]   A. Barth, G. D. Anna, M. Rapetti, and M. Siebert, "Projects BorWin2 and HelWin1 – Large Scale Multilevel Voltage-Sourced Converter Technology for Bundling of Offshore Windpower," in *CIGRE Session*, 2012, pp. 1–11.

[35]   ABB, "It's time to connect with offshore wind supplement," 2013.

[36]   Aalborg Universitet, "VECTOR CONTROL OF PMSG FOR GRID-CONNECTED WIND TURBINE APPLICATIONS," 2009.

[37]   B. Bahrani, S. Kenzelmann, and A. Rufer, "Multivariable-PI-Based Current Control of Voltage Source Converters With Superior Axis Decoupling Capability," *Ind. Electron. IEEE Trans.*, vol. 58, no. 7, pp. 3016–3026.

[38]   C. Schauder and H. Mehta, "Vector analysis and control of advanced static VAr compensators," *Gener. Transm. Distrib. IEE Proc. C*, vol. 140, no. 4, pp. 299–306.

[39]   ABB, "A powerful combination," 2015.

[40]   V. F. Lescale, P. Holmberg, R. Ottersten, and Y. J. Hafner, "Parallelling offshore wind farm HVDC ties on offshore side," 2012.

[41]   N. Pogaku, M. Prodanovic, and T. C. Green, "Modeling, Analysis and Testing of Autonomous Operation of an Inverter-Based Microgrid," *IEEE Trans. Power Electron.*, vol. 22, no. 2, pp. 613–625, Mar. 2007.

[42]   E. Barklund, N. Pogaku, M. Prodanovic, C. Hernandez-Aramburo, and T. C. Green, "Energy Management in Autonomous Microgrid Using

Stability-Constrained Droop Control of Inverters," *IEEE Trans. Power Electron.*, vol. 23, no. 5, pp. 2346–2352, Sep. 2008.

[43] Z. Liu, J. Liu, Y. Zhao, W. Bao, and Y. Zhang, "Output impedance modeling and stability criterion for parallel inverters with master-slave sharing scheme in AC distributed power system," in *2012 Twenty-Seventh Annual IEEE Applied Power Electronics Conference and Exposition (APEC)*, 2012, pp. 1907–1913.

[44] Y. Pei, G. Jiang, X. Yang, and Z. Wang, "Auto-master-slave control technique of parallel inverters in distributed AC power systems and UPS," in *2004 IEEE 35th Annual Power Electronics Specialists Conference (IEEE Cat. No.04CH37551)*, pp. 2050–2053.

[45] J. Descloux and M. A. Denis, "Protection contre les courts-circuits des réseaux à courant continu de forte puissance," 2013.

[46] T. Lianxiang and O. Boon-Teck, "Protection of VSC-multi-terminal HVDC against DC faults," in *2002 IEEE 33rd Annual IEEE Power Electronics Specialists Conference. Proceedings (Cat. No.02CH37289)*, vol. 2, pp. 719–724.

[47] L. Tang and B.-T. Ooi, "Elimination of 'Harmonic Transfer Through Converters' in VSC-Based Multiterminal DC Systems by AC/DC Decoupling," *IEEE Trans. Power Deliv.*, vol. 23, no. 1, pp. 402–409, Jan. 2008.

[48] BSI, *Technical Guidelines for Radial HVDC Networks*. UK: British Standards Online, 2014.

[49] M. Bazargan, "DC fault analysis of MMC based HVDC system for large offshore wind farm integration," in *2nd IET Renewable Power Generation Conference (RPG 2013)*, 2013, pp. 2.10–2.10.

[50] L. Tang and B.-T. Ooi, "Locating and Isolating DC Faults in Multi-Terminal DC Systems," *IEEE Trans. Power Deliv.*, vol. 22, no. 3, pp. 1877–1884, Jul. 2007.

[51] J. Rafferty, D. J. Morrow, and L. Xu, "Analysis of VSC-based HVDC system under DC faults," in *IECON 2013 - 39th Annual Conference of the IEEE Industrial Electronics Society*, 2013, pp. 459–464.

[52] J. Yang, J. E. Fletcher, and J. O'Reilly, "Multiterminal DC Wind Farm Collection Grid Internal Fault Analysis and Protection Design," *IEEE Trans. Power Deliv.*, vol. 25, no. 4, pp. 2308–2318, Oct. 2010.

[53] Alstom Grid, "HVDC-VSC : transmission technology of the future," 2011. [Online]. Available:

http://www.alstom.com/Global/CleanGrid/Resources/Documents/HVDC-VSC transmission technology of the future - Think Grid n%C2%B08 .pdf.

[54] Alstom Grid, *Network Protection and Automation Guide - Protective Relays, Measurement & Control*. Alstom Grid, 2011.

[55] National Grid Electricity Transmission plc, *The Grid Code*, no. 5. 2015.

[56] G. Ramtharan, A. Arulampalam, J. B. Ekanayake, F. M. Hughes, and N. Jenkins, "Fault ride through of fully rated converter wind turbines with AC and DC transmission systems," *IET Renew. Power Gener.*, vol. 3, no. 4, pp. 426–438, 2009.

[57] S. K. Chaudhary, R. Teodorescu, P. Rodriguez, and P. C. Kjar, "Chopper controlled resistors in VSC-HVDC transmission for WPP with full-scale converters," in *2009 IEEE PES/IAS Conference on Sustainable Alternative Energy (SAE)*, 2009, pp. 1–8.

[58] H. Geng, G. Yang, D. (David) Xu, and B. Wu, "Unified Power Control for PMSG-Based WECS Operating Under Different Grid Conditions," *IEEE Trans. Energy Convers.*, vol. 26, no. 3, pp. 822–830, Sep. 2011.

[59] A. Johnson, N. Tleis, and J. Greasley, "The Development of Connection Requirements for Offshore Generation and Transmission in Great Britain (GB)," no. Summer, pp. 1–8, 2009.

[60] C. Feltes, H. Wrede, F. W. Koch, and I. Erlich, "Enhanced Fault Ride-Through Method for Wind Farms Connected to the Grid Through VSC-Based HVDC Transmission," *IEEE Trans. Power Syst.*, vol. 24, no. 3, pp. 1537–1546, 2009.

[61] L. Xu and B. R. Andersen, "Grid connection of large offshore wind farms using HVDC," *Wind Energy*, vol. 9, no. 4, pp. 371–382, Jul. 2006.

[62] X. Hu, J. Liang, D. J. Rogers, and Y. Li, "Power Flow and Power Reduction Control Using Variable Frequency of Offshore AC Grids," *IEEE Trans. Power Syst.*, vol. 28, no. 4, pp. 3897–3905, Nov. 2013.

[63] J. J. Grainger and W. D. Stevenson, *Power System Analysis*. McGraw-Hill, 1994.

[64] R. Bacher, *Optimization in Planning and Operation of Electric Power Systems*. Heidelberg: Physica-Verlag HD, 1993.

[65] A. von Meier, *Electric Power Systems: A Conceptual Introduction*. John Wiley & Sons, 2006.

[66] J. D. Weber, "IMPLEMENTATION OF A NEWTON-BASED OPTIMAL POWER FLOW INTO A POWER SYSTEM SIMULATION ENVIRONMENT," University of Illinois, 1997.

[67] R. V Amarnath and N. V Ramana, "STATE OF ART IN OPTIMAL POWER FLOWSOLUTION METHODOLOGIES."

[68] H. Dommel and W. Tinney, "Optimal Power Flow Solutions," *IEEE Trans. Power Appar. Syst.*, vol. PAS-87, no. 10, pp. 1866–1876, Oct. 1968.

[69] M. M. A. Abdelaziz, H. E. Farag, E. F. El-Saadany, and Y. A.-R. I. Mohamed, "A Novel and Generalized Three-Phase Power Flow Algorithm for Islanded Microgrids Using a Newton Trust Region Method," *IEEE Trans. Power Syst.*, vol. 28, no. 1, pp. 190–201, Feb. 2013.

[70] M. Bjelogrlic, M. S. Calovic, P. Ristanovic, and B. S. Babic, "Application of Newton's optimal power flow in voltage/reactive power control," *IEEE Trans. Power Syst.*, vol. 5, no. 4, pp. 1447–1454, 1990.

[71] M. Huneault and F. D. Galiana, "A survey of the optimal power flow literature," *IEEE Trans. Power Syst.*, vol. 6, no. 2, pp. 762–770, May 1991.

[72] M. a. Abido, "Optimal power flow using particle swarm optimization," *Int. J. Electr. Power Energy Syst.*, vol. 24, pp. 563–571, 2002.

[73] M. M. A. Abdelaziz and E. F. El-Saadany, "Maximum loadability consideration in droop-controlled islanded microgrids optimal power flow," *Electr. Power Syst. Res.*, vol. 106, pp. 168–179, Jan. 2014.

[74] M. J. Dolan, E. M. Davidson, I. Kockar, G. W. Ault, and S. D. J. McArthur, "Distribution Power Flow Management Utilizing an Online Optimal Power Flow Technique," *IEEE Trans. Power Syst.*, vol. 27, no. 2, pp. 790–799, May 2012.

[75] CIGRE Working Group B3.26, "Guidelines for the Design and Construction of AC Offshore Substations for Wind Power Plants," 2012.

[76] IEC, *Communication networks and systems for power utility automation*. UK, 2013.

[77] National Grid, "National Electricity Transmission System Security and Quality of Supply Standard," *Security*, 2014.

[78] Forewind, "Forewind - Zone development." [Online]. Available: http://www.forewind.co.uk/zone-development/zone-development-overview.html. [Accessed: 20-Jul-2012].

[79] REPower, "REpower 5M – Proven Technology in New Dimensions." pp. 1–3.

[80] BSI, *BS IEC 60287: Electric cables — Calculation of the current rating.* UK, 2006.

[81] J. J. Grainger and W. D. Stevenson, *Power system analysis*. McGraw-Hill, 1994.

[82] M. Heathcote, *J & P Transformer Book*. Newnes, 2011.

[83] "The Smart Way." [Online]. Available: http://www.energy.siemens.com/hq/pool/hq/power-transmission/HVDC/HVDC-PLUS/HVDC-PLUS_The-Smart-Way.pdf. [Accessed: 11-Dec-2014].

[84] M. Merlin and T. Green, "Cell Capacitor Sizing in Multilevel Converters: Cases of the MMC and AAC." Institution of Engineering and Technology, 28-Oct-2014.

[85] J. Peralta, H. Saad, S. Dennetiere, J. Mahseredjian, and S. Nguefeu, "Detailed and Averaged Models for a 401-Level MMC–HVDC System," *IEEE Trans. Power Deliv.*, vol. 27, no. 3, pp. 1501–1508, Jul. 2012.

[86] H. Saad, J. Peralta, S. Dennetiere, J. Mahseredjian, J. Jatskevich, J. A. Martinez, A. Davoudi, M. Saeedifard, V. Sood, X. Wang, J. Cano, and A. Mehrizi-Sani, "Dynamic Averaged and Simplified Models for MMC-Based HVDC Transmission Systems," *IEEE Trans. Power Deliv.*, vol. 28, no. 3, pp. 1723–1730, Jul. 2013.

[87] X. Li, Q. Song, W. Liu, H. Rao, S. Xu, and L. Li, "Protection of Nonpermanent Faults on DC Overhead Lines in MMC-Based HVDC Systems," *IEEE Trans. Power Deliv.*, vol. 28, no. 1, pp. 483–490, Jan. 2013.

[88] N. R. Chaudhuri and A. Yazdani, "An aggregation scheme for offshore wind farms with VSC-based HVDC collection system," in *2011 IEEE Power and Energy Society General Meeting*, 2011, pp. 1–8.

[89] A. Yazdani and R. Iravani, *Voltage-Sourced Converters in Power Systems: Modeling, Control, and Applications*. John Wiley & Sons, 2010.

[90] N. S. Nise, *Control Systems Engineering*, Fifth Edit. John Wiley & Sons, 2008.

[91] M. Liserre *, F. Blaabjerg, and A. Dell'Aquila, "Step-by-step design procedure for a grid-connected three-phase PWM voltage source converter," *Int. J. Electron.*, vol. 91, no. 8, pp. 445–460, Aug. 2004.

[92] N. Pogaku, M. Prodanovic, and T. C. Green, "Inverter-based microgrids: small-signal modelling and testing," *Power Electron. Mach. Drives, 2006. PEMD 2006. 3rd IET Int. Conf.*, pp. 499–504.

[93] L. Zhang, "SECURITY AND RELIABILITY OF ELECTRIC POWER SYSTEMS Œ Power System Reliability and Transfer Capability Improvement by VSC- HVDC (HVDC Light ©)," in *Cigré Conference in Estonia*, 2007, pp. 1–7.

[94] J. G. Slootweg, S. W. H. de Haan, H. Polinder, and W. L. Kling, "General model for representing variable speed wind turbines in power system dynamics simulations," *IEEE Trans. Power Syst.*, vol. 18, no. 1, pp. 144–151, Feb. 2003.

[95] N. Stannard and J. R. Bumby, "Performance aspects of mains connected small-scale wind turbines," *Gener. Transm. Distrib. IET*, vol. 1, no. 2, p. 324, 2007.

[96] National Grid, *National Electricity Transmission System Security and Quality of Supply Standard*. United Kingdom, 2012.

[97] L. Xu, L. Yao, and C. Sasse, "Grid Integration of Large DFIG-Based Wind Farms Using VSC Transmission," *IEEE Trans. Power Syst.*, vol. 22, no. 3, pp. 976–984, Aug. 2007.

[98] Power Systems Relay Committee, "IEEE Guide for Power System Protective Relay Applications Over Digital Communication Channels IEEE Power and Energy Society," no. April. 2013.

[99] RTDS Technologies, "RTDS: Power System User's Manual." .

[100] H. Dommel, "Digital Computer Solution of Electromagnetic Transients in Single-and Multiphase Networks," *IEEE Trans. Power Appar. Syst.*, vol. PAS-88, no. 4, pp. 388–399, Apr. 1969.

[101] dSPACE GmbH, "dSPACE – ControlDesk Next Generation," 2015. [Online]. Available: https://www.dspace.com/en/ltd/home/products/sw/experimentandvisualization/controldesk.cfm. [Accessed: 29-Jun-2015].

[102] DNP Users Group, "DNP - Overview of the DNP3 Protocol," 2011. [Online]. Available: https://www.dnp.org/Pages/AboutDefault.aspx. [Accessed: 29-Jun-2015].

[103] OPC Foundation, "What is OPC? - OPC Foundation," 2015. [Online]. Available: https://opcfoundation.org/about/what-is-opc/. [Accessed: 29-Jun-2015].

[104] "OPC Toolbox - MATLAB - MathWorks United Kingdom," *The MathWorks, Inc.*, 2015. [Online]. Available: http://uk.mathworks.com/products/opc/?s_tid=srchtitle. [Accessed: 29-Jun-2015].

[105] T. M. Inc, "Electrical Power Systems Simulation - SimPowerSystems - Simulink." [Online]. Available: http://uk.mathworks.com/products/simpower/. [Accessed: 11-May-2015].

A. Appendix – Optimal Power Flow formulation

An algorithm has been developed to identify a feasible post-fault operating condition following a fault in an offshore AC hub. At present, the only requirement of the post-fault operating condition is that all network constraints are honoured. A future aim is to ensure that an operating condition is found which maximises transmission capacity through the remaining healthy transmission links.

The post-fault operating condition is found using a classical optimal power flow (OPF) method known as the gradient method. In this application, the gradient method is an extension of the Newton-Raphson power flow method as defined in [68]. The objective of the Newton-Raphson power flow is to solve a set of non-linear power flow equations for a given fixed network. The key information obtained from the power flow is the voltage magnitude, voltage angle and power flow between nodes [81]. The single line diagram (SLD) of the electrical network used in this work is given in Figure 1.
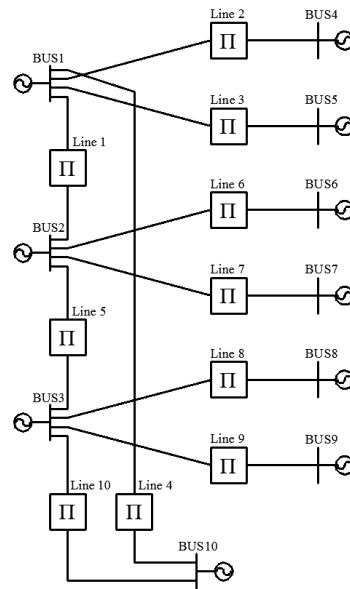
Figure 8.1 - 10 bus equivalent model of AC-hub

Each of the transmission lines shown in the SLD of the network is represented by a nominal pi-section and hence consists of series impedance and shunt capacitance which is split between each end of the line. The network consists of

198

10 buses in total. Buses 1, 2 and 3 are droop controlled generator buses which collectively maintain voltage and frequency while distributing active (P_g) and reactive (Q_g) power generation between them as determined by their respective droop gains. Buses 4 to 10 are generator buses which are available for dispatch. Note that in this application as all buses have active sources connected to them, which represent Voltage Source Converters (VSCs), they are all considered as generator buses. Of course it is necessary that some of these buses absorb active power (i.e. like a classical load) hence this is treated as negative generation.

A.1.   Newton-Raphson Power-flow solution:

A typical branch element Y_{ij} of the network is defined as:

$$Y_{ij} = |Y_{ij}|\angle\theta_{ij} = |Y_{ij}|\cos\theta_{ij} + j|Y_{ij}|\sin\theta_{ij}$$
$$= G_{ij} + jB_{ij}$$
(8.1)

The voltage at any bus i in the network is defined as:

$$V_i = |V_i|\angle\delta_i$$
(8.2)

Denoting P_i and Q_i as the net real and reactive powers entering the network at bus i and accounting for all branches connected to bus i, the following power flow equations can be written:

$$P_i = \sum_{n=1}^{N} |Y_{in}V_iV_n|\cos(\theta_{in} + \delta_n - \delta_i)$$
(8.3)

$$Q_i = -\sum_{n=1}^{N} |Y_{in}V_iV_n|\sin(\theta_{in} + \delta_n - \delta_i)$$
(8.4)

Now letting P_{gi} and P_{di} denote the scheduled active power generation and demand at bus i respectively and Q_{gi} and Q_{di} denote the scheduled reactive power generation and demand at bus i respectively, the active and reactive power mismatch is given by:

$$\Delta P_i = (P_{gi} - P_{di}) - P_i$$
(8.5)

$$\Delta Q_i = (Q_{gi} - Q_{di}) - Q_i \qquad (8.6)$$

In solving the power-flow problem the goal becomes to reduce the power mismatch to zero. This ensures that the power calculated flowing into the bus is equal to the scheduled power generation minus scheduled demand. When this conditioned is achieved, the power-balance equations can be written:

$$g_{i\prime} = P_i - (P_{gi} - P_{di}) = 0 \qquad (8.7)$$

$$g_{i\prime\prime} = Q_i - (Q_{gi} - Q_{di}) = 0 \qquad (8.8)$$

For a standard Newton-Raphson power flow, there are four potentially unknown quantities associated with each bus i including P_i, Q_i, δ_i and $|V_i|$. In addition, there are up to two equality constraint equations associated with each bus i. The general practise in power flow studies is to identify each bus i from three types of buses in the network. For each bus type two of the four quantities are specified and the other two remain unknown. The three types of buses include:

1. Slack bus (reference bus): δ_i and $|V_i|$ are specified, P_i and Q_i are unknown (usually node 1).
2. Load bus (PQ bus): P_i and Q_i are specified, δ_i and $|V_i|$ are unknown.
3. Voltage controlled bus (PV bus): P_i and $|V_i|$ are specified, δ_i and Q_i are unknown.

If the master-slave control scheme were implemented in the offshore AC hub, this would correspond to Bus 1 being defined as the slack bus and buses 2:10 being defined as PQ buses. Therefore, a vector $[x]$ of all unknown variables and a vector $[y]$ of all specified variables can be defined:

$$
\begin{aligned}
[x] &= [\delta_{2:10}, \ V_{2:10}]\text{'} \\
[y] &= [\delta_1, \ V_1, \ P_{2:10}, \ Q_{2:10}]\text{'}
\end{aligned}
\qquad (8.9)
$$

Defining $[g]$ as the vector of mismatch equations:

$$
[g(x,y)] =
\begin{bmatrix}
P_{2:10}(\delta_{1:10}, V_{1:10}) - (P_{g2:10} - P_{d2:10}) = 0 \\
Q_{2:10}(\delta_{1:10}, V_{1:10}) - (Q_{g2:10} - Q_{d2:10}) = 0
\end{bmatrix}
\qquad (8.10)
$$

Using Newton's method, a linear system of mismatch equations is defined:

$$J^0[\Delta x^0] = [\Delta g^0] \tag{8.11}$$

Where $[\Delta x^0]$ is a vector of the initial changes in $[x]$, $[\Delta g^0]$ is a vector of the initial changes in $[g]$ and J^0 is an initial matrix of $\left[\frac{\partial g}{\partial x}\right]$, otherwise known as the Jacobian.

By solving for $[\Delta x^0]$, new values for the unknown variables in $[x]$ are identified:

$$[x^1] = [x^0] + [\Delta x^0] \tag{8.12}$$

Repeating this process until the changes in $[x]$ become so small that they satisfy a chosen precision index $\varepsilon > 0$; that is, until $[\Delta x]$ are both less than ε.

The Jacobian index is defined as follows:

$$J = \left[\frac{\partial g}{\partial x}\right] = \begin{bmatrix} \dfrac{\partial P}{\partial \delta} & |V|\dfrac{\partial P}{\partial |V|} \\[2mm] \dfrac{\partial Q}{\partial \delta} & |V|\dfrac{\partial Q}{\partial |V|} \end{bmatrix} \tag{8.13}$$

Where,

$$\frac{\partial P}{\partial \delta} = \begin{bmatrix} \dfrac{\partial P_2}{\partial \delta_2} & \cdots & \dfrac{\partial P_2}{\partial \delta_{10}} \\ \vdots & \ddots & \vdots \\ \dfrac{\partial P_{10}}{\partial \delta_2} & \cdots & \dfrac{\partial P_{10}}{\partial \delta_{10}} \end{bmatrix}; |V|\frac{\partial P}{\partial |V|} =$$

$$\begin{bmatrix} |V_2|\dfrac{\partial P_2}{\partial |V_2|} & \cdots & |V_{10}|\dfrac{\partial P_2}{\partial |V_{10}|} \\ \vdots & \ddots & \vdots \\ |V_2|\dfrac{\partial P_{10}}{\partial |V_2|} & \cdots & |V_{10}|\dfrac{\partial P_{10}}{\partial |V_{10}|} \end{bmatrix};$$

$$\frac{\partial P}{\partial \delta} = \begin{bmatrix} \dfrac{\partial Q_2}{\partial \delta_2} & \cdots & \dfrac{\partial Q_2}{\partial \delta_{10}} \\ \vdots & \ddots & \vdots \\ \dfrac{\partial Q_{10}}{\partial \delta_2} & \cdots & \dfrac{\partial Q_{10}}{\partial \delta_{10}} \end{bmatrix}; |V|\frac{\partial P}{\partial |V|} = \tag{8.14}$$

$$\begin{bmatrix} |V_2|\dfrac{\partial Q_2}{\partial |V_2|} & \cdots & |V_{10}|\dfrac{\partial Q_2}{\partial |V_{10}|} \\ \vdots & \ddots & \vdots \\ |V_2|\dfrac{\partial Q_{10}}{\partial |V_2|} & \cdots & |V_{10}|\dfrac{\partial Q_{10}}{\partial |V_{10}|} \end{bmatrix};$$

And,

$$\frac{\partial P_i}{\partial \delta_j} = -\left|V_i V_j Y_{ij}\right| \sin\left(\theta_{ij} + \delta_j - \delta_i\right)$$

$$\frac{\partial P_i}{\partial \delta_i} = \sum_{\substack{n=1 \\ n \neq i}}^{N} \left|V_i V_n Y_{in}\right| \sin(\theta_{in} + \delta_n - \delta_i)$$

$$\frac{\partial Q_i}{\partial \delta_j} = -\left|V_i V_j Y_{ij}\right| \cos\left(\theta_{ij} + \delta_j - \delta_i\right)$$

$$\frac{\partial Q_i}{\partial \delta_i} = \sum_{\substack{n=1 \\ n \neq i}}^{N} \left|V_i V_n Y_{in}\right| \sin(\theta_{in} + \delta_n - \delta_i) \tag{8.15}$$

$$\left|V_j\right| \frac{\partial P_i}{\partial |V_j|} = -\frac{\partial Q_i}{\partial \delta_j}$$

$$\left|V_i\right| \frac{\partial P_i}{\partial |V_i|} = \frac{\partial Q_i}{\partial \delta_i} + 2|V_i|^2 G_{ii}$$

$$\left|V_j\right| \frac{\partial Q_i}{\partial |V_j|} = \frac{\partial P_i}{\partial \delta_j}$$

$$\left|V_i\right| \frac{\partial Q_i}{\partial |V_i|} = -\frac{\partial P_i}{\partial \delta_i} - 2|V_i|^2 B_{ii}$$

A.2. Newton-Raphson power flow with droop control:

It is assumed that droop control will be used in the offshore AC hub. This implies that there is no single slack bus, which maintains the power balance in the network but rather three buses acting equally to share control of the power balance. In addition, the voltage and frequency are no longer fixed at any single point in the network. To account for this, additional terms must be specified in the Newton-Raphson power flow.

For each droop controlled bus i, the active and reactive power is determined as follows:

$$P_{gi} = -K_{wi}(\omega_i - \omega_{i0}) \tag{8.16}$$

$$Q_{gi} = -K_{vi}(V_i - V_{i0}) \tag{8.17}$$

The power mismatch equations for each droop controlled bus i are defined in equations (8.18) and (8.19). For non-droop controlled buses, they are defined in equations (8.7) and (8.8).

$$g_{i\prime} = \sum_{n=1}^{N} |Y_{in}V_iV_n| \cos(\theta_{in} + \delta_n - \delta_i)$$
$$- (-K_{wi}(\omega - \omega_{i0}) - P_{di}) = 0 \tag{8.18}$$

$$g_{i\prime\prime} = -\sum_{n=1}^{N} |Y_{in}V_iV_n| \sin(\theta_{in} + \delta_n - \delta_i)$$
$$- (-K_{vi}(V_i - V_{i0}) - Q_{di}) = 0 \tag{8.19}$$

Therefore, a vector $[x]$ of all unknown variables and a vector $[y]$ of all specified variables can be defined:

$$[x] = [\delta_{1:10}, V_{1:10}, \omega]$$
$$[y] = \left[P_{4:10}, Q_{4:10}, K_{wi_{1:3}}, K_{vi_{1:3}}, \omega_{i0_{1:3}}, V_{i0_{1:3}} \right] \tag{8.20}$$

The Jacobian is defined as follows:

$$\mathbf{J} = \left[\frac{\partial g}{\partial x}\right] = \begin{bmatrix} \dfrac{\partial P}{\partial \delta} & |V|\dfrac{\partial P}{\partial |V|} & \dfrac{\partial P}{\partial \omega} \\ \dfrac{\partial Q}{\partial \delta} & |V|\dfrac{\partial Q}{\partial |V|} & \dfrac{\partial Q}{\partial \omega} \end{bmatrix} \tag{8.21}$$

Where,

$$\frac{\partial P}{\partial \delta} = \begin{bmatrix} \dfrac{\partial P_1}{\partial \delta_1} & \cdots & \dfrac{\partial P_1}{\partial \delta_{10}} \\ \vdots & \ddots & \vdots \\ \dfrac{\partial P_{10}}{\partial \delta_1} & \cdots & \dfrac{\partial P_{10}}{\partial \delta_{10}} \end{bmatrix} \quad |V|\frac{\partial P}{\partial |V|} = \begin{bmatrix} |V_1|\dfrac{\partial P_1}{\partial |V_1|} & \cdots & |V_{10}|\dfrac{\partial P_1}{\partial |V_{10}|} \\ \vdots & \ddots & \vdots \\ |V_2|\dfrac{\partial P_{10}}{\partial |V_1|} & \cdots & |V_{10}|\dfrac{\partial P_{10}}{\partial |V_{10}|} \end{bmatrix} \quad \frac{\partial P}{\partial \omega} = \begin{bmatrix} \dfrac{\partial P_1}{\partial \omega} \\ \vdots \\ \dfrac{\partial P_{10}}{\partial \omega} \end{bmatrix}$$

$$\frac{\partial P}{\partial \delta} = \begin{bmatrix} \dfrac{\partial Q_1}{\partial \delta_1} & \cdots & \dfrac{\partial Q_1}{\partial \delta_{10}} \\ \vdots & \ddots & \vdots \\ \dfrac{\partial Q_{10}}{\partial \delta_1} & \cdots & \dfrac{\partial Q_{10}}{\partial \delta_{10}} \end{bmatrix} \quad |V|\frac{\partial P}{\partial |V|} = \begin{bmatrix} |V_1|\dfrac{\partial Q_1}{\partial |V_1|} & \cdots & |V_{10}|\dfrac{\partial Q_1}{\partial |V_{10}|} \\ \vdots & \ddots & \vdots \\ |V_1|\dfrac{\partial Q_{10}}{\partial |V_1|} & \cdots & |V_{10}|\dfrac{\partial Q_{10}}{\partial |V_{10}|} \end{bmatrix} \quad \frac{\partial Q}{\partial \omega} = \begin{bmatrix} \dfrac{\partial Q_1}{\partial \omega} \\ \vdots \\ \dfrac{\partial Q_{10}}{\partial \omega} \end{bmatrix} \tag{8.22}$$

And,

$$\frac{\partial P_i}{\partial \delta_j} = -|V_iV_jY_{ij}| \sin(\theta_{ij} + \delta_j - \delta_i) \tag{8.23}$$

$$\frac{\partial P_i}{\partial \delta_i} = \sum_{\substack{n=1 \\ n \neq i}}^{N} |V_i V_n Y_{in}| \sin(\theta_{in} + \delta_n - \delta_i)$$

$$\frac{\partial Q_i}{\partial \delta_j} = -|V_i V_j Y_{ij}| \cos(\theta_{ij} + \delta_j - \delta_i)$$

$$\frac{\partial Q_i}{\partial \delta_i} = \sum_{\substack{n=1 \\ n \neq i}}^{N} |V_i V_n Y_{in}| \sin(\theta_{in} + \delta_n - \delta_i)$$

$$|V_j|\frac{\partial P_i}{\partial |V_j|} = -\frac{\partial Q_i}{\partial \delta_j}$$

$$|V_i|\frac{\partial P_i}{\partial |V_i|} = \frac{\partial Q_i}{\partial \delta_i} + 2|V_i|^2 G_{ii}$$

$$|V_j|\frac{\partial Q_i}{\partial |V_j|} = \frac{\partial P_i}{\partial \delta_j}$$

$$|V_i|\frac{\partial Q_i}{\partial |V_i|} = -\frac{\partial P_i}{\partial \delta_i} - 2|V_i|^2 B_{ii} - |V_i|K_{vi}$$

$$\frac{\partial P}{\partial \omega} = -K_{wi}$$

$$\frac{\partial Q}{\partial \omega} = 0$$

A.3.   Optimal power flow without inequality constraints:

This application of the gradient method is an extension of the Newton-Raphson power flow method as defined in [68]. An objective function f is defined which must be minimised subject to equality and inequality constraints. To begin with the minimisation of losses is selected as an objective function:

$$f = \sum_{i=1}^{N} P_i = \sum_{i=1}^{N} P_{gi} \tag{8.24}$$

Where N is the total number of buses.

The generation of active power in the network is predominantly from the wind turbines, with the interconnector to Norway generating enough active power to utilise any excess transmission capacity. Correspondingly, buses 1 to 3 are the loads (although modelled as negative generation) within the network that transfer

the active power to the UK main interconnected transmission system (MITS). In this work, buses 1, 2 and 3 are droop controlled and buses 4 to 10 are PQ buses.

For the OPF, there is no change to the vector of unknown variables $[x]$ from that specified for the Newton-Raphson power flow, however the vector of specified variables $[y]$ is split up into control $[u]$ and fixed $[p]$ parameters.

In a normal operating condition, the active power output from the wind turbines is determined by the power exerted by the wind and therefore it must be considered a fixed parameter at any moment in time. The active power output from the interconnector to Norway must also be considered as fixed. The active power being absorbed by the HVDC links connected to the UK are available for dispatch and hence can be included as control parameters. Only droop controlled busses can contribute in reactive power control.

The following vectors are defined:

$$[x] = [\delta_{1:10}, V_{1:10}, \omega]$$
$$[u] = \left[K_{\omega i_{1:3}}, K_{v i_{1:3}}\right] \tag{8.25}$$
$$[p] = \left[P_{4:10}, Q_{4:10}, \omega_{i0_{1:3}}, V_{i0_{1:3}}\right]$$

Using the classical optimisation method of Lagrangian multipliers, the minimum of the objective function as defined in (8.24), subject to the equality constraints, is found by minimising the unconstrained Lagrangian function:

$$\mathcal{L}(x, u, p) = f(x, u) + [\lambda]^T [g(x, u, p) = 0] \tag{8.26}$$

Where $[\lambda]$ includes as many auxiliary variables λ_i as there are equality constraints. To obtain a minimum, the following conditions are required:

$$\left[\frac{\partial \mathcal{L}}{\partial x}\right] = \left[\frac{\partial f}{\partial x}\right] + \left[\frac{\partial g}{\partial x}\right]^T [\lambda] = 0$$
$$\left[\frac{\partial \mathcal{L}}{\partial u}\right] = \left[\frac{\partial f}{\partial u}\right] + \left[\frac{\partial g}{\partial u}\right]^T [\lambda] = 0 \tag{8.27}$$
$$\left[\frac{\partial \mathcal{L}}{\partial \lambda}\right] = [g(x, u, p)] = 0$$

Note that (8.27) contains the transpose of the Jacobian matrix from the Newton-Raphson power flow solution. Also note that $\left[\frac{\partial \mathcal{L}}{\partial u}\right] = [\nabla f]$, which is the gradient vector of the objective function.

The steps taken in performing the OPF algorithm is as follows:

1. Assume starting set of control variables [u]

The starting set of control variables are as defined as:

$$[u] = \left[K_{\omega i_{1:3}}, K_{vi_{1:3}}\right] \tag{8.28}$$

2. Solve NR power flow to ensure equality constraints are satisfied $(g(x, u, p) = 0)$)

A feasible power flow solution is found using Newton's method as described in section A.1 and section A.2, which yields the Jacobian matrix.

3. Define Lagrangian function $\mathcal{L}(x, u, p)$ and solve for Lagrange multipliers $[\lambda]$

The lagrangian function is defined as:

$$\mathcal{L}(x, u, p) = \sum_{i=1}^{10} P_{gi} + [\lambda_{1:20}]^T \begin{bmatrix} g_{1:10'} \\ g_{1:10''} \end{bmatrix} \tag{8.29}$$

Solving for the Lagrange multipliers:

$$[\lambda] = -\left[\frac{\partial g}{\partial x}\right]^{T-1} \left[\frac{\partial f}{\partial x}\right] \tag{8.30}$$

Where,

$$\left[\frac{\partial g}{\partial x}\right] = J$$

$$\left[\frac{\partial f}{\partial x}\right] = \begin{bmatrix} \sum \frac{\partial P}{\partial \delta} \\ \sum \frac{\partial P}{\partial |V|} \\ \sum \frac{\partial P}{\partial \omega} \end{bmatrix} \tag{8.31}$$

And,

$$\sum \frac{\partial P}{\partial \delta} = \begin{bmatrix} \dfrac{\partial P_1}{\partial \delta_1} + \cdots \dfrac{\partial P_1}{\partial \delta_{10}} \\ \vdots \quad + \cdots \quad \vdots \\ \dfrac{\partial P_{10}}{\partial \delta_1} + \cdots \dfrac{\partial P_{10}}{\partial \delta_{10}} \end{bmatrix}$$

$$\sum \frac{\partial P}{\partial |V|} = \begin{bmatrix} \dfrac{\partial P_1}{\partial |V_1|} + \cdots \dfrac{\partial P_1}{\partial |V_{10}|} \\ \vdots \quad + \cdots \quad \vdots \\ \dfrac{\partial P_{10}}{\partial |V_1|} + \cdots \dfrac{\partial P_{10}}{\partial |V_{10}|} \end{bmatrix} \tag{8.32}$$

$$\sum \frac{\partial P}{\partial \omega} = \begin{bmatrix} \dfrac{\partial P_1}{\partial \omega} \\ \vdots \\ \dfrac{\partial P_{10}}{\partial \omega} \end{bmatrix}$$

4. Compute gradient of objective function $[\nabla \mathcal{F}]$

The gradient of the objective function is defined by:

$$[\nabla f] = \left[\frac{\partial f}{\partial u}\right] + \left[\frac{\partial g}{\partial u}\right]^T [\lambda] \tag{8.33}$$

Where,

$$\left[\frac{\partial g}{\partial u}\right] = \begin{bmatrix} \dfrac{\partial g}{\partial K_\omega} \\ \dfrac{\partial g}{\partial K_v} \end{bmatrix}$$

$$\left[\frac{\partial f}{\partial u}\right] = \begin{bmatrix} \dfrac{\partial f}{\partial K_\omega} \\ \dfrac{\partial f}{\partial K_v} \end{bmatrix} \tag{8.34}$$

And,

$$\frac{\partial g_i}{\partial K_{\omega i}} = \omega - \omega_{i0} \; where \; i \in [u]$$

$$\frac{\partial g_i}{\partial K_{v i}} = V_i - V_{i0} \; where \; i \in [u]$$

$$\frac{\partial f_i}{\partial K_{\omega i}} = \omega - \omega_{i0} \; where \; i \in [u] \tag{8.35}$$

$$\frac{\partial f_i}{\partial K_{v i}} = 0 \; where \; i \in [u]$$

5. If gradient is within prescribed tolerance, the minimum has been reached

207

The maximum value of the gradient vector is then checked to see if it is less than the tolerance which is assumed as 1e-3.

6. Otherwise check feasible direction of steepest descent

The feasible direction of steepest descent $[r]$ is formed according to the following conditions:

$$r_i = \begin{cases} 0, & if \dfrac{\partial f}{\partial u_i} < 0 \ and \ u_i = u_i^{max} \\[2mm] 0, & if \dfrac{\partial f}{\partial u_i} > 0 \ and \ u_i = u_i^{min} \\[2mm] -\dfrac{\partial f}{\partial u_i}, & otherwise \end{cases} \qquad (8.36)$$

7. Find a new set of control variables $[u]_{new}$

$$[u^{new}] = [u^{old}] + [\Delta u] \qquad (8.37)$$

Where,

$$[\Delta u] = -kc[r] \qquad (8.38)$$

And,

$k = 1e - 6;$

$c = -\sum r_i^2\,;$

The linear parameter constraints of the elements in $[u]$ are also maintained by the following:

$$u_i = \begin{cases} u_i^{max}, & if \ (u_i + \Delta u_i) > u_i^{max} \\ u_i^{min}, & if (u_i + \Delta u_i) < u_i^{min} \\ u_i + \Delta u_i, & otherwise \end{cases} \qquad (8.39)$$

A.4. Constrained optimal power flow applied (including loss minimisation and inequality constraints):

The penalty method is used to implement these inequality constraints, therefore the objective function must include an additional term to account for the penalties of each active constraint:

$$f = \sum_{i=1}^{N} P_i + \sum_{j=1}^{M} w_j \qquad (8.40)$$

Where there are M violated functional inequality constraints. The physical constraints in the network that need to be considered include:

- Upper and lower voltage limits at all buses in the network
- Current limits flowing through each line
- Apparent power transfer limit through the VSCs

The following penalty functions are therefore applied:

w_{iV}

$$= \begin{cases} K_{iV}{}^{min}\left(V_i{}^{min} - V_i\right)^2 \cdot \mathrm{sgn}\left(V_i{}^{min} - V_i\right) \leq 0 \,; & V_i < V_i{}^{min} \\ 0 \,; & V_i{}^{min} \leq V_i \leq V_i{}^{max} \\ K_{iV}{}^{max}(V_i - V_i{}^{max})^2 \cdot \mathrm{sgn}(V_i - V_i{}^{max}) \leq 0 \,; & V_i > V_i{}^{max} \end{cases} \quad \begin{matrix}(8.41\\ )\end{matrix}$$

w_{iIf}

$$= \begin{cases} K_{iIf}\left(Y_a(V_m - V_n) - I_f{}^{max}\right)^2 \cdot \mathrm{sgn}\left(I_f - I_f{}^{max}\right) \leq 0 \,; I_f > I_f{}^{max} \\ 0 \,; \qquad\qquad\qquad\qquad\qquad\qquad 0 \leq I_f \leq I_f{}^{max} \end{cases} \quad \begin{matrix}(8.42\\ )\end{matrix}$$

w_{iIt}

$$= \begin{cases} K_{iIt}(Y_a(V_n - V_m) - I_t{}^{max})^2 \cdot \mathrm{sgn}(I_t - I_t{}^{max}) \leq 0 \,; I_t > I_t{}^{max} \\ 0 \,; \qquad\qquad\qquad\qquad\qquad\qquad 0 \leq I_t \leq I_t{}^{max} \end{cases} \quad \begin{matrix}(8.43\\ )\end{matrix}$$

w_{iMVA}

$$= \begin{cases} K_{iMVA}\left(\left(P_i{}^2 + Q_i{}^2\right) - (S_i{}^{max})^2\right)^2 \cdot \mathrm{sgn}(S_i - S_i{}^{max}) \leq 0 \,; S_i > S_i{}^{max} \\ 0 \,; \qquad\qquad\qquad\qquad\qquad\qquad\qquad 0 \leq S_i \leq S_i{}' \end{cases} \quad \begin{matrix}(8.44\\ )\end{matrix}$$

The steepness of the penalty function is determined by the applicable constants from $[k]$:

$$[k] = \left[K_{iV}{}^{min}, K_{iV}{}^{max}, K_{iIf}, K_{iIt}, K_{iMVA}\right] \qquad (8.45)$$

The values of $[k]$ for now are determined through trial and error.

The Lagrangian is updated to account for the inequality constraint functions as follows:

$$\mathcal{L}(x, u, p) = f(x, u) + [w]^T[h(x, u, p) \leq 0]$$
$$+ [\lambda]^T[g(x, u, p) = 0] \tag{8.46}$$

Therefore to obtain a minimum, it is assumed that the following is necessary:

$$\left[\frac{\partial \mathcal{L}}{\partial x}\right] = \left[\frac{\partial f}{\partial x}\right] + \left[\frac{\partial w}{\partial x}\right] + \left[\frac{\partial g}{\partial x}\right]^T [\lambda] = 0$$

$$\left[\frac{\partial \mathcal{L}}{\partial u}\right] = \left[\frac{\partial f}{\partial u}\right] + \left[\frac{\partial w}{\partial u}\right] + \left[\frac{\partial g}{\partial u}\right]^T [\lambda] = 0 \tag{8.47}$$

$$\left[\frac{\partial \mathcal{L}}{\partial \lambda}\right] = [g(x, u, p)] = 0$$

It is therefore necessary to obtain the partial differentials of each of the penalty functions in $[w]$ with respect to $[x]$ and $[u]$.

Partial differentials of voltage limit weighting functions:

$$\left[\frac{\partial w_{iV}{}^{min}}{\partial x}\right] = \left[\frac{\partial w_{iV}{}^{min}}{\partial |V_i|}\right] = -2K_{iV}{}^{min}|V_i|$$

$$\left[\frac{\partial w_{iV}{}^{min}}{\partial u}\right] = 0$$

$$\left[\frac{\partial w_{iV}{}^{max}}{\partial x}\right] = \left[\frac{\partial w_{iV}{}^{max}}{\partial |V_i|}\right] = 2K_{iV}{}^{max}|V_i| \tag{8.48}$$

$$\left[\frac{\partial w_{iV}{}^{max}}{\partial u}\right] = 0$$

Partial differentials of line current limit weighting functions:

$$\left[\frac{\partial w_{ilf}}{\partial x}\right] = \left[\frac{\partial w_{ilf}}{\partial \delta}\right] = Re\left(\frac{\partial w_{ilf}}{\partial \delta}\right) + Im\left(\frac{\partial w_{ilf}}{\partial \delta}\right)$$

$$\left[\frac{\partial w_{ilf}}{\partial x}\right] = \left[\frac{\partial w_{ilf}}{\partial |V_i|}\right] = Re\left(\frac{\partial w_{ilf}}{\partial |V_i|}\right) + Im\left(\frac{\partial w_{ilf}}{\partial |V_i|}\right)$$

$$\left[\frac{\partial W_{ilf}}{\partial u}\right] = 0$$

$$\left[\frac{\partial w_{ilt}}{\partial x}\right] = \left[\frac{\partial w_{ilt}}{\partial \delta}\right] = Re\left(\frac{\partial w_{ilt}}{\partial \delta}\right) + Im\left(\frac{\partial w_{ilt}}{\partial \delta}\right) \tag{8.49}$$

$$\left[\frac{\partial w_{ilt}}{\partial x}\right] = \left[\frac{\partial w_{ilt}}{\partial |V_i|}\right] = Re\left(\frac{\partial w_{ilt}}{\partial |V_i|}\right) + Im\left(\frac{\partial w_{ilt}}{\partial |V_i|}\right)$$

$$\left[\frac{\partial W_{ilf}}{\partial u}\right] = 0$$

And where,

$$\text{Re}\left(\frac{\partial w_{iIf}}{\partial \delta}\right) = 2K_{iIf}\left(Y_{ft}(V_f - V_t)\right)\left(\frac{\partial \text{Re}(w_{iIf})}{\partial \delta_f} + \frac{\partial \text{Re}(w_{iIf})}{\partial \delta_t}\right)$$

$$\text{Im}\left(\frac{\partial w_{iIf}}{\partial \delta}\right) = 2K_{iIf}\left(Y_{ft}(V_f - V_t)\right)\left(\frac{\partial \text{Im}(w_{iIf})}{\partial \delta_f} + \frac{\partial \text{Im}(w_{iIf})}{\partial \delta_t}\right)$$

$$\text{Re}\left(\frac{\partial w_{iIf}}{\partial |V|}\right) = 2K_{iIf}\left(Y_{ft}(V_f - V_t)\right)\left(\frac{\partial \text{Re}(w_{iIf})}{\partial |V_f|} + \frac{\partial \text{Re}(w_{iIf})}{\partial |V_t|}\right)$$

$$\text{Im}\left(\frac{\partial w_{iIf}}{\partial |V|}\right) = 2K_{iIf}\left(Y_{ft}(V_f - V_t)\right)\left(\frac{\partial \text{Im}(w_{iIf})}{\partial |V_f|} + \frac{\partial \text{Im}(w_{iIf})}{\partial |V_t|}\right)$$

$$\text{Re}\left(\frac{\partial w_{iIt}}{\partial \delta}\right) = 2K_{iIt}\left(Y_{ft}(V_t - V_f)\right)\left(\frac{\partial \text{Re}(w_{iIt})}{\partial \delta_f} + \frac{\partial \text{Re}(w_{iIt})}{\partial \delta_t}\right) \qquad (8.50)$$

$$\text{Im}\left(\frac{\partial w_{iIf}}{\partial \delta}\right) = 2K_{iIf}\left(Y_{ft}(V_t - V_f)\right)\left(\frac{\partial \text{Im}(w_{iIt})}{\partial \delta_f} + \frac{\partial \text{Im}(w_{iIt})}{\partial \delta_t}\right)$$

$$\text{Re}\left(\frac{\partial w_{iIf}}{\partial |V|}\right) = 2K_{iIf}\left(Y_{ft}(V_t - V_f)\right)\left(\frac{\partial \text{Re}(w_{iIt})}{\partial |V_f|} + \frac{\partial \text{Re}(w_{iIt})}{\partial |V_t|}\right)$$

$$\text{Im}\left(\frac{\partial w_{iIf}}{\partial |V|}\right) = 2K_{iIf}\left(Y_{ft}(V_t - V_f)\right)\left(\frac{\partial \text{Im}(w_{iIt})}{\partial |V_f|} + \frac{\partial \text{Im}(w_{iIt})}{\partial |V_t|}\right)$$

Given that the admittance between each bus is given by:

$$Y_{ft} = |Y_{ft}|\cos\theta_{ft} + |Y_{ft}|\sin\theta_{ft} \qquad (8.51)$$

Finally,

$$\frac{\partial \text{Re}(w_{iIf})}{\partial \delta_f} = \frac{\partial \text{Re}(w_{iIt})}{\partial \delta_f} = -|Y_{ft}|\cos\theta_{ft}|V_f|\sin\delta_f - |Y_{ft}|\sin\theta_{ft}|V_f|\cos\delta_f$$

$$\frac{\partial \text{Re}(w_{iIf})}{\partial \delta_t} = \frac{\partial \text{Re}(w_{iIt})}{\partial \delta_t} = |Y_{ft}|\cos\theta_{ft}|V_t|\sin\delta_t - |Y_{ft}|\sin\theta_{ft}|V_t|\cos\delta_t$$

$$\frac{\partial \text{Im}(w_{iIf})}{\partial \delta_f} = \frac{\partial \text{Im}(w_{iIt})}{\partial \delta_f} = |Y_{ft}|\cos\theta_{ft}|V_f|\cos\delta_f - |Y_{ft}|\sin\theta_{ft}|V_f|\sin\delta_f$$

$$\frac{\partial \text{Im}(w_{iIf})}{\partial \delta_t} = \frac{\partial \text{Im}(w_{iIt})}{\partial \delta_t} = |Y_{ft}|\cos\theta_{ft}|V_t|\cos\delta_t + |Y_{ft}|\sin\theta_{ft}|V_t|\sin\delta_t \qquad (8.52)$$

$$\frac{\partial \text{Re}(w_{iIf})}{\partial |V_f|} = \frac{\partial \text{Re}(w_{iIt})}{\partial |V_f|} = |Y_{ft}|\cos\theta_{ft}\cos\delta_f - |Y_{ft}|\sin\theta_{ft}\sin\delta_f$$

$$\frac{\partial \text{Re}(w_{iIf})}{\partial |V_t|} = \frac{\partial \text{Re}(w_{iIt})}{\partial |V_t|} = |Y_{ft}|\cos\theta_{ft}\cos\delta_t - |Y_{ft}|\sin\theta_{ft}\sin\delta_t$$

$$\frac{\partial \text{Im}(w_{ilf})}{\partial |V_f|} = \frac{\partial \text{Im}(w_{ilt})}{\partial |V_f|} = |Y_{ft}| \cos \theta_{ft} \sin \delta_f + |Y_{ft}| \sin \theta_{ft} \cos \delta_f$$

$$\frac{\partial \text{Im}(w_{ilf})}{\partial |V_t|} = \frac{\partial \text{Im}(w_{ilt})}{\partial |V_t|} = |Y_{ft}| \cos \theta_{ft} \sin \delta_t - |Y_{ft}| \sin \theta_{ft} \cos \delta_t$$

Partial differentials of apparent power limit weighting functions:

$$
\left[\frac{\partial w_{iMVA}}{\partial x}\right] = \begin{bmatrix} \dfrac{\partial w_{iMVA}}{\partial \delta_i} \\[2mm] \dfrac{\partial w_{iMVA}}{\partial |V_i|} \end{bmatrix}
$$

$$
= \begin{bmatrix} 4K_{iMVA}\left(\left(P_1(\delta_{1:10}, V_{1:10})^3 \cdot \dfrac{\partial P_1}{\partial \delta_{1:10}}\right) + \left(Q_1(\delta_{1:10}, V_{1:10})^3 \cdot \dfrac{\partial Q_1}{\partial \delta_{1:10}}\right)\right) \\[4mm] 4K_{iMVA}\left(\left(P_1(\delta_{1:10}, V_{1:10})^3 \cdot \dfrac{\partial P_1}{\partial |V_{1:10}|}\right) + \left(Q_1(\delta_{1:10}, V_{1:10})^3 \cdot \dfrac{\partial Q_1}{\partial |V_{1:10}|}\right)\right) \end{bmatrix} \quad (8.53)
$$

$$
\left[\frac{\partial w_{iMVA}}{\partial u}\right] = \begin{bmatrix} \dfrac{\partial w_{iMVA}}{\partial P_i} \\[2mm] \dfrac{\partial w_{iMVA}}{\partial Q_i} \end{bmatrix} = \begin{bmatrix} 4K_{iMVA}P_{gi}{}^3 \\[2mm] 4K_{iMVA}Q_{gi}{}^3 \end{bmatrix}, where\ i \in [u]
$$

The optimal power flow algorithm is then performed using the procedure described in section A.3 but including the necessary modifications to account for the penalty functions.

A.5. Constrained optimal power flow applied (inequality constraint minimisation only):

The OPF was considered with the goal of just eliminating physical constraints. The objective function then becomes as follows:

$$f = \sum_{j=1}^{M} w_j \qquad (8.54)$$

The Lagrangian is updated accordingly as follows:

$$\mathcal{L}(x, u, p) = [w]^T [h(x, u, p) \leq 0] \\ + [\lambda]^T [g(x, u, p) = 0] \qquad (8.55)$$

Therefore to obtain a minimum, it is assumed that the following is necessary:

$$\left[\frac{\partial \mathcal{L}}{\partial x}\right] = \left[\frac{\partial w}{\partial x}\right] + \left[\frac{\partial g}{\partial x}\right]^T [\lambda] = 0$$

$$\left[\frac{\partial \mathcal{L}}{\partial u}\right] = \left[\frac{\partial w}{\partial u}\right] + \left[\frac{\partial g}{\partial u}\right]^T [\lambda] = 0 \qquad (8.56)$$

$$\left[\frac{\partial \mathcal{L}}{\partial \lambda}\right] = [g(x, u, p)] = 0$$

Again, the same method as that described in section A.3 is utilised to reach a minimum condition.